

Theoretical models for Dark Matter: from WIMPs to Primordial Black Holes

RACCO, Davide

Abstract

Among the many candidates proposed to explain nature of Dark Matter, Weakly Interacting Massive Particles have been the most supported in the last decades, because of their natural explanation of the Dark Matter abundance and their connection to the hierarchy problem. Other intriguing candidates are Primordial Black Holes. In this Thesis we touch on both frameworks for the explanation of Dark Matter. As for WIMP candidates, we discuss two possible theoretical frameworks. On the side of Effective Field Theories, we propose a method to use them consistently for the recast of collider searches. As for simplified models, in presence of gauge anomalies we highlight the enhanced reach of indirect searches. Then we illustrate a model for the generation of Primordial Black Holes relying on the metastability of the Higgs vacuum. Another signature of this remarkable property of the Standard Model could be the generation of a background of gravitational waves.

Reference

RACCO, Davide. *Theoretical models for Dark Matter: from WIMPs to Primordial Black Holes*. Thèse de doctorat : Univ. Genève, 2018, no. Sc. 5256

DOI : [10.13097/archive-ouverte/unige:108633](https://doi.org/10.13097/archive-ouverte/unige:108633)

URN : [urn:nbn:ch:unige-1086338](http://nbn-resolving.org/urn:nbn:ch:unige-1086338)

Available at:

<http://archive-ouverte.unige.ch/unige:108633>

Disclaimer: layout of this document may differ from the published version.



UNIVERSITÉ
DE GENÈVE

UNIVERSITÉ DE GENÈVE
Section de Physique
Département de Physique Théorique

FACULTÉ DES SCIENCES
Professeur Antonio RIOTTO

Theoretical Models for Dark Matter: from WIMPs to Primordial Black Holes

THÈSE

présentée à la Faculté des sciences de l'Université de Genève
pour obtenir le grade de Docteur ès sciences, mention physique

par

Davide RACCO

de

Modena (Italie)

Thèse N° 5256

GENÈVE

Atelier de reproduction de la Section de Physique
2018



**UNIVERSITÉ
DE GENÈVE**

FACULTÉ DES SCIENCES

DOCTORAT ÈS SCIENCES, MENTION PHYSIQUE

Thèse de Monsieur Davide RACCO

intitulée :

**«Theoretical Models for Dark Matter:
from WIMPs to Primordial Black Holes»**

La Faculté des sciences, sur le préavis de Monsieur A. W. RIOTTO, professeur ordinaire et directeur de thèse (Département de physique théorique), Monsieur F. RIVA, professeur assistant (Département de physique théorique), Monsieur G. F. GIUDICE, professeur (Département de physique théorique, Organisation européenne pour la recherche nucléaire - CERN, Genève, Suisse), autorise l'impression de la présente thèse, sans exprimer d'opinion sur les propositions qui y sont énoncées.

Genève, le 10 septembre 2018

Thèse - 5256 -

Le Décanat

N.B. - La thèse doit porter la déclaration précédente et remplir les conditions énumérées dans les "Informations relatives aux thèses de doctorat à l'Université de Genève".

Abstract

The quest for Dark Matter is one of the most exciting domains in Physics. Among the many candidates proposed to explain its nature, Weakly Interacting Massive Particles have been the most supported in the last decades, because of their success in a natural explanation of the current Dark Matter abundance and their ubiquitous presence in models addressing the hierarchy problem. Other candidates that have been attracting some attention recently are Primordial Black Holes, which would have formed in the early history of the universe. In this Thesis we touch on both frameworks for the explanation of Dark Matter. As for WIMP candidates, we discuss the interplay between their experimental searches and theoretical frameworks. On the side of Effective Field Theories, we propose a method to use them consistently for the recast of collider searches. On the side of simplified models, in the presence of apparent gauge anomalies at low energies we highlight the enhanced reach of indirect searches. In the last part of this Thesis we illustrate a model for the generation of PBHs relying on a feature already present in the Standard Model, the metastability of the Higgs vacuum. Another signature of this remarkable property of the Standard Model could be the generation of a background of gravitational waves. The observation of either of these signatures would represent a spectacular confirmation of the metastability of the Higgs vacuum.

Acknowledgements

If you talk to a man in a language he understands, that goes to his head.

If you talk to him in his language, that goes to his heart.

– Nelson Mandela

La persona che merita più ringraziamenti alla fine di questi quattro anni di dottorato è *Toni Riotto*, per essere stato un costante punto di riferimento nella mia vita accademica e personale. Ricordo di quando parlammo una volta di come le collaborazioni siano più ricche ed efficaci quando si condivide una base di amicizia, e il mio dottorato con lui ne è stato uno splendido esempio. Mi sento onorato di averlo avuto come mentore durante quest'esperienza.

La segunda persona a quien quiero dar mis agradecimientos es *José Ramón Espinosa*, por todo el apoyo y la disponibilidad con las que acompañó mi estancia en Barcelona (sin dejar de lado su paciencia con mi aprendizaje del español). Aquellos seis meses constituyeron un período de los más felices durante mi doctorado, y por ello tengo que agradecerse en primer lugar.

I want to thank also *Vincent Desjacques*, *Andrey Katz*, *Alex Kehagias*, *Andrea Wulzer* and *Fabio Zwirner*, the other professors who accompanied me along this PhD with many teachings and precious suggestions.

Nei ringraziamenti ai miei collaboratori, meritano un posto d'onore *Matteo Biagetti*, *Enrico Morgante* e *Gabriele Franciolini*, per l'amicizia che ci lega e per il piacere con cui abbiamo collaborato nella ricerca e nell'insegnamento.

I think that most of my progresses during this PhD came from the collaboration with other PhD students and Postdocs, and I want to thank them in particular for everything we learnt together: *Fotis Farakos*, *Dani Figueroa*, *Ahmed Ismail*, *Thomas Jacques* and *Mohamed Rameez*.

Enfin, je veux remercier tous les autres professeurs et chercheurs du groupe de Cosmologie de l'Université de Genève avec qui j'ai partagé une partie de mon chemin. Merci en particulier à *Pierre Fleury*, pour son aide dans la révision du résumé.

Passando ai ringraziamenti privati, voglio citare innanzitutto *Davide Costanzo* e *Diego Mauro* della Casa della Gazzosa. Ricordo come iniziò tutto da un "Davide, mi è venuta un'idea luminosa: e se cercassimo casa insieme?", e ancora oggi, tra un "alè" e un "fiuu", ci sosteniamo quotidianamente.

Otros grandes amigos que han acompañado mi estancia ginebrina desde el principio son *Santiago Codesido* y *Sandra Espiñeira*. Gracias por todo lo que vivimos juntos, y lo que vendrá en el futuro.

Gli altri protagonisti della mia vita a Ginevra sono stati i membri dell'Italian Ghetto: *Vittorio Tansella*, *Marcello Spera*, *Sara Riccò*, *Giulia Cusin*, *Giuseppe Fanizza*, *Margherita Boselli*, *Tommaso Colombo*, *Tommaso Brotto*, *Giuseppe Licari* e *Davide Lombardo*. Grazie a voi non mi sono mai sentito lontano da casa.

Ringrazio profondamente la mia famiglia, per avermi sempre incoraggiato a perseguire il meglio e per avermi sostenuto in ogni momento.

Il ringraziamento finale va a *Margherita*, per tutto l'amore e il sostegno che mi ha dato, per la fiducia nel futuro che mi sa regalare, e per essere sempre al mio fianco.

Members of the Jury

Prof. **Antonio Riotto**

Département de Physique Théorique & Center for Astroparticle Physics
Université de Genève, Switzerland

Prof. **Gian Francesco Giudice**

Theoretical Physics Department
CERN, Switzerland

Prof. **Francesco Riva**

Département de Physique Théorique
Université de Genève, Switzerland

List of publications

Papers appearing in this thesis

- [1] D. Racco, A. Wulzer and F. Zwirner, *Robust collider limits on heavy-mediator Dark Matter*, JHEP **1505** (2015) 009, arXiv: [1502.04701](#).
- [2] A. Ismail, A. Katz and D. Racco, *On dark matter interactions with the Standard Model through an anomalous Z'* , JHEP **1710** (2017) 165, arXiv: [1707.00709](#).
- [3] J. R. Espinosa, D. Racco and A. Riotto, *A Cosmological Signature of the Standard Model Higgs Vacuum Instability: Primordial Black Holes as Dark Matter*, Phys. Rev. Lett. **120**, 121301 (2018), arXiv: [1710.11196](#).
- [4] J. R. Espinosa, D. Racco and A. Riotto, *Primordial Black Holes from Higgs Vacuum Instability: Avoiding Fine-tuning through an Ultraviolet Safe Mechanism*, to appear in JCAP, arXiv: [1804.07731](#).
- [5] J. R. Espinosa, D. Racco and A. Riotto, *A Cosmological Signature of the Standard Model Higgs Vacuum Instability: Gravitational Waves*, submitted to Eur. Phys. Jour. C, arXiv: [1804.07732](#).

Other journal papers

- [6] M. Biagetti, V. Desjacques, A. Kehagias, D. Racco and A. Riotto, *The Halo Boltzmann Equation*, JCAP **1604** (2016) no.04, 040, arXiv: [1508.07330](#).
- [7] E. Morgante, D. Racco, M. Rameez and A. Riotto, *The 750 GeV Diphoton excess, Dark Matter and Constraints from the IceCube experiment*, JHEP **1607** (2016) 141, arXiv: [1603.05592](#).
- [8] T. Jacques, A. Katz, E. Morgante, D. Racco, M. Rameez and A. Riotto, *Complementarity of DM searches in a consistent simplified model: the case of Z'* , JHEP **1610** (2016) 071, arXiv: [1605.06513](#).
- [9] F. Farakos, A. Kehagias, D. Racco and A. Riotto, *Scanning of the Supersymmetry Breaking Scale and the Gravitino Mass in Supergravity*, JHEP **1606** (2016) 120, arXiv: [1605.07631](#).

White papers and conference proceedings

- [10] J. Abdallah *et al.*, *Simplified Models for Dark Matter Searches at the LHC*, Phys. Dark Univ. **9-10** (2015) 8, arXiv: [1506.03116](#).
- [11] D. Abercrombie *et al.*, *Dark Matter Benchmark Models for Early LHC Run-2 Searches: Report of the ATLAS/CMS Dark Matter Forum*, arXiv: [1507.00966](#).

- [12] D. RACCO, *Robust Collider Limits on Heavy-mediator Dark Matter*, Frascati Phys. Ser. **61** (2016) 133, [Link to Fulltext](#).

Résumé

Un des plus grands mystères dans notre compréhension de l'univers est la composition de plus de 80% de la matière dans le cosmos. Depuis près d'un siècle, nous avons accumulé beaucoup de preuves que le composant essentiel de la matière est invisible. Dès les premières observations de galaxies et amas de galaxies, jusqu'aux plus récentes mesures du fond diffus cosmologique (CMB) et des structures à grande échelle dans notre univers, nous avons développé un cadre cohérent de la présence d'un élément additionnel tout au long de l'histoire du cosmos. Ce composant est appelé matière noire, car il n'émet pas de lumière, et son existence se manifeste seulement à travers de ses effets gravitationnels.

L'hypothèse qu'une modification de la Relativité Générale, notre théorie de la gravité, puisse expliquer ces effets est désormais abandonnée par la plupart des physiciens, à cause de son échec dans la description des structures à grande échelle. On peut affirmer qu'une nouvelle composante doit être incluse dans le contenu de l'univers à côté de la matière ordinaire dans la forme de gaz et étoiles. Une possibilité plausible qui fût investiguée est que cette matière non lumineuse pourrait se trouver dans la forme d'objets astrophysiques connus, comme des astéroïdes, planètes ou naines blanches, appelés conjointement Massive Astrophysical Compact Halo Objects (MACHOs). Les observations de phénomènes de lentillage gravitationnel dans les dernières décennies ont rejeté cette hypothèse.

La possibilité la plus soutenue et la plus enthousiasmante à cause de ses implications pour la physique des interactions fondamentales est que la matière noire soit une nouvelle particule. Une idée très attractive est de mettre en relation la solution de ce problème du modèle cosmologique avec autres problèmes du Modèle Standard de la Physique des particules. Deux parmi eux en particulier contiennent d'excellents candidats pour la matière noire. Le premier est le problème de la hiérarchie entre l'échelle de masse de l'interaction électrofaible et de l'interaction gravitationnelle, qui amène à plusieurs propositions de particules massives interagissant faiblement (WIMPs), et le deuxième est le problème de CP fort, qui suggère une nouvelle particule légère et faiblement couplée appelée axion.

Les WIMPs ont été sûrement le candidat plus soutenu dans la communauté, à cause d'une coïncidence extrêmement suggestive. Le mécanisme habituel permettant à une particule, initialement en équilibre thermique dans l'Univers primordial, d'atteindre une abondance constante, s'avère, dans le cas de la matière noire, coïncider précisément avec les échelles de couplage et de masse attendus pour une particule qui résoudrait le problème de la hiérarchie. Une force d'interaction comme celle d'une WIMP offre de bonnes possibilités pour la recherche de ce candidat avec trois classes d'expériences. Les recherches directes essaient de révéler l'interaction d'une particule de matière noire avec un détecteur; les recherches indirectes cherchent des produits d'annihilation de la matière noire parmi les rayons cosmiques; enfin, les collisionneurs de particules pourraient produire des particules de matière noire, qui s'échapperaient du détecteur en laissant une tranche d'énergie manquante dans l'événement.

Du côté théorique, une pléthore de modèles contiennent de bons candidats WIMP de ma-

tière noire, ce qui a motivé l'utilisation de théories de champ effectives (EFTs) pour l'exposition des résultats des recherches expérimentales. Chaque modèle peut être décrit à énergies faibles par une EFT, contenant seulement les degrés de liberté plus légers qu'une certaine valeur d'énergie appelé "cutoff", et l'effet de physique à hautes énergies est inclus au travers d'opérateurs effectifs non renormalisables. Le grand avantage est qu'avec un nombre limité de paramètres une EFT peut décrire n'importe quelle théorie complète qui ait le même spectre de masse aux énergies faibles. Leur limite est que, dans les recherches aux collisionneurs, le régime de validité en énergie des EFTs risque d'être dépassé. Cela motiva dans ce contexte l'introduction de modèles simplifiés pour la présentation des résultats expérimentaux. Ces théories contiennent non seulement le candidat de matière noire, mais aussi les particules médiatrices de son interaction avec le Modèle Standard.

D'autres candidats de matière noire qui ont reçu beaucoup d'attention récemment sont les trous noirs primordiaux (PBHs). Ces trous noirs ne viendraient pas des stages finaux d'évolution d'une étoile massive, mais se seraient formés il y a très longtemps dans l'histoire de l'univers, par l'effondrement de grandes surdensités de matière. L'intervalle possible pour leurs masses s'étend de la masse d'astéroïdes (concentrés dans une taille subnucléaire) jusqu'à des centaines de masses solaires. Ils seraient observables à travers l'effet de lentillage gravitationnel comme les MACHOs, mais aussi lors d'événements de fusionnement de trous noirs ou de leur émission de rayons γ , en dépendant de leur masse.

Cette Thèse contient dans le Chapitre 1 une exposition détaillée des preuves de l'existence de la matière noire sur des échelles largement différentes dans l'univers, et des mécanismes principaux grâce auxquels la matière noire pourrait avoir rejoint son abondance actuelle dans l'histoire du cosmos. Nous passons ensuite en revue les candidats principaux qui ont été proposés et les progrès des recherches expérimentales de matière noire sous la forme de WIMP.

La deuxième partie de cette Thèse concerne les cadres théoriques proposés pour l'exposition des recherches expérimentales. Dans le Chapitre 2 nous analysons la question de la validité des EFTs à l'échelle d'énergie des collisionneurs de particules, et nous proposons une méthode conservative mais cohérente pour leur utilisation dans ce contexte. Dans le Chapitre 3 nous nous concentrons sur les modèles simplifiés et les recherches indirectes. Parmi les modèles utilisés par les collaborations expérimentales pour l'exposition de leurs résultats, plusieurs contiennent des anomalies de jauge. Nous soutenons que cela n'implique pas que la théorie soit simplement incohérente, mais que cela pourrait être vu comme une caractéristique intéressante du modèle: même le Modèle Standard est anomal, lorsque considéré à énergies inférieures à la masse du quark top. Nous montrons que les propriétés de ces théories impliquent une large annihilation de matière noire en bosons vecteurs du Modèle Standard, ce qui amplifie les possibilités de détection indirect de matière noire au dessus d'un TeV.

Dans la troisième partie de la Thèse nous nous focalisons sur les PBHs. Nous proposons dans le Chapitre 4 un nouveau mécanisme pour leur production, qui dépend d'une caractéristique déjà présente dans le Modèle Standard extrapolé à hautes énergies: notre configuration du vide du potentiel du champs de Higgs est métastable. Si le champs de Higgs avait exploré la région instable vers la fin de l'époque inflationnaire, alors une possible empreinte pourrait être la génération de PBHs. Une autre empreinte de ce mécanisme, que nous discutons dans le Chapitre 5, est la génération d'un fond stochastique d'ondes gravitationnelles, qui pourrait être révélé par des expériences comme Advanced Ligo et LISA. Nous calculons le spectre de puissance et le bispectre de ce signal, afin de caractériser ses propriétés. L'observation d'une de ces empreintes représenterait une confirmation unique de la remarquable instabilité du vide du Modèle Standard.

Summary

One of the greatest mysteries in our understanding of the universe is what composes nearly the 80% of matter. Since nearly a century, we have been accumulating evidences that the essential component of matter in the universe is invisible to our eyes, at least through light. From the first observations of galaxies and galaxy clusters, until the most recent measurements of the Cosmic Microwave Background and of the Large Scale Structures in our universe, we have built up a consistent picture, although not detailed yet, of the presence of an extra ingredient of matter along the cosmic history. This component is called Dark Matter, for the reason that it does not emit light, and its existence manifests itself only through gravitational effects. There is no particle of the Standard Model of fundamental interactions that could compose this extra component, not even the neutrino.

The hypothesis that a modification of General Relativity, our current theory of gravity, could account for these effects, is pushed aside by most physicists today, because of its inability to account consistently for all evidences for the existence of Dark Matter. We can affirm that some new component has to be added to the content of the universe, together with the ordinary matter in the form of gases and stars. A plausible possibility which was investigated is that this non luminous matter could be in the form of astrophysical known objects, as asteroids, planets or white dwarves, collectively called Massive Astrophysical Compact Halo Objects (MACHOs). The observations of lensing phenomena in the last decades have discarded this hypothesis.

The most supported and exciting hypothesis for its implications for the physics of fundamental interactions is that Dark Matter is formed of an unknown particle. Several directions have been proposed by the community of cosmologists and particle physicists, and the search for Dark Matter is now one of the most active domains in Physics. An attractive idea is to link the solution of this problem of our cosmological model with other issues of the Standard Model of particle physics. Two of them in particular lead naturally to excellent Dark Matter candidates. The first is the problem of the hierarchy between the mass scales of the electroweak interactions and of the gravitational force, which brings to various proposals of Weakly Interacting Massive Particles (WIMPs), and the second is the strong CP problem, which points to a new light and weakly coupled particle called axion.

The WIMPs have been by far the most supported candidate in the community, because of an extremely suggestive coincidence. The standard mechanism, called freeze out, by which a particle initially in thermal equilibrium in the early universe can reach after a certain time a fixed abundance, turns out to yield the observed quantity of Dark Matter precisely for the range of couplings and masses which are expected for a particle addressing the hierarchy problem. This remarkable fact, dubbed WIMP miracle, has rightly motivated many efforts both in the theoretical and experimental communities.

An interaction strength as the one of a WIMP offers good possibilities for the search of this candidate through three classes of experimental searches. The first one is direct detection, in which a large and sensitive detector tries to reveal the interaction with an incoming Dark Matter

particle. The detector is located underground, in order to shield it from cosmic rays and sources of undesired noise. The second class is indirect detection, which includes all the observations of the sky that look for annihilation (or decay) events of Dark Matter particles into ordinary particles. The outcome could be the production of γ rays, charged cosmic rays as electrons or protons and their antiparticles, or neutrinos. The difficulty of such a search is to distinguish the signal from the cosmic ray background, which is difficult to estimate with a high precision. Finally, also particle colliders allow to search for the possible production of Dark Matter pairs, which would escape unobserved from the detector. This event could be tagged by looking for a large amount of missing energy recoiling against a visible object, which at the Large Hadron Collider could be a jet, an electroweak boson or a heavy quark.

Within the theoretical community, lots of different frameworks have addressed the WIMP hypothesis, from supersymmetry to models with extra dimensions, or models where the Higgs boson is a composite state. Each of these classes contains in turn many specific theories, often containing more than one Dark Matter candidate each. This plethora of full theoretical models for the description of Dark Matter have motivated the use of Effective Field Theories (EFTs) for the recast of the results of experimental searches. Any model can be described at low energies by an EFT, containing only the degrees of freedom lighter than a given energy cutoff, and incorporating the effect of physics at higher energies through effective non-renormalisable operators. The big advantage is that the number of possible EFTs is limited, so that any model displaying a gap in the spectrum can be mapped into an EFT with a limited number of parameters. In the context of collider searches, there is the risk though of reaching energy scales close to or above the cutoff, violating the validity regime of the EFT. This has motivated the introduction of simplified models for the recast of collider searches. These models contain not only the DM candidate, but also the particles mediating its interactions with the Standard Model.

Other possible Dark Matter candidates which have recently gained attention are Primordial Black Holes (PBHs). These black holes would not have arisen as the final stage of the life cycle of massive stars, but would have formed very early in the cosmological history by the collapse of large overdensities of matter. Their possible mass range extends from the mass of asteroids (compressed within the size of a nucleus) to hundreds of solar masses. They would be observable not only through lensing similarly to MACHOs, but also through black hole merging events or γ rays, depending on their mass.

This Thesis contains in Chapter 1 a detailed discussion of the evidences for the existence of Dark Matter on vastly different scales in the universe, and of the main mechanisms by which Dark Matter could have reached its current abundance in the cosmological history. We then review the main candidates which have been proposed and the progress of the experimental searches for WIMP Dark Matter.

The second part of the Thesis deals with the theoretical frameworks proposed for the recast of experimental searches. In Chapter 2 we analyse the issues with the validity of EFTs at collider energy scales, and we propose a conservative but robust method to use them for the recast of collider searches. The simulation of the signal, to be performed for the recast of the experimental bound, can be limited to the subset of events for which the total energy involved is below the cutoff of the EFT, which should be treated as a free parameter. This allows to obtain a consistent EFT bound, which has the virtue of being very general and easily convertible into a corresponding model completion. We also show that the use of simplified models for the recast of missing energy searches eventually reduces to the addition, on top of the EFT signal, of the resonant production of the mediator between dark and ordinary matter, which is better constrained by other experimental searches. In Chapter 3 we focus on simplified models and indirect searches. Within the set of simplified models used by experimental collaborations,

some of them are anomalous, which means that the charge assignments under a new gauge interaction are such that the theory cannot be extrapolated to very high energies. We argue that this should not imply that the theory is just inconsistent, but it could be seen as an interesting feature of the model. Even the Standard Model of particle physics is anomalous, if we consider it below the mass scale of the top quark. We analyse the features of these apparently anomalous models, and we show that a very interesting consequence is an enhanced annihilation rate of Dark Matter particles into Standard Model vector bosons, which largely improves the reach of indirect searches for Dark Matter masses above the TeV.

In the third part of this Thesis we focus instead on PBHs. We propose in Chapter 4 a new mechanism for the generation of the large overdensities which could seed their generation, relying on a feature already built in the Standard Model: the instability of the Higgs vacuum. An important prediction of the Standard Model, if it is extrapolated to high energies assuming no contributions of new physics, is that our vacuum configuration of the Higgs potential is metastable: we do not live in an absolute minimum of the potential. If the Higgs field probed the unstable region towards the end of the inflationary epoch, then a possible signature could be the generation of PBHs. Another signature of this mechanism, which we discuss in Chapter 5, is the generation of a stochastic background of gravitational waves, which could be detectable by current and planned experiments as Advanced LIGO and LISA. We compute both the power spectrum and the bispectrum of this signal, in order to characterise their properties. The confirmation of either of these signatures could represent a unique confirmation of the remarkable feature of the vacuum instability of the Standard Model.

*The effort to understand the universe
is one of the very few things that lifts human life
a little above the level of farce,
and gives it some of the grace of tragedy.*

– Steven Weinberg

Contents

Abstract	iii
Acknowledgements	v
Members of the Jury	vii
List of publications	ix
Résumé	xi
Summary	xiii
I The existence of Dark Matter	1
1 Evidences and candidates for Dark Matter	3
1.1 Evidences for the existence of Dark Matter	3
1.1.1 Observations on galactic scales	4
1.1.2 Observations on intergalactic scales	4
1.1.3 Observations on cosmological scales	6
1.2 Attempted (and excluded) explanations for Dark Matter	8
1.2.1 MOND: MODified Newtonian Dynamics	8
1.2.2 MACHOs: Massive Astrophysical Compact Halo objects	9
1.3 Production mechanisms of DM in the early universe	10
1.3.1 Freeze out	11
1.3.2 Freeze out and decay	12
1.3.3 Freeze in	13
1.3.4 Asymmetric dark matter	15
1.4 Particle candidates for Dark Matter	16
1.4.1 WIMPs: Weakly Interacting Massive Particles	16
1.4.1.1 Candidates from supersymmetry	16
1.4.1.2 Lightest Kaluza-Klein particle	17
1.4.1.3 Minimal Dark Matter	18
1.4.2 SuperWIMPs	19
1.4.3 Sterile Neutrinos	19
1.4.4 Axions	20
1.5 WIMP searches	23
1.5.1 Direct searches	24
1.5.2 Indirect searches	26

1.5.3	Collider searches	30
II	WIMP Dark Matter	35
2	Consistent recast of collider searches within Effective Field Theories	37
2.1	Effective Field Theories and their regime of validity	37
2.2	Limit-setting strategy	41
2.2.1	ATLAS mono-jet recast	41
2.2.2	Results and discussion	43
2.3	Simplified model reinterpretation	47
2.3.1	Comparison with other approaches in the literature	52
2.3.2	Further developments of this method in the literature	54
2.4	Conclusions	56
2.A	Model A: axial-vector mediator	57
2.B	Model B: coloured scalar mediators	58
2.C	Formulae for the relic density	59
3	Dark Matter interactions with the Standard Model through an anomalous Z'	63
3.1	Introduction	63
3.2	Low-Energy Effective Theory	65
3.2.1	Anomalous $U(1)'$ gauge theory	66
3.2.2	Mixed anomalies in a $SU(N) \times U(1)'$ gauge theory	67
3.3	Dark Matter Models with Heavy Anomalous Z'	70
3.4	Application to Dark Matter Models	73
3.4.1	Annihilation cross sections into the SM gauge bosons	73
3.4.2	Relic abundance	77
3.4.3	Indirect detection	77
3.4.3.1	Gamma ray continuum searches	77
3.4.3.2	Gamma ray line searches	79
3.4.3.3	Neutrino telescopes	81
3.4.4	Colliders and direct detection	82
3.4.5	Summary of results	84
3.5	Comments on the Validity of Our Results	85
3.6	Conclusions	87
3.A	Ward Identities for non-Abelian spontaneously broken gauge theories	88
3.B	Effective triple gauge boson couplings	92
III	Cosmological signatures of the Higgs instability	95
4	A cosmological signature of the Higgs instability: Primordial Black Holes as Dark Matter	97
4.1	Instability of the Standard Model Higgs vacuum	97
4.2	Dynamics of the Higgs background and fluctuations	100
4.2.1	Quantum fluctuations during inflation	100
4.2.2	Quantum to classical transition of the Higgs background	102
4.2.3	Excitation of the Higgs fluctuations	103
4.2.4	Dynamics after inflation: reheating	104

4.3	Analytical estimates of the comoving curvature perturbations	105
4.3.1	Curvature perturbations during inflation	105
4.3.2	Curvature perturbations during reheating	106
4.4	Primordial Black Holes as Dark Matter	108
4.4.1	Motivations and prospects for Primordial Black Holes	108
4.4.2	Formation of Primordial Black Holes	109
4.4.3	Constraints on Primordial Black Holes	111
4.4.4	Models for the generation of Primordial Black Holes	114
4.5	Generation of Primordial Black Holes through the Higgs instability	116
4.6	Homogeneity of the Higgs field and fine-tuning	119
4.7	Getting rid of the AdS regions altogether	122
4.8	Conclusions	125
4.A	Dynamics of the Higgs hitting the pole	126
4.B	Energy densities and their perturbations in the thermal phase	127
4.C	Some considerations about the Non-Gaussianity	128
5	A cosmological signature of the Higgs instability: Gravitational Waves	131
5.1	Gravitational waves as a signature of the Higgs instability	131
5.2	Equation of motion and its solution for Gravitational Waves	133
5.2.1	Equation of motion of GWs	133
5.2.2	The source term for GWs	134
5.2.3	A compact expression for GWs with a numerical integration over time . .	135
5.3	The Power Spectrum of Gravitational Waves	138
5.3.1	Two-point function of GWs	138
5.3.2	The energy density of GWs	139
5.4	Bispectrum of Gravitational Waves	140
5.5	Numerical results for the Energy Density and Bispectrum of GWs	142
5.5.1	Energy density of GWs	142
5.5.2	The spectral tilt of GWs at low and high frequencies	144
5.5.3	The three-point correlator of GWs and its consistency relations	145
5.6	Conclusions	149
5.A	Analytical results for the functions $\mathcal{I}_c, \mathcal{I}_s$	149
5.B	Four and Six-Point Functions of the Curvature Perturbation	150
5.B.1	Four-point function of the curvature perturbation	150
5.B.2	Six-point function of the curvature perturbation	151

Bibliography	153
---------------------	------------

Part I

The existence of Dark Matter

1

Evidences and candidates for Dark Matter

In this Chapter we review the many evidences of the existence of Dark Matter (DM) and the main proposals about its nature.

In Sec. 1.1 we discuss the observations pointing to the presence of DM on a broad range of scales in our Universe. This increasing amount of evidence led physicists and astronomers to propose various alternative explanations, along two possible directions. A first option could be a modification of our model for gravity on the galactic scale, leading to the proposal of MOND reviewed in Sec. 1.2.1. The other possibility amounts to adding other components of matter. This could be ordinary non-luminous matter, either in form of astrophysical remnants called MACHOs (Sec. 1.2.2) or Primordial Black Holes (Sec. 4.4). The most variegated and studied scenario is that DM is made of some yet unknown particle (Sec. 1.4), with the most supported candidate over the last decades being a Weakly Interacting Massive Particle (WIMP).

The first two proposal (MOND and MACHOs) are now discarded, whereas Primordial Black Holes have been receiving an increasing attention during the last years thanks to the latest experimental progresses. The option that the DM is composed of a new particle is by far the one which opens most avenues of investigation, and offers the possibility to solve at the same time other problems of the Standard Model (SM) of particle physics.

Given the focus of the Chapters 2 and 3, in this introductory Chapter we illustrate in more detail WIMP DM. We review the production mechanisms of WIMP DM in the early universe (Sec. 1.3), the main candidates addressing other problems of the SM (Sec. 1.4.1), and their experimental searches (Sec. 1.5). We postpone a detailed introduction to Primordial Black Holes to Section 4.4.

There are many excellent reviews on DM in the literature. For a detailed historical outline, see Ref. [13]. Comprehensive reviews which focus both on observational evidences and experimental probes for DM are Refs. [14–20], whereas for reviews on the possible candidates for DM one can see Refs. [21, 22].

1.1 Evidences for the existence of Dark Matter

The observational evidences can be classified depending on the typical scale at which the effects of DM are manifest: from the galactic (Sec. 1.1.1) to intergalactic (Sec. 1.1.2) and cosmological scales (Sec. 1.1.3).

The impressive amount of evidences accumulated over almost a century on so widely different scales in the universe leaves no doubt about the existence of DM. Historically (due to the reach of the observations) we first understood the existence of DM from observation on intergalactic and galactic scale in the 1930s. If we had though to highlight the most striking evidence for DM in the form of an extra component of matter (either new particle(s) or PBHs), this would be the observation of the Cosmic Microwave Background (CMB) and its interplay with the Large Scale Structures (LSS) that we see in the universe.

1.1.1 Observations on galactic scales

The first observations of non-luminous matter were done by Oort in 1932. His measurements of the brightest stars in the Milky Way suggested that part of the gravitational mass of the galaxy was missing if one only considered those stars, and this fact brought him to claim that the disk of the galaxy was composed for two thirds by “dark matter” including stars less luminous than the Sun, and gas and dust in the interstellar medium. Many years later, in 1959, Kinman observed some deviations in the velocities of the globular clusters contained in the Milky Way with respect to what expected from a pure disk mass model, and already suggested a linearly rising mass distribution beyond the disk.

Also the observations of the spiral galaxy nearest to us, M31 (Andromeda), done by Babcock in 1939, suggested that the ratio between gravitational and luminous mass was increasing in the outer regions of the galaxy. Later measurements of the rotation curve of this galaxy in 1957 and 1975 showed a flat region. The studies were deepened in the following years, in particular by Vera Rubin, who showed that, for a large sample of spiral galaxies, the rotation curve of stars inside the galaxy did not fall off as predicted by Keplerian gravity, but kept a flat profile for a large distance outside the main disk. Since the radial velocity, in the approximation of a circular motion and spherical symmetry, is given by $v = \sqrt{GM(r)/r}$ (where $G = 6.67 \times 10^{-11} \text{ N} \cdot \text{m}^2\text{kg}^{-2}$ is the gravitational constant and $M(r)$ is the gravitational mass contained inside a sphere of radius r centered in the barycentre of the galaxy) these results imply a dark matter mass density proportional to r^{-2} within a large region outside the main disk of the galaxy. Fig. 1.1 shows an example of a measured rotation curve.

1.1.2 Observations on intergalactic scales

One year after Oort (1933), Fritz Zwicky measured the velocities of galaxies within the Coma galaxy cluster, and deduced that the gravitational mass contained in the cluster was hundreds of times greater than the luminous mass. Among the few possible explanations, he also quoted Oort’s proposal of “dark matter”.

The large set of observations gathered from the early ’30s to the end of the ’80s provided plenty of evidence that, in the framework of general relativity, a large part of the mass inside and surrounding galaxies is not interacting through electromagnetic or nuclear interactions. An important probe for the distribution of dark matter is the observation of gravitational lensing, i. e. the study of images of far galaxies bent or replicated because of the passage of light near a very massive galaxy cluster. This kind of observations have showed that the most massive clusters are largely dominated by dark matter, with ratios of gravitational to luminous matter of the order of some hundreds.

An important and suggestive evidence came in 2006 with the observation of the so called Bullet Cluster [26]. This system is composed of two primary galaxy concentrations, which passed through each other ≈ 100 Myr ago. As a result of this collision, the various components of the two galaxy clusters (dark matter, X-ray emitting plasma, and galaxies visible

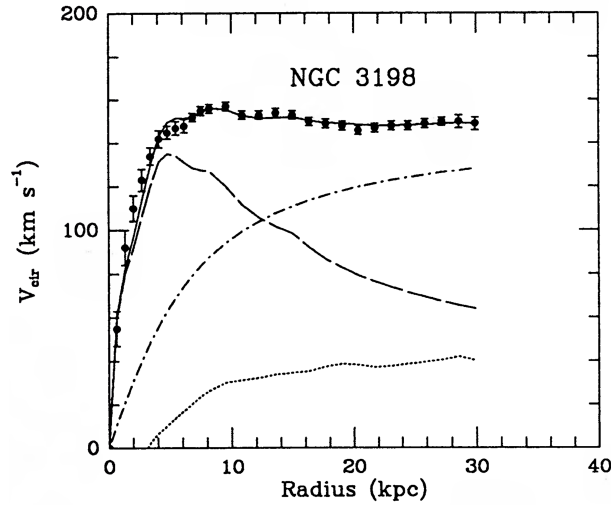


Figure 1.1: Rotation curve of stars in the galaxy NGC 3198 as a function of the radial distance. The dotted, dashed and dash-dotted lines are respectively the contributions of gas, disk and dark matter to the gravitational mass contained in the galaxy (figure taken from [23], with original data reported in [24, 25]).

in the optical spectrum) underwent different interactions with the components of the other cluster. While the intergalactic gas slowed down during the collision because of its electromagnetic interactions, the dark matter components passed through each other without significant consequences, showing that they can interact only gravitationally or through a very weak self-interaction. The stars contained in galaxies very rarely collide, given the large distances between them. Under these conditions, the outcome of the collision is a displacement between the barycentres of the hot gas distribution (visible in the X-ray spectrum by the Chandra satellite) and the dark matter distribution (which can be inferred by the analysis of the weak gravitational lensing of background structures). The result is displayed in Fig. 1.2.

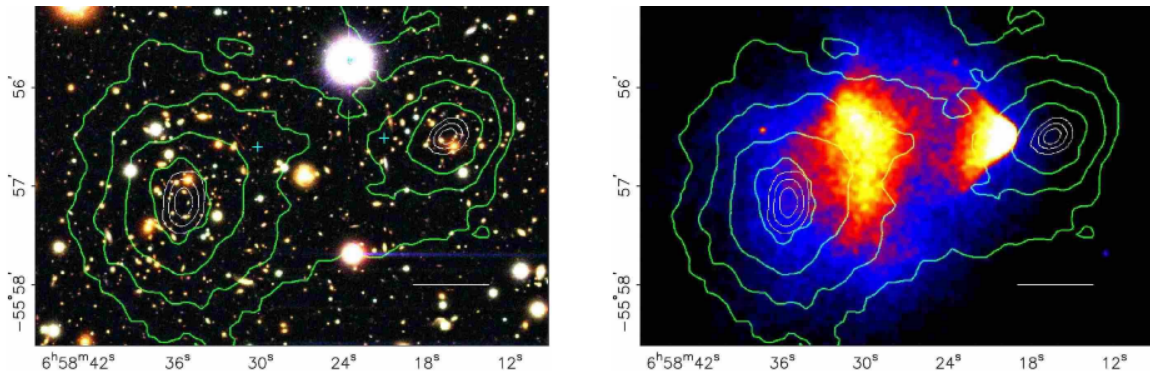


Figure 1.2: Images of the Bullet cluster. In the left panel, a colour optical image showing the galaxies, which make up only a few percent of the mass of the cluster. In the right panel, an X-ray image from the Chandra telescope, showing where the bulk of the gas in the cluster is located. In both panels, the green contours show the mass distribution inferred from gravitational lensing [26].

This spectacular observation is very important, because it allows to constrain the strength of dark matter self-interactions, and because it is an argument against the proposals of modified gravitation (Sec. 1.2.1). Indeed, if one rejects the dark matter hypothesis, it is hard to explain

without contradicting very basic assumptions on the nature of gravity why the weak gravitational lensing points to a barycentre displaced with respect to the centre-of-mass of the ordinary matter distribution. A more recent and comprehensive analysis [27] listed 72 similar systems, reinforcing the strength of this evidence for the existence of DM and deriving an upper limit of $\sigma_{\text{DM}}^{\text{self}}/m_{\text{DM}} < 0.47 \text{ cm}^2/\text{g}$ on the self-interaction of DM.

1.1.3 Observations on cosmological scales

The most indisputable evidences for the existence of DM are probably those coming from the study of the universe on cosmological scales.

The observations of the Cosmic Microwave Background (CMB), from the first experiments able to resolve small angular scales (Maxima, Boomerang in 2000 and WMAP in 2003) until the recent measurements by Planck in 2015, have progressively confirmed the so called Λ CDM paradigm of cosmology to an impressive level of accuracy. The small anisotropies (at a level of $\sim 10^{-5}$) in the nearly homogeneous black body spectrum of microwave radiation at 2.7 K tell us a great deal of information about the components of the universe around the recombination epoch.

The power spectrum of these anisotropies, as a function of the angular scales (or equivalently of the multipole ℓ in a multipole expansion) is shown in Fig. 1.3.

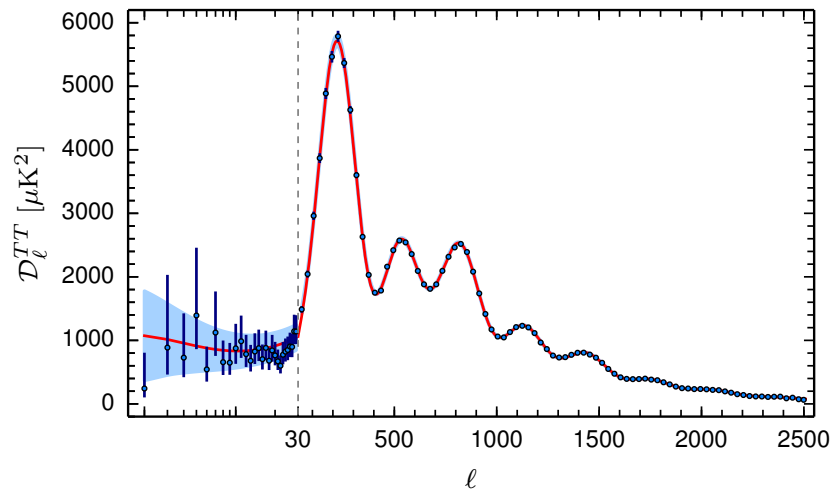


Figure 1.3: Power spectrum of angular anisotropies in the local temperature of the CMB as measured by Planck (from [28]).

The oscillating shape of the spectrum is determined by the Baryon Acoustic Oscillations (BAO) in the plasma of coupled baryon and photons until the recombination. These sound waves evolve under the effect of gravitational attraction and radiation pressure, and at the decoupling time these oscillations are “frozen” in the baryon fluid, which does not propagate sound waves after decoupling from radiation. The precise positions and heights of the peaks in the power spectrum are highly sensitive to the cosmological parameters, and in particular to the DM and baryon energy densities $\Omega_{\text{CDM}} \equiv \rho_{\text{CDM}}/\rho_c$, $\Omega_b \equiv \rho_b/\rho_c$, where $\rho_c = 3H^2 M_{\text{P}}^2$ is the critical density for a flat universe and M_{P} is the reduced Planck mass $1/\sqrt{8\pi G}$. The books [29–32] offer detailed expositions of this topic. The fit shown with a red line in Fig. 1.3 has only six free parameters, and is in astonishing agreement with the data. The inferred values for the

energy densities of DM and baryons are [33]

$$\begin{aligned}\Omega_{\text{CDM}}h^2 &= 0.1197 \pm 0.0022 \\ \Omega_b h^2 &= 0.02222 \pm 0.00023\end{aligned}\tag{1.1}$$

where $h = H/(100 \text{ km s}^{-1} \text{ Mpc}^{-1}) \sim 0.7$ is the rescaled Hubble parameter. Therefore the DM energy density is 25.7% of the total, and is roughly 5 times more abundant than the baryon one (5.8%). The remaining vacuum energy density is the 68.5% of the total.

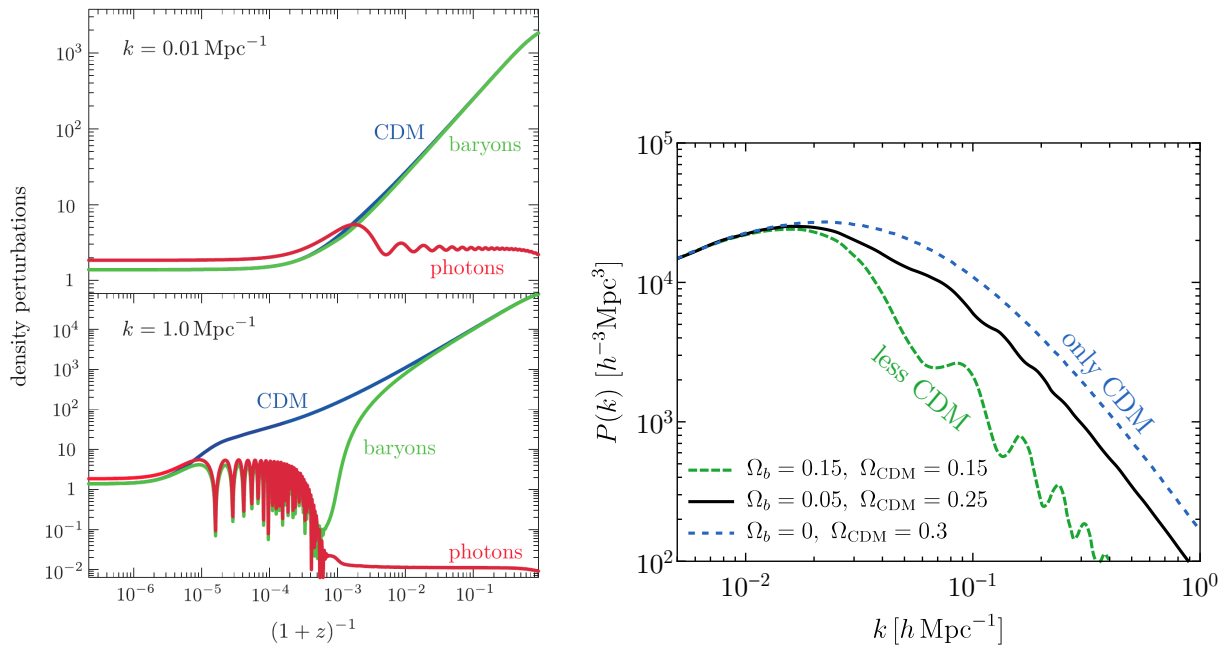
Baryons decouple from photons at recombination (at a redshift $z \sim 1100 - 1400$, 380 kyr after the end of inflation), whereas DM already decoupled from the thermal bath much earlier (whatever is the mechanism that fixes its abundance). This is crucial for the formation of structures [32, 34], as we are going to see now (we will come back to this point in Chapter 4). The density fluctuations of the radiation fluid (and thus also of baryons, as long as they are coupled to photons) oscillate with constant amplitude for each mode, they do not grow. On the contrary, the density fluctuations in both the DM¹ and baryon fluids are frozen in the super Hubble regime (i. e. when the corresponding mode $k < H$), and after they enter the Hubble radius they slowly grow as $\ln a$ (a being the scale factor) if the universe is still Radiation Dominated (RD), otherwise they grow faster, as a , during the phase of Matter Domination (MD).

Let us consider modes $k > k_{\text{eq}} \sim 0.1 h \text{ Mpc}^{-1}$, k_{eq} being the Hubble radius at the time t_{eq} of equality ($z_{\text{eq}} \sim 3400$, $t_{\text{eq}} = 60$ kyr after the end of inflation) between radiation and total matter. On these scales, the perturbations in the CDM sector begin to grow as $\ln a$ as soon as DM decouples from the thermal bath (see Fig. 1.4a), and DM slowly starts to form structures. In the meantime baryons and photons are coupled, so that baryon perturbations have constant amplitude. When baryons decouple from radiation, their amplitudes start growing as a , but given that DM is 5 times more abundant than baryons, the latter feel the gravitational attraction of protostructures made of DM. Therefore the amplitude of baryon perturbations quickly catches up with the DM perturbations. The overall effect of DM is then to increase the power spectrum of baryon perturbations on small scales. This is shown in Fig. 1.4b, which shows the matter power spectrum for fixed $\Omega_{\text{tot}} = 1$, $\Omega_{\Lambda} = 0.7$ and for different values of Ω_{CDM} , Ω_b . In particular, without the presence of DM the baryon perturbations could not have grown enough on the scales relevant for galaxy formation until the recent epoch of vacuum energy domination, during which perturbations stop growing. In conclusion, without the presence of DM which decoupled from the thermal bath much earlier than recombination (and by fixing the other parameters of ΛCDM), the structures in which we live could not have formed.

An important distinction between the DM candidates concerning their effect on Large Scale Structure (LSS) formation is based on their free-streaming length. For Hot Dark Matter (HDM), this is comparable to the scale of galaxy clusters, which implies that it has been relativistic through most of the cosmic history. This scenario is strongly constrained as it poorly enhances the formation of structure, and the current bound is that HDM can constitute no more than 1% of Ω_{DM} . The SM left-handed neutrinos ν_L constitute indeed a subdominant HDM component, with an energy density $\Omega_{\nu}h^2 = (\sum m_{\nu_i})/93 \text{ eV} \sim 10^{-3} - 10^{-2}$.

If the free-streaming scale of DM is smaller than the typical galactic scale, then the matter power spectrum would be suppressed on scales smaller than 10^2 kpc because of the higher kinetic energy which causes the escape of DM from gravitational wells. In this case, the DM would decouple before the QCD phase transition, and is called Warm Dark Matter (WDM).

¹We specialise the discussion for a moment to Cold Dark Matter, that is DM which is non relativistic when it decouples from the SM thermal bath. At the end of this section we explain this distinction more in detail.



(a) Evolution of density perturbations for two modes $k = 0.01 \text{ Mpc}^{-1}$ and $k = 1 \text{ Mpc}^{-1}$ (from [34]).

(b) Matter power spectrum in the linear theory for fixed $\Omega_\Lambda = 0.7$ and $\Omega_m = 0.3$, and varying $\Omega_{\text{CDM}}/\Omega_b$ (adapted from [35]).

Figure 1.4: Impact of (Cold) DM on the matter power spectrum at scales $k \gtrsim k_{\text{eq}}$. Baryon perturbations on scales smaller than k_{eq}^{-1} would have increased much less without the presence of DM.

Cold Dark Matter (CDM) has a negligible free-streaming length on cosmological scales, and is the paradigm which is most in agreement with observations. WIMPs and axions are typical examples of CDM candidates.

There are hints in the direction of WDM from the discrepancy between the low number of satellite galaxies observed in the Universe with respect to the predictions of CDM simulations: this phenomenon, the so-called *missing satellite problem*, is still under discussion, but seems to favour the WDM case. Another problem of the CDM paradigm is the predicted steep profile for the dark matter density near the centre of galaxies (*cuspy halo problem*), because of the lower velocity profile which binds more particles to the bottom of the potential. It is difficult to check this prediction experimentally, and more importantly to understand the impact of baryonic physics which is hard to include in CDM simulations. The current impression from numerical simulations is that the feedback of baryonic interactions helps to alleviate both the missing satellite and the cuspy halo problem.

1.2 Attempted (and excluded) explanations for Dark Matter

1.2.1 MOND: Modified Newtonian Dynamics

The evidences for DM on galactic scales (Sec. 1.1.1) come from an inconsistency between the observations and the Newtonian model for the gravitational interaction. In analogy to similar

crises faced by astronomy in the past (discovery of Neptune as “dark matter”², and precession of the perihelion of Mercury explained through a modification of gravity), a possibility is that the radial velocities of stars far from the centre of the galaxy are higher than expected because they are subject to a gravitational force stronger than the Newtonian one. This was the perspective of the proposal by Milgrom in 1983 of MOND (MODified Newtonian Dynamics) [36], which postulated the following equation for the motion of a test particle subject to a gravitational field $-\vec{\nabla}\Phi_N$:

$$\tilde{\mu}\left(\frac{|\mathbf{a}|}{a_0}\right)\mathbf{a} = -\vec{\nabla}\Phi_N, \quad \tilde{\mu}(x) \rightarrow \begin{cases} 1 & \text{for } x \rightarrow \infty, \\ x & \text{for } x \rightarrow 0, \end{cases} \quad (1.2)$$

where $a_0 \approx 10^{-10} \text{ m s}^{-2}$ is a preferred scale of acceleration. Outside the mass distribution of a galaxy, $|\vec{\nabla}\Phi_N| = GM_b/r^2$, where M_b understands only the baryonic mass. Eq. (1.2) implies the Newtonian limit for $a > a_0$, whereas for weak gravitational fields ($a \ll a_0$) the acceleration is the geometric mean of the Newtonian one and a_0 . As a consequence, Eq. (1.2) predicts a flat rotation curve for galaxies. The emergence of this typical acceleration scale a_0 , below which the effects of DM are relevant, was found to be predictable also within Λ CDM [37]. Eq. (1.2) would explain the empirical Tully-Fisher correlation: observations suggest with increasing evidence [38] that the total baryonic mass of a disk galaxy is proportional to the fourth power of the asymptotic rotation velocity. MOND predicts this kind of correlation, whereas the DM scenario has to rely on N-body simulations to estimate this dependence, still without contradicting it in principle.

Eq. (1.2) clearly cannot be treated as a fundamental law, and can only be conceived as an effective description of some underlying theory. A relativistic formulation that reduces to the MOND equation in the weak field limit was proposed by Bekenstein in 2004 [39], and is called TeVeS (Tensor-Vector-Scalar theory). In this formulation, one needs to introduce a timelike 4-vector field \mathcal{U}_α , together with a scalar field ϕ . This model manages to reproduce the additional lensing far from the centres of galaxies, which is needed to reconcile the observations with the visible matter content of galaxies. The TeVeS formulation gives a viable theoretical framework leading to the MOND equation (1.2). The main problems of this modified gravity approach are the following three [40].

First of all, MOND does not explain well the dynamics of galaxy clusters as the Bullet cluster (Sec. 1.1.2). We can argue that the DM paradigm explains more successfully than MOND the dynamics of galaxy clusters. Also the spectrum of the CMB anisotropies is hardly reproduced. The height of the third peak, in particular, should be very small in a baryon dominated model that lacks the extra gravitational force supplied by dark matter.

Finally, and most importantly, TeVeS gives completely different predictions about the power spectrum of matter perturbations, as shown in Fig. 1.5. In the Λ CDM paradigm, the peaks of the BAO are highly suppressed as the baryons fall into the potential wells created by dark matter, while in a model without DM the oscillations should be as apparent in the baryonic matter distribution as in the CMB.

1.2.2 MACHOs: Massive Astrophysical Compact Halo objects

To explain the strong hierarchy between the gravitational and luminous mass in galaxies, the most straightforward proposal is that we do not correctly model the population of low mass

²In the 18th century, the observations of the motion of Uranus were in contrast with the Newtonian laws applied to the known content of the Solar system; the proposal of introducing a new ingredient to the matter components, i. e. the introduction of a new planet, led to the discovery of Neptune.

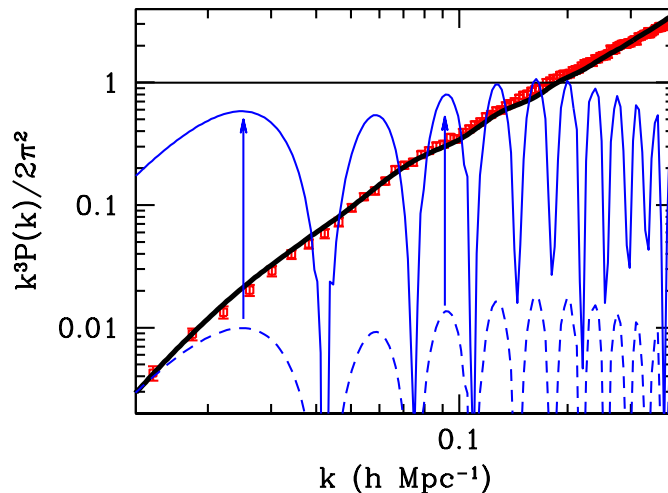


Figure 1.5: The matter power spectrum extracted from the data of the Sloan Digital Sky Survey (red points with error bars), compared with the predictions of the Λ CDM model (black line), a no dark matter model with $\Omega_b = 0.2$, $\Omega_\Lambda = 0.8$ (blue dashed line), and the TeVeS predictions (blue solid line). The TeVeS model, which amplifies the perturbations with respect to the dashed line prediction, reaches the amount of inhomogeneities needed for the structure formation, but is in total disagreement with respect to the observed power spectrum, where the BAO are highly suppressed (from [40]).

stars, stellar remnants and planetary mass bodies [16]. Compact astronomical bodies that constitute a significant component of the mass of the galaxy are referred to as Massive Astrophysical Compact Halo Objects (MACHOs). Their luminous faintness or opacity prevents us from searching for MACHOs in direct imaging, leaving as the only probe the search for their gravitational effects, in particular the gravitational lensing that they induce. In the case of the images of single stars, the passage of a massive lensing body has the effect of a brightening of the star on a time scale related to the mass and velocity of the intervening object, and typically ranges between a few weeks and a year.

Various experiments in the past two decades have investigated the number density of MACHOs in the Milky Way with a mass around $10^{-7} - 1 M_\odot$ through this effect of microlensing: the MACHO project, OGLE (Optical Gravitational Lensing Experiment) and EROS (Expérience pour la Recherche d'Objets Sombres). None of them found conclusive evidence, and they placed upper limits on the fraction of Ω_{CDM} under the form of MACHOs in the mass regime of $(10^{-7} \div 30) M_\odot$, where M_\odot denotes the mass of the Sun.

Because of these bounds, the proposal of DM in the form stellar and planetary remnants was progressively discarded. Primordial Black Holes constitute a DM candidate with similar prospects for detection through microlensing, but they could have *a priori* any mass. Furthermore, their particular nature opens up many other possible observational probes. We describe in detail this scenario in Section 4.4.

1.3 Production mechanisms of DM in the early universe

In this section, we discuss the main mechanisms by which dark matter could have been produced in the universe after the end of the inflation (the so-called reheating phase), and has reached the current abundance.

1.3.1 Freeze out

Freeze out is the simplest mechanism that fixes the abundance of a species in an expanding universe [29, 41, 42].

If two particles, say A and χ , can interact with each other through the reaction $AA \rightleftharpoons \chi\chi$, then, when initially the Universe is very hot (at temperatures $T \gg m_A, m_\chi$), the two species annihilate into each other maintaining the chemical equilibrium. When T drops below the higher of the two masses, say m_χ , then the number density n_χ of χ , in the hypothesis that χ remains in thermal equilibrium, must follow the non-relativistic equilibrium Boltzmann distribution $n_{\chi,\text{eq}} \sim e^{-m_\chi/T}$. Hence, the particles χ annihilate into particles A so as to follow the Boltzmann distribution.

Therefore, n_χ should drop to zero as the Universe cools down, unless the reaction $\chi\chi \rightarrow AA$ at a certain point becomes inefficient. This will happen indeed because of the expansion of the Universe, which dilutes the concentration of non-relativistic particles proportionally to a^{-3} . When the annihilation rate $n_\chi \langle \sigma v \rangle$ (where $\langle \sigma v \rangle$ is the thermally averaged cross section for the reaction $\chi\chi \rightarrow AA$) decreases below the Hubble rate, the annihilation of the χ particles will substantially cease. The consequence is that n_χ keeps the same value it had at the moment of the freeze out, when $n_\chi \langle \sigma v \rangle \approx H$. The particle χ could be the dark matter candidate, and A could represent SM particles (or other particles belonging to the dark sector and unstable on cosmological scales).

The quantitative study of freeze-out requires the Boltzmann equations, a set of differential equations that describe the evolution of the number densities of interacting species in an expanding universe. In the case we are discussing, the equation for n_χ reads

$$\frac{dn_\chi}{dt} = -3Hn_\chi - \langle \sigma v \rangle (n_\chi^2 - n_{\chi,\text{eq}}^2). \quad (1.3)$$

The first term on the right hand side of Eq. (1.3) accounts for the dilution due to the expansion, the second term comes from the $\chi\chi \rightarrow AA$ process, while the third one comes from the opposite reaction $AA \rightarrow \chi\chi$. This equation can be solved numerically, with the result shown in fig. 1.6.

Let us denote quantities evaluated at the freeze out time with a subscript f . The freeze-out condition $n \langle \sigma v \rangle = H$, together with the Friedmann equation for a radiation dominated Universe $H^2 \sim T_f^4 / M_{\text{P}}^2$, brings to

$$n_{\chi f} \sim \frac{T_f^2}{M_{\text{P}} \langle \sigma v \rangle}. \quad (1.4)$$

It is customary to define $x \equiv m/T$, and the yield $Y \equiv n/s$, where s is the entropy density of the Universe, which goes as $Y \sim nT^{-3} \sim na^3$ and is equivalent to the comoving number density. The thermal relic density of χ is then (the subscript 0 denotes present-day quantities)

$$\Omega_{\text{DM}}^{\text{f.o.}} = \frac{m_\chi n_{\chi 0}}{\rho_c} = \frac{m_\chi T_0^3}{\rho_c} \frac{n_{\chi 0}}{T_0^3} \sim \frac{m_\chi T_0^3}{\rho_c} \frac{n_{\chi f}}{T_f^3} \sim \frac{x_f T_0^3}{\rho_c M_{\text{P}} \langle \sigma v \rangle}, \quad (1.5)$$

where the first approximation follows from $Y_f = Y_0$ and $s_f = s_0$ (isoentropic expansion of the universe) with the approximation $g_{*f} \approx g_{*0}$ [29], and in the last passage we used Eq. (1.4).

If we impose $\Omega_{\text{DM}} \sim 0.3$ in Eq. (1.5), and we assume that the coupling constant g between χ and A is of the order of the EW coupling, on dimensional grounds $\langle \sigma v \rangle \sim g^4 / (16\pi^2 m_\chi^4)$ and m_χ turns out to be in the range 100 GeV – 1 TeV. Then, a weakly interacting particle with a weak scale mass (which is the most straightforward requirement to solve the gauge hierarchy problem) naturally leads to the correct relic abundance. This exciting coincidence was called

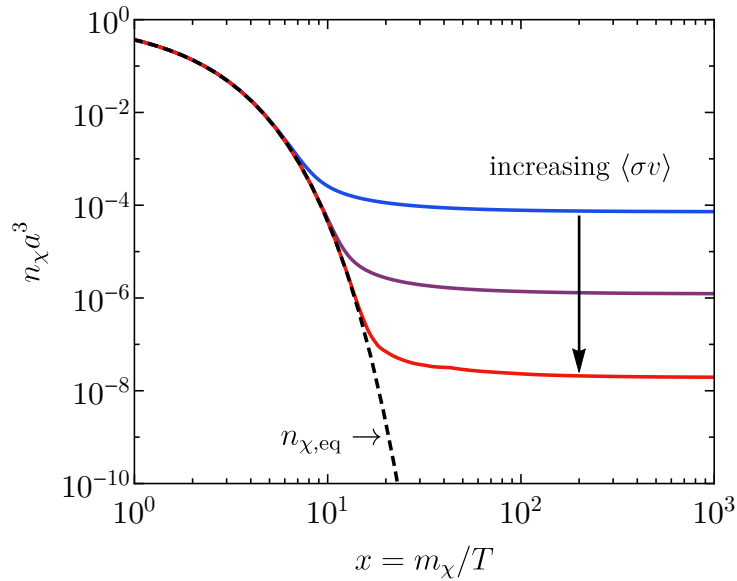


Figure 1.6: Comoving number density ($n_\chi a^3$) of a stable species X during the process of thermal freeze out, as a function of $x = m_\chi/T$. The larger is the cross section for the process $\chi\chi \rightarrow AA$, the lower is the thermal relic density of χ .

WIMP miracle, where WIMP stands for Weakly Interacting Massive Particle, and motivated in the last decades a wide belief that the most likely particle candidate for dark matter is a WIMP.

An important point in this result is that the thermal relic density is mainly dependent on the cross section σ , rather than on the mass m_χ , which appears in Eq. (1.5) only through x_f , which is typically of the order of 20 for a WIMP candidate and does not vary much for different choices of m_χ . Moreover, this mechanism is independent of the early thermal history of the Universe and of the interactions at high energy scales.

1.3.2 Freeze out and decay

A slightly more sophisticated mechanism with respect to the freeze out might offer a viable option to get the correct relic abundance, even if the particle χ undergoing the freeze out had a mass slightly above the weak scale (for example around 1 TeV), or it were electrically charged, but unstable on long time scales because of extremely weak interactions (e. g. gravitational ones).

This mechanism, which opens many possibilities from the particle physics point of view, goes under the name of *freeze out and decay*. In this case, the species χ undergoes the freeze out mechanism yielding a thermal relic density Ω_χ . Then, because of very weak interactions (as gravitational ones), χ can further decay to some particle Ψ . If this coupling is weak, the effect of Ψ on the freeze out of χ is negligible. The result at late times is that the species χ nearly disappears, leaving a relic density for Ψ given by (if each χ produces only one particle Ψ)

$$\Omega_\Psi = \frac{m_\Psi}{m_\chi} \Omega_\chi. \quad (1.6)$$

If we now specialise this general framework, by assuming that χ is a WIMP (now with a more relaxed constraint on m_χ), and that m_Ψ is comparable or slightly lower than m_χ , then Ψ turns out to have the correct relic abundance to be the DM candidate: a name used to denote this

species is *superWIMP*, as it should interact super-weakly and have a mass of the order of the weak scale. In this case, since χ is unstable and is not the DM particle, it does not need to be neutral (see also Sec. 1.4.2).

If the decay channel of χ includes, together with Ψ , some Standard Model (SM) particles, a limit on the lifetime of χ comes from the requirement that it does not decay after the nucleosynthesis, in order not to introduce a late time production of SM particles that could influence the nucleosynthesis in a way incompatible with observations.

1.3.3 Freeze in

The production mechanism called *freeze in* can be seen in some sense as the opposite with respect to the freeze out mechanism, in particular for its implications on the properties of the dark matter candidate. It was originally proposed in [43] (in relation to a model with a scalar singlet S interacting with the Higgs boson via a quartic term), and independently discussed in full detail in [44]. See [45] for a recent review.

In this framework one assumes that the dark matter candidate χ is thermally decoupled from the thermal bath at early times, because of its feeble interactions. Another assumption is that the initial number density of χ is negligible, for example because after reheating the reactions that produce χ in the final state are inefficient. Although the interactions with the thermal bath are feeble, χ is still produced, with a yield which turns out to be inversely proportional to the temperature T , and therefore increasing in time. Then the number density of χ keeps growing until the temperature drops below m_χ , and the reactions that produce χ become kinematically disfavoured. From that moment on, the number density of χ will substantially remain frozen because the interaction rate will be lower than the Hubble rate.

The most relevant feature of this mechanism is that n_χ is greater for higher couplings of χ to the thermal bath, contrarily to the freeze out case (see Fig. 1.7).

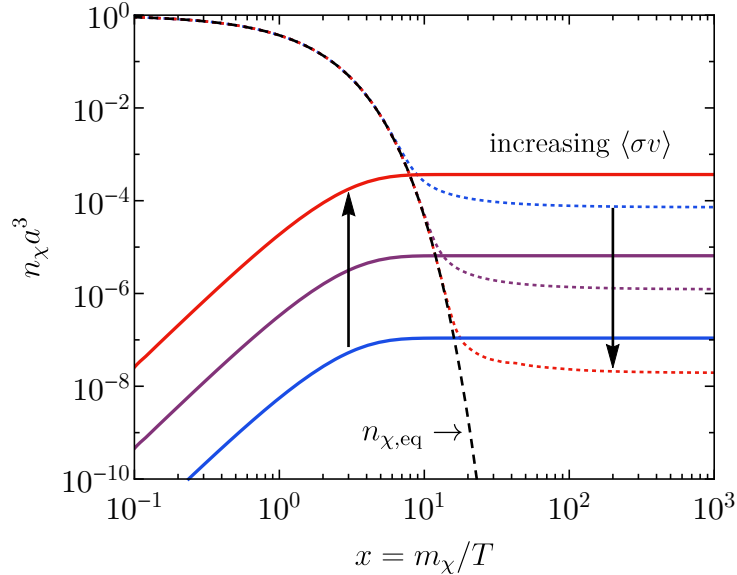


Figure 1.7: Evolution of the relic yield Y for the freeze out mechanism (solid coloured lines) and freeze in via a Yukawa interaction (dashed coloured), deviating from the equilibrium density (solid black). The arrows indicate the effect of increasing the coupling strength for the two processes (adapted from [44]).

We now estimate the yields expected for two possible renormalisable interaction terms, to show that they turn out to be decreasing with temperature (and hence increasing with time). The yield, being an adimensional quantity must be the ratio of the two dimensional quantities which are involved, the decay rate Γ (for a three field interaction, or $n\langle\sigma v\rangle$ for a two-to-two particles scattering) and the Hubble rate $H \sim T^2/M_{\text{P}}$.

For a Yukawa interaction $\lambda\psi_1\psi_2\chi$ among three fields with masses $m_1 > m_2, m_\chi$, the decay rate in the rest frame of ψ_1 must be $\Gamma^{\text{RF}} \sim \lambda^2 m_1$. The corresponding rate in the comoving frame can be obtained by dividing for the boost factor T/m_1 ; then $Y_\chi \sim \Gamma/H \sim \lambda^2 m_1^2 M_{\text{P}}/T^3$. By evaluating the yield for the temperature $T \approx m_1$ at which the production is dominant (with respect to later times when $T < m$) we get

$$Y_\chi \sim \lambda^2 \frac{M_{\text{P}}}{m_1}. \quad (1.7)$$

In the case of the quadrilinear interaction $\mathcal{L}_{\text{int}} = \lambda\chi^2\psi_1^2$, at early times the corresponding cross section will be proportional to λ^2/T^2 for dimensional reasons (when the two species are relativistic, $T \gtrsim m_1, m_\chi$), $n_\chi \sim T^3$ and $Y_\chi \sim n\langle\sigma v\rangle H^{-1} \sim \lambda^2 M_{\text{P}}/T$ which gives a final yield (for $T \approx m_1$) of the same order as before, $Y_\chi \sim \lambda^2 M_{\text{P}}/m_1$.

Even if the details of the freeze in mechanism and of the calculation of the relic density change from case to case, the relevant point that emerges from this estimates is that the yield predicted by this mechanism has opposite features with respect to the one predicted by freeze out. We can estimate the latter from Eq. (1.4) by inserting $\langle\sigma v\rangle \sim \lambda^2/m_\chi^2$ and $T \sim m_\chi$:

$$Y_{\text{FO}} \sim \frac{1}{\lambda^2} \frac{m_\chi}{M_{\text{P}}}. \quad (1.8)$$

We can see that the two mechanisms generally yield the correct relic abundance of dark matter for different regimes of the mass scales and interaction couplings (see Fig. 1.8).

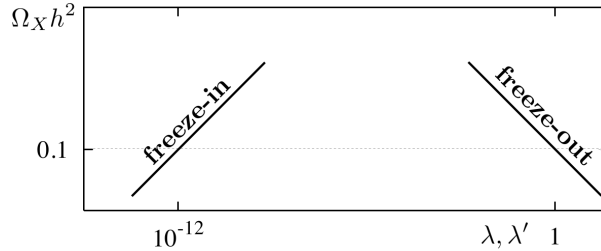


Figure 1.8: Schematic picture of the relic abundances due to freeze in and freeze out as a function of coupling strength (from [44]).

We conclude by observing that the yield predicted by the freeze in mechanism mainly depends on the particle (ψ_1 in our notation) which produces the dark matter particle χ , while the prediction from the freeze out depends on χ . Moreover, the comparison between the two results shows that, in order to get $\Omega_{\text{DM}} \approx 0.3$, the coupling constant must be of the order of the ratio between the weak scale and the Planck mass, $\lambda \sim v/M_{\text{P}}$: therefore, freeze in candidates are likely to arise in theories where small couplings arise at linear order in the weak scale. For a further discussion about possible candidates from supersymmetry or extra dimensions, see [44].

1.3.4 Asymmetric dark matter

The mechanisms we have discussed until now give relic abundances of dark matter that depend on microscopic quantities related to the interaction and couplings of the dark sector. For example, we have seen that in the freeze out mechanism Ω_{DM} depends in first approximation only on the annihilation cross section for the process $\chi\chi \rightarrow AA$.

In our Universe the densities of dark matter and baryonic matter are comparable, $\Omega_{\text{DM}} \approx 5\Omega_b$ (Eq. 1.1), and they always kept this ratio given that their energy densities scale both as a^{-3} as the Universe expands. Then, the production mechanisms for the two species brought to similar yields even if they took place at different times, and with completely different dynamics. This is a quite surprising coincidence if we assume the freeze out mechanism for dark matter and some different scenario for baryogenesis: this can be an accident, or could be discussed on anthropic grounds, or could be the dynamical result of two related production mechanisms for the two species. The latter framework goes under the name of *asymmetric dark matter*. This idea was proposed some time ago [46–48], and then regained much consideration in recent years (see for example [49, 50] and the reviews [51, 52]).

Baryogenesis (see [53] for a review) is related to the asymmetry between the amount of matter and antimatter in the Universe. This asymmetry is quantified by the difference between baryon and antibaryon number densities over the photon number density, $\eta = (n_b - n_{\bar{b}})/n_\gamma$, and is experimentally measured as 6×10^{-10} . In order to explain dynamically this asymmetry, the Sakharov conditions have to be fulfilled: baryogenesis must have happened out of the thermal equilibrium, and there must be interactions that violate the baryon number B and C , CP transformations.

One of the most promising options to solve this problem is to link it to another problem of the SM, the masses of neutrinos. If we add the right-handed neutrinos to the SM with a Majorana mass term and Yukawa couplings to the lepton and Higgs doublet, then the total leptonic number L is violated, and non-perturbative phenomena could have communicated an L violation to the baryonic sector during the leptogenesis [54, 55].

Independently from the mechanism that explains a slight initial asymmetry between baryons and antibaryons in the early Universe, later annihilations of baryon and antibaryons remove the symmetric part of the two components (decaying eventually into photons), leaving only the asymmetric part, until this reaction is efficient. The result of this process is indeed that the component which had a slightly smaller number density nearly disappears.

At this point, it is clear that the coincidence of the orders of magnitude of Ω_{DM} and Ω_b is unexpected. Starting from these considerations, many production mechanisms for dark matter, similar to the baryogenesis paradigm, stem out. As general features of this mechanism, we can list the following ones. An asymmetry between particle and antiparticle number density is initially created in the visible and/or the dark sector, at the same time or at different ones. For the dark sector, this requires some CP violating process which must also violate the quantum number that makes DM stable. Some process communicates the asymmetry between the two sectors and then decouples, freezing their amounts. Then the symmetric components, in each of the two sectors, must finally annihilate away through some efficient reaction. In analogy with the SM, this could happen in the dark sector through the annihilation of particle and antiparticle into the vector mediators of some dark force, or maybe through higher dimension operators. The final result is that the annihilations of dark matter leave only the asymmetric component which turns out to have a number density comparable to Ω_b .

It is interesting to notice that, within this framework, indirect searches are generically irrelevant because the annihilation processes cannot occur for the relic DM particles in absence of their antiparticles.

1.4 Particle candidates for Dark Matter

1.4.1 WIMPs: Weakly Interacting Massive Particles

As we have discussed in Sec. 1.3.1, the freeze out mechanism presents a *WIMP miracle*, i. e. it naturally predicts a correct Ω_{DM} for a weakly interacting particle with a mass of the order of the weak scale. The requirement that there are new particles at the weak (or TeV) scale (with some non-negligible interaction with the Standard Model) is the most straightforward one to solve the hierarchy problem. The coincidence that two very different problems at the microscopic and the macroscopic scale pointed to the same prediction has motivated for some decades a strong belief in the particle physics community that this should be the common solution to both problems.

Furthermore, the mass scale and the interaction strength (comparable to the weak one of the SM) of the WIMP motivate the hope of an accessible detection (at least with respect to other classes of candidates) with some of the methods described in Sec. 1.5, because the freeze out mechanism offers a lower bound on the interaction rate with the SM.

1.4.1.1 Candidates from supersymmetry

Supersymmetry (SUSY) is a vast field, which emerged back in the '70s in the study of string theories, and has motivated a large activity in the following decades. The key property of supersymmetric theories is the extension of the usual spacetime and gauge symmetries by a symmetry linking bosonic and fermionic fields. It is impressive that some of the most critical problems of the SM, as the hierarchy problem, or dark matter, or the inclusion of quantum gravity can find in SUSY respectively a solution, a WIMP (and a SuperWIMP) candidate, and a possible connection to supergravity and superstring theories. Moreover, the unification of gauge couplings at a scale $M \sim 10^{16}$ GeV featured by the simplest supersymmetric extension of the SM, the Minimal Supersymmetric Standard Model (MSSM), offers a significant hint for Grand Unified Theories (GUT) at high scales.

We refer to the excellent reviews [56–58] for a detailed introduction to SUSY and MSSM. Ref. [14] discusses at length the properties of Supersymmetric Dark Matter.

We do not enter here into the details of model building for supersymmetric theories, and we recall a result which is relevant for our discussion on SUSY candidates for DM. In the construction of a supersymmetrised version of the SM, it turns out that, without the imposition of some discrete symmetry, there could appear terms in the Lagrangian (in particular, in the superpotential) which violate the B and L symmetries. These are highly constrained by experiments, so that the solution is to impose a \mathbb{Z}_2 symmetry, called matter parity, which forbids these terms to appear. This symmetry can be equivalently rephrased in terms of the R -parity. Its quantum numbers for each field are given by $(-1)^{3B-L+2s}$, where s is the spin. The result is that all the SM fields have an R -parity number equal to $+1$, and all their supersymmetric partners (which are fermionic for SM bosons, and viceversa, and are typically denoted with a tilde) have a -1 . This has important physical consequences: the lightest particle with R -parity equal to -1 cannot decay into lighter particles because otherwise it would violate R -parity, therefore it is absolutely stable. This is exactly the type of discrete symmetry that can make the DM candidate stable on cosmological scales. Therefore, the MSSM predicts a DM candidate if the Lightest Supersymmetric Particle (LSP) is electrically neutral.

We now review the possible candidates in supersymmetric theories.

The prototypical SUSY candidate for DM is the lightest *neutralino*. This is the name given

to each of the mass eigenstates which arise as a mixing of the four neutral fermion fields³ \tilde{B} , \tilde{W}^0 , \tilde{H}_d^0 and \tilde{H}_u^0 . These fields have the same quantum numbers, therefore the mass eigenstates (usually denoted⁴ by $\tilde{\chi}_i^0$, $i = 1, \dots, 4$) are a mixing among them. The lightest neutralino can be the LSP, depending on the overall mass spectrum of the full model.

The other important DM candidate is the *gravitino*, the spin-3/2 superpartner of the graviton in supergravity theories. Its mass is related to the supersymmetry breaking scale F (which has mass dimension 2) by $m_{\tilde{G}} = F/(\sqrt{3}M_{\text{P}})$. Depending on the masses of the gravitino and the neutralino, the lightest between them is the LSP. As discussed in section 1.4.2, the gravitino is likely to be a SuperWIMP candidate, i. e. a very weakly interacting candidate that decoupled from the thermal bath in the early universe through the mechanism of the freeze out and decay described in Sec. 1.3.2.

Other two possible SUSY candidates for DM are now excluded because of experimental constraints. The *sneutrino* is the scalar superpartner of the neutrino, and is potentially a viable DM candidate because it is a colour singlet and is electrically neutral. The constraint from LEP on the invisible Z decay width rules out a sneutrino lighter than $m_Z/2$, and its interactions via the Z boson yield scattering cross sections with nucleons too large to escape the constraints from direct searches. Extended models with right-handed neutrinos may reopen the possibility of sneutrino dark matter by lowering the interaction cross section. Finally, another DM candidate could be an electrically neutral *R-hadron*, the supersymmetrised versions of the hadrons of the SM, built up of squarks and gluinos. They are a candidate of Strongly Interacting Massive Particles (also called SIMP). They are basically ruled out by the strong constraint from the Earth heat flow: when the dark matter capture rate in Earth is efficient, the rate of energy deposition by dark matter self-annihilation products would grossly exceed the measured heat flow of Earth. These limits exclude a nucleon-DM cross section higher than around $10^{-34} - 10^{-33}$ cm² [59], severely restricting the chances that this could be the DM candidate.

1.4.1.2 Lightest Kaluza-Klein particle

Another important class of DM candidates is given by the so-called Lightest Kaluza-Klein particles, which arise in models with extra dimensions with respect to the usual four spacetime dimensions.

The ancestor of these models is the unfruitful attempt made by Kaluza in 1919 and improved by Klein in 1926, with the intention to unify gravity and electromagnetism. Extradimensional models returned to be amply studied at the end of the 1990s with more emphasis on phenomenology. An important paper by Arkani-Hamed, Dimopoulos and Dvali (ADD) in 1998 [60] suggested that spacetime can have more than 4 dimensions and all the SM particles be confined to a four-dimensional submanifold, referred to as a 3-brane. The only fundamental force whose interactions spread in the extra dimensions is gravity, and in the higher dimensional spacetime general relativity holds. The limit on the size of the extra dimensions would be fixed by the experimental tests on Newton's law of gravitation, which are now probing the μm scale. In this proposal, the weakness of gravitational forces is due to the leak of gravity into the extra dimensions, and the hierarchy problem is translated into the problem of the discrepancy between the large size of the extra dimensions and the value of the Planck length.

Shortly after, the Randall-Sundrum model [61, 62] proposed to enlarge spacetime to a 5-dimensional anti-de Sitter space time, with the SM particles still confined to a 3-brane. The

³In the MSSM, due to the properties of the superpotential, one has to introduce two Higgs doublets H_u and H_d .

⁴Due to the (well motivated) widespread belief in the '80s and the '90s that the SM could be completed by a SUSY theory at the weak scales, also DM was nearly identified with the neutralino in the community. This explains the common notation χ for the DM particle, which we do not contravene in this Chapter.

weak scale is generated from the Planck scale through an exponential hierarchy, arising from the background metric: in this way, only a modest fine-tuning is required with respect to what is needed in ADD model.

These proposals encouraged many phenomenological investigations of models of extra dimensions, also called Kaluza-Klein (KK) models. See [63, 64] for some reviews on this subject. The common feature of these models is the presence of towers of discrete levels of excited states with respect to the ordinary SM particles, due to the quantisation of the momentum of the fields (gravitons, or in some cases also the SM particles) along the extra dimensions. The first level of excited states can be produced at energies of the order of $1/R$, where R is the radius of compactification of the extra dimension, which ranges from the order of the meV^{-1} ($\approx \text{mm}$) in ADD models, to the TeV^{-1} ($\approx 10^{-18} \text{ m}$) when ordinary particles can propagate in the extra dimension, or even to M_{P}^{-1} .

The excited KK states are in general not stable, since they can decay to states of lower energy. The discrete \mathbb{Z}_2 symmetry that ensures the stability of the Lightest KK Particle (LKP) is the Kaluza-Klein parity, a discrete symmetry related to the conservation of momentum along the extra dimension. This symmetry remains unbroken in a some specific class of models named Universal Extra Dimensions (UED) [65], where also the SM fields can propagate to the extra dimensions. This symmetry allows for the LKP, if it is electrically neutral with interactions of a strength comparable to that of the electroweak force, and if the extra dimension has a size of the order of the TeV^{-1} , to be the DM candidate.

Depending on the details of the models, there are a few particles which could be the LKP. Among the most plausible candidates we cite the KK partners of the photon and of the graviton. We refer the reader to [66, 67] for reviews on DM candidates in this class of theories.

1.4.1.3 Minimal Dark Matter

The two classes of model that we have just discussed (SUSY and extra-dimensional models) are strongly motivated by the hierarchy problem. An alternative approach is to focus just on the DM problem, and to add to the SM the minimal set of ingredients and assumptions. The proposal of *Minimal Dark Matter* (MDM), originally formulated in [68], and further developed in [69–72], adopts the perspective that the DM stability could be ensured not by ad-hoc discrete symmetries (as R -parity, or the KK parity) but by accidental symmetries.

In the SM the baryon number conservation (which renders protons stable) is just an accidental symmetry of the most generic renormalisable Lagrangian that is admissible given the SM charges. Analogously, in the MDM scenario one adds to the SM a (scalar or spinor) multiplet \mathcal{X} with suitable charge assignments such that one of the components of \mathcal{X} does not admit renormalisable operators leading to its decay and is a stable DM candidate.

The requirements on \mathcal{X} are that it does not introduce Landau poles in the running of the coupling constants before the Planck scale M_{P} , that the DM component \mathcal{X}^0 is absolutely stable and neutral under $SU(3)_c$ (given the bounds from the Earth heat flow cited in Sec. 1.4.1.1) and $U(1)_{\text{EM}}$, and that \mathcal{X} has a vanishing hypercharge (to prevent a tree level vector coupling with the Z boson which contradicts the null detections of direct searches).

Quite remarkably, it turns out that there is only one multiplet respecting all these conditions: a fermionic 5-plet of $SU(2)_L$. Once the multiplet is fixed, the only free parameter of the model is the tree-level mass $M_{\mathcal{X}}$ of the multiplet. The various components get small mass splittings due to their self-energy diagrams with $SU(2)_L$ boson loops. The neutral component turns out to be the lightest state (which is crucial for its stability) with a mass splitting with \mathcal{X}^{\pm} of 166 MeV. The mass $M_{\mathcal{X}}$ is constrained by requiring the correct relic abundance via freeze out. The proper calculation takes into account the coannihilations with the charged components of \mathcal{X} ,

the Sommerfeld enhancement, which is the amplification (for attractive interactions) of the annihilation cross section of $\mathcal{X}^0\mathcal{X}^0$ in presence of a light mediator [69], and the formation of bound states [72]. The final result for the fermionic 5-plet is $M_{\mathcal{X}} = 11.5$ TeV.

The high energy searches of this DM candidate, either at a future collider or at a storage ring of nuclei which could interact with the DM around us, are very difficult. A clear signature could come from the production of \mathcal{X}^\pm and its decay to \mathcal{X}^0 , but unfortunately their mass splitting is just above m_{π^\pm} , allowing for a large branching ratio $\mathcal{X}^\pm \rightarrow \mathcal{X}^0\pi^\pm$. This reduces the free path of \mathcal{X}^\pm to a few cm, and suppresses the cleaner decay channel $\mathcal{X}^\pm \rightarrow \mathcal{X}^0e^\pm\nu_e$. Direct searches have better chances to detect the MDM candidate, which interacts with nucleons at one loop, and the model is within reach of future experiments [73].

The most relevant constraints on MDM come from γ ray searches, in particular from HESS observations of γ ray lines from the Galactic Centre [71], and put this model under serious pressure. Possible generalisations which rescue this scenario could be to assign a tiny electrical charge to \mathcal{X} (millicharged DM), or to lower the cutoff below M_P , and to allow the DM to be stable on cosmological times but not absolutely stable [74].

1.4.2 SuperWIMPs

SuperWIMP candidates are related to the production mechanism of freeze out and decay, described in Sec. 1.3.2. From the observational point of view, the extremely weak interactions of this candidate tend to disfavour the hope of detection. Nevertheless, the interesting point about this production mechanism is that it reduces the requirements about its producer, which in this scenario can be a more generic WIMP with a mass above the TeV and does not need to be neutral, since it is not the DM candidate.

The classic example of a superWIMP is a weak scale gravitino \tilde{G} , the spin-3/2 partner of the graviton (see Sec. 1.4.1.1). In this case the role of the WIMP is played by the Next to Lightest Supersymmetric Particle (NLSP), which can be a charged slepton, or the sneutrino, or the chargino, or the neutralino. Other candidates of superWIMP include axinos (the supersymmetric partners of axions), and graviton and axion states in extra-dimensional models.

1.4.3 Sterile Neutrinos

Also the models addressing the problem of neutrino masses offer an attractive DM candidate: the right-handed neutrinos ν_R . These fermions would be gauge singlets, and therefore it would be possible to write a Majorana mass term for them, in addition to the Yukawa couplings to the left-handed lepton doublet L_L and the Higgs $SU(2)_L$ doublet H . The corresponding Lagrangian for the so-called ν MSM (Neutrino Minimal Standard Model) is (by a superscript c we denote the conjugate $SU(2)_L$ doublet and Lorentz spinors)

$$\mathcal{L}_{\nu\text{MSM}} = \mathcal{L}_{\text{SM}} - Y_\nu \overline{L}_L H^c \nu_R - \frac{1}{2} M \overline{(\nu_R)^c} \nu_R. \quad (1.9)$$

The mass eigenstates for the neutrinos, after electroweak symmetry breaking, are a mixture of ν_L and ν_R ; let us call the corresponding eigenvalues m_ν and M_N , and the corresponding eigenstates ν and N . In the simplest model addressing the smallness of the neutrino masses with respect to the other SM particles, the *type-I see-saw* mechanism, $M \gg Y_\nu v$ and the mass of the heavy neutrinos (or *sterile* neutrinos, given that they interact with the SM only through the small mass mixing) is

$$M_N \approx M \approx \frac{Y_\nu^2 v^2}{2m_\nu}. \quad (1.10)$$

Another option is to get a sterile neutrino mass of the order of a few keV, by postulating tiny Yukawa couplings, of the order of 10^{-10} , a value which is some orders of magnitude below the smallest Yukawa coupling in the SM ($Y_e \approx 3 \cdot 10^{-6}$). This option is motivated by the possibility of solving through this minimal modification of the SM three great puzzles such as neutrino masses, dark matter and baryogenesis [75–77]. A keV sterile neutrino is a candidate of Warm Dark Matter (WDM, see Sec. 1.1.3), so it could possibly alleviate some alleged problems in the predictions of CDM for the Large Scale Structures.

In this scenario, the lightest sterile neutrino, say N_1 , is the dark matter candidate. Given its low mass, the main physical decay channel appears only at one loop through the small mixing with ν_L (see Fig. 1.9). The overall result is a decay $N_1 \rightarrow \nu_L \gamma$, with a peculiar experimental signature given by the observation of an X-ray with defined energy $M_N/2$. This is indeed the experimental search that has the best possibilities to probe this scenario.

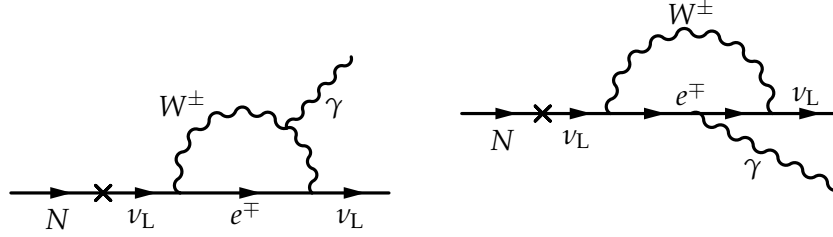


Figure 1.9: Feynman diagrams at one loop for the decay of a sterile neutrino N into a photon and a left-handed neutrino ν_L . The cross on the fermionic line denotes the ν_L component of the mass eigenstate N , which is a mixture of ν_L and ν_R .

1.4.4 Axions

The most important and well-motivated DM candidates together with WIMPs are *axions* and Axion-Like Particles (ALPs). The QCD axion was introduced as a solution to the strong CP problem [78–80]. The QCD Lagrangian should include a Chern-Simons term

$$\mathcal{L}_{\theta\text{QCD}} = \frac{\theta}{32\pi^2} \text{Tr} G^{\mu\nu} \tilde{G}_{\mu\nu}, \quad (1.11)$$

where $G^{\mu\nu}$ is the gluon field strength tensor and $\tilde{G}^{\mu\nu} = \frac{1}{2}\epsilon^{\mu\nu\rho\sigma}G_{\rho\sigma}$ is its dual tensor, and the trace runs over the colour indices. This term is a four-divergence,

$$G_{\mu\nu}^a \tilde{G}^{a\mu\nu} = \partial_\mu \left[\epsilon^{\mu\nu\rho\sigma} \left(G_\nu^a G_{\rho\sigma}^a - \frac{g_s}{3} f_{abc} G_\nu^a G_\rho^b G_\sigma^c \right) \right], \quad (1.12)$$

so that at the classical level it would be unphysical, but this is not the case at the quantum level in a non-Abelian gauge theory, due to the presence of instantons.

The operator in Eq. (1.11) violates parity and time reversal, but not charge conjugation, therefore it violates CP. Another source of CP violation in the SM comes from the Yukawa matrices Y_u, Y_d which generate quark masses after EW symmetry breaking. By performing a chiral global rotation on the quarks, we can change the coefficient in front of Eq. (1.11), so that the physical combination is just

$$\theta_{\text{QCD}} = \theta + \arg \det (Y_u Y_d). \quad (1.13)$$

By mean of a chiral rotation, we can make the Yukawa matrices real while changing the value of the coefficient of $G\tilde{G}$, and the physically relevant coefficient is θ_{QCD} .

This term has some measurable effects, the most notable being a contribution to the neutron electric dipole moment $d_n = 3 \cdot 10^{-16} \theta_{\text{QCD}} e \cdot \text{cm}$. The null detection of this static neutron dipole moment brings to the experimental limit $|d_n| < 3 \times 10^{-26} e \cdot \text{cm}$, which implies $|\theta_{\text{QCD}}| \lesssim 10^{-10}$. The absence of an explanation in the SM for the tiny value of this dimensionless parameter is the *strong CP problem* (see [81, 82] for reviews).

The Peccei-Quinn solution of this problem is to make this coefficient dynamical. One introduces a $U(1)_{\text{PQ}}$ global chiral symmetry, under which some quarks are charged, which is broken spontaneously by a complex scalar field φ . A simple possibility is to write a potential $V(\varphi) = \lambda(|\varphi|^2 - f_a^2/2)^2$, so that $\langle \varphi \rangle = (f_a/\sqrt{2}) \exp(ia/f_a)$. The field a is the Goldstone boson of $U(1)_{\text{PQ}}$, and it is called axion, while f_a is the axion decay constant. Let us assume that the mixed anomaly between $U(1)_{\text{PQ}}$ and $SU(3)_c$ is non vanishing (because of the SM quarks or new heavy quarks charged under $SU(3)_c$), with an anomaly coefficient \mathcal{C} given by $\mathcal{C}\delta_{ab} = 2 \text{Tr} Q_{\text{PQ}} T_a T_b$ where T_a are the $SU(3)_c$ generators. Then we can perform a local chiral rotation of the quarks with an angle a/f_a and, due to the anomaly, the action changes into

$$S \rightarrow S + \int d^4x \frac{\mathcal{C}}{32\pi^2} \frac{a}{f_a} \text{Tr} G^{\mu\nu} \tilde{G}_{\mu\nu}. \quad (1.14)$$

This implies that we can reabsorb θ_{QCD} into the axion field a by just performing a chiral rotation. A key point is that the axion Lagrangian is shift invariant at tree level, a being the Goldstone boson of $U(1)_{\text{PQ}}$. The last ingredient to solve the strong CP problem comes from the calculation at the non-perturbative level of the axion potential. In the dilute instanton gas approximation, one finds that the vacuum energy depends on a as $E(a) \propto 1 - \cos(\mathcal{C}a/f_a)$. The periodic potential for the axion is minimised at $a = 0 \pmod{2\pi}$. This is the Peccei-Quinn-Weinberg-Wilczek solution of the strong CP problem: the axion field brings dynamically the coefficient in front of the $G\tilde{G}$ term to 0.

We now discuss the phenomenological consequence of the existence of the axion. For more detailed reviews on the axions and their experimental probes, one can see Refs. [83–88].

Its mass turns out to be (from now on, we redefine $f_a/\mathcal{C} \rightarrow f_a$)

$$m_a \approx \frac{m_\pi f_\pi}{f_a} = (6 \mu\text{eV}) \cdot \left(\frac{10^{12} \text{ GeV}}{f_a} \right). \quad (1.15)$$

For a value of f_a around the TeV we get $m_a \sim \text{keV}$, while for higher values of f_a around the GUT scale we obtain $m_a \sim 10^{-9} \text{ eV}$. The couplings of the axion to matter are all suppressed by f_a^{-1} ; therefore, if the axion decay constant is large enough, it is extremely hard to detect its interactions with matter. Axions can then be extremely light and weakly coupled to the SM. Similar fields arise very generically in string theory, and are called Axion-Like Particles (ALPs).

ALPs would be a DM candidate in the form of a scalar condensate oscillating around its minimum. Depending on the value of m_a , it could have various effects on galactic and cosmological scales. Recently, the hypothesis that DM could be constituted of ultralight ALPs with a mass 10^{-22} eV and a de Broglie wavelength of about 1 kpc has been receiving increasing attention [89].

Many astrophysical and cosmological probes constrain the parameter space of axions. Their interaction with the SM which is most relevant from the phenomenological point of view is the one with photons, through the coupling

$$\mathcal{L}_{a\gamma\gamma} = -\frac{g_{a\gamma\gamma}}{4} a F^{\mu\nu} \tilde{F}_{\mu\nu} \propto \frac{a}{f_a} \vec{E} \cdot \vec{B}. \quad (1.16)$$

The coupling of the axions to photons implies for example the emission of axions by stars and exploding supernovæ, which offers some important constraints from the cosmological side.

From the experimental side, Eq. (1.16) tells that the passage of an axion in a very strong magnetic field can bring to its conversion in a photon. This is the phenomenon exploited by various current experiments (like ADMX and CAST), and at the core of many recent proposals. We show in Fig. 1.10 a recent summary of the current constraints on ALPs in the plane $(m_a, g_{a\gamma})$.

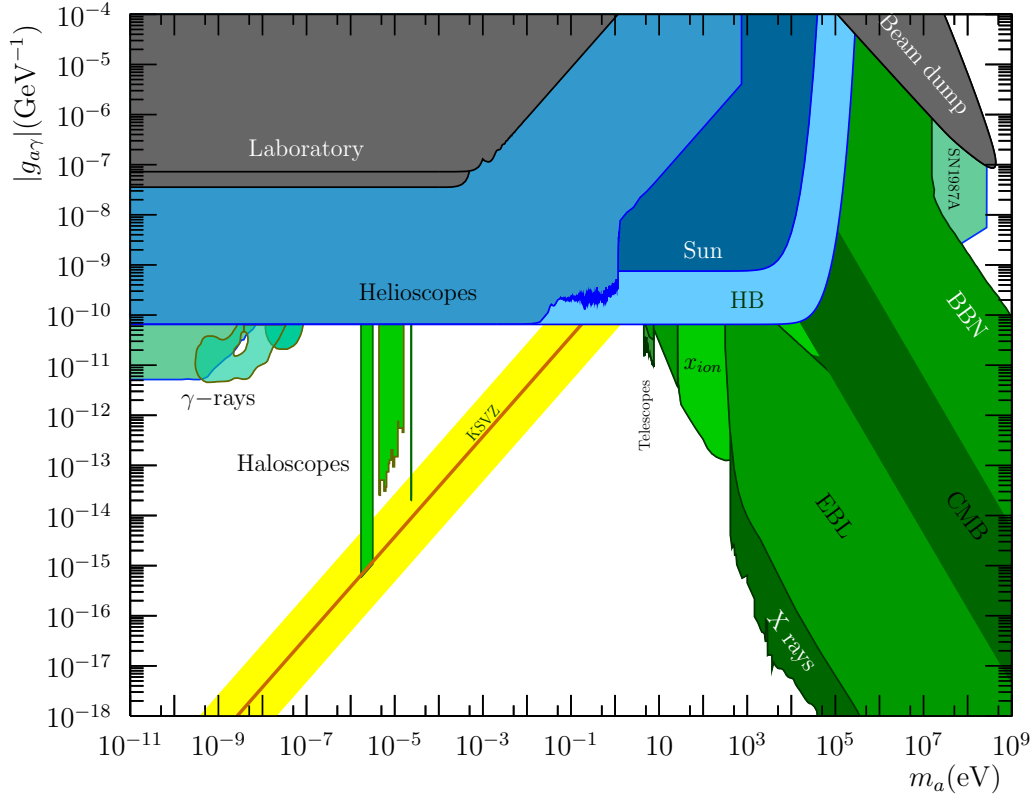


Figure 1.10: Current constraints on ALPs in the $(m_a, g_{a\gamma})$ plane. The grey constraints come from purely laboratory results, the blue ones are related to helioscopes (experiments aiming to detect axions from the Sun) and stellar physics, and the green ones refer to haloscopes (experiments looking for axions constituting the DM in the halo) and cosmological arguments. The yellow band refers the favoured region for the QCD axion. The figure is taken from [88], to which we refer for the description of the constraints.

In Fig. 1.11 we show a summary of the proposed and planned experiments dedicated to ALPs, which are going to cover most of the relevant parameter space for the QCD axions in the range $m_a = 10^{-8} - 1$ eV. The number of proposed experiments testifies the remarkable interest attracted by the field of axion searches in recent years.

For the sake of this Thesis, we do not enter into the details of the vast domain of axions searches and axion cosmology, and we refer in particular to the excellent recent reviews [86, 88].

We conclude this section with a brief summary about the cosmological production of axions. The hypothesis of a standard thermal relic production with $\Omega_a \approx \Omega_{\text{CDM}}$ requires $m_a \sim 80$ eV, which would imply a decay time for $a \rightarrow \gamma\gamma$ too short on cosmological scales. Therefore, some other production mechanism for the axion must take place: we can distinguish two possible cases, depending on whether the breaking of $U(1)_{\text{PQ}}$ happens before inflation or after its end. In any of these cases, axions behave as cold dark matter, even if their mass is tiny, because they

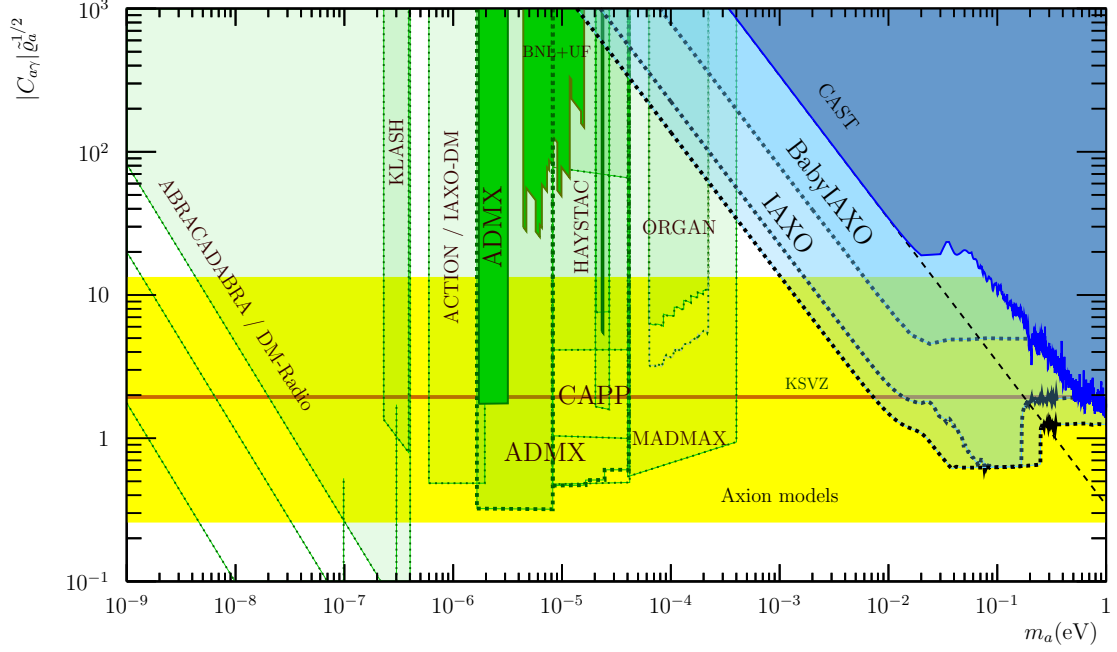


Figure 1.11: Forecasts for the sensitivity of planned and proposed experiments to measure the coupling $g_{a\gamma}$, shown in the plane $(m_a, g_{a\gamma} f_a (2\pi/\alpha_{\text{em}}) \sqrt{\Omega_a/\Omega_{\text{CDM}}})$, where Ω_a is the axion energy density. The colour code is the same as in Fig. 1.10. The figure is taken from [88], to which we refer for the description of the various experiments.

are produced out of the thermal equilibrium with a low energy distribution.

Before the breaking of $U(1)_{\text{PQ}}$, the axion mass is negligible. If $U(1)_{\text{PQ}}$ is spontaneously broken before inflation, each of patches of spacetime with a different value of $\langle a \rangle$ inflated to a region larger than our observable Universe, which displays an homogeneous $\langle a \rangle$. In that case, the relevant contribution of axions came when QCD effects became relevant, at an energy scale around 1 GeV. At this point, the field a rolls from its initial value a_i towards the true minimum, where it begins to oscillate and contributes to the local energy density as non-relativistic matter; this phenomenon is called *vacuum realignment*. The current axion energy density is then

$$\Omega_a \simeq 0.15 \left(\frac{f_a}{10^{12} \text{ GeV}} \right)^{7/6} \left(\frac{a_i}{f_a} \right)^2. \quad (1.17)$$

If the PQ phase transition occurs after the end of inflation, then our observable Universe should consist of a mixture of many patches with different expectation values $\langle a \rangle$. Along their boundaries there could lie topological defects as domain walls or axionic strings, with observable effects. Which of these two scenarios could have been realised in nature depends on the interplay between the PQ scale f_a and the Hubble rate during inflation, which is currently constrained to be $H_I \lesssim 4 \cdot 10^{14} \text{ GeV}$ from the measurements of the tensor-to-scalar ratio r [90].

1.5 WIMP searches

In this Section, we summarise the possible experimental searches for WIMP dark matter, distinguishing three broad categories: direct, indirect and collider searches.

1.5.1 Direct searches

Direct searches try to detect the interaction of DM particles of our galaxy with a detector on the Earth. The relative motion of the Earth with respect to the Milky Way imply a relatively large flux of DM particles through our planet. Hence one of the possible experimental searches for DM consists in monitoring a large detector made of a specific material with high density, in order to maximise the cross section of a DM particle with one of the nuclei of the detector [91]. The expected signal is extremely low, and can be observed only if the background of cosmic rays and other sources is minimised: this is accomplished by putting the detectors underground, usually in mines or inside a mountain under a thick layer of rock. This choice reduces the background from cosmic rays with respect to the surface of the Earth at the order of one over a thousand. In order to quantify the expected number of events, many inputs from different research fields must be specified. Refs. [92–96] offer detailed reviews on the subject of direct detection.

The flux of DM particles depends both on the local density and on the velocity distribution of DM (see e.g. [97] for a detailed discussion). The Standard Halo Model describes an isotropic, isothermal sphere with an energy density profile $\rho(r) \propto r^{-2}$. The local DM energy density is usually taken equal to $\rho_0 = 0.3 \text{ GeV/cm}^3$. The velocity distribution corresponding to the Standard Halo Model is the Maxwell distribution, truncated at an escape velocity v_{esc} , above which a DM particle is not gravitationally bound to the Milky Way. The traditional value is $v_{\text{esc}} = 650 \text{ km/s}$, and Ref. [98] updated this value to $498 \text{ km/s} < v_{\text{esc}} < 608 \text{ km/s}$ at 90% CL, with a median of $v_{\text{esc}} = 544 \text{ km/s}$. The standard deviation for the velocity distribution of DM particles is typically assumed to be $\sigma_v = 220/\sqrt{2} \text{ km/s}$. The velocity of DM particles in the detector frame is the sum of the peculiar DM velocity and of the Sun's velocity of about 220 km/s with respect to the centre of the Milky Way, with a small contribution due to the motion of the Earth with respect to the Sun. The astrophysical dependencies are the most relevant uncertainties for direct detection. Their impact on the final constraints was studied in Refs. [99–101] and more recently in Ref. [102].

In direct detection experiments, a careful choice of the material of the detector must be done. Indeed, the larger are the atomic number and the spin of the nucleus, the more the event rate is increased respectively for spin-independent and spin-dependent cross sections with DM, i. e. cross sections that do not depend (or do) on the spin of the nuclei. Furthermore, materials with higher density maximise the cross section of the interaction, and then of course the larger is the detector and the more targets are offered to an incoming WIMP. Last but not least, the cost of the material is one of the key expenses for the experiment, so that a balance between all these different properties has to be sought. The recoil energy left by a scattered DM particle is measured through the heat deposition, and ionisation or scintillation signals. Some examples of the materials chosen to be highly sensitive to spin-independent searches are liquid xenon (in particular XENON1T and LUX), germanium (CDMS, EDELWEISS, CoGeNT), calcium tungstate (CRESST), sodium iodide (DAMA). For spin-dependent interactions, it is convenient to choose materials containing fluorine, which has a non-zero intrinsic spin: some examples of these experiments are PICO, COUPP and SIMPLE.

The key quantity for a direct detection experiment is the energy threshold for the detection of a signal. The experiments listed before aim at the detection of the recoil of a WIMP with a nucleus (nuclear recoil), and they are sensitive to a recoil energy of roughly a keV. The expression of the recoil energy for the scattering of an incoming DM particle with mass m_χ with a nucleus of mass m_N depends on the reduced mass of $\mu_N = m_\chi m_N / (m_\chi + m_N)$, and is maximum for $m_\chi \sim m_N$. For lighter DM particles, the recoil energy would be too small, so that the sensitivity of direct detection experiments quickly degrades for m_χ below some GeV. For heavier DM par-

ticles, μ_N saturates to m_N , but the reach of the exclusion limit weakens because the DM flux is proportional to $n_\chi = \rho_0/m_\chi$: for a fixed energy density, the heavier are the DM particles the less abundant they are. These two considerations explain the shape of direct detection bounds.

The evaluation of the scattering rate on the detector requires the elastic scattering cross section between DM and the nucleus. This cross section can be derived from the microscopic theory through the following steps [103–105].

First, we compute the differential cross section for the scattering between a parton (a quark or a gluon) and DM from the microscopic theory. This can be safely computed by using an effective field theory (EFT) approach, if the WIMP mass is not comparable to mass of its mediator with the SM, because of the non-relativistic environment of the process.

Then one must convert the microscopic cross section for the parton-DM interaction to a cross section between a nucleon (a neutron or a proton) and DM. This is done by using the hadronic matrix elements, i. e. the matrix elements for the operators containing quark or gluon fields, with the introduction of the form factors, experimentally measured functions that depend on the momentum exchanged in the interaction.

Eventually, from the cross section between DM and a nucleon we can obtain the scattering cross section with the nuclei by mean of the nuclear wavefunctions, which are measured experimentally by nuclear physicists. The final result is parametrised in terms of a basis of non-relativistic matrix elements between the DM χ and the nucleus N , which are classified according to the Galilean invariants for the process: the spins \vec{s}_χ , \vec{s}_N , the transverse DM velocity \vec{v}^\perp and the exchanged momentum \vec{q} . There are two of these operators which are not suppressed by the DM velocity, and are usually taken as benchmarks for the presentation of the exclusion results, respectively for spin-independent (SI) and spin-dependent (SD) scattering:⁵

$$\bar{\chi}\chi\bar{q}q, \bar{\chi}\gamma^\mu\chi\bar{q}\gamma_\mu q \rightarrow \mathcal{O}_1^{\text{NR}} \equiv \mathbb{1} \quad \bar{\chi}\gamma^\mu\gamma_5\chi\bar{q}\gamma_\mu\gamma_5 q \rightarrow \mathcal{O}_4^{\text{NR}} \equiv \vec{s}_\chi \cdot \vec{s}_N. \quad (1.18)$$

In Fig. 1.12 we show the current limits on the SI cross section of nucleon and DM from various experiments, and in Fig. 1.13 we show the analogous limits for a SD cross section. Due to the strong enhancement with the atomic number of the nucleus for the SI scattering, where all the nucleons interact coherently with the DM, these bounds are six orders of magnitude stronger than the SD scattering.

Fig. 1.12 (left) shows also the expected contribution from the neutrino background from the Sun, the interaction of cosmic rays with the Earth's atmosphere and from astrophysical sources like Supernovæ. This contribution will be a limitation for the current detectors, because this background it is indistinguishable from a DM signal. The only solution to go beyond this barrier in the sensitivity is to design experiments which are sensitive to the direction of the incoming neutrino (or DM particle).

In recent years, the theoretical community has been devoting a lot of effort to the design of new techniques for the next generations of direct detection experiment. The main goals are lowering the energy threshold by considering events different from nuclear recoils, in order to improve the reach for DM masses in the range keV-GeV, or measuring the direction of the incoming particle leaving a signal in the detector. Physical phenomena which could be exploited to lower the threshold include electronic recoils from ionization events [115–117], electronic excitation and de-excitation with the consequent photon emission [115, 118], molecular dissociation with the production of ions, and finally phonon or heat production [115, 119], electron scattering in semiconducting materials [117, 120–122], in Dirac materials [123], in superfluids

⁵Notice that, due to the effect of the Renormalisation Group flow, even if at scale some effective operator has a vanishing coefficient it could be generated at a lower scale. In particular, operators which are absent at the electroweak scale could be generated at the low-energy scale which is relevant for direct detection [106–110].

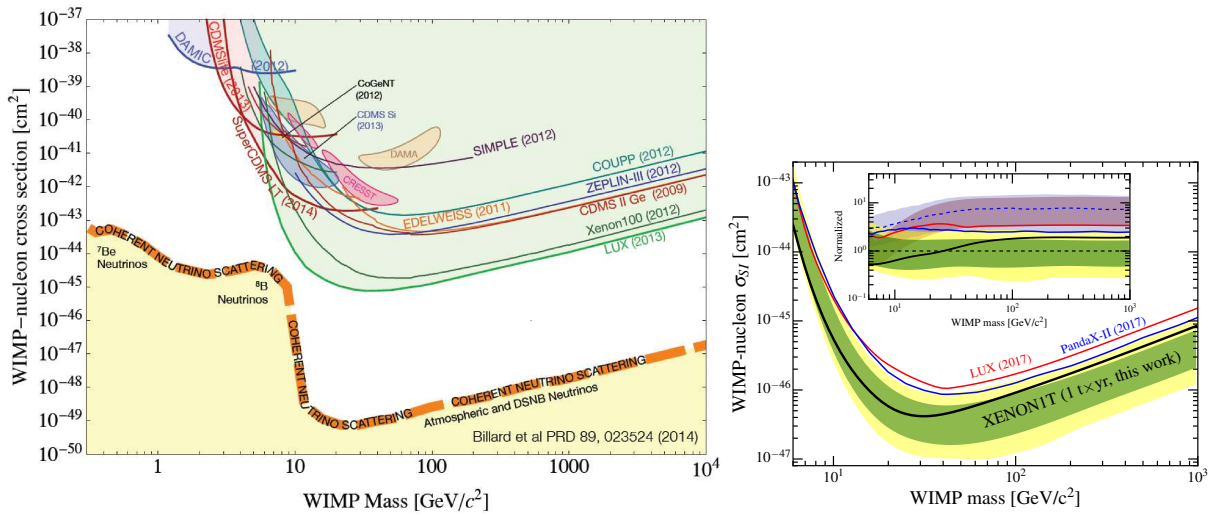


Figure 1.12: *Left:* upper limits on the spin-independent scattering between WIMP and nucleon, with the expected background from neutrino scattering [111]. *Right:* the most updated spin-independent limits from Xenon1T [112].

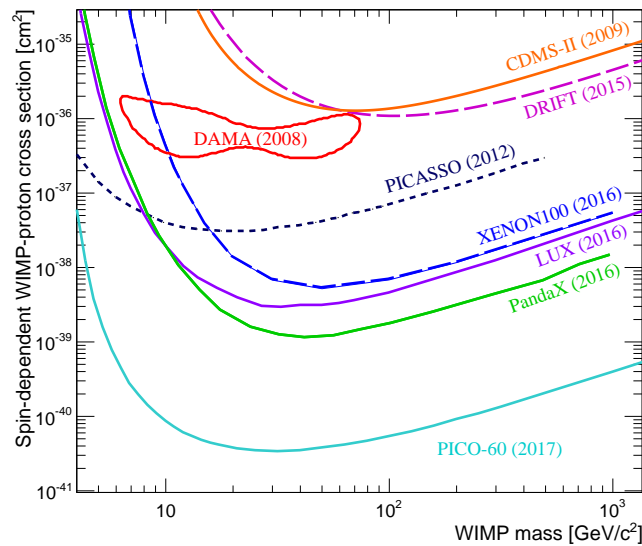


Figure 1.13: Recent compilation [113] of the upper limits on the spin-dependent scattering between WIMP and protons assuming pure proton coupling. The strongest bounds currently come from PICO-60 [114].

[124, 125] and in superconductors [126–128], brehmsstrahlung in low recoil energy nuclear scatterings [129]. Searches in the low mass range could have directional sensitivity if performed with 2D graphene targets, as recently proposed in [130]. Radically new proposals include the study of tracks left by DM particles in ancient minerals [131].

1.5.2 Indirect searches

Indirect techniques are based on the search of radiation produced in DM annihilations in the universe. The flux of the radiation produced by these annihilations is proportional to the annihilation rate Γ_{ann} , which in turn depends on the square of the DM density, $\Gamma_{\text{ann}} \propto n_{\text{DM}}^2$.

Therefore the most promising directions to look at, in order to maximise the probability of detecting the products of these interactions, are the regions where DM accumulates, which are also called in this context amplifiers. Examples of such DM-dense environments on which we are commenting later are the Galactic Centre, dwarf Spheroidal Galaxies (dSph), and the Sun.

Independently of the primary annihilation channel of the DM pair, the subsequent decay chain leads to the production of a variety of SM final states, and in particular γ rays, protons and antiprotons, electrons and positrons, and neutrinos. This is shown schematically in Fig. 1.14. If the DM mass is above a few hundreds GeV, then the radiation of EW bosons is not suppressed by the boson masses, and the electroweak corrections enhance the production of secondary annihilation products [132].

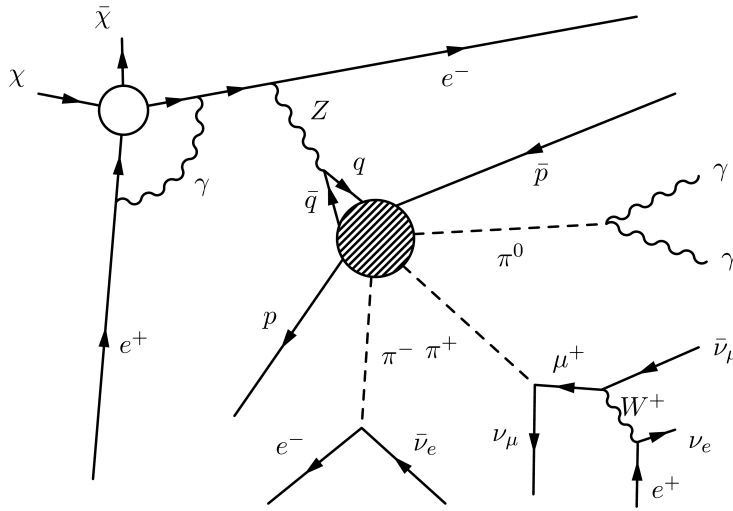


Figure 1.14: Example of a DM annihilation process (two DM particles $\chi\bar{\chi}$ into e^+e^-) producing a final state with many SM decay products thanks to electroweak corrections (from [133]).

Electrically charged decay products of DM are deviated by the electric and magnetic fields present in the galaxy, and the uncertainties in the models for the diffusion of cosmic rays can impact the exclusion bounds relying on the observations of charged cosmic rays as p^\pm and e^\pm . The latest measurements of charged cosmic rays come from the AMS-02 experiment, hosted by the International Space Station. Their measurement of the fluxes of cosmic rays in the e^\pm [134, 135] and $p\bar{p}$ [136] channels ignited an intense discussion in the community, due to alleged excesses of antiparticles measured in the high energy tail of the spectrum. In the case of the antiproton excess, detailed analyses of the model assumed for the cosmic ray propagation showed that the measurements were in not in significant tension with the expected background [137]. In the case of the positron excess, there is a general consensus about a disagreement between the measurement and the expectation, but various astrophysical explanations have been proposed. In particular, a nearby population of pulsars could produce both primary and secondary positrons [138–141], or they could be created in the shock region of a supernova remnant [142].

The indirect search of DM annihilations through the observation of γ rays leads to one of most stringent and solid constraints of the field, from the observations of Fermi-LAT of dwarf Spheroidal Galaxies (dSph) [143, 144]. These satellite galaxies of the Milky Way, being quite poor in stars and rich in DM, represent a perfect focus for the observation of DM annihilations into photons. Fermi-LAT measured the γ ray continuum spectrum, without detecting any excess and imposing a bound on the annihilation cross section of DM into SM particles leading to a spectrum of photons in the final decay products. The uncertainties on the integrated DM

density for these objects is very limited [16], so that these constraints are robust.

The Fermi-LAT satellite, together with the terrestrial telescope HESS, have also observed the centre of the Milky Way in the γ -ray spectrum, to look for spectral lines corresponding to photons generated as primary annihilation products of DM. Also in this case, the absence of excesses leads to exclusion limits that we use for a recast in Chapter 3. These constraints, focussing on a rather small region around the centre of the galaxy, are more sensitive to the assumed DM profile around the centre, as we discuss in Section 3.4.3.1. Despite this uncertainty, these constraints can be important for $m_{\text{DM}} \gtrsim \mathcal{O}(100)$ GeV if the DM can annihilate significantly to $\gamma\gamma$ or $Z\gamma$ for example.

Also the Fermi observations lead in 2009 to a claim of detection of a signal, pointing towards a 30-50 GeV DM particle and yielding a photon spectrum similar to the one generated by annihilations into $b\bar{b}$ quarks [145, 146]. The presence of the excess was confirmed by the Fermi collaboration, and later analyses proposed various possible astrophysical explanation for this signal. The suggestions include a population of unresolved millisecond pulsars [147–150], enhanced Compton emissions from recent cosmic ray outburst [151–153], a space dependence of the parameters describing the cosmic ray propagation [154], or a reexamination of the density of cosmic ray accelerators [155, 156]. Another claim of detection came in 2014 from the observation of an unidentified spectral line in the X-ray spectrum from some galaxy clusters [157, 158]. This very weak line lies at an energy of 3.57 keV, which is argued not to correspond to any atomic transition in the galactic plasma, and it is proposed to come from the decay of a sterile neutrino into $\gamma\nu_L$ (see Fig. 1.9). Other groups objected that this spectral line could be due to chlorine and potassium emission lines [159, 160] or challenged the analysis technique of the original papers [161–164].

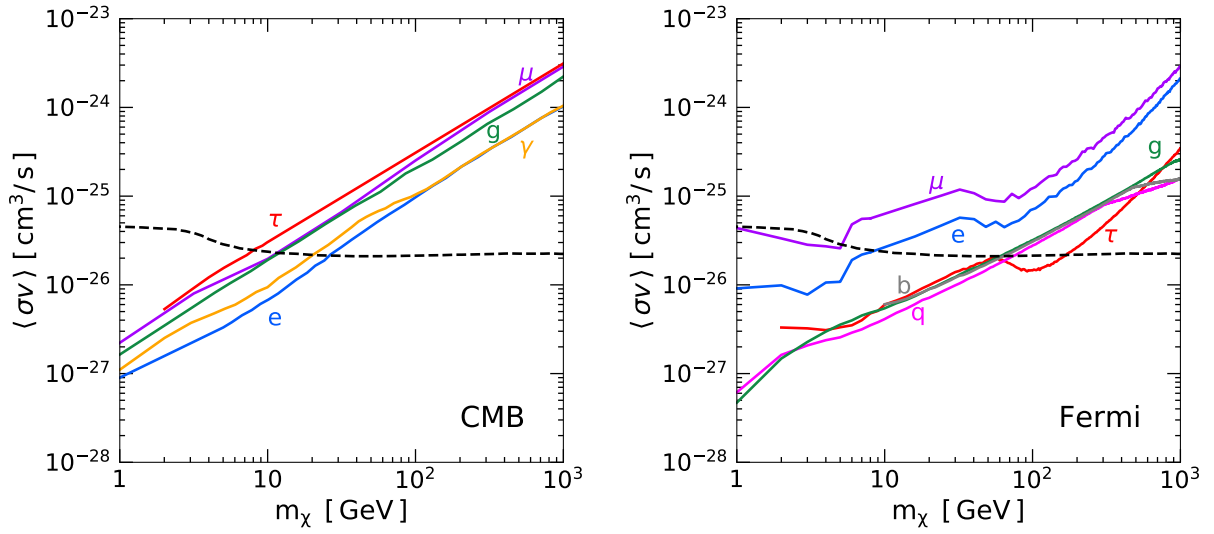
The debate on these measurements of charged cosmic rays, γ and X rays is still ongoing, and there are supporters of the DM explanation, but we can say that no conclusive evidence of a DM observation has been made so far by indirect searches.

Another important constraint in the low DM mass region ($m_{\text{DM}} \lesssim 10$ GeV) comes from the measurement of the CMB. DM annihilations into (primary or secondary) photons during the recombination epoch can impact on the temperature and polarisation anisotropy of the CMB. The Planck measurements did not find evidences for these features, leading to the constraints reported in [33].

We show in Fig. 1.15 the recast performed in Ref. [165] of the constraints from the observations of the CMB by Planck (Fig. 1.15a), of dSph by Fermi-LAT (Fig. 1.15b) and of e^\pm fluxes from AMS (Fig. 1.15c). For each of these bounds, the recast of Ref. [165] (which recomputes the fluxes and does conservative assumptions when needed) assumes in Fig. 1.15 a 100% branching ratio of DM annihilations into a given pair of SM particles, and computes the secondary fluxes of photons (or e^\pm respectively). The black line shows, for comparison, the annihilation cross section predicted by the standard freeze-out mechanism.

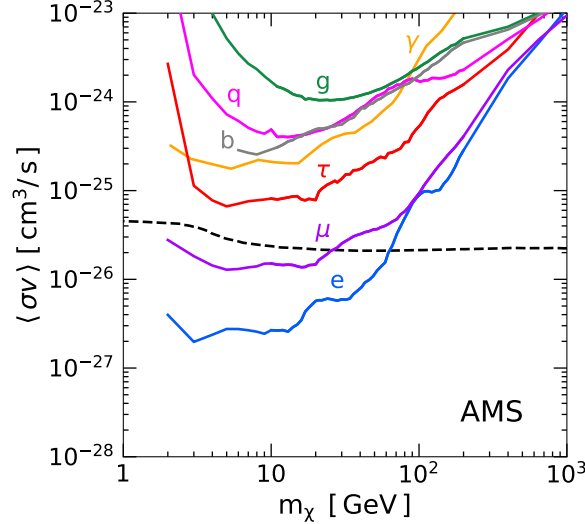
Another possibility is to look for the annihilations coming from the Sun: DM travelling in the solar system can lose some of its kinetic energy when scattering off a nucleus in the Sun, and remain bound to the solar gravitational potential. Its number density n_{DM} then begins to increase with respect to the average galactic one. This is counterbalanced by the annihilation of DM particles, proportional to n_{DM}^2 ⁶. This process eventually reaches an equilibrium, when the capture rate of DM particles in the Sun (whose nuclei are mainly free protons) is equal to (twice of) their annihilation rate into SM particles. Among the final annihilation products, neutrinos are the only particles that can escape from the centre of the Sun and be detected by

⁶The evaporation of DM particles from the Sun, that is the escape from the gravitational potential well of the fastest DM particles, is negligible for $m_{\text{DM}} \gtrsim 10$ GeV.



(a) CMB observations by Planck [33]. Light and b -quarks overlap with the gluon line.

(b) Fermi-LAT observations of γ rays from dSph [143, 144].



(c) AMS observations of e^\pm fluxes in cosmic rays [134, 135].

Figure 1.15: Upper limits at 95% C.L. on the thermally averaged annihilation cross section of DM particles, assuming for each line a 100% BR in the indicated channel (figures taken from [165]). The black dashed line show the predicted cross section for a thermal relic [166].

experiments. Hence, a possible search consists in looking for unexpected fluxes of neutrinos coming from the centre of the Sun. When neutrinos interact with matter via a charged EW current, they convert into a charged lepton which (if energetic enough) produces a Cherenkov cone of radiation when travelling in water. This is the principle used by neutrino detectors, whose sensitive target is a huge tank of water (as SuperKamiokande) or a large volume of ice in Antarctica (IceCube). Especially when the converted lepton is a muon (rather than an electron), the track of the produced cone is better reconstructed, due to lower energy loss of the muon via brehmsstrahlung. This allows a precise determination of the direction of the incoming neutrino, which is crucial to disentangle this signal from the background of neutrinos produced

from the showers of cosmic rays in the terrestrial atmosphere. We show in Fig. 1.16 the latest limits coming from the IceCube [167] and SuperKamiokande [168] experiments. These bounds constrain the elastic scattering cross section between DM and protons. The reason is that, when assuming that the number density in the Sun has reached an equilibrium, one is imposing the equality of the annihilation and the capture rate. Therefore the bound on the number of annihilation processes in the Sun measured by neutrino telescopes directly translates into a limit on the capture rate, as if the Sun were acting as a direct detection experiment with a good sensitivity to SD cross section.

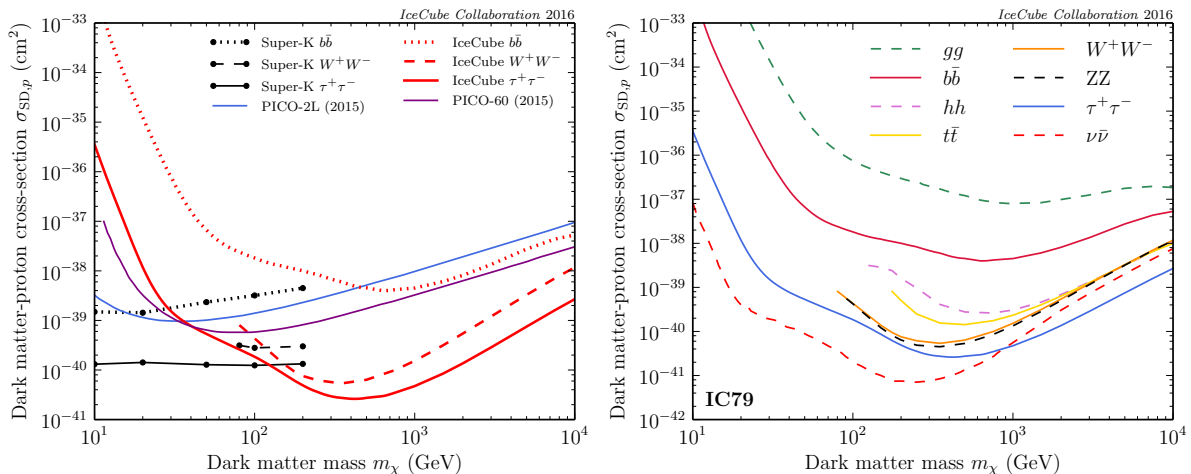


Figure 1.16: Upper exclusion limits on the SD scattering cross section of DM with protons from IceCube and SuperKamiokande (figures taken from [167]).

1.5.3 Collider searches

Another option to investigate the origin of DM is trying to detect its possible production at particle colliders. In this section, we focus on the search of DM at LHC, with the detectors ATLAS and CMS.

Because of the very weak interaction with ordinary matter, DM is expected not to leave any track in the detectors and to escape from them undetected. Therefore, its experimental signature is a rather large amount of missing transverse energy⁷ (\cancel{E}_T), in presence of another recoiling visible object as one or more jets [169, 170], a photon [171, 172] an electroweak boson [173, 174], a heavy quark [175–177] or a Higgs boson [178, 179]. None of these analyses has found any evidence of physics beyond the SM so far. In Fig. 1.17 we draw some representative Feynman diagrams for the production of \cancel{E}_T with a hard jet or photon emitted from the initial state.

The main SM background for these searches comes from the events where the missing transverse momentum is due to $Z \rightarrow \nu\bar{\nu}$, or $W \rightarrow \ell\nu$ if the lepton is misidentified as a jet, or it is not isolated, or it is emitted out of the geometric acceptance region. This background could be reduced in principle in an e^+e^- collider, where the total energy of the collision can be tuned far from the resonant production of the Z and the colliding particles could be polarised (in order to suppress the cross sections for the weak interactions); this cannot be done in a hadronic

⁷This quantity is defined as $\cancel{E}_T \equiv |\vec{\cancel{p}}_T|$, where $\vec{\cancel{p}}_T$ is the opposite of the sum, over all the reconstructed particles, of their momenta projected onto the plane orthogonal to the beam direction.

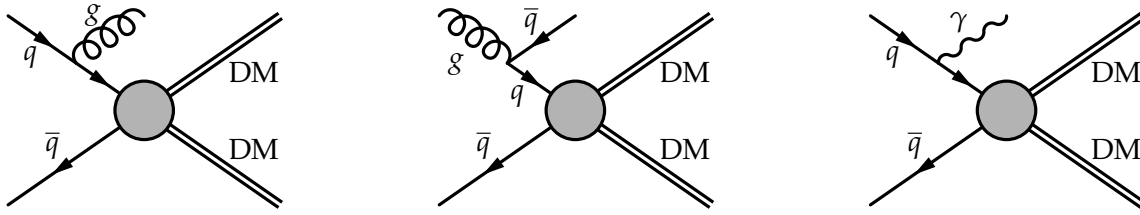


Figure 1.17: Typical Feynman diagrams for the production of DM at LHC with an additional jet or photon from the initial state radiation. Notice that the gluon or photon of the final state could be radiated by some mediator particle exchanged in the DM-SM effective vertex.

collider as the LHC, where the initial energy and polarisation of the colliding partons cannot be constrained.

It is typically assumed that the DM candidate is produced in pairs, due to some discrete symmetry like a \mathbb{Z}_2 parity. This is natural to expect due to the stability of DM on cosmological scales: indeed, in the presence of such a discrete symmetry, the lightest particle with a given quantum number for that symmetry is absolutely stable. This is what happens for example in supersymmetry with the R -parity (Sec. 1.4.1.1) and in extra-dimensional models with the Kaluza-Klein parity (Sec. 1.4.1.2).

We notice that the observation of missing particles at colliders would just reveal that some particles weakly interacting with the SM were produced, but this would not be yet an evidence that this could be the DM candidate. In case of a positive detection by the experimental collaborations, further studies (or even further collider experiments) are needed to understand the mass and the lifetime of that particle, in order to confirm its viability as a DM candidate. In many conceivable scenarios of a WIMP DM with some mediators with the SM, the direct search of these mediators could have more chances to detect a signal than the search for the DM pair in the form of \cancel{E}_T . We will come back to this point also in Chapter 2.

We now discuss the recast of the null results obtained by the experimental collaborations, focussing for concreteness on the \cancel{E}_T plus monojet searches. The result obtained by the analysis is an upper limit on the cross section for the production of $j + \cancel{E}_T$ for each of the signal regions considered by the analysis, which usually differ by the imposed cut on the p_T of the leading jet and the \cancel{E}_T . This exclusion limit can then be recast within a particle physics model, to obtain exclusion limits on a suppression scale or a coupling.

In the first experimental analyses performed at the LHC, the ATLAS and CMS collaborations chose to recast the searches within Effective Field Theories (EFT), following what done for example by Refs. [180–198].

In the EFT framework, one considers the lowest dimensional effective operators that describe the interaction of DM pairs with SM particles, in particular quarks and gluons in the context of LHC searches. The free parameters of the EFTs are just the DM mass, an interaction scale typically denoted by Λ or M_* which appears in front of the effective operator to adjust the overall mass dimension, the relative coefficients of the operators under consideration, and the cutoff scale M_{cut} of the theory (see Sec. 2.1).

The big advantage of the EFT framework is that with a finite set of parameters one can describe in absolute generality any underlying completion. The only limitation is that the effective description is valid as long as the energy scale of the process under consideration is below the cutoff M_{cut} . This condition is safely satisfied in low energy environments as direct and indirect searches, whereas at the typical collider energies this requirement fails unless the cutoff is at least a few TeV. This caveat was considered and taken into account in Refs. [185, 187, 189, 192, 193, 195, 197–203], and it was studied systematically in the series of papers [204–206],

nicely summarised in [133].

These considerations led the experimental community to reconsider their choice of the EFT for the recast of DM searches, and to adopt simplified models. In these theories, one adds on top of an effective description the first degrees of freedom that would show up at the cutoff scale. In other words, simplified models contain with a minimalistic approach the DM candidate and its mediator(s) with the SM, still keeping a certain level of generality but introducing some larger model dependence with respect to EFTs. Simplified models were already being used for the recast of SUSY searches. In the context of DM, after some early papers in which they were introduced [207–210], the experimental and theoretical communities began to interact in order to agree on a set of representative simplified models [10, 11, 211–214]. These are now used in the recasts of the experimental DM searches, whenever the effective vertex for the DM and the related SM particles allows to propose a straightforward completion into a simplified model. As an example, we can cite an effective vertex $\bar{\chi}\gamma^\mu\gamma_5\chi\bar{q}\gamma_\mu\gamma_5q$ made of two axial vector bilinears for DM and quark currents: it readily suggests a vector mediator between the two currents (although other completions are possible, see Sec. 2.3).

During the same period of time, it was also proposed to use the effective theories for the recast by properly accounting for their limited validity range, via a *truncation* method. This procedure allows to derive in a consistent way the exclusion limits within the EFTs. We discuss in detail in Chapter 2 the method proposed in Ref. [1] (summarised also in [12]) and further discussed in [215–217]. A similar method, with some further assumptions, was proposed in [205], and has been implemented in many subsequent experimental analyses when a simplified model reinterpretation was readily available. In some cases, for example for the effective vertex with two photons and two DM particles [218], such a completion is not evident and the experimental collaborations used the slightly more general prescription of Ref. [1]. We conclude this section by showing in Figs. 1.18 and 1.19 the most recent preliminary results of DM searches at colliders, performed by ATLAS and reinterpreted within Z' simplified models.

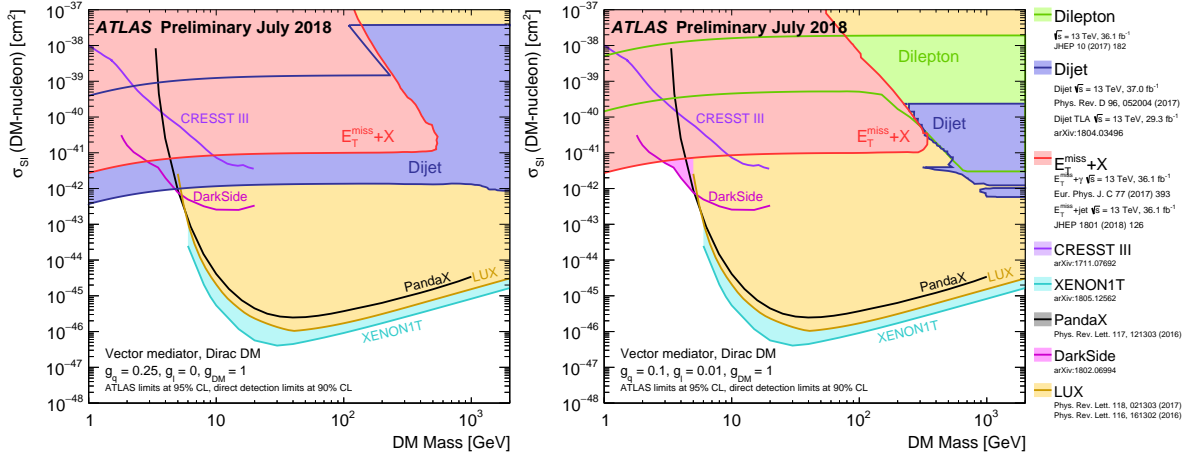


Figure 1.18: Compilation of mono- X (X standing for jet, photon, EW boson), dijet, dilepton searches performed by ATLAS, reinterpreted within a simplified model with a vector Z' mediator and Dirac DM with the couplings specified in the plots. The couplings are assumed to be vectorial, implying a spin-independent proton-DM elastic cross section. The collider reach within these assumptions is compared to the reach of the direct searches listed in the legend. In particular, in the *left* plot it is assumed that the Z' does not couple to leptons, whereas the *right* plot assumes a coupling $g_l = 0.01$ (from [219]).

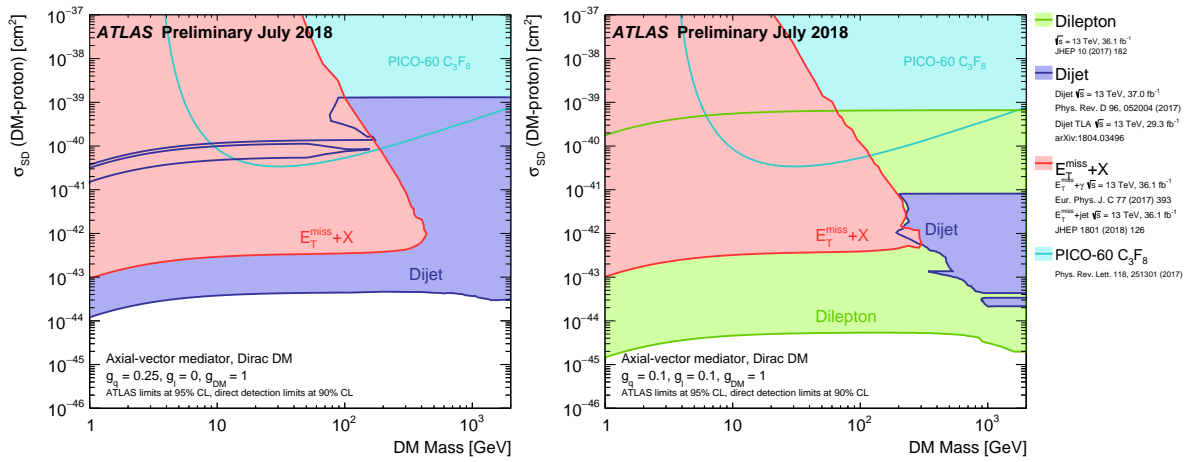


Figure 1.19: The same as in Fig. 1.18, for the case of axial couplings of the Z' to SM fermions, leading to a spin-dependent proton-DM elastic cross section.

Part II

WIMP Dark Matter

Consistent recast of collider searches within Effective Field Theories

In this Chapter, based on Ref. [1], we discuss how to consistently use Effective Field Theories (EFTs) to set universal bounds on heavy-mediator Dark Matter at colliders, without prejudice on the model underlying a given effective interaction. We illustrate the method for a Majorana fermion, universally coupled to the SM quarks via a dimension-6 axial-axial four-fermion operator. We recast an ATLAS mono-jet analysis and show that a considerable fraction of the parameter space, seemingly excluded by a naïve EFT interpretation, is actually still unexplored. Consistently set EFT limits can be reinterpreted in any specific underlying model. We provide two explicit examples for the chosen operator and compare the reach of our model-independent method with that obtainable by dedicated analyses. The important conclusion that we draw from this comparison is that the improved reach of the simplified model with respect to the EFT is driven by the resonant production of the mediator between DM and SM, which is much better constrained by direct searches of the mediator. The method we propose is simple and general, and it has been applied recently also in the context of EFTs describing physics beyond the SM in the electroweak sector.

2.1 Effective Field Theories and their regime of validity

After the discovery of a Higgs boson compatible with the SM, and the non-detection so far of new particles at the LHC, searches for WIMP DM (discussed in Section 1.5.3) are becoming a central theme for the LHC general purpose experiments. The WIMP miracle receives further support from the fact that WIMPs are ubiquitous in new physics models of EW symmetry breaking, as we have seen in Sections 1.4.1.1 and 1.4.1.2. This is an appealing and intensively explored possibility, but WIMP DM might well originate from a completely unrelated sector. Moreover, we currently have no idea of how the complete EW symmetry breaking sector looks like, thus there is not much we can say a priori on the specific properties of WIMP DM.

In the situation described above, a general and model-independent exploration appears mandatory. Commitment to specific benchmark models (or classes of benchmark models) should be treated as an accessory step in the interpretation. The goal is to search for WIMP DM in a comprehensive way, leaving no unexplored corners in theory space.

In the case of heavy-mediator DM, this program can be carried out, at least to some extent. The working hypothesis is that the DM candidate X interacts with the SM through the exchange

of one or more particles, called mediators, whose mass is well above the mass m_{DM} of the DM particle. This assumption is motivated by the present lack of evidence for new particles at the LHC, but it is not the only possibility. The case in which the mediator is a SM particle, such as a weak or the Higgs boson, is equally plausible and deserves equal attention. Light and very weakly coupled mediators can be also conceived.

Focusing on the heavy-mediator case for the rest of this Chapter, it is relatively easy to set up a model-independent strategy for DM searches. We can exploit the fact that the dynamics of the DM particle can be universally described, in the appropriate kinematical regime, by a low-energy EFT Lagrangian[180–198], invariant under the SM gauge group and the Lorentz group:

$$\mathcal{L}_{\text{EFT}} = \mathcal{L}_{\text{SM}} + \mathcal{L}_X + \mathcal{L}_{\text{int}}. \quad (2.1)$$

In the above equation, \mathcal{L}_{SM} denotes the SM Lagrangian, \mathcal{L}_X is the free Lagrangian for the DM particle X , and \mathcal{L}_{int} contains the operators describing the DM interactions with the SM particles, plus possible additional interactions in the DM and SM sectors. If we knew the true microscopic DM theory, these operators could be computed by integrating out the mediators. However, their form is universal and the lack of information on the mediator dynamics merely prevents us from computing the value of their coefficients, which are thus free input parameters of the EFT.

The allowed operators in \mathcal{L}_{int} can be classified according to their mass dimension d , for different hypotheses on the DM quantum numbers. In many relevant cases the DM quantum numbers forbid renormalisable interactions with $d \leq 4$, and the lowest-dimensional operators have $d = 5, 6$. For the physics to be considered in this Chapter, we can assume that the $d = 5$ operators are negligible and the leading operators have $d = 6$:

$$\mathcal{L}_{\text{int}} = \frac{1}{M_*^2} \sum_i c_i \mathcal{O}_i, \quad (2.2)$$

where the sum runs over all $d = 6$ operators \mathcal{O}_i allowed by the symmetries, c_i are dimensionless coefficients and the overall effective coupling strength is parametrised by a dimensionful coupling $1/M_*^2$.

While the EFT can be formally defined independently of any consideration about its microscopic origin, its range of applicability and thus its physical relevance depend on the underlying theory. Namely, the EFT provides an accurate description of the underlying model only for elementary scattering processes taking place at a low enough centre-of-mass energy E_{cm} , below a certain critical scale M_{cut} usually called the EFT cutoff. This cutoff is determined by the mass of the mediators in the microscopic theory but it is unknown from the viewpoint of the EFT and it should thus be treated as a free parameter, on the same footing as those introduced above.

The EFT is then characterised by at least three parameters:

- the DM mass m_{DM} ;
- the scale M_* of the interaction;
- the cutoff scale M_{cut} .

If a single operator appears in Eq. (2.2), the corresponding dimensionless coefficient can be absorbed in M_* , otherwise the EFT parameters also include the c_i coefficients. With these free parameters, the EFT faithfully reproduces the predictions of any microscopic theory for all processes taking place at $E_{\text{cm}} < M_{\text{cut}}$. Given that the effective operators in Eq. (2.2) may have many possible microscopic origins, exemplified by the plethora of models in the literature, this simplification is particularly useful.

Notice that M_{cut} and M_* are logically independent parameters, however they can be approximately related by

$$M_{\text{cut}} = g_* M_* \quad (2.3)$$

where g_* is a suitably defined coupling strength of the underlying microscopic theory. The simplest way to motivate the above equation is the analogy with the Fermi theory of weak interactions, where the cutoff M_{cut} is the mass of the W boson (the mediator in this context), g_* is the $SU(2)_L$ gauge coupling g_w and $1/M_*^2$ is the Fermi constant G_F : they indeed obey Eq. (2.3) up to numerical factors. Alternatively, the physical meaning of g_* can be appreciated by noticing that the EFT interaction strength is given, for processes taking place at a given centre-of-mass energy E_{cm} , by the dimensionless combination E_{cm}^2/M_*^2 . At the mediator scale, i.e. the cutoff scale M_{cut} , this strength becomes $M_{\text{cut}}^2/M_*^2 = g_*^2$, providing further justification for interpreting g_* as the typical mediator coupling. Using Eq. (2.3) to re-express M_* in terms of g_* will be important in Section 2.2, in order to draw the current limits on a plane suited for theoretical interpretation.

The EFT can be straightforwardly used to predict the cross-sections for a number of relevant reactions, namely the DM annihilation in the Early Universe, which determines the thermal relic density, the present-day annihilation, which controls indirect detection, and the DM scattering on nucleons, which direct search experiments try to detect. Indeed, all these reactions take place at safely small E_{cm} and therefore, up to subtle effects that might be encountered in the relic density calculation, the EFT predictions are automatically trustable. If collider searches could be added to the list, we would reach the truly remarkable conclusion that all the experimental information on heavy-mediator DM can be simultaneously interpreted and compared in a completely model-independent fashion, with no prejudice on the specific nature of the mediator and of its couplings to DM and to the SM. However, the usage of the EFT at colliders is problematic, because the energy of the reaction in which the DM is produced is not necessarily smaller than M_{cut} , and this risks to invalidate the EFT predictions. The effect is quantitatively amplified by the requirement of extra hard objects (e.g., one jet), in addition to the pairs of DM particles, for the signal to be triggered and disentangled from the background. This problem has been discussed at length in the recent literature (see e.g. Refs. [185, 187, 189, 192, 193, 195, 197–206]), the goal of the present article is to illustrate a simple and practical solution.

The basic observation is that the processes for DM production at colliders can be split into two kinematically distinct classes, characterised by a centre-of-mass energy below and above M_{cut} , respectively. The former class defines our theoretical signal, and its rate is accurately predicted by the EFT. The latter would instead require the knowledge of the microscopic theory and its contribution to the cross-section is thus unpredictable within the EFT. Under certain conditions, to be described below, the second class can be simply ignored and an experimental limit can be set on the signal defined, as explained above, by the DM production reaction restricted to $E_{\text{cm}} < M_{\text{cut}}$. This is possible if the experimental search is performed as a counting experiment in one or several signal regions, defined by a certain set of cuts on the visible final state particles. The low and high E_{cm} processes both contribute to each signal region, but in a purely additive way, since low and high E_{cm} regions are quantum-mechanically distinguishable and do not interfere. Therefore a lower bound on the expected cross-section is obtained by considering only the “well-predicted” signal events, namely those restricted to the $E_{\text{cm}} < M_{\text{cut}}$ region. If the result of the search is negative, an exclusion upper bound σ_{exc} is set on the cross-section, which we can interpret through the inequality

$$\sigma_{\text{EFT}}^S \Big|_{E_{\text{cm}} < M_{\text{cut}}} \leq \sigma_{\text{true}}^S < \sigma_{\text{exc}} \quad (2.4)$$

where σ_{true}^S denotes the “true” signal as it would be computed in the unknown microscopic theory. Regardless of what the latter theory is, the restricted EFT signal σ_{EFT}^S systematically underestimates the cross-section and thus provides a conservative, but correct, exclusion limit. This is shown schematically in Fig. 2.1.

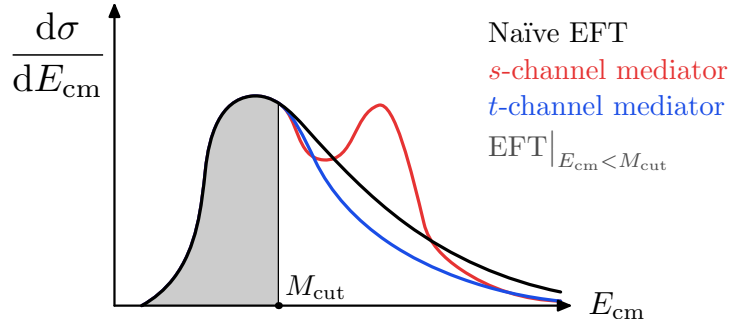


Figure 2.1: Illustrative sketch of Eq. (2.4). The differential cross section $d\sigma/dE_{\text{cm}}$ for a process like $q\bar{q} \rightarrow X\bar{X}$ is shown for a generic EFT (black line) and two corresponding UV completions, one with a mediator exchanged in the s -channel which can be resonantly produced (red line) and one with an hypothetical t -channel mediator which cannot be resonantly excited in the range shown here (blue line). By the definition of M_{cut} , the three lines must coincide below M_{cut} . The grey shaded area, corresponding to $\sigma_{\text{EFT}}^S|_{E_{\text{cm}} < M_{\text{cut}}}$, is by construction smaller than the cross section σ_{true}^S in the completion of the EFT, whatever this is.

Similar approaches have been applied recently in the context of EFTs describing the effects of new physics beyond the SM in the electroweak sector [220–225] or in QCD [226].

The rest of the Chapter is organised as follows.

In Section 2.2 we illustrate our limit-setting strategy in the explicit example of a four-fermion operator obtained as the product of axial currents involving the SM quarks and a SM-singlet Majorana fermion DM. This choice is partly motivated by the fact that direct and indirect detection experiments have a poor sensitivity to this operator, thus collider searches are expected to be the most sensitive ones, but the same method can be applied to all other operators. We quantify the reach of current collider searches by recasting the ATLAS mono-jet [227], and show how the latter can be presented in a theoretically useful way. Besides the methodological proposal, the important physics point is that, from the general EFT viewpoint, the present collider bounds on DM have not yet probed the most plausible region of parameter space. To access such region, we need not only more energy and luminosity, as expected in the forthcoming runs of the LHC, but also improvements in the experimental analyses.

In Section 2.3 we describe another relevant feature of our strategy, the fact that the limits set in the EFT can be straightforwardly re-interpreted as constraints on any specific microscopic model. This is because the EFT parameters can be computed in the underlying microscopic theory and expressed in terms of the fundamental parameters of the latter (for previous discussions of the interplay between EFT and underlying microscopic models in DM searches at colliders, see again Refs. [185, 187, 189, 192, 193, 195, 197–206]). We consider two representative models, Model A and Model B, which both give rise to the same axial-axial effective operator, and compare the limits derived from the EFT with those obtainable from a dedicated interpretation of the mono-jet search within the two models. Since our signal cross-section systematically underestimates that of the microscopic theory, we obtain conservative limits. We find that these limits differ significantly from those obtained in the full models only in the kinematical region where the mediators can be resonantly produced. In such a case, however, more comprehensive experimental strategies, complementing the event selection used for heavy-mediator DM

searches with other selections that can take full advantage of the resonant production of the mediators (single or in pairs, with one or more jets in the event), should be able to provide stronger bounds. We end this section by discussing two aspects of our simple and practical approach that can be helpful for the comparison with a similar but more model-dependent approach put forward in [205, 206].

In Section 2.3.2 we resume two refinements of the study of [1]. Ref. [215] performs a detailed recast of the experimental analysis by simulating the showering and hadronisation processes, and more importantly analyses (together with the companion Ref. [216]) the implications for DM model building of the fact that collider searches (recast within EFTs) are now able to constrain only strongly coupled theories. Ref. [217] describes how it is possible to extend this procedure to a more sophisticated experimental analysis, which goes beyond the so called cut-and-count procedure and relies on the shape of the kinematical distributions.

We finally present our conclusions in Section 2.4. Some back-up material is collected in three appendices. Appendices 2.A and 2.B provide details on Model A and Model B, respectively. Appendix 2.C collects the approximate analytical formulae used to draw the relic density constraint in some of the figures.

2.2 Limit-setting strategy

For the present study, we assume that the DM particle is a Majorana fermion, singlet under the SM gauge group and represented by a self-conjugate four-component spinor $X = X^c$, whose free Lagrangian reads

$$\mathcal{L}_X = \frac{1}{2} \bar{X} (i\not{\partial} - m_{\text{DM}}) X. \quad (2.5)$$

As for the interactions between X and the SM particles, we just choose a representative example to illustrate our limit-setting strategy, assuming that they can be described, in the low-energy limit, by the single¹ axial-axial four-fermion operator²

$$\mathcal{O} = -\frac{1}{M_*^2} (\bar{X} \gamma^\mu \gamma^5 X) \left(\sum_q \bar{q} \gamma_\mu \gamma^5 q \right), \quad (2.6)$$

where the sum is over all quark flavours ($q = u, d, c, s, t, b$), the dimensionless coefficient c has been re-absorbed in the definition of M_* , and the overall minus sign is purely conventional in the present context. This effective operator mediates DM pair-production at the LHC, a process which is however undetectable and impossible to trigger because of the lack of visible objects in the final state. Searches are performed by considering extra visible emissions (see Section 1.5.3). Below we restrict our attention to the mono-jet searches, because they currently show the best sensitivity, but our considerations also apply to the other channels.

2.2.1 ATLAS mono-jet recast

Searches for a jet plus missing transverse energy (\cancel{E}_T) have been performed at the LHC by the ATLAS and CMS collaborations (see Refs. in Section 1.5.3). We focus here on the ATLAS

¹Radiative corrections may generate additional operators [106–110], this can be important when comparing with direct dark matter searches but does not play a role in the present context.

²This operator is twice the M6 operator in [184], and formally coincides with the D8 operator in [186], which is often taken as a benchmark for experimental searches. Notice however that we are dealing with a Majorana spinor normalised as in Eq. (2.5), while D8 involves a canonically normalised Dirac spinor.

analysis in Ref. [227] because it is particularly suited to illustrate the general point we would like to make.

The search is performed as a counting experiment in four overlapping signal regions (SR), with pre-selected events characterized by $\cancel{E}_T > 120$ GeV, one jet with $p_T^{\text{jet}} > 120$ GeV, $|\eta| < 2$ and at most one additional jet with $p_T > 30$ GeV and $|\eta| < 4.5$. If found, the second jet is asked to be separated in the azimuthal direction from the \vec{p}_T^{miss} by a cut $\Delta\phi > 0.5$. Additional requirements, namely on the primary vertex reconstruction and on the absence of extra jets with anomalous charged/calorimetric composition, are not directly relevant for our study, since their impact crucially depends on the detector response, which we cannot simulate. The four signal regions SR*i* ($i = 1, 2, 3, 4$) are defined by increasingly strong cuts on \cancel{E}_T and on p_T^{jet} . The results are presented as upper bounds, σ_{exc}^i , on the visible cross-section in each region. The SR definitions and the exclusion limits are summarized in Table 2.1.

signal region	SR1	SR2	SR3	SR4
p_T^{jet} and \cancel{E}_T	>120	>220	>350	>500
σ_{exc} [pb]	2.7	0.15	$4.8 \cdot 10^{-2}$	$1.5 \cdot 10^{-2}$

Table 2.1: Signal region definitions (cuts expressed in GeV) and 95% CL limits from Ref. [227].

We reinterpret these limits as follows. The expected signal in each SR is expressed as

$$\sigma_{\text{SR}i} = \sigma \times A_i \times \epsilon_i, \quad (2.7)$$

where σ denotes the total signal cross-section defined as in Eq. (2.4), A_i is the geometric cut acceptance, as obtained from a leading-order parton-level simulation, and the efficiency ϵ_i is the correction due to showering, hadronisation and detector effects. Acceptances and efficiencies depend on the DM mass m_{DM} and on the cutoff M_{cut} , while the operator scale M_* only enters the total cross-section as an overall factor $1/M_*^4$. We compute the parton-level quantities σ and A_i by MadGraph 5 [228] simulations, while we estimate the ϵ_i corrections by matching with the limits on the D8 operator scale reported in Ref. [227]. In practice, we simulate the same D8 operator signal considered in Ref. [227] (i.e. $M_{\text{cut}} = \infty$ in Eq. (2.4)), we compute $\sigma \times A_i$ and we determine ϵ_i such as to reproduce the ATLAS limit on the effective operator scale as a function of the DM mass. Actually, since only the third SR is used by ATLAS to set the limit, only ϵ_3 can be obtained in this way. The same efficiencies are used for the other SRs, although we see no reason why the efficiency should stay the same in all the regions. The result of this procedure gives rather small efficiencies, of around 60%, approximately constant over the whole DM mass range. We verified that this considerable signal loss is mainly due to the fact that our simulation does not include the showering-level production of extra jets, a significant fraction of which are vetoed in the ATLAS event selection. Notice that the efficiencies for our signal might be significantly different from those estimated in the naïve EFT because, although based on the same effective operator D8 of Eq. (2.6), our signal is constrained by M_{cut} to the low invariant mass region, thus it is expected to have different kinematical distributions. A complete simulation in different regions of m_{DM} and M_{cut} , including showering and matching, would be needed for an accurate analysis, but goes beyond the aim of the present illustrative example.

Under the assumptions explained above, the expected signal takes the form

$$\begin{aligned} \sigma_{\text{SR}i}(M_*, m_{\text{DM}}, M_{\text{cut}}) &= \sigma(M_*, m_{\text{DM}}, M_{\text{cut}}) \times A_i(m_{\text{DM}}, M_{\text{cut}}) \times \epsilon \\ &= \left[\frac{1 \text{ TeV}}{M_*} \right]^4 \times \bar{\sigma}(m_{\text{DM}}, M_{\text{cut}}) \times A_i(m_{\text{DM}}, M_{\text{cut}}) \times \epsilon, \end{aligned} \quad (2.8)$$

where the overall scaling of the cross section with M_* has been factored out and the result expressed in terms of a reference cross-section $\bar{\sigma}$ computed for $M_* = 1$ TeV. The reference cross-section times the acceptances are obtained by MadGraph 5 [228] simulations of DM pair plus one parton production, duly restricted by the hard jet kinematical cuts that define each SR. \cancel{E}_T cuts are automatically imposed because the jet and the missing transverse momentum, i.e. the transverse momentum of the DM pair, are back-to-back in our parton-level sample. For our illustrative parton level analysis, an advantage of choosing the analysis performed in Ref. [227] is that the cuts applied on p_T^{jet} and \cancel{E}_T are identical for each SR (see Table 2.1). This is always the case at a parton level analysis, whereas different values of p_T^{jet} and \cancel{E}_T in an event can only occur when properly simulating the showering and hadronisation processes. A more detailed simulation of the signal (with the same truncation procedure that we describe) to account for these effects was performed in Ref. [215].

The theoretical restriction $E_{\text{cm}} < M_{\text{cut}}$, which ensures the validity of the EFT description as explained in Section 2.1, should be imposed as a cut on the total invariant mass of the hard final states of the reaction, namely as

$$[p(DM_1) + p(DM_2) + p^{\text{jet}}]^2 < M_{\text{cut}}^2. \quad (2.9)$$

For our parton level simulation this is equivalent to a cut $\sqrt{\hat{s}} < M_{\text{cut}}$ on the total partonic centre-of-mass energy, however when going to the showered and matched level one should be careful not to cut on $\sqrt{\hat{s}}$ but on the variable in Eq. (2.9), with p^{jet} the leading jet four-momentum.

A scan is performed in the $(m_{\text{DM}}, M_{\text{cut}})$ plane for each SR and the values of $\sigma \times A_i$ are used to construct two-dimensional interpolating functions. A significant dependence on m_{DM} is only found for $m_{\text{DM}} \gtrsim 80$ GeV, while for smaller values $\sigma \times A_i$ is basically constant in m_{DM} . Once the signal cross-sections are known, the 95% CL limits are imposed as constraints

$$\sigma_{\text{SR}i}(M_*, m_{\text{DM}}, M_{\text{cut}}) < \sigma_{\text{exc}}^i, \quad (2.10)$$

out of which the 95% CL allowed regions are immediately found in the three-dimensional parameter space $(M_*, m_{\text{DM}}, M_{\text{cut}})$. The limits from the various signal regions can be studied separately or combined. For our illustrative purposes, the combination will be performed by just taking the overlap of the four allowed regions. The results of this simple limit-setting procedure are discussed in the following section.

2.2.2 Results and discussion

At fixed m_{DM} and M_{cut} , the ATLAS limits in Eq. (2.10) become lower bounds on the scale M_* , reported in Fig. 2.2 as functions of m_{DM} and for different values of $M_{\text{cut}} = 350, 450, 600, 800, 1250, 2000, 8000$ GeV. The four boxes in the figure correspond to the four different signal regions.

The upper line in each plot, $M_{\text{cut}} = 8$ TeV, corresponds to the naïve EFT limit, obtained without imposing any restriction on the centre-of-mass energy of the hard scattering.³ The limit deteriorates for decreasing M_{cut} because of two distinct effects. The first one is that the total reference cross-section $\bar{\sigma}$ decreases, because it is restricted to a smaller kinematical range. This effect is unavoidable and ultimately due to the fact that the EFT cannot be trusted above its cut-off: trying to extrapolate the EFT above M_{cut} would be inconsistent, and this is precisely why

³The naïve EFT limit in SR3 differs from the ATLAS result on the D8 operator by a $\sqrt[4]{2}$ factor, which reflects the factor 2 enhancement of the cross-section for a Majorana DM particle with respect to the Dirac case considered in Ref. [227], if the same operator is used and the normalisation in Eq. (2.5) taken into account.

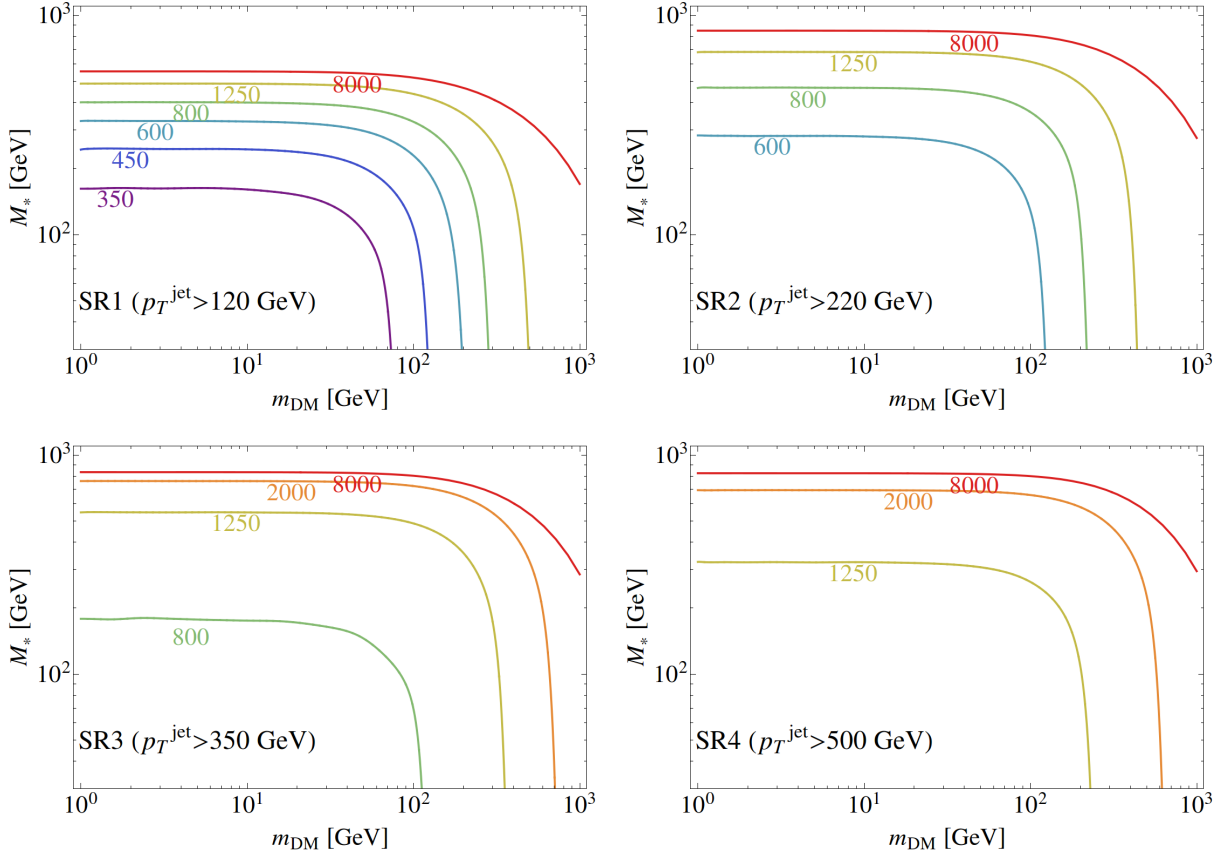


Figure 2.2: 95% c.l. lower bounds on M_* , as functions of m_{DM} , for some representative values of M_{cut} (in GeV), for the four signal regions of Ref. [227].

we restrict our signal to the $E_{\text{cm}} < M_{\text{cut}}$ region. The second effect is that the acceptances are also reduced, because the kinematical distributions of the restricted signal become softer, thus for decreasing M_{cut} it becomes increasingly difficult to pass the cuts on $p_{\text{T}}^{\text{jet}}$ and on \cancel{E}_{T} . Being dependent on the selection, this effect could be mitigated by softer cuts, compatibly with the minimal \cancel{E}_{T} trigger requirement and with the fact that the SM background rapidly increases in the softer region. These considerations show that our signal is kinematically different from the naïve EFT prediction: an optimized limit in all M_{cut} regions would require a dedicated analysis, which however goes beyond the scope of the present study and can be properly performed only by the experimental collaborations.

Going back to our results in Fig. 2.2, we notice that for large M_{cut} the best limits are obtained from the SRs with harder cuts, namely from SR2, SR3 and SR4, which all have comparable reach. The low-cut region SR1 is instead not competitive with the other ones. The situation changes for low M_{cut} , because the cut acceptances decrease faster in the SR with harder cuts than in those with softer ones, and the limits start being dominated by the latter. For instance, when M_{cut} goes below 500 GeV or so, the strongest M_* bound starts coming from SR1, while the other SRs are no longer sensitive.

The behaviour of the limits as functions of m_{DM} is also easily understood. When m_{DM} is lowered much below M_{cut} and the kinematical cuts, the cross-section becomes independent of m_{DM} and the limit saturates. The limit deteriorates as m_{DM} increases, because the latter starts having a negative impact on the energy budget of the reaction. The limit eventually disappears

above a certain threshold, which corresponds to the region where the DM particle is too heavy to be produced with a centre-of-mass energy below M_{cut} . The minimal centre-of-mass energy is given by

$$E_{\text{cm}}^{\text{min}} = p_{\text{T}}^{\text{jet}} + \sqrt{\left(p_{\text{T}}^{\text{jet}}\right)^2 + 4m_{\text{DM}}^2}, \quad (2.11)$$

where $p_{\text{T}}^{\text{jet}}$ is the common jet and \cancel{E}_{T} cut of each SR, out of which the mass threshold is then found to be ⁴

$$m_{\text{DM}}^{\text{max}} = \frac{M_{\text{cut}}}{2} \sqrt{1 - 2 \frac{p_{\text{T}}^{\text{jet}}}{M_{\text{cut}}}}. \quad (2.12)$$

We thus see once again that soft SRs are favoured for low M_{cut} , not only because they produce better M_* limits, but also because they have an extended reach in the DM mass.⁵

The combined limits from all four SRs, obtained as the intersection of the allowed regions as described above or equivalently by taking the strongest M_* bound at each point, are displayed in the left panel of fig. 2.3.

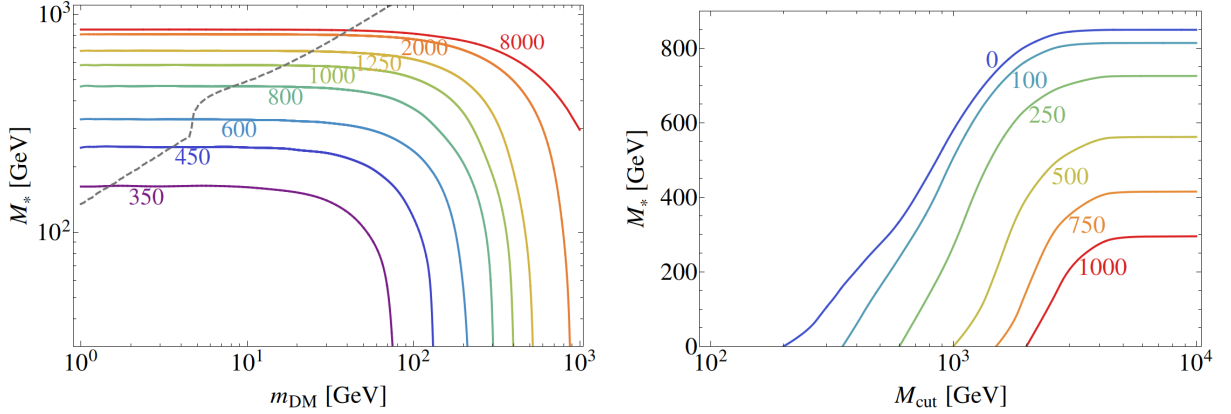


Figure 2.3: Our combination of the lower bounds on M_* . *Left:* As a function of m_{DM} , for the same representative values of M_{cut} as in fig. 1. The dashed grey line is the relic density constraint. *Right:* As a function of M_{cut} , for some representative values of m_{DM} (in GeV).

The main conclusion we can draw is that the naïve EFT limit is fairly accurate when M_{cut} is significantly above 1 TeV, while it considerably overestimates the actual exclusion for lower values of M_{cut} . As an equivalent way to express the same information, the right panel of fig. 2.3 shows the limit on M_* as a function of M_{cut} for some fixed representative values of m_{DM} : 0, 100, 250, 500, 750, 1000 GeV. This representation is perhaps more convenient, as the dependence on m_{DM} is rather smooth, and significant only in a limited range. Furthermore, it gives an idea of the search reach in the low M_{cut} region. For reference, the dashed line on the left-hand panel of Fig. 2.3 shows the constraint from the relic density (under-abundant below the line and over-abundant above it), computed with the approximate analytical formulae for the EFT collected in Appendix 2.C.

The plots described above summarise the experimental situation in a simple and concise way, however they do not tell us how much of the theoretically allowed parameter space has

⁴The threshold effectively occurs for lower values of m_{DM} when M_{cut} gets close to the LHC threshold of 8 TeV, because of the rapid large- x decrease of the parton distribution functions.

⁵Formally, low $p_{\text{T}}^{\text{jet}}$ improves the mass reach for any value of M_{cut} . However, at large M_{cut} the threshold has a very poor sensitivity to the actual value of $p_{\text{T}}^{\text{jet}}$ and all SRs have practically the same reach.

been actually tested and how much is still unexplored. Namely, it is hard to establish a priori the reasonable M_{cut} values, and whether the corresponding M_* limit should be regarded as a strong or a weak one. We can do better if we remember that M_{cut} and M_* are actually connected by Eq. (2.3). Clearly, we do not know what g_* is, but we do have some control on its value. We definitely know that it must be $g_* < 4\pi$, since taking it larger would make the EFT non-perturbative below the cutoff. This implies an upper bound on M_{cut} for any given M_* . In principle, there is no lower bound on g_* , it could be arbitrarily small pushing M_{cut} to smaller and smaller values. However, in a WIMP-like scenario we definitely expect $g_* \sim g_w \sim 1$, to implement the WIMP miracle recalled in the introduction. Values of g_* of order unity, and not radically smaller than that, should thus be considered as plausible benchmarks.

The exclusion limits at fixed g_* , in the $(m_{\text{DM}}, M_{\text{cut}})$ plane, are shown by the coloured solid lines in fig. 2.4, for the representative values $g_* = 1.8, 2, 4, 6, 4\pi$. The black solid line is the limit one would obtain in the naïve EFT.

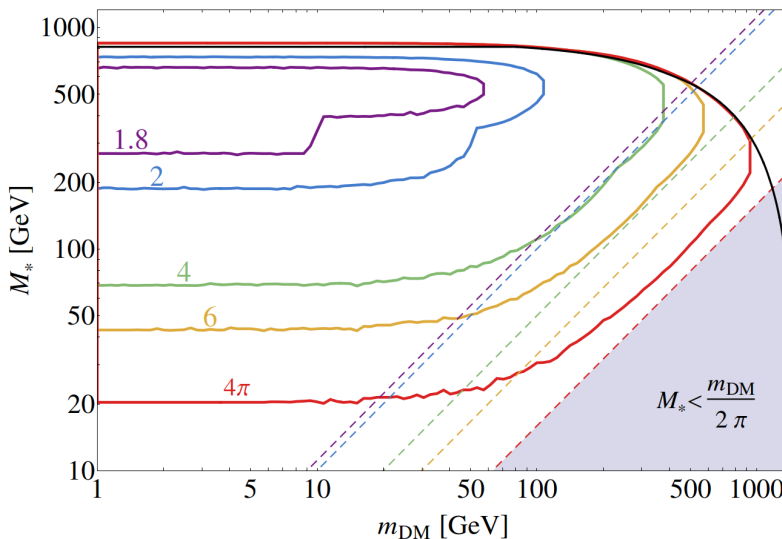


Figure 2.4: The solid lines enclose the excluded regions in the plane (m_{DM}, M_*) , for some representative values of g_* , combining the four signal regions of ref. [227]. The black line is the limit one would obtain with the naïve EFT. The grey triangle is theoretically forbidden because of the self-consistency requirement $M_* > 2m_{\text{DM}}/g_*$, for $g_* = 4\pi$. The dashed lines show, with the same colour code as for the solid lines, how the grey triangle expands for smaller values of g_* .

We stress that closed excluded regions are obtained in this case, a fact that can be understood in the following terms. For a given m_{DM} , the limit must disappear at sufficiently large M_* , because the signal cross-section rapidly decreases for increasing M_* . However, the limit must also disappear for too low M_* , because at fixed g_* lowering M_* means lowering $M_{\text{cut}} = g_* M_*$, which deteriorates and eventually kills the signal and the acceptances. There also exist values of m_{DM} where these two competing effects do not allow to obtain an exclusion for any value of M_* , which is why the curves close on the right. As a consequence, there are values of g_* for which no limit on M_* can be set, not even for $m_{\text{DM}} = 0$.

Our finding is quantitatively impressive: with the experimental results available so far, a satisfactory exploration of the parameter space has been possible only for g_* above 4 or 6: the reference value $g_* = 1$ is not excluded, and the smallest coupling we are sensitive to is $g_* \sim 1.8$. Making progress in this direction would require more energy and integrated luminosity at the

LHC, as expected in the forthcoming runs, but also improving the sensitivity to the small M_{cut} region as explained above. Indeed, the lower exclusion limits, in the low m_{DM} region, are predicted by Eq. (2.11) to occur near $g_* M_* = E_{\text{cm}}^{\text{min}} \simeq 2p_{\text{T}}^{\text{jet}}$, where we take the lowest possible value for $p_{\text{T}}^{\text{jet}}$, corresponding to 120 GeV for SR1 of [227]. This shows once again the importance of keeping the first signal region at the lowest $p_{\text{T}}^{\text{jet}}$ and \cancel{E}_{T} values compatible with the trigger and background conditions.

As a last comment, we remind the reader that not all the points in Fig. 2.4 are theoretically allowed within the EFT framework. We are working here under the assumption of heavy-mediator DM, which means, as explained in the introduction, that m_{DM} should be well below M_{cut} , or at least $m_{\text{DM}} < M_{\text{cut}}/2$, because otherwise there is no hope for the DM being produced within the range of validity of the EFT. This leads to the constraint $M_* = M_{\text{cut}}/g_* > 2m_{\text{DM}}/g_*$. For $g_* = 4\pi$ this produces the grey theoretically forbidden region in Fig. 2.4. For $g_* < 4\pi$ the boundary of the grey triangle moves as indicated by the dashed lines, with g_* specified by the same colour code as for the solid lines. However, Eq. (2.11) guarantees that (in contrast with what we would obtain in the naïve EFT), the experimentally excluded region can at most approach the theoretically excluded one. Indeed, the closeness of the solid lines to the corresponding dashed lines gives a measure of how much the available EFT parameter space has been explored for the different values of g_* .

2.3 Simplified model reinterpretation

In the previous section we consistently derived from experimental data universal bounds on the EFT defined by the operator (2.6), as functions of the three relevant mass parameters (M_* , m_{DM} , M_{cut}). We now show how such bounds can be re-interpreted in any specific microscopic model underlying the chosen effective interaction. Since it collects only the contribution to the (positive-definite) signal cross-section coming from the kinematical region $E_{\text{cm}} < M_{\text{cut}}$, where by definition the EFT is reliable, and it sets to zero the contribution corresponding to $E_{\text{cm}} > M_{\text{cut}}$ (see Fig. 2.1), our prescription for using consistently the EFT leads to underestimating the signal cross-section. We then expect our bounds to be systematically more conservative than those obtained by the direct comparison of a specific microscopic model with the experimental data. The aim of the present section is to perform a quantitative comparison of the limits derived with the two methods and to comment on the interpretation and practical consequences of any significant difference in the results.

We consider two illustrative simplified models, characterized by quite different dynamics at the mediator scale, but nevertheless giving rise to the same leading effective operator (2.6) in the low-energy EFT.

In Model A, DM annihilation into quark-antiquark pairs and the inverse process occur via the s -channel exchange of a spin-1 Z' boson of mass $m_{Z'}$, coupled to the axial-vector currents of quarks and DM with strengths g_q and g_X , respectively. Very similar simplified models were discussed in refs. [191, 229–232].

In Model B, the same processes occur via the t/u -channel exchange of color-triplet scalars of mass \tilde{m} , with the same gauge quantum numbers as the squarks \tilde{q} of supersymmetric extensions of the SM, but with a universal Yukawa coupling of strength g_{DM} to quarks and DM. Very similar simplified models were discussed in refs. [233–238]. We have collected some useful details on the two models in Appendices 2.A and 2.B, respectively.

Before comparing the interpretation of the experimental results in the EFT and in the two simplified models, we display in Fig. 2.5 the tree-level Feynman diagrams contributing to the

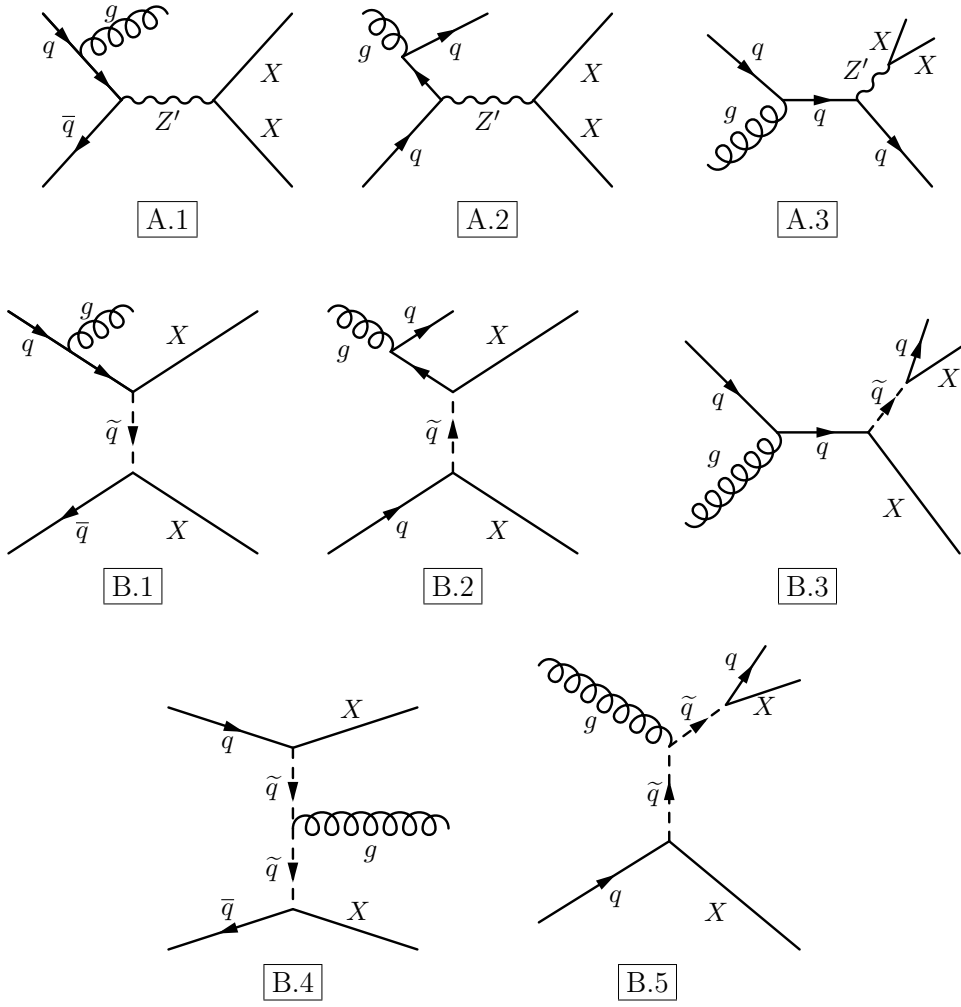


Figure 2.5: Feynman diagrams describing the jet + \cancel{E}_T DM signal at hadron colliders for models A (Z' mediator) and B (\tilde{q} mediator) considered in the text.

three hard partonic processes associated with the scattering $pp \rightarrow \text{jet} + \text{MET}$:

$$\text{(I): } q(p_1) + \bar{q}(p_2) \rightarrow X(p_3) + X(p_4) + g(k); \quad (2.13)$$

$$\text{(II): } q(p_1) + g(p_2) \rightarrow X(p_3) + X(p_4) + q(k); \quad (2.14)$$

$$\text{(III): } \bar{q}(p_1) + g(p_2) \rightarrow X(p_3) + X(p_4) + \bar{q}(k). \quad (2.15)$$

The symbols in brackets label the four-momenta of the corresponding particles. Process I is described by diagram A1 in Model A, by diagrams B1 and B4 in Model B. In the case of diagrams A1 and B1, it is understood that we should add the corresponding diagrams with the gluon radiated from the antiquark rather than from the quark line. Process II is described by diagrams A2 and A3 in Model A, and by diagrams B2, B3 and B5 in Model B, plus those obtained by exchanging the momenta p_3 and p_4 of the Majorana DM fermion X . Process III is described by the same diagrams of process II, with the prescription that all the arrows on the quark and squark lines should be reversed.

The limits from our consistent EFT analysis and directly from the simplified models are obtained as follows. In the EFT, we compute the EFT parameters in each simplified model and we just apply the constraints derived in the previous section. The scale M_* of the effective

operator (2.6) is given by

$$M_* = \frac{m_{Z'}}{\sqrt{g_q g_X}} \quad (\text{Model A}), \quad M_* = \frac{2\tilde{m}}{g_{\text{DM}}} \quad (\text{Model B}). \quad (2.16)$$

The cutoff scale $M_{\text{cut}'}$, at which the EFT description loses its validity, is identified with the mediator mass M_{med} , i.e. with $m_{Z'}$ in Model A and with \tilde{m} in Model B. Then, after this identification, the effective coupling g_* is:

$$g_* = \sqrt{g_q g_X} \quad (\text{Model A}), \quad g_* = \frac{g_{\text{DM}}}{2} \quad (\text{Model B}). \quad (2.17)$$

To extract limits directly in the simplified models, we recast the ATLAS mono-jet analysis of ref. [227] as in Section 2.2.1, with the only difference that now the signal cross-section is computed in the complete simplified model, i.e. with the diagrams in Fig. 2.5 and with no M_{cut} restriction, for any value of M_{med} and of m_{DM} . For each point of the simplified model parameter space, the expected signal rate is computed in each SR and the corresponding exclusion limits are applied.

For Model A, the result in the full model is illustrated by the purple lines in Fig. 2.6, as an exclusion limit on M_* as a function of $M_{\text{med}} \equiv m_{Z'}$, for two representative values of $m_{\text{DM}} \equiv m_X$ and for two postulated values of the (width/mass) ratio of the mediator: $\Gamma_{Z'}/m_{Z'} = 1/8\pi$ (solid) and $\Gamma_{Z'}/m_{Z'} = 1/3$ (dashed). We will see below that using the $(m_{Z'}, M_*)$ plane to represent the result suffers from an important limitation. Furthermore, M_* is not a natural variable for the simplified model, where it is a derived quantity rather than a fundamental parameter. In this context, other ways of representing the limits could be more effective. The choice of the $(m_{Z'}, M_*)$ plane is however convenient for comparing these results with the EFT limits and with other studies of Model A, such as those in Refs. [187, 200]. In the figure, our consistent EFT limits, as reinterpreted in Model A, are represented by blue solid lines, while the black dashed horizontal line shows the naïve EFT limit, formally obtained by sending M_{cut} to infinity for fixed M_* . For reference, the orange lines correspond to the correct relic abundance for a thermal freeze out, computed here with the approximate analytical formulae for Model A reported in Appendix 2.C.

First, we can visually check that our consistent EFT limits are actually correct model independent constraints, as they lie systematically below those obtained by working directly with the simplified model. Notice that this is not true for the naïve EFT limits, which overestimate the exclusion for very low mediator mass. Second, we observe that the limits obtained directly in Model A are slightly stronger than the EFT ones, and that this effect is considerably amplified for a moderately light mediator in the case of the smaller $\Gamma_{Z'}/m_{Z'}$ ratio. The reason for this behaviour is that the simplified model cross-section can get significantly enhanced with respect to the EFT one, leading to a stronger bound, only thanks to the resonant production of the mediator, which can only take place if the latter is light enough. Furthermore, the resonant enhancement is of order $\pi m_{Z'}/\Gamma_{Z'}$, and this is why it is more pronounced for a narrow mediator.

These considerations are made quantitative by the solid and dashed red lines in Fig. 2.6, with the same conventions as before. These lines represent the limits on the simplified model obtained by computing the signal rate restricting the invariant mass of the Z' propagators within two widths from its pole mass. The fact that the red lines are so close to the purple lines representing the “true” limit, when they are both significantly above the blue line, confirms that the resonant production is what drives the enhancement. It also suggests that in this kinematical region DM searches in the simplified model should be actually regarded as

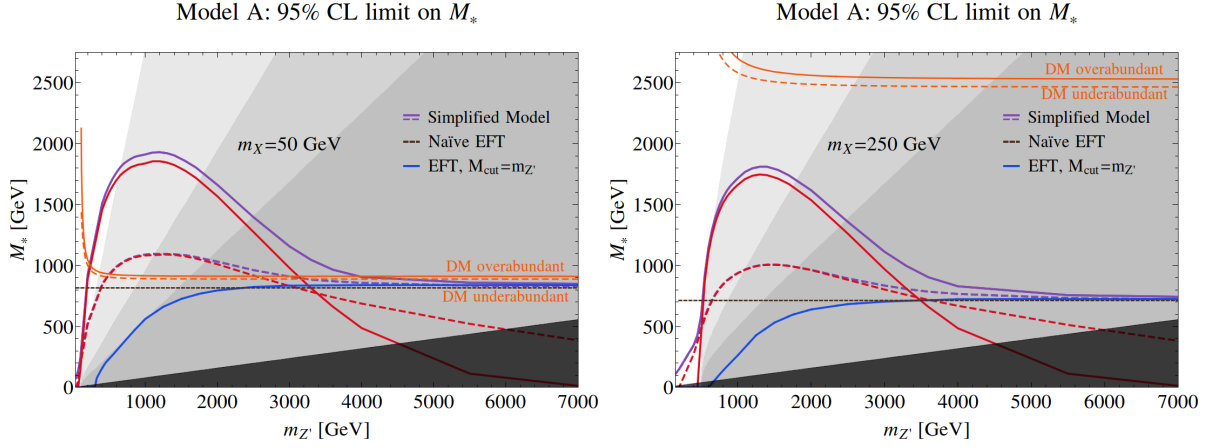


Figure 2.6: 95% CL limit on M_* for Model A, as a function of $m_{Z'}$, for $m_X = 50$ GeV (left) and $m_X = 250$ GeV (right). The horizontal dashed line corresponds to the limit obtained in the naïve EFT. The blue line gives the limit consistently extracted in the EFT with $M_{\text{cut}} = m_{Z'}$. All the other lines refer to the full model, and assume either $\Gamma_{Z'} = m_{Z'}/(8\pi)$ (solid) or $\Gamma_{Z'} = m_{Z'}/3$ (dashed). The purple lines show the limits obtained in the full model. The red lines correspond to the resonant production of the mediator. The orange lines correspond to the correct relic abundance for a thermal freeze-out, computed according to the formulae for Model A reported in appendix 2.C. From the top left to the bottom right, the increasingly dark grey shaded areas correspond to $\Gamma_{Z'}/m_{Z'} > 1/(8\pi), 1/3, 1$ and to $g_* > 4\pi$.

mediator searches, and the results reported as limits on $\sigma(pp \rightarrow Z') \times \text{BR}(Z' \rightarrow XX)$. Also, Z' resonant production followed by the decay into quark-antiquark pairs, leading to a peak in the di-jet invariant mass distribution, may be a complementary signal to be looked for [239], with or without the extra jet: in such a case, we would obtain a limit on $\sigma(pp \rightarrow Z') \times \text{BR}(Z' \rightarrow q\bar{q})$. We will comment further on this in the conclusions.

We now turn to the aforementioned limitation of the $(m_{Z'}, M_*)$ plane, which was already noticed for example in Ref. [200], but we find important to emphasise. Model A has four parameters: $m_{\text{DM}}, m_{Z'}, g_q, g_X$. In Fig. 2.6, the DM mass is set to a fixed value and each point of the plane uniquely determines $m_{Z'}$ and M_* . Then also the product $g_q g_X$ is fixed by the left-hand side of eq. (2.16), namely

$$g_q g_X = \frac{m_{Z'}^2}{M_*^2}. \quad (2.18)$$

Only one combination of the two couplings is left free at this point, and it might seem a good idea to fix it point-by-point to fit the values of $\Gamma_{Z'}/m_{Z'}$ that were assumed in drawing the purple lines in the figure. However, we must take into account that, for fixed $g_q g_X$, the accessible values of $\Gamma_{Z'}/m_{Z'}$ are bounded from below:

$$\frac{\Gamma_{Z'}}{m_{Z'}} = \alpha g_q^2 + \beta g_X^2 \geq g_q g_X \sqrt{4\alpha\beta} = \frac{m_{Z'}^2}{M_*^2} \sqrt{4\alpha\beta}, \quad (2.19)$$

where α and β are suitably defined coefficients (see Appendix 2.A) that do not depend on g_q and g_X , and have only a mild dependence on the spectrum through phase space. This means that the $(m_{Z'}, M_*)$ plane is divided into regions, whose boundaries are curves (or, approximately, straight lines), where $\Gamma_{Z'}/m_{Z'}$ is always larger than a certain value. Some representative regions are displayed as grey shaded areas in Fig. 2.6: from the top left to the bottom right, they correspond to $\Gamma_{Z'}/m_{Z'} > 1/(8\pi), 1/3, 1$. The fourth and darkest region at the bottom right

corresponds to $g_* = \sqrt{g_q g_X} > 4\pi$, where neither the EFT nor the simplified model admit a consistent perturbative description. In the neighbouring region where $\Gamma_{Z'}/m_{Z'} > 1$, the EFT can still be consistently used, but the same does not apply to the chosen underlying simplified model: the fact that $\Gamma_{Z'}/m_{Z'} > 1$ is telling us that in such strong coupling regime the simple mediator interpretation of the origin of the effective interaction breaks down. Even in the perturbative regime, the direct simplified model lines are obtained by assuming a given $\Gamma_{Z'}/m_{Z'}$, thus they become inconsistent on the right of the boundary of the corresponding $\Gamma_{Z'}/m_{Z'}$ region, because they cannot be associated to any physical point of the simplified model parameter space. On the left plot, for instance, we should have stopped drawing the purple and red solid lines corresponding to $\Gamma_{Z'}/m_{Z'} = 1/(8\pi)$ where they cross the boundary between the white and the very light grey region, at $m_{Z'} \sim 600$ GeV. Similarly, we should have stopped the purple and red dashed lines, corresponding to $\Gamma_{Z'}/m_{Z'} = 1/3$, where they cross the boundary of the two light grey regions, at $m_{Z'} \sim 1.1$ TeV. The only justification for keeping them is that the limits on the width are theoretical constraints, while the actual location of the curves is the result of the experimental analysis, which might improve its sensitivity in the future. When this will happen the exclusion curves will move up and will exit more and more out of the inconsistent regions. As far as current data are concerned, however, this observation shows that the DM limits are actually rather poor, especially in the region of narrow mediator width, which corresponds to a weakly-interacting particle. But after all, this is exactly what we concluded from our exploration of the EFT parameter space: ‘small’ g_* effective couplings of order one are still unconstrained. Here we have just verified that the simplified model can not help us much in this respect.

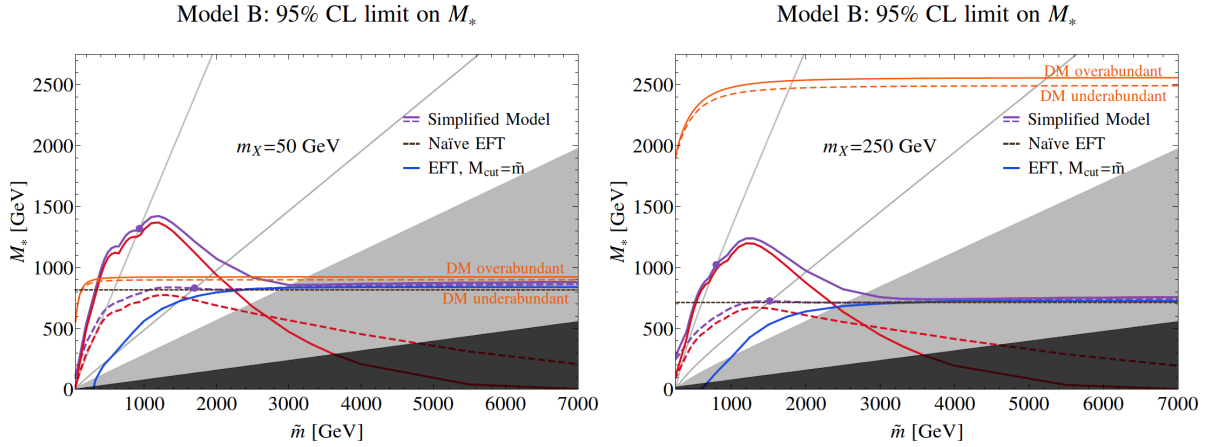


Figure 2.7: The same as in fig. 2.6, but for model B. The only difference is that, from top left to bottom right, the two diagonal lines correspond to $\Gamma_{\tilde{q}}/\tilde{m} = 1/8\pi, 1/3$, and the grey areas to $\Gamma_{\tilde{q}}/\tilde{m} > 1$ and to $g_* = g_{DM}/2 > 4\pi$.

Very similar considerations apply to Model B, whose bounds are depicted in Fig. 2.7. Also in this case the enhancement of the limit obtained directly in the simplified model is mostly due to the resonant production of the mediator, which can occur even in the so-called ‘ t -channel mediator’ case if an extra jet is emitted in the final state. This process corresponds (see diagrams B.3 and B.5 in fig. 2.5) to an associated DM- \tilde{q} production followed by the \tilde{q} decay into DM plus jet. A second point worth stressing for Model B is that the issue with the (\tilde{m}, M_*) plane is even more severe than in Model A, because the model has only three parameters, therefore after fixing m_{DM} , \tilde{m} and M_* the (width/mass) ratio of the mediator is fixed. In this case, fig. 2.7

shows two lines corresponding to $\Gamma_{\tilde{q}}/\tilde{m} = 1/8\pi, 1/3$, a grey area where $\Gamma_{\tilde{q}} > \tilde{m}$, and a dark grey area where $g_* = g_{DM}/2 > 4\pi$. The only physical points of the four exclusion curves derived in Model B (purple and red, solid and dashed) are those at the intersection with the lines corresponding to the assumed value of $\Gamma_{\tilde{q}}/\tilde{m}$, marked as full purple dots.

2.3.1 Comparison with other approaches in the literature

We are not the first to address the issues related with the naïve use of the EFT for DM in kinematical regimes extending beyond its range of validity: as already mentioned, they have been studied at length in the literature [185, 187, 189, 192, 193, 195, 197–206]. In particular, Refs. [204–206] proposed a criterion (subsequently adopted in most DM searches at LHC, as discussed in Sec. 1.5.3) to estimate how sensitive the naïve limits on M_* are to the unsafe region of the EFT and how much they deteriorate if the latter region is excluded from the analysis. Below we discuss two aspects of our approach in a way that can be helpful for the comparison with this previous literature.

The first point to be discussed concerns the choice of the kinematical variable to be used for discriminating the safe EFT region from the unsafe one. From the EFT viewpoint, the natural variable is clearly the hard scale of the process, E_{cm} : this was our choice. However, within specific ‘mediator’ models, or more precisely classes of models, another possible choice is the variable Q_{tr} , as proposed in Refs. [204–206]. $Q_{\text{tr}} = +\sqrt{|Q_{\text{tr}}^2|}$ is defined as the maximal virtuality of the mediator propagator, computed over the Feynman diagrams contributing to the partonic DM production process under study. Since $Q_{\text{tr}} < E_{\text{cm}}$, using Q_{tr} to define the safe kinematical region of the EFT means gaining signal cross-section, thus obtaining a stronger and still reliable limit. Notice that, since the definition of Q_{tr} depends on whether the mediator propagates in the s or in the t channel in the two-body annihilation $q\bar{q} \leftrightarrow XX$, Q_{tr} is not suited for setting a model-independent limit. However, one might still consider the two possibilities in turn and set separate limits for the two cases of s - and t -channel mediation. While this does not exhaust all possibilities⁶, it might be still worth doing if it considerably enhances the reach.

To explore the exclusion reach of this method and compare it with ours, we start by recalling the expressions for Q_{tr} in Models A (s -channel) and B (t -channel), corresponding to the diagrams in Fig. 2.5 and the conventions in Eqs. (2.13)–(2.15). In Model A, for both process I and process II (the kinematics of III is identical to that of II, so it does not need a separate discussion), Q_{tr} is just the invariant mass of the DM pair

$$Q_{\text{tr}}^2 = (p_3 + p_4)^2 = (p_1 + p_2 - k)^2 \quad (\text{AI, AII}). \quad (2.20)$$

In model B, instead, we have to consider process I and II,III separately. In the case of process I, Q_{tr} reads⁷

$$Q_{\text{tr}}^2 = \max \{ (p_1 - k - p_4)^2 = (p_3 - p_2)^2, (p_1 - p_4)^2 = (p_3 - p_2 + k)^2, \\ (p_1 - k - p_3)^2 = (p_4 - p_2)^2, (p_1 - p_3)^2 = (p_4 - p_2 + k)^2 \} \quad (\text{BI}), \quad (2.21)$$

while for process II,III we have

$$Q_{\text{tr}}^2 = \max \{ (p_1 - p_3)^2 = (p_4 - p_2 + k)^2, (p_3 + k)^2 = (p_1 + p_2 - p_4)^2, \}$$

⁶The effective interaction might well be generated by the combined exchange of s - and t -channel mediators, or by radiative effects not falling in any of these two categories.

⁷Notice that, if in Model B we had assumed a Dirac DM particle, only half of the conditions in Eqs. (2.21) and (2.22) should have been imposed. Therefore, the model dependence of this strategy depends on the assumptions made both on the mediator (s -channel or t -channel) and on the nature of the DM particle (Dirac or Majorana fermion, complex or real scalar).

$$(p_1 - p_4)^2 = (p_3 - p_2 + k)^2, (p_4 + k)^2 = (p_1 + p_2 - p_3)^2 \quad (\text{BII}). \quad (2.22)$$

Notice that the subprocesses are quantum-mechanically distinguishable and therefore it makes sense to adopt a different definition of Q_{tr} for each of them.

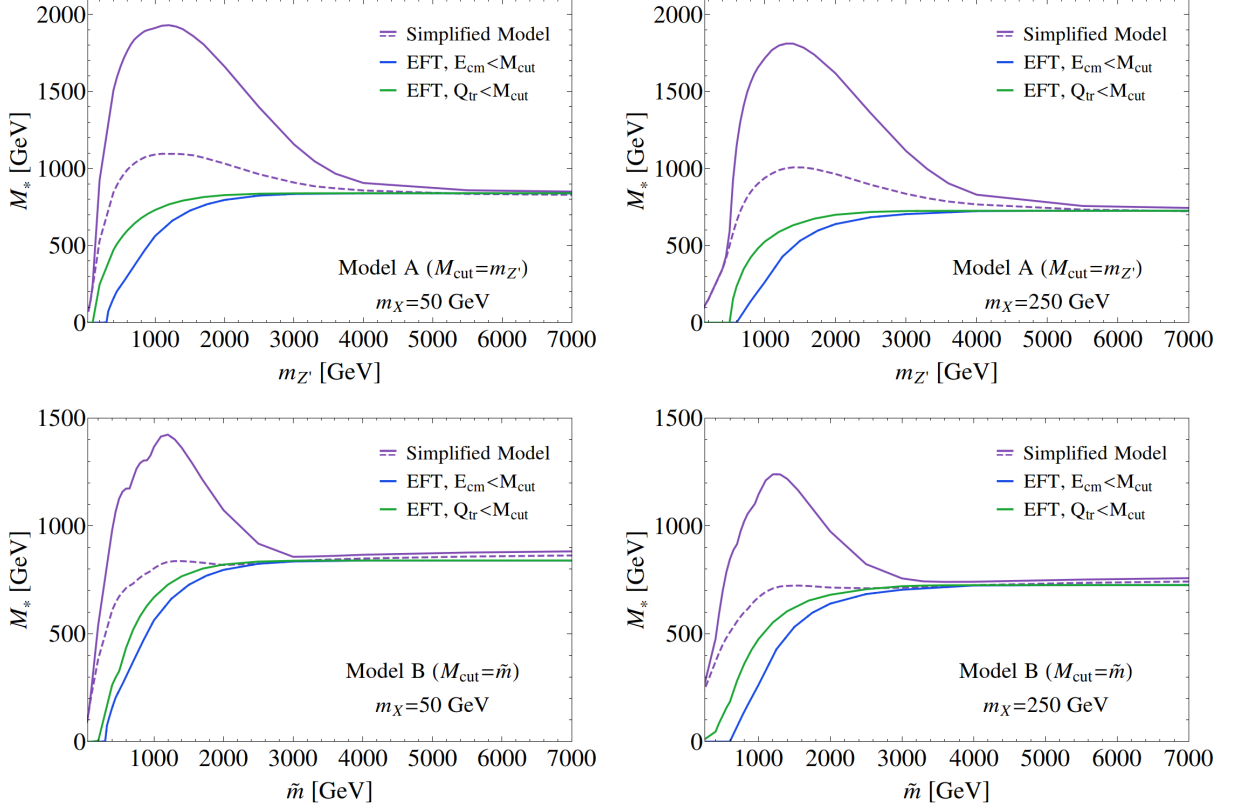


Figure 2.8: Limits on M_* as functions of M_{med} obtained for Models A and B with three different methods. The purple lines are derived in the full models, assuming two representative values of the ratio $\Gamma_{\text{med}}/M_{\text{med}}$: $1/(8\pi)$ (solid) and $1/3$ (dashed). The solid blue line is derived in the EFT with our method as described in the text. The solid green line is derived in the EFT by imposing the condition on Q_{tr} proposed in Refs. [204–206]. *Upper plots:* Model A. *Lower plots:* Model B.

The result of the comparison is displayed in Fig. 2.8, where we show the limits on M_* as functions of M_{med} , obtained for Models A (upper plots) and B (lower plots) with three different methods. The purple and blue lines represent the full model and our approach to the EFT, respectively, namely the same curves as in Figs. 2.6 and 2.7. The green line is also derived in the EFT, but with the cut $Q_{\text{tr}} < M_{\text{cut}}$ instead of $E_{\text{cm}} < M_{\text{cut}}$. In the limit of heavy mediators, all the lines coincide as expected. The differences are in the region of relatively light mediators, where the EFT limit obtained with Q_{tr} has, as expected, a better reach in M_* than our method. However, in our view the improvement is not sufficiently significant, especially when compared with that obtainable in the full simplified model, to motivate the use of Q_{tr} rather than E_{cm} . Our recommendation is thus to stick to the simple and model-independent version of our method, possibly trying to extend the reach by the direct search of the mediator which, as described in the previous section, is the sole responsible of the improved reach of the simplified model.

A second aspect to be mentioned is that the consistent EFT limits in the (m_{DM}, M_*) plane, at

fixed g_* , cannot be inferred from those obtained in the naïve EFT by just performing a rescaling of M_* . Indeed such a rescaling cannot lead to closed exclusion curves such as those we obtained in Fig. 2.4. One might be tempted to consider a rescaling here because the EFT cross-section is proportional to $1/M_*^4$, so that the reduction of the cross-section caused by the kinematical cut might be reabsorbed into an effective M_* . Namely, one might consider defining the ratio⁸

$$R(M_*, m_{\text{DM}}, g_*) = \frac{\sigma(M_*) \Big|_{Q_{\text{tr}} < M_{\text{cut}} = g_* M_*}}{\sigma(M_*)}, \quad (2.23)$$

where σ denotes the signal cross-section computed in the naïve EFT for a given signal region. At fixed g_* and m_{DM} , R is a function of M_* , which tends to one for sufficiently high M_* and to zero for sufficiently low M_* , because of the effect of the kinematical cut illustrated in Eq. (2.11). Given that R measures the reduction of the cross-section with respect to the naïve EFT, one might think of getting the limit on M_* at each m_{DM} , call it \tilde{M}_* , starting from the limit obtained in the naïve EFT, call it M_*^{EFT} , and solving the implicit equation

$$\tilde{M}_* = \left[R(\tilde{M}_*, m_{\text{DM}}) \right]^{\frac{1}{4}} M_*^{\text{EFT}}. \quad (2.24)$$

The effective operator scale \tilde{M}_* obtained in this way is the one that reproduces, in the EFT with the cut on Q_{tr} , the same signal cross-section that was needed for setting the bound at M_*^{EFT} in the naïve EFT. Namely, Eq. (2.24) is equivalent to

$$\sigma(\tilde{M}_*) \Big|_{Q_{\text{tr}} < M_{\text{cut}} = g_* \tilde{M}_*} = \sigma(M_*^{\text{EFT}}), \quad (2.25)$$

where we have exploited the fact that in the naïve EFT $\sigma(M_*)$ simply scales as $1/M_*^4$.

The above method for obtaining \tilde{M}_* is more elaborate than directly comparing the experimental limit on the cross-section with the prediction of the kinematically restricted EFT, as we suggested in section 2.1. Furthermore, the rescaling method might obscure the fact that Eq. (2.25), or equivalently Eq. (2.24), has either zero (which means that no limit can be set) or two solutions for \tilde{M}_* , but it never has only one. The behaviour of the restricted EFT cross-section, compared with the naïve EFT, is pictorially represented in Fig. 2.9.

The cross-section vanishes before approaching $M_* = 0$, because of the cut $Q_{\text{tr}} < g_* M_*$. Therefore there are two values of M_* for which the cross-section equals the experimental limit, which means that the excluded region has one upper but also one lower limit in M_* , differently from the naïve EFT as depicted in the figure. Therefore, the true limit cannot be set by just rescaling the naïve EFT exclusion curve. The quantitative impact on the excluded regions in the (m_{DM}, M_*) plane, for different values of g_* , was already displayed in Fig. 2.4 for our kinematical requirement $E_{\text{cm}} < g_* M_*$.

2.3.2 Further developments of this method in the literature

In this Section we briefly comment on some later developments of the method proposed in this Chapter.

The starting point of the discussion of Refs. [215, 216] is the result that the recast of DM searches within the EFT can constrain, as for the current status of experimental bounds, only effective couplings $g_* > 1$, as we have seen in Section 2.2 and in particular in Fig. 2.4. This

⁸Using Q_{tr} or E_{cm} makes no difference for the point we want to make here.

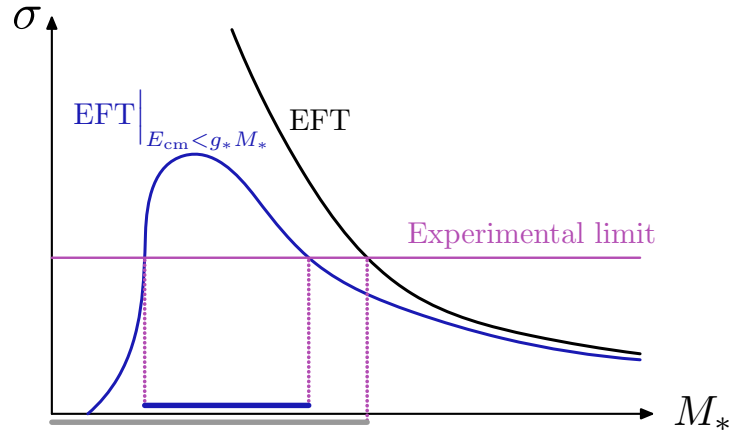


Figure 2.9: A pictorial representation of how the bounds on M_* depend on the prescription for computing the signal in the EFT. The signal cross-section is displayed as a function of M_* , for fixed g_* and m_{DM} . The black and the blue lines correspond to the naïve EFT and to our consistent prescription, respectively. The horizontal purple line represents the experimental limit. The resulting excluded interval for M_* is reported near the horizontal axis for the two prescriptions.

implies that the EFT can be useful to constrain only strongly coupled models. Even more, an effective description has to be sought in these cases, due to the failure of a perturbative description.

A concern could arise when considering the consistency of a description in which DM is a light and weakly coupled particle arising from a strongly interacting sector. This is the outcome though if there is an approximate global symmetry which protects the DM mass from large corrections. An example of this mechanism in the SM is the pion, which is a composite state emerging from strongly coupled QCD, and whose mass is small due to the approximate chiral symmetry $SU(2)_V \times SU(2)_A$ broken by the small u, d quark masses.

Ref. [216] analyses the scenarios which could realise a similar mechanism in relation to the dark sector. DM could then be a scalar pseudo-Goldstone boson of a non-linearly realised symmetry, or a composite fermion with chiral symmetry, or the Goldstino of non-linearly realised supersymmetry. Having these completions in mind, the authors then identify the relevant effective operators allowed by symmetries, and perform in Ref. [215] a recast of the ATLAS monojet search at $\sqrt{s} = 8$ TeV with 20.3 fb^{-1} of integrated luminosity. They use the same prescription proposed in this Chapter, and simulate more carefully the signal, by including hadronisation and showering effects. The final results they obtain are qualitatively similar to what showed in Fig. 2.4.

In Ref. [217] the concern is the adaptation and improvement of the strategy exposed in this Chapter to the case in which the experimental analysis exploits the information contained in the kinematical distributions of the measured samples. A cut-and-count analysis, as the one performed in [227] and recast in this Chapter, has the advantage of being straightforward to recast in a preferred model. In order to obtain the bound, indeed, it is sufficient to impose the acceptance cuts of the analysis, count the surviving events and compare this number to the measured one. Clearly this procedure does not make use of the large amount of information contained in the sample of the events passing the analysis cuts, and both the latest experimental searches of Run 1 and the current ones at Run 2 of LHC rely on the comparison of the shapes of the \cancel{E}_T distributions of signal and background.

This poses a problem though for a consistent use of the EFT. The signal in a full model is the

sum of the events S predicted in the truncated EFT (consisting of the events when $E_{\text{cm}} < M_{\text{cut}}$) plus the events Δ for which $E_{\text{cm}} > M_{\text{cut}}$. Given that the latter contribution Δ is unknown, how can we consistently use only the former contribution S to get a sensible constraint? The final result of the rigorous and detailed discussion of Ref. [217] is remarkably simple. Put in plain terms, a consistent procedure is to compare, for each bin i of the histogram of the relevant kinematical distribution (say \cancel{E}_T), the signal of the truncated EFT (call it S_i) plus the corresponding SM background B_i and the observed number of events O_i . If the bin is overfluctuating, $S_i + B_i < O_i$, then an extra contribution Δ_i from the signal events for which $E_{\text{cm}} > M_{\text{cut}}$ could help alleviate the tension between model and observation, so it has to be ignored in the computation of the likelihood function \mathcal{L} , given that the goal is to compute a conservative robust bound. If instead the bin is underfluctuating, $S_i + B_i > O_i$, then it should be included in the likelihood as usual. Notice that the discarded overfluctuating bins, although they are not included in \mathcal{L} , are still to be considered among the degrees of freedom of the χ^2 distribution by which compatibility or incompatibility is established.

The procedure described in Ref. [217] is suitable for a recast of an exclusion limit (in case of a discovery, the procedure is not adequate) for any theory in which part of the signal contribution is unknown (and positive, as it is the case for a truncated EFT and the events lying beyond its regime of validity).

2.4 Conclusions

We described a simple strategy to set robust and model-independent limits on heavy-mediator DM at the LHC. Our method is based on the generic form of the operators in the EFT containing only the DM and the SM particles, with no assumptions on the underlying dynamics. However, it also takes into account the presence of a cutoff scale M_{cut} above which the EFT loses its validity. M_{cut} must be regarded as one of the free parameters of the EFT, on the same footing as the DM mass m_{DM} and the effective interaction scale M_* . We have to do so if we aim at a comprehensive exploration of the whole range of theoretical possibilities. The parameter M_{cut} can be traded for g_* , the typical coupling strength at the mediator scale. As explained in Section 2.1, g_* can be defined in the EFT alone, and further characterised for any assumed underlying model.

We applied our method explicitly to the ATLAS mono-jet search of Ref. [227], obtaining the exclusion contours in the (m_{DM}, M_*) plane shown in Fig. 2.4, for fixed representative values of g_* . We believe that this kind of plots illustrates the current experimental situation in an accurate and comprehensive way, providing a fair assessment of the LHC sensitivity to heavy-mediator DM. At the moment, we are only sensitive to large values of g_* , while the region $g_* \sim 1$, which is arguably the most natural one for WIMP DM, is still largely untested. Making progress requires higher energy and luminosity, but also an optimisation of the experimental search strategies. As pointed out in section 2.2, our signal is kinematically different from that of the naive EFT, in particular it is characterised by softer \cancel{E}_T and p_T^{jet} distributions. The reach of the searches would then benefit from a sensitivity improvement in the soft region.

In Section 2.3 we considered two different simplified models, both giving rise to the same effective operator considered in Section 2.2. We compared our EFT limits, reinterpreted in the two models, with those obtained from a dedicated comparison of the experimental bounds with the prediction of the two models, reaching two main conclusions. First, the limits set within the simplified models can be considerably stronger than the EFT ones, but only because of the resonant production of the mediator, which enhances the simplified model cross-section. Therefore, a DM search performed within a simplified model (in the only interesting region

where the limit is potentially stronger than in the EFT) is actually not a search for DM, but a search for the mediator, and as such it should be interpreted. The canonical $\sigma \times \text{BR}$ limit as a function of the mediator mass appears to be the best option for presenting the experimental results. The second conclusion is that the current experimental sensitivity is still rather poor, even when working within a simplified model. In particular the region of weak coupling, i.e. narrow mediator, is mostly unexplored, in accordance with what we found in our EFT analysis. We finally discussed two aspects of our approach, to facilitate the comparison with the recent literature. We found that the usage of the variable Q_{tr} in place of E_{cm} to define the safe kinematical region of the EFT does not improve the sensitivity significantly enough to pay back for the increased model-dependence. We also remarked that just rescaling the naïve EFT limit does not account for the impossibility, within mono-jet searches, of excluding arbitrarily low values of M_* at fixed m_{DM} and g_* .

In summary, we have found that the LHC sensitivity to the heavy-mediator DM hypothesis is still limited and wide regions of the parameter space still wait to be explored. On the experimental side, improving the analysis in the soft region would be of great help. On the phenomenological side, more comprehensive methods should be elaborated to cover each different region of the parameter space with the most suitable strategy. Non-resonant DM signals are well described by the EFT which, as outlined in this Chapter, when consistently used provides a robust model-independent way to approach the problem. Within specific models, this needs to be supplemented by resonant mediator searches, which however should be performed by exploiting fully the predictive power of the assumed mediator dynamics. This means taking into account all the mediator production mechanisms (single and/or pair) and all its possible decay modes, including the one to visible objects which might give complementary informations.

2.A Model A: axial-vector mediator

We collect here some details on the first of the two simplified models considered in the text, Model A. Previous discussions of very similar models can be found in Refs. [191, 229–232]. The mediator is a neutral vector boson Z' , singlet under the SM gauge group, with mass $m_{Z'}$, a universal axial coupling g_q to quarks, no renormalisable couplings to leptons, and an axial coupling g_X to the Majorana DM fermion X of mass m_X . Since the model is introduced for purely illustrative purposes, without making reference to an underlying more fundamental theory, we introduce an explicit Z' mass term and we neglect Z - Z' mixing, as well as anomalies and their cancellation mechanisms.

The model Lagrangian is

$$\mathcal{L}_A = \mathcal{L}_{SM} + \mathcal{L}_X + \mathcal{L}_{Z'} + \mathcal{L}_{\text{int}}^A, \quad (2.26)$$

$$\mathcal{L}_{Z'} = -\frac{1}{4}Z'_{\mu\nu}Z'^{\mu\nu} + \frac{1}{2}m_{Z'}^2 Z'_\mu Z'^\mu, \quad (2.27)$$

$$\mathcal{L}_{\text{int}}^A = Z'_\mu \left(g_q \sum_q \bar{q} \gamma^\mu \gamma^5 q + g_X \bar{X} \gamma^\mu \gamma^5 X \right) \equiv Z'_\mu J_{Z'}^\mu, \quad (2.28)$$

where \mathcal{L}_{SM} is the SM Lagrangian, \mathcal{L}_X is the free Lagrangian for X in (2.5), $Z'_{\mu\nu} = \partial_\mu Z'_\nu - \partial_\nu Z'_\mu$, and the sum in (2.28) runs over all quark flavours ($q = u, d, c, s, t, b$). The model has four parameters,

$$g_q, \quad g_X, \quad m_{Z'} \equiv M_{\text{med}}, \quad m_X \equiv m_{\text{DM}}, \quad (2.29)$$

which can all be taken to be real and positive (in principle, g_q and g_X could have either sign, but this is not relevant for the present study).

Notice that the choice of a purely axial interaction, universal for all quark flavours, is crucial to generate the effective interaction (2.6) from (2.28) in the low-energy limit. At leading order in $E/m_{Z'} \ll 1$, the approximate solution of the Z' equations of motion is

$$Z'^{\mu} = -\frac{1}{m_{Z'}^2} J_{Z'}^{\mu},$$

which substituted in (2.26) gives

$$\mathcal{L}_{\text{EFT}}^A = -\frac{g_X^2}{2m_{Z'}^2} (\bar{X}\gamma^{\mu}\gamma^5 X)(\bar{X}\gamma_{\mu}\gamma^5 X) \quad (2.30)$$

$$-\frac{g_q^2}{2m_{Z'}^2} \sum_q (\bar{q}\gamma^{\mu}\gamma^5 q) \sum_q (\bar{q}\gamma_{\mu}\gamma^5 q) \quad (2.31)$$

$$-\frac{g_q g_X}{m_{Z'}^2} (\bar{X}\gamma^{\mu}\gamma^5 X) \sum_q (\bar{q}\gamma_{\mu}\gamma^5 q). \quad (2.32)$$

The effective interaction term (2.32) between the SM quarks and the DM field reproduces the one in (2.6) as long as

$$M_* = \frac{m_{Z'}}{\sqrt{g_q g_X}}. \quad (2.33)$$

Notice also that integrating out the heavy Z' generates two additional four-fermion operators, (2.30) and (2.31). However, (2.30) is subject only to very mild constraints from the limits on DM self-interactions. The four-quark operator (2.31) can be probed by the searches for contact interactions [197, 240], but can be parametrically suppressed by choosing $g_X > g_q$ for fixed g_* .

At tree-level, and including only two-body decays, the total decay width of the Z' is

$$\Gamma_{Z'} = \frac{m_{Z'}}{12\pi} \left[2g_X^2 \left(1 - \frac{4m_X^2}{m_{Z'}^2} \right)^{3/2} + \sum_q 3g_q^2 \left(1 - \frac{4m_q^2}{m_{Z'}^2} \right)^{3/2} \right], \quad (2.34)$$

with the obvious modifications if some of the final states are not kinematically accessible.

2.B Model B: coloured scalar mediators

We collect here some details on the second of the two simplified models considered in the text, Model B. Previous discussions of very similar models can be found in Refs. [233–238]. In Model B, the interactions between the SM quarks and the DM particle X are mediated by three families of degenerate complex scalars of mass \tilde{m} , with the same gauge quantum numbers of the corresponding left- and right-handed quarks. Since they are identical to the squarks of supersymmetric extensions of the SM, we denote them with the same symbols, $(\tilde{u}_{iL}, \tilde{d}_{iL}, \tilde{u}_{iR}, \tilde{d}_{iR})$, where $i = 1, 2, 3$ are family indices. Similarly, the Majorana fermion X mimicks, although in the simplified fashion specified by its interactions below, the lightest neutralino of supersymmetric models.

The model Lagrangian reads

$$\mathcal{L}_B = \mathcal{L}_{\text{SM}} + \mathcal{L}_X + \mathcal{L}_{\tilde{q}} + \mathcal{L}_{\text{int}}^B, \quad (2.35)$$

$$\begin{aligned} \mathcal{L}_{\tilde{q}} &= \sum_{i=1}^3 \left[(\partial^\mu \tilde{u}_{iL})^\dagger (\partial_\mu \tilde{u}_{iL}) + (\partial^\mu \tilde{d}_{iL})^\dagger (\partial_\mu \tilde{d}_{iL}) + (\partial^\mu \tilde{u}_{iR})^\dagger (\partial_\mu \tilde{u}_{iR}) + (\partial^\mu \tilde{d}_{iR})^\dagger (\partial_\mu \tilde{d}_{iR}) \right. \\ &\quad \left. - \tilde{m}^2 \left(\tilde{u}_{iL}^\dagger \tilde{u}_{iL} + \tilde{d}_{iL}^\dagger \tilde{d}_{iL} + \tilde{u}_{iR}^\dagger \tilde{u}_{iR} + \tilde{d}_{iR}^\dagger \tilde{d}_{iR} \right) \right] + \dots, \end{aligned} \quad (2.36)$$

$$\mathcal{L}_{int}^B = -g_{DM} \left[\sum_{i=1}^3 \left(\tilde{u}_{iL} \overline{u_{iL}} + \tilde{d}_{iL} \overline{d_{iL}} + \tilde{u}_{iR} \overline{u_{iR}} + \tilde{d}_{iR} \overline{d_{iR}} \right) X + \text{h.c.} \right], \quad (2.37)$$

where \mathcal{L}_{SM} and \mathcal{L}_X are the same as in Model A, and the dots in (2.36) denote the squark gauge interactions, generated by promoting ordinary derivatives to SM covariant derivatives. Notice that the mass degeneracy and the universality of the Yukawa couplings among quarks, squarks and DM evade the typical problems of supersymmetric models with flavour-changing neutral currents. The model has three parameters,

$$g_{DM}, \quad \tilde{m} \equiv M_{\text{med}}, \quad m_X \equiv m_{DM}, \quad (2.38)$$

which can all be taken to be real and positive (g_{DM} can be complex, but it can be chosen to be real and positive by absorbing its phase into a redefinition of the squark fields).

As for Model A, we can derive the EFT by solving the classical equations of motion for the squarks in the low-energy limit $E \ll \tilde{m}$:

$$\tilde{u}_{iL} = -\frac{g_{DM}}{\tilde{m}^2} \overline{X} u_{iL}, \quad \tilde{u}_{iR} = -\frac{g_{DM}}{\tilde{m}^2} \overline{X} u_{iR}, \quad \tilde{d}_{iL} = -\frac{g_{DM}}{\tilde{m}^2} \overline{X} d_{iL}, \quad \tilde{d}_{iR} = -\frac{g_{DM}}{\tilde{m}^2} \overline{X} d_{iR}. \quad (2.39)$$

Substituting into \mathcal{L}_B yields

$$\begin{aligned} \mathcal{L}_{EFT}^B &= \frac{g_{DM}^2}{\tilde{m}^2} \sum_{i=1}^3 \left[(\overline{X} u_{iL}) (\overline{u_{iL}} X) + (\overline{X} u_{iR}) (\overline{u_{iR}} X) + (\overline{X} d_{iL}) (\overline{d_{iL}} X) + (\overline{X} d_{iR}) (\overline{d_{iR}} X) \right] \\ &= -\frac{g_{DM}^2}{4\tilde{m}^2} (\overline{X} \gamma^\mu \gamma^5 X) \left[\sum_{i=1}^3 \left(\overline{u}_i \gamma_\mu \gamma^5 u_i + \overline{d}_i \gamma_\mu \gamma^5 d_i \right) \right], \end{aligned} \quad (2.40)$$

where for the second equality we have used the Fierz identities and the fact that when X is a Majorana spinor $\overline{X} \gamma^\mu X = 0$. The effective interaction term (2.40) between the SM quarks and the DM particle reproduces the one in (2.6) as long as

$$M_* = \frac{2\tilde{m}}{g_{DM}}. \quad (2.41)$$

At tree-level, and assuming $\tilde{m} > m_X + m_q$, where q is the corresponding quark, the decay width of the generic \tilde{q} is

$$\Gamma_{\tilde{q}} = \frac{\tilde{m}}{16\pi} g_{DM}^2 \sqrt{1 + \frac{(m_q^2 + m_X^2)^2}{\tilde{m}^4} - 2 \frac{m_q^2 + m_X^2}{\tilde{m}^2}} \left(1 - \frac{m_q^2}{\tilde{m}^2} - \frac{m_X^2}{\tilde{m}^2} \right). \quad (2.42)$$

2.C Formulae for the relic density

We collect here the approximate analytical formulae used for the calculation of the relic density in the EFT (Fig. 2.3), in Model A (Fig. 2.6) and in Model B (Fig. 2.7), before requiring that it reproduces the recent precise determination by the Planck collaboration [33] (for our purposes, the latter can be rounded to $\Omega_{DM} h^2 = 0.12$ with negligible error). They can be straightforwardly

derived from the existing literature (see e.g. [29, 41]). Up to terms of order $1/x_f$, where x_f is the value of $x = m_X/T$ at freeze-out:

$$\Omega_{\text{DM}} h^2 \approx 1.07 \cdot 10^9 (\text{GeV})^{-1} \frac{x_f}{\sqrt{g_*} M_{\text{P}} \frac{1}{16 m_X^2} \left(a + \frac{3b}{x_f} \right)}, \quad (2.43)$$

where h is the dimensionless Hubble parameter, $g_* \sim 100$ is the number of relativistic degrees of freedom, $M_{\text{P}} \simeq 2.4 \times 10^{18}$ GeV is the reduced Planck mass, m_X is the mass of the DM particle in GeV, and

$$x_f = \ln(\lambda) - \frac{1}{2} \ln[\ln(\lambda)] + \ln \left[1 + \frac{6b}{a} \frac{1}{\ln(\lambda)} \right], \quad (2.44)$$

$$\lambda = 0.038 \frac{2}{\sqrt{g_*}} M_{\text{P}} m_X \left(\frac{a}{16 m_X^2} \right). \quad (2.45)$$

In the EFT, introducing the dimensionless parameters $\alpha_q = m_q/m_X$,

$$a = \sum_q \frac{96}{\pi} \left(\frac{m_X}{M_*} \right)^4 \alpha_q^2 \sqrt{1 - \alpha_q^2}, \quad (2.46)$$

$$b = \sum_q \frac{4}{\pi} \left(\frac{m_X}{M_*} \right)^4 \left(8 - 16\alpha_q^2 + 11\alpha_q^4 \right) \left(1 - \alpha_q^2 \right)^{-1/2}, \quad (2.47)$$

where the sums run over the quark flavours whose mass is below m_X .

In the two models underlying the EFT, we introduce two additional dimensionless parameters, $\beta = m_X/M_{\text{med}}$ and $\gamma = \Gamma_{\text{med}}/M_{\text{med}}$, to account for the finite mass M_{med} and width Γ_{med} of the mediator. Then in Model A (Z' mediator)

$$\begin{aligned} a &= \sum_q \frac{96}{\pi} g_q^2 g_X^2 \frac{\beta^4 \sqrt{1 - \alpha_q^2}}{(4\beta^2 - 1)^2 + \gamma^2} \alpha_q^2 \left(1 - 8\beta^2 + 16\beta^4 \right), \quad (2.48) \\ b &= \sum_q \frac{4}{\pi} g_q^2 g_X^2 \frac{\beta^4}{\sqrt{1 - \alpha_q^2} [(4\beta^2 - 1)^2 + \gamma^2]^2} \left\{ (8 - 16\alpha_q^2 + 11\alpha_q^4)(1 + \gamma^2) \right. \\ &\quad - 8\beta^2 \left[(8 - 16\alpha_q^2 + 14\alpha_q^4) + 3\alpha_q^2(2 - \alpha_q^2)\gamma^2 \right] \\ &\quad + 16\beta^4 \left[(8 - 16\alpha_q^2 + 26\alpha_q^4) + 3\alpha_q^2(4 - 3\alpha_q^2)\gamma^2 \right] \\ &\quad \left. + 768 \beta^6 (\beta^2 - 1) \alpha_q^4 \right\}, \quad (2.49) \end{aligned}$$

and in Model B (\tilde{q} mediator)

$$\begin{aligned} a &= \sum_q \frac{6g_{\text{DM}}^4}{\pi} \frac{\beta^4 \sqrt{1 - \alpha_q^2}}{(1 + \beta^2 - \alpha_q^2 \beta^2)^2 + \gamma^2} \alpha_q^2, \quad (2.50) \\ b &= \sum_q \frac{g_{\text{DM}}^4}{4\pi} \frac{\beta^4}{\sqrt{1 - \alpha_q^2} [(1 + \beta^2 - \alpha_q^2 \beta^2)^2 + \gamma^2]^3} \left\{ (8 - 16\alpha_q^2 + 11\alpha_q^4)(1 + \gamma^2)^2 \right. \\ &\quad + 4\beta^2(1 - \alpha_q^2)(4 - 18\alpha_q^2 + 11\alpha_q^4)(1 + \gamma^2) \\ &\quad \left. + 2\beta^4(1 - \alpha_q^2)^2 [(8 - 48\alpha_q^2 + 33\alpha_q^4) + (8 - 24\alpha_q^2 + 11\alpha_q^4)\gamma^2] \right\} \end{aligned}$$

$$\begin{aligned} &+4\beta^6(1-\alpha_q^2)^3(4-10\alpha_q^2+11\alpha_q^4) \\ &+ \beta^8(1-\alpha_q^2)^4(8+11\alpha_q^4) \} . \end{aligned} \tag{2.51}$$

Dark Matter interactions with the Standard Model through an anomalous Z'

In this Chapter, based on Ref. [2], we study a model with a Dark Matter (DM) candidate whose interactions with baryonic matter are mediated by a heavy *anomalous* Z' . We emphasise that when the DM is a Majorana particle, its low-velocity annihilations are dominated by loop suppressed annihilations into the gauge bosons, rather than by p -wave or chirally suppressed annihilations into the SM fermions.

Since the Z' is anomalous, these kinds of DM models are effective field theories (EFTs) with a well-defined cutoff, where heavy spectator fermions restore gauge invariance at high energies. We describe these EFTs, estimate their cutoff and properly take into account the effect of the Chern-Simons terms one obtains after the spectator fermions are integrated out.

The result is that, while for light DM collider and direct detection experiments usually provide the strongest bounds, the bounds at higher masses are dominated by indirect detection experiments, due to the strong annihilation into W^+W^- , ZZ , $Z\gamma$ and possibly into gg and $\gamma\gamma$. We emphasise that these annihilation channels are generically significant because of the structure of the EFT, and therefore these models are prone to strong indirect detection constraints. We select some particular Z' models for illustration, but the results apply to any $U(1)'$ theory with arbitrary charge assignments.

3.1 Introduction

As a framework for the recast of DM experimental searches at colliders, the communities of theorists and experimentalists have progressively embraced in the last years the simplified models. A typical simplified DM model extends the SM by a DM candidate as well as a mediator that communicates between the SM and dark sectors. The approach is usually minimalistic in the number of assumptions: rather than building a self-consistent theory, the goal is to include in the description the first degrees of freedom which would show up at the cutoff of the effective low energy Lagrangian. The choice of considering simplified models for the recast of collider searches, was motivated by the discussion about the limited validity of an EFT description for DM in a high energy environment as the LHC [200, 204–206].

Even though it is hard to believe that any simplified model accurately describes all physics

beyond the SM, the essential idea is that the key ingredients that determine the experimental signatures related to the DM should be captured correctly by these models. For these purposes simplified models must be able to make proper predictions for the thermal relic abundance, direct detection experiments, neutrino and γ ray telescopes, and collider experiments. In this Chapter, we will investigate this requirement in the context of simplified models with spin-1 mediators.

The idea that the interaction between the SM particles and DM is mediated by a heavy neutral spin-1 boson, that we will further call Z' , is not new. Refs [191, 209, 231, 241–249] form just a partial list of the related contributions. In this Chapter we concentrate on a Majorana fermion DM candidate whose interactions with the SM are mediated by a heavy Z' , corresponding to a symmetry that appears to be *anomalous* at the electroweak scale. Anomaly cancellation at high scales is necessary for the overall consistency of the theory, as well as for more practical purposes like the calculation of the couplings of the Z' to the SM gauge bosons, which largely determine the DM signatures in indirect detection experiments. Moreover, many of the Z' models employed in describing the results of LHC searches, including the “axial” Z' model, are anomalous [213, 250]. All such “anomalous” theories must descend from the UV complete ones, where the anomalies are either cancelled by spectator fermions [251], or via the Green-Schwarz mechanism [252–254]. As has been recently shown in Ref. [255], these spectator fermions can be potentially responsible for non-trivial collider signatures and can be more easily accessible at the LHC than the DM itself.

In this Chapter we will take a different approach. In fact, it is not always necessary to analyse a *full UV-complete model* to make important predictions for DM signatures in relevant experiments. In particular, we are interested in the anomalous Z' couplings to the SM gauge bosons. These couplings determine the annihilation cross sections of DM into SM gauge bosons, affecting the γ ray fluxes from dSph and the Galactic Centre, as well as signals in neutrino telescopes. To calculate these observables, it is sufficient to consider an EFT with the anomalous Z' after the heavy spectators have been integrated out.

In fact, EFTs with low-energy anomalies from integrating out heavy chiral fermions have been considered as early as the 1980s, mostly in the context of the SM without the top quark [256, 257]. Indeed the $SU(2)_L \times U(1)_Y$ electroweak symmetry is anomalous in the absence of the top quark and should be analysed as an effective field theory with extra degrees of freedom, with couplings which compensate for the loss of gauge invariance at the 1-loop level. This approach was further generalised by Preskill in Ref [258]. More recently, the influence of anomalous Z' couplings to the SM gauge bosons has been studied in the context of DM [207, 243, 259–261].

Here we essentially take the same approach. We formulate simplified models of DM with anomalous Z' mediators as consistent effective field theories with a cutoff Λ . We will show, in agreement with the results of [258], that this cutoff can be much heavier than the mass of the Z' and therefore the non-decoupling effects of the heavy spectators can be efficiently captured by the EFT, without explicitly considering these fermionic degrees of freedom. As expected, this EFT uniquely determines the couplings between the heavy Z' and the SM gauge bosons in which we are interested [262, 263].

Because we are considering an EFT, we will find that some of our amplitudes, including $\chi\chi \rightarrow VV$, where χ is the DM particle and V is a SM gauge boson, grow quadratically with energy. This should not be surprising, as the EFT necessarily contains higher dimensional operators, without which gauge invariance is lost. The growth of such amplitudes is tamed at the scale Λ , where the spectator fermions appear. Similar physics was considered also in Ref. [264], which appeared simultaneously with Ref. [2], with a focus on energies around the MeV scale.

In this Chapter we explicitly calculate the annihilation rates of the dark matter into SM gauge bosons and estimate the bounds associated with these rates. We choose as examples three anomalous Z' models, that illustrate some generic patterns. We emphasise that while the concrete bounds are always model dependent, the techniques that we illustrate here are completely generic and can be used in any EFT with an anomalous Z' mediator.

We find that for DM heavier than ~ 200 GeV, these higher dimensional operators dictate that DM annihilation at low velocities is dominated by final states involving gauge bosons. This results in considerable bounds from indirect detection experiments. At larger velocities, such as at DM freeze-out, p -wave annihilation into fermions overcomes these operators, which are loop suppressed, and so the DM relic abundance calculation is mostly unaffected by the requirement of anomaly cancellation. We also compare our new indirect detection constraints with direct detection and collider limits. We find that for heavy DM, γ ray and neutrino telescopes (depending on the concrete model) provide the strongest bounds on anomalous Z' simplified DM models.

The remainder of this chapter is organised as follows. In Section 3.2, we describe the effect of integrating out heavy fermions in a consistent theory, yielding an EFT with apparent anomalies at low energy scales. We focus on the induced loop level operators corresponding to these anomalies, and show that the maximum EFT cutoff can be significantly larger than the Z' mass. Then in Section 3.3 we specialise to the case of simplified models of DM and motivate a selection of toy models which serve to illustrate the effects of the higher dimensional operators on physical observables. Section 3.4 contains the experimental bounds on these simplified models, paying particular attention to the impact of loop-induced DM annihilation to gauge bosons on indirect detection constraints. We briefly discuss some limitations of our analysis in Section 3.5, including the assumption that the spectator fermions are heavy. Section 3.6 contains our conclusions. Most analytical results of our calculations are contained in the final appendices. Appendix 3.A contains a derivation of the Ward identities for the SM gauge bosons, accounting for the spontaneous breaking and the non-Abelian nature of the SM gauge group. Appendix 3.B collects the results for the effective vertices with the Z' and the SM gauge bosons.

3.2 Low-Energy Effective Theory

In this section we will review the construction of an EFT for a new gauge group which appears to be anomalous at low energies. New couplings need to be introduced to restore the gauge invariance of the full theory. We will also see how the couplings between the exotic and SM gauge bosons should be calculated, from anomaly considerations. We will closely follow the original work by Preskill [258] (as well as slightly more detailed handwritten notes [265]). We also borrow some results from more recent works [266, 267] that made practical use of these results in a slightly different context of MSSM augmented with anomalous Z' s.

The EFTs that we are describing here can be thought of as descending from a fully gauge invariant theory with a spontaneously broken gauge symmetry, after some heavy fermions have been integrated out. Given that these fermions are chiral and get masses from gauge symmetry breaking, like the fermions in the SM, the theory below the scale of the heavy fermions appears to be anomalous. In fact, this is exactly what happens in the SM if we integrate out the heaviest fermion of the SM, the top quark [268, 269]. Although the full SM is perfectly anomaly free, as one would expect from a consistent gauge invariant theory, integrating out the top leaves both the hypercharge and the $SU(2)_L$ symmetries anomalous, as well as giving rise to a $SU(2)_L \times U(1)_Y$ mixed anomaly. We will return back to the example of the SM in Sec. 3.5 and

Fig. 3.13, where we use it as a concrete example to discuss the limit of validity of this effective description.

The basic procedure of cancelling the anomalies in this low energy EFT comes at the price of introducing non-renormalizability. To see this in a working example, we first consider the simplest possible case of a $U(1)'$ anomalous Abelian theory in Sec. 3.2.1, and we move in Sec. 3.2.2 to the phenomenologically relevant case of mixed anomalies in a $SU(N) \times U(1)'$ gauge theory.

3.2.1 Anomalous $U(1)'$ gauge theory

We first consider an anomalous $U(1)'$ theory, where the triangle diagrams with fermion loops (similar to the ones in Fig. 3.2, with three Z' bosons on the external legs) are non-vanishing. Since the theory is anomalous, gauge invariance is lost and the effective action Γ under a $U(1)'$ gauge transformation $Z'_\mu \rightarrow Z'_\mu + \partial_\mu \omega / g'$ has the following variation:

$$\delta_\omega \Gamma = \frac{g'^2}{48\pi^2} \left(\sum_i Q_i^3 \right) \int d^4x \omega Z'^{\mu\nu} \tilde{Z}'_{\mu\nu}, \quad (3.1)$$

where $Z'^{\mu\nu}$ is the field strength associated with Z' and $\tilde{Z}'_{\mu\nu} = \frac{1}{2} \epsilon_{\mu\nu\rho\sigma} Z'^{\rho\sigma}$ is its dual tensor. Here g' stands for the “gauge” coupling of the $U(1)'$ and the sum runs over all the fermions that are charged under the $U(1)'$. This transformation simply manifests the fact that in an anomalous theory the gauge invariance is lost.

In our example, the $U(1)'$ gauge invariance can be easily restored by introducing a scalar a that transforms under a gauge transformation as $a \rightarrow a + v \omega$, where v stands for the scale of the $U(1)'$ breaking, or, equivalently $v \equiv m_{Z'} / g'$. Then, the transformation (3.1) can be restored by introducing the following term:

$$\mathcal{L} = -\frac{g'^2}{48\pi^2} \left(\sum_i Q_i^3 \right) \frac{a}{v} Z'^{\mu\nu} \tilde{Z}'_{\mu\nu}. \quad (3.2)$$

Even though (3.2) appears to cancel the anomaly with a new degree of freedom a , this term is just a Wess-Zumino counterterm that we have added to the action and a is not a genuine degree of freedom. First, it is worth noticing that in spite of the form of Lagrangian term (3.2), the total Lagrangian is *independent* of the field a and depends only on its derivative $\partial_\mu a$. This becomes manifest if we perform a rotation on the fermions $\psi_i \rightarrow e^{-iQ_i a / v} \psi_i$.¹ While such a rotation eliminates the term (3.2), the path integral measure transforms non-trivially under this rotation (as shown by Fujikawa [270]), inducing a term in the effective action that looks like $\sim (\partial_\mu a) \psi^\dagger \bar{\sigma}^\mu \psi$.

The kinetic term of the field a , which should also be gauge invariant, is of the form

$$\mathcal{L} = \frac{1}{2} \left(\partial_\mu a - g' v Z'_\mu \right)^2 \quad (3.3)$$

Even if we start from a theory that does not have this term, it is induced radiatively by the diagrams in Fig. 3.1.

This Lagrangian is nothing but a $U(1)$ theory that has been higgsed via a Stückelberg mechanism. In the unitary gauge the scalar degree of freedom a can be set (locally) to zero at any

¹Here we use the two-component notation for fermions. In four-component notation, $\Psi_i \rightarrow e^{iQ_i a \gamma_5 / v} \Psi_i$ and the variation of the action is proportional to the axial vector current, $\delta\Gamma \sim (\partial_\mu a) (\bar{\Psi}_i \gamma^\mu \gamma_5 \Psi_i)$.

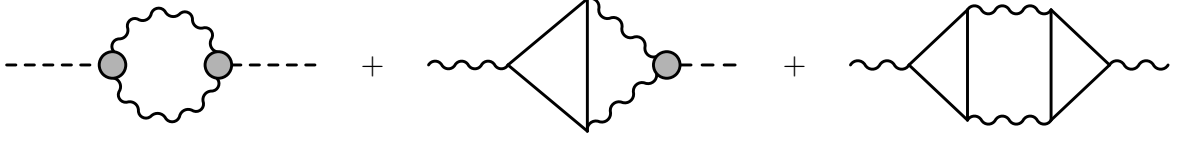


Figure 3.1: Kinetic term for the field a and the mass term for the Z' gauge boson induced by the radiative corrections in the $U(1)$ anomalous theory. Note that each blob corresponds to the couplings (3.2) and is therefore naturally of the size of the fermionic triangle loop.

point in space, leaving us simply with an effective theory of the massive gauge bosons with anomalous fermionic field content.

Of course, our effective theory cannot be extrapolated to infinitely high energies, and the calculability requirement sets the cutoff of the theory. In any non-unitary gauge, the presence of the cutoff is evident from the term (3.2) of mass dimension 5 in the Lagrangian, while in the unitary gauge we can see it from the bad UV behavior of the two-point function of the Z' (Fig. 3.1). In order to estimate the cutoff of the effective theory, we should remember that loop effects, similar to those that produce the term (3.3) (see Fig. 3.1), will also produce terms that look like

$$\sim \frac{1}{(4\pi v)^{p-2}} \frac{1}{v^{p-2}} \left(\partial_\mu a - g' v Z'_\mu \right)^p \quad (3.4)$$

for every power $p \geq 2$. In order to have a consistent EFT, each order in the perturbative expansion (3.4) should be smaller than its predecessor such that the expansion is valid.² Taking this requirement into account (see [258] for the details of this derivation) one finds the following cutoff estimation of the EFT:

$$\Lambda \sim \frac{64\pi^3 m_{Z'}}{g'^3 |\sum_i Q_i^3|}. \quad (3.5)$$

3.2.2 Mixed anomalies in a $SU(N) \times U(1)'$ gauge theory

Now we extend this logic to models with more complicated gauge symmetries and mixed anomalies between the $U(1)'$ and non-Abelian gauge groups. This is exactly the situation in which we are interested, where the anomalous Z' couples to the DM, and the mixed anomaly will eventually determine the strength of its interaction with the SM gauge bosons.

The treatment of the mixed anomalies will follow a similar logic to one we used in the previous Section. Let us consider the case of a mixed anomaly $SU(N)^2 \times U(1)'$

$$\sum_i \text{tr}(t^a t^b Q_i) = \mathcal{A} \delta^{ab} \quad (3.6)$$

where t^a are the generators of $SU(N)$, and $a, b = 1, \dots, N^2 - 1$. The matrix element between the Z' and the $SU(N)$ gauge bosons $G_\mu \equiv G_\mu^a t^a$ is nominally divergent, signalling that the theory is non-renormalisable, because there is no tree level coupling between the Z' and the $SU(N)$ gauge bosons.

In this case the form of the anomalous transformation is slightly less straightforward to derive. However, it can be obtained by invoking the Wess-Zumino consistency condition [271]. Under $U(1)'$ and $SU(N)$ transformations with transformation parameters ω_1 and $\omega_N \equiv \sum_a \omega_N^a t^a$,

²While we will hereafter dub this expansion as a “loop expansion”, it is important to keep in mind that the couplings from Eq. (3.2) and the fermion loop are of the same order of magnitude.

respectively, the action transforms as:

$$\delta_{\omega_1} \Gamma = C_1 \frac{g_N^2}{8\pi^2} \mathcal{A} \int d^4x \omega_1 \text{tr} \left(G^{\mu\nu} \tilde{G}_{\mu\nu} \right) \quad (3.7)$$

$$\delta_{\omega_N} \Gamma = C_N \frac{g_1 g_N}{4\pi^2} \mathcal{A} \int d^4x \tilde{Z}'^{\mu\nu} \text{tr} \left(\omega_N \partial_\mu G_\nu \right) \quad (3.8)$$

Note that we have only kept the components of the transformations that correspond to the mixed anomaly, and their sum is fixed by the Wess-Zumino consistency condition to be $C_1 + C_N = 1$. In particular, the presence of the mixed anomaly means that we cannot simultaneously have $SU(N) \times U(1)'$ gauge invariance, since either C_1 or C_N must be non-zero. Conversely, the orthogonal combination $C_1 - C_N$ is unconstrained. This combination depends on the counterterms that we introduce in the effective action, analogous to the Wess-Zumino term of Eq. (3.2). In the $SU(N) \times U(1)'$ model we are considering, the full Lagrangian after the introduction of the Stückelberg field a and the relevant counterterms reads³

$$\mathcal{L} = \frac{1}{2} \left(\partial_\mu a - m_{Z'} Z'_\mu \right)^2 \quad (3.9a)$$

$$- \frac{1}{2} b^{Z'Z'Z'} a Z'_{\mu\nu} \tilde{Z}'^{\mu\nu} - \frac{1}{2} b^{Z'GG} a G_{\mu\nu}^a \tilde{G}^{a\mu\nu} \quad (3.9b)$$

$$+ d^{Z'GG} Z'_\mu G_\nu^a \tilde{G}^{a\mu\nu} . \quad (3.9c)$$

The first term in (3.9a) is the same anomaly-induced mass term for the Z' that we have seen in Eq. (3.3). The Wess-Zumino terms of (3.9b) restore the $U(1)'$ gauge invariance in the Lagrangian. Their coefficients b^{ABC} are physical and are proportional to the mixed anomaly \mathcal{A}^{ABC} ,

$$b^{ABC} \sim \frac{1}{m_{Z'}} \mathcal{A}^{ABC} , \quad (3.10)$$

$$\mathcal{A}^{ABC} = \sum_f \left(Q_{f_L}^A Q_{f_L}^B Q_{f_L}^C - Q_{f_R}^A Q_{f_R}^B Q_{f_R}^C \right) . \quad (3.11)$$

The last line in (3.9c) contains the generalised Chern-Simons couplings: these terms are unphysical and they are not gauge invariant neither under $U(1)'$ nor $SU(N)$. They are a local counterterm which allows to cancel the variation of the action for a $SU(N)$ or a $U(1)'$ transformation, so they parametrise how we distribute the mixed anomaly.

The coefficients C_1, C_N in Eqs. (3.7-3.8) can be modified by adjusting the coefficients of the Wess-Zumino terms in Eq. (3.9b) and of the generalised Chern-Simons couplings in Eq. (3.9c). In an arbitrary $SU(N) \times U(1)'$ gauge theory, there is no *a priori* motivation to choose particular values of C_1 and C_N , which can be used, in particular, to insist that the anomaly preserves either $U(1)'$ or $SU(N)$ gauge invariance. However, in the SM augmented with the anomalous Z' the situation is different. While we expect that at the scale Λ , or below, the spectator fermions restore the full gauge invariance, we should also insist that even below the spectator fermion scale the SM electroweak gauge group is exactly gauge invariant. Otherwise, the anomaly would affect the electroweak gauge group. This requirement will set for us the coefficient in front of the generalised Chern-Simons counterterm and consequently the value of the combination $C_1 - C_N$. Indeed, using the freedom to set $C_1 - C_N$ we can always choose the

³If we were dealing with a $U(1) \times U(1)'$ symmetry, we would also get analogous terms which are relevant for the $U(1) \times U(1)'^2$ anomaly: a Wess-Zumino term $-\frac{1}{2} b^{Z'Z'B} a Z'_{\mu\nu} \tilde{B}^{\mu\nu}$ and a generalised Chern-Simons term $d^{Z'Z'B} Z'_\mu B_\nu \tilde{Z}'^{\mu\nu}$.

counterterm such that either $C_1 = 0$, namely require the $U(1)$ gauge invariance, or $C_N = 0$, which would mean that the $SU(N)$ is gauge invariant. In the SM with the Z' , we require that the gauge transformations of the $SU(2)_L \times U(1)_Y$ vanish, but *not* of the $U(1)'$.

This requirement of gauge invariance under the electroweak group is crucial for the calculation. It further removes any ambiguities in the calculation of the Z' vertex with a pair of SM gauge bosons. We now outline this calculation. For illustrative purposes we will assume for the moment an unbroken electroweak symmetry with massless fermions.

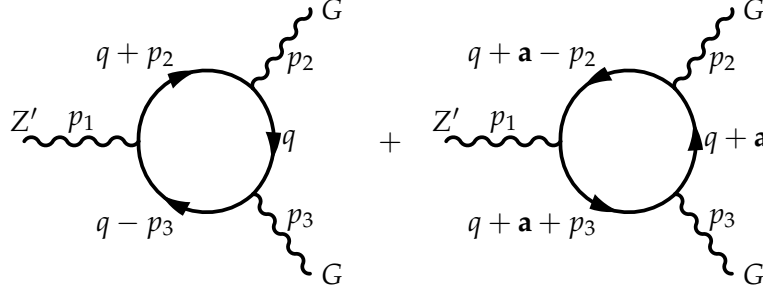


Figure 3.2: Diagrams relevant for the $Z'GG$ vertex function calculation. The integration variable q of one diagram can be shifted with respect to the other by an arbitrary momentum a .

The calculation of the $Z'GG$ vertex function involves the calculation of the pair of diagrams shown in Fig. 3.2, where we understand the sum over all the fermions charged under the $U(1)'$ and the relevant SM gauge group. In an anomaly free theory one can always shift the integration momentum of one diagram with respect to the other by an arbitrary momentum a_μ , without changing the finite answer. This is no longer true in an anomalous theory. As we will immediately see the momentum shift a is *not arbitrary* in our setup, and in fact for a given generalised Chern-Simons counterterm it is completely determined by the required gauge invariance of the EW group. Choosing a value for the d^{ABC} coefficients in Eq. (3.9c) is completely equivalent to a shift in the integration variable $q^\mu \rightarrow q^\mu + a^\mu$.

Our objective is to make sure that only the gauge transformation of the effective action with respect to the $U(1)'$ does not vanish, which is equivalent to the requirement that the Ward (Slavnov-Taylor) identities for the EW gauge group hold. Namely, in the case of unbroken $SU(2)_L \times U(1)_Y$ we get

$$p_\mu \Gamma_{3\text{-point}}^{\mu\nu\rho} = 0 \quad (3.12)$$

where p_μ is the momentum of the SM gauge boson, which would correspond to p_2 and p_3 in Fig. 3.2.

When we are dealing with the mixed anomaly, the expression that one gets in (3.12) is a_μ -dependent. Because the anomalies do not cancel out, each separate term of $\Gamma_{3\text{-point}}^{\mu\nu\rho}$ is nominally linearly divergent. Therefore, because of the freedom to shift the integration momentum by a_μ , we expect the Ward identity to take the form

$$p_\mu \Gamma_{3\text{-point}}^{\mu\nu\rho} \sim \int d^4q \left[f^{\mu\nu\rho}(q_\sigma + a'_\sigma) - f^{\mu\nu\rho}(q_\sigma) \right], \quad (3.13)$$

with the leading term of $f^{\mu\nu\rho}$ in q causing the linear divergence of the integral. The shift momentum a' is a linear combination of a and the external momenta. After expanding the first term we find that the result does not vanish, and reduces to a surface term (see [265] and [267, App. D.1] for further details)

$$2i\pi^2 a'^{\sigma} \lim_{q^2 \rightarrow \infty} q^2 q_\sigma f^{\mu\nu\rho}(q), \quad (3.14)$$

which is finite and a -dependent. There is no choice of a_μ to set the Ward identities in Eq. (3.13) to zero simultaneously for all three incoming momenta p_i in Fig. 3.2. However, there is *always* a choice of a_μ that preserves the Ward identities of the electroweak gauge group. This is exactly the choice we will proceed with.

It is also worth noting that there is in fact a one-to-one correspondence between the generalised Chern-Simons counterterm (and, consequently $C_1 - C_N$ combination in Eqs. (3.7) and (3.8)) and the momentum shift a that we are required to choose. If we choose the counterterm such that C_N vanishes, and consequently, the effective action is invariant under the $SU(N)$ transformation (that we identify with the EW group transformation), we will not need any momentum shift between the two diagrams to restore gauge invariance. This is because the counterterm is imposing EW gauge invariance already. On the other hand, if we are not enforcing gauge invariance at the Lagrangian level with an appropriate generalised Chern-Simons counterterm, we are obliged to do it by choosing a non-trivial momentum shift, so that eventually all the three (and higher) point functions of the theory are well defined. In all of our further calculations we will set the counterterm to zero and calculate the necessary momentum shift to restore gauge invariance.

Finally, in the SM the electroweak symmetry is broken and we consider the effects of the breaking, including fermion masses and the contributions from the Nambu-Goldstone bosons of $SU(2)_L \times U(1)_Y$, in our explicit calculation in Sec. 3.4. In principle, we use exactly the same procedure that we have described before, except that when calculating the Ward identities, we have to include the contribution of the Goldstone boson and possible contributions due to the non-Abelian nature of $SU(2)_L$. We derive in Appendix 3.A the appropriate Ward (Slavnov-Taylor) identities for the SM gauge bosons. In any case, eventually the spontaneous electroweak symmetry breaking is a minor effect that does not change the picture conceptually.

3.3 Dark Matter Models with Heavy Anomalous Z'

In this section we describe in more detail the dark matter models with Z' mediated interactions that we will consider. As we outline these models, we will make no requirement that the low-energy fermion content of our theory cancels all the gauge anomalies. This is a common step in the DM literature, which typically assumes that extra fermions, resolving anomaly cancellation, appear at high scales. Below the mass scale of these fermions we get an effective field theory similar to the one that we have formulated in the previous section.

We begin with a SM singlet Majorana fermion χ that couples axially to the gauge boson Z' of some new $U(1)'$ symmetry. The choice of this setup is mostly motivated by the null results of DM direct detection experiments. The vectorial couplings of the Majorana fermion to the Z' are naturally precluded and therefore the scattering in the direct detection experiments is either spin-dependent or velocity-suppressed at tree level. The spin and velocity independent interactions are often negligible. Because the DM is not charged under the SM gauge groups, it has no impact on the mixed anomalies, in which we are mostly going to be interested in order to calculate the DM annihilations into SM particles.

While Majorana particles, being real fields, cannot be charged under an *exact* Abelian group, they can couple to the gauge boson if the gauge group is broken. In the latter case the fermions get their masses via the Higgs mechanism (e.g. via couplings like $\sim \Phi \bar{\psi} \psi$), or, in the case of vector-like fermions, as a result of mixing with other singlet fermions. Because of the possible mixing effects, the coupling of Z' to DM does not need be equal to the coupling to the SM.

In general, the $U(1)'$ will be anomalous without the introduction of additional fermions besides χ . Indeed, gauging any flavor-universal symmetry other than $B - L$, Y -sequential or

linear combination thereof, leads to mixed anomalies between the gauge groups of the SM and the new $U(1)'$. These must be resolved by new fermions with non-trivial SM charge. Here we do not try to build a full UV-complete model (for explicit attempts to do this see e.g. [251, 255]), as for our purposes the only relevant quantities are the anomaly coefficients in the EFT that solely include the SM, χ , and Z' . At sufficiently high energies, above the cutoff Λ (see Sec. 3.2), all gauge anomalies must cancel.

As we are interested in the effects of anomalies, it is interesting to consider explicit models and discern the phenomenological importance of the effects of the Z' couplings to the gauge bosons. The first model we will be concerned with is one where the SM fermions are axially charged under $U(1)'$. In choosing this particular case we are mostly motivated by the vast existing literature on DM simplified models, that usually assumes a $U(1)'$ with pure axial charges as a standard benchmark point [213, 231, 250]. This choice however comes with its own obvious shortcoming, that eventually renders it somewhat non-generic compared to the landscape of other options.

For a SM fermion f the usual SM Yukawa coupling $y_f H \bar{f} f$ is gauge invariant only if the Higgs doublet also has dark charge [272]. If H is charged under $U(1)'$, in turn, then the Z' acquires at least some mass from electroweak symmetry breaking and mixes with the Z . This Z - Z' mixing is constrained by electroweak precision, and even though it can be viable if the Z' mass is heavier than a few TeV [8], we prefer to avoid these complications, which would defocus us from the goal of showing the phenomenological impact of anomaly-induced interactions. If we assume that the SM Higgs is not charged under the $U(1)'$, the only option is to promote the Yukawa couplings to $U(1)'$ spurions, by writing the Yukawa terms as

$$\left(\frac{\langle\Phi\rangle}{M_*}\right)^{2n} \tilde{y}_f H \bar{f} f, \quad (3.15)$$

where $\langle\Phi\rangle$ is the vacuum expectation value of a field Φ that spontaneously breaks $U(1)'$, M_* is some suppression scale dictated by the UV completion, and n is the ratio of the fermion axial $U(1)'$ charge to the Φ charge. In this framework, the natural size of the Yukawa couplings is driven by the size of $\langle\Phi\rangle/M_*$. Although this approach is generally consistent with the smallness of the SM Yukawas, it becomes difficult to reproduce the top Yukawa coupling in this way. To “fix” this problem we assume that the top quark couples *vectorially* to the Z' . The other fermions are taken to have axial couplings, except for the neutrinos which necessarily have purely left-handed couplings. We will further call this particular symmetry $U(1)_{\text{ax}}^{\prime c_V}$.

As with the scalar that could be responsible for a DM Majorana mass term, the particular characteristics of the scalars that generate SM fermion Yukawas are not relevant to the interactions at hand. For our purposes, the only other effect of the scalars which acquire $U(1)'$ -breaking vacuum expectation values is to provide mass to the Z' .⁴ We simply parametrise these effects by a mass term $\frac{1}{2}m_{Z'}^2(Z')^2$, and generally ignore the details of the scalar sector from here on.⁵

In order to summarise these considerations and to fix our notation, we show here the newly added terms to the Lagrangian:

$$\mathcal{L}_{\text{DM}} = -\frac{1}{4}Z'_{\mu\nu}Z'^{\mu\nu} + \frac{1}{2}m_{Z'}^2 Z'^2 + \frac{1}{2}\bar{\chi}(i\partial - m_\chi)\chi +$$

⁴For more comments on the possible relevant effects of the $U(1)'$ -breaking Higgs see [247].

⁵As we have mentioned, another possibility to deal with the fermion masses problem would be to charge the SM Higgs under the $U(1)'$ and deal with the $Z - Z'$ mixing similarly to [8]. See also [273] for some important insights on this framework.

$$+ \frac{1}{2} g_\chi Z'^\mu \bar{\chi} \gamma_\mu \gamma_5 \chi + g_{Z'} Z'_\mu \sum_f \bar{f} \left(g_V^f \gamma^\mu + g_A^f \gamma^\mu \gamma_5 \right) f, \quad (3.16)$$

where the coupling of the Z' to the SM fermions f is given by $g_{Z'}$ times the charges g_V^f and g_A^f , which are given in Table 3.1, and g_χ is the coupling to the Majorana DM χ .

The predictions of this “modified axial model” $U(1)'_{\text{ax}^V}$ are not generic. If we do not link the solution of the flavour problem with the DM theory (which is possible but by not necessary) by assuming that the Yukawa couplings are spurions for the $U(1)'$, and we insist that the SM Higgs is uncharged under the new force, the charges of the SM fermions must be vector-like under $U(1)'$. This implies that the mixed anomalies with the $U(1)_{\text{EM}}$ and $SU(3)_c$ must vanish. At sufficiently large DM masses this strongly suppresses the $\gamma\gamma$ and gg annihilation channels of the DM, but does not qualitatively change other channels. As an example of this model we choose $U(1)'_{B+L}$, which is simply one representative point in a large class of models.

Finally we choose to also show a leptophilic model (for this purpose, $U(1)'_L$). This choice is special because we have no constraints from the LHC and direct detection, and all the constraints come from indirect detection searches.⁶

	$SU(3)_c$	$SU(2)_L$	$U(1)_Y$	$U(1)_{B-L}$	$U(1)'_{\text{ax}^V}$	$U(1)'_{B+L}$	$U(1)'_L$
$\begin{pmatrix} \nu_L^e \\ e_L \end{pmatrix}, \begin{pmatrix} \nu_L^\mu \\ \mu_L \end{pmatrix}, \begin{pmatrix} \nu_L^\tau \\ \tau_L \end{pmatrix}$	1	2	$-\frac{1}{2}$	-1	-1	$+1$	$+1$
$(e_R)^C, (\mu_R)^C, (\tau_R)^C$	1	1	1	$+1$	-1	-1	-1
$\begin{pmatrix} u_L \\ d_L \end{pmatrix}, \begin{pmatrix} c_L \\ s_L \end{pmatrix}$	3	2	$\frac{1}{6}$	$+\frac{1}{3}$	-1	$+\frac{1}{3}$	0
$(u_R)^C, (c_R)^C$	$\bar{\mathbf{3}}$	1	$-\frac{2}{3}$	$-\frac{1}{3}$	-1	$-\frac{1}{3}$	0
$(d_R)^C, (s_R)^C$	$\bar{\mathbf{3}}$	1	$\frac{1}{3}$	$-\frac{1}{3}$	-1	$-\frac{1}{3}$	0
$\begin{pmatrix} t_L \\ b_L \end{pmatrix}$	3	2	$\frac{1}{6}$	$+\frac{1}{3}$	-1	$+\frac{1}{3}$	0
$(t_R)^C$	$\bar{\mathbf{3}}$	1	$-\frac{2}{3}$	$-\frac{1}{3}$	$+1$	$-\frac{1}{3}$	0
$(b_R)^C$	$\bar{\mathbf{3}}$	1	$\frac{1}{3}$	$-\frac{1}{3}$	-1	$-\frac{1}{3}$	0
Higgs Φ	1	2	$\frac{1}{2}$	0	0	0	0

Table 3.1: Charges of the SM matter content under some choices of $U(1)'$ that we further analyse in this Chapter.

Taking all this into account we present the charges of the SM fields under the new $U(1)'$ s in Table 3.1. For comparison, we also show $B - L$, which is anomaly free and does not require any extra terms in the effective action.

Since our axial vector model features flavour non-universal Z' quark couplings, we parenthetically consider here the flavour constraints on this kind of Z' . Even though the axial- Z' couplings are diagonal in the flavour basis, the quark rotations that diagonalise the Yukawa

⁶Strictly speaking, this model is not totally invisible to direct detection experiments due to radiative couplings to the hadrons (for works along these lines see [274]). However the effect is expected to be so small that we disregard it here.

matrix generally induce off-diagonal couplings between quark mass eigenstates [10]. To estimate the size of the associated flavour-changing neutral currents (FCNCs), we must make assumptions about the structure of the quark rotations. Note that the only measured misalignment between the quark flavour and mass eigenstates is from the CKM matrix V_{CKM} , which is a combination of the two left-handed quark rotations. Conversely, the $U(1)_{\text{ax}'}^{c_V}$ model only contains non-universality in the right-handed up-quark sector. Of course, if the mixing angles in the RH sectors are completely anarchical, the structure that we discuss is not viable. However, this is not the only option, especially if we take into account the hierarchical structure of V_{CKM} . First, FCNCs may be completely avoided if the right-handed quark flavour and mass eigenstates are identical (this would invoke either a fine-tuning or some other structure that would explain the vanishing rotation angles).

Alternatively, let us assume that the flavour structures of the RH and LH quark sectors are similar, such that the product of the rotations between the up- and down-type RH quark $U(1)'$ flavour and mass eigenstates is $\sim V_{\text{CKM}}$. Then, since the non-universality is only in the third generation, the $Z'\bar{c}_R u_R$ coupling will go as $\sim V_{\text{CKM}}^{ub*} V_{\text{CKM}}^{cb}$, which is quite small, without dangerous consequences for D mixing. Non-universal couplings in the down-type sector are also induced at the loop level, leading to effects such as $B - \bar{B}$ mixing.

Finally we note that a kinetic mixing term $B_{\mu\nu} F'^{\mu\nu}$, where B and F are the $U(1)_Y$ and $U(1)'$ field strengths respectively, is fully allowed by the symmetries of the theory. Sizable kinetic mixing can lead to observable effects that are interesting but separate from those caused by the triple gauge vertices induced by anomalies. We henceforth assume negligible mixing, and concentrate on the anomalous couplings among the SM and $U(1)'$ gauge bosons.

3.4 Application to Dark Matter Models

In this section we present the main results of this Chapter. First, we will use the results of Sec. 3.2 to explicitly calculate the annihilation cross sections of DM particles into SM gauge bosons. In the following subsections we show the prospects for the direct and indirect detection, as well as LHC searches. We will emphasise the complementarity of these searches to properly analyse the possible parameter space of these models.

3.4.1 Annihilation cross sections into the SM gauge bosons

The objective in this Section is to explicitly calculate these relevant annihilation cross sections that arise at the one-loop level. To begin, we outline the calculation of the coupling between three gauge bosons induced by anomalies, starting with the $Z'-\gamma-\gamma$ vertex. We take a single fermion f of electric charge Q_f^{em} to run in the loop diagrams of Fig. 3.2, whose amplitude we write as $\epsilon_\mu(p_1)\epsilon_\nu^*(p_2)\epsilon_\rho^*(p_3)\Gamma^{\mu\nu\rho}$. Note that we use p_1 for the Z' momentum, while the momenta p_2, p_3 stand for the photon momenta. If the fermion's $U(1)'$ coupling is vectorial, then by Furry's theorem the vertex vanishes. Without loss of generality we assume a $Z'f\bar{f}$ vertex with strength $ig_{Z'}\gamma^\mu(g_V^f + g_A^f\gamma^5)$ with the understanding that only g_A^f will contribute.⁷ As described in Sec. 3.2, contracting the external gauge boson momenta with the triangle amplitude gives non-vanishing results due to surface terms (see [265, 267] for further calculation details). The

⁷Note that this parametrization is completely generic and suitable for analyzing any anomalous Z' . If we turn back to the models we have outlined in Sec. 3.3, we see that in those particular models all the SM fermions have either $g_V = 0$ or $g_A = 0$, but this is not guaranteed for a generic Z' .

resulting Ward identities depend, as explained in Sec. 3.2, on the loop momentum shift a :

$$(p_1)_\mu \Gamma^{\mu\nu\rho} = \frac{g_{Z'} e^2 g_A^f (Q_f^{\text{em}})^2}{8\pi^2} \epsilon^{\nu\rho\alpha\beta} a_\alpha (p_1)_\beta \quad (3.17a)$$

$$(p_2)_\nu \Gamma^{\mu\nu\rho} = \frac{g_{Z'} e^2 g_A^f (Q_f^{\text{em}})^2}{8\pi^2} \epsilon^{\mu\rho\alpha\beta} (a + 2p_3)_\alpha (p_2)_\beta \quad (3.17b)$$

$$(p_3)_\rho \Gamma^{\mu\nu\rho} = \frac{g_{Z'} e^2 g_A^f (Q_f^{\text{em}})^2}{8\pi^2} \epsilon^{\mu\nu\alpha\beta} (a - 2p_2)_\alpha (p_3)_\beta \quad (3.17c)$$

At this stage we can either tune the (Wess-Zumino and) generalised Chern-Simons term of Eq. (3.9) to get rid of any a_μ dependence in these expressions or, alternatively, set the generalised Chern-Simons term to zero and find an appropriate momentum shift to maintain the necessary Ward identities. We choose the latter recipe to resolve this problem. We make the phenomenologically motivated choice of retaining $U(1)_{\text{EM}}$ gauge invariance, which corresponds to the requirement that Eqs. (3.17b) and (3.17c) vanish. This, in turn, may be accomplished by setting $a = 2(p_2 - p_3)$, yielding the Ward identities

$$(p_1)_\mu \Gamma^{\mu\nu\rho} = \frac{g_{Z'} e^2 g_A^f (Q_f^{\text{em}})^2}{2\pi^2} \epsilon^{\nu\rho\alpha\beta} (p_2)_\alpha (p_3)_\beta \quad (3.18)$$

$$(p_2)_\nu \Gamma^{\mu\nu\rho} = (p_3)_\rho \Gamma^{\mu\nu\rho} = 0$$

Next, to calculate the relevant cross section, we write the most general form of the amplitude using the standard Rosenberg parametrization [275]

$$\Gamma^{\mu\nu\rho} = \frac{g_{Z'} e^2 g_A^f (Q_f^{\text{em}})^2}{\pi^2} \left(I_1 \epsilon^{\alpha\nu\rho\mu} (p_2)_\alpha + I_2 \epsilon^{\alpha\nu\rho\mu} (p_3)_\alpha \right. \\ \left. + I_3 \epsilon^{\alpha\beta\nu\mu} (p_2)^\rho (p_2)_\alpha (p_3)_\beta + I_4 \epsilon^{\alpha\beta\nu\mu} (p_3)^\rho (p_2)_\alpha (p_3)_\beta \right. \\ \left. + I_5 \epsilon^{\alpha\beta\rho\mu} (p_2)^\nu (p_2)_\alpha (p_3)_\beta + I_6 \epsilon^{\alpha\beta\rho\mu} (p_3)^\nu (p_2)_\alpha (p_3)_\beta \right) \quad (3.19)$$

where $I_i, 1 \leq i \leq 6$ are form factors to be computed. By dimensional analysis, the effect of any divergences must be in I_1 and I_2 , while the remaining form factors are finite. We thus use the Ward identities of Eq. (3.18) to fix the divergent form factors, and calculate the others explicitly. The final result is [267]

$$\begin{aligned} I_1(p_2, p_3; m_f) &= (p_2 \cdot p_3) I_3(p_2, p_3; m_f) + p_3^2 I_4(p_2, p_3; m_f) \\ I_2(p_2, p_3; m_f) &= -I_1(p_3, p_2; m_f) \\ I_3(p_2, p_3; m_f) &= -C_{12}(p_3^2, p_1^2, p_2^2, m_f^2, m_f^2, m_f^2) \\ I_4(p_2, p_3; m_f) &= C_{11}(p_3^2, p_1^2, p_2^2, m_f^2, m_f^2, m_f^2) + C_1(p_3^2, p_1^2, p_2^2, m_f^2, m_f^2, m_f^2) \\ I_5(p_2, p_3; m_f) &= -I_4(p_3, p_2; m_f) \\ I_6(p_2, p_3; m_f) &= -I_3(p_2, p_3; m_f) \end{aligned} \quad (3.20)$$

where the C functions are Passarino-Veltman loop functions [276]. When there are multiple fermions charged under both electromagnetism and $U(1)'$, Eq. (3.19) is readily generalised by summing over the available loop fermions.

The above vertex may now be used to calculate physical observables. For instance, the amplitude for DM annihilation to photons immediately follows, and the resulting cross section

takes a rather compact form⁸

$$\sigma(\chi\chi \rightarrow \gamma\gamma) = \frac{\alpha_{\text{em}}^2 g_\chi^2 g_{Z'}^4}{\pi^3} \frac{m_\chi^2 \sqrt{s}}{m_{Z'}^4 \sqrt{s - 4m_\chi^2}} \left| \sum_f c_A^f N_c^f (Q_f^{\text{em}})^2 \left[2m_f^2 C_0(0, 0, s, m_f^2, m_f^2, m_f^2) + 1 \right] \right|^2, \quad (3.22)$$

where the explicit form of the Passarino-Veltman function involved is

$$C_0(0, 0, s, m_f^2, m_f^2, m_f^2) = \frac{1}{2s} \log^2 \left(\frac{\sqrt{s(s - 4m_f^2)} + 2m_f^2 - s}{2m_f^2} \right). \quad (3.23)$$

The +1 term inside the squared brackets of the sum in Eq. (3.22) represents precisely the anomaly coefficient. If this is zero, then at high s the cross section goes roughly as $1/s^2$. If the anomaly coefficient is different from zero, then at high s the cross section is constant: this anomalous behaviour will be tamed of course at the cut-off scale of this effective description, where the heavy fermions restore the gauge invariance.

The result of Eq. (3.22) should be compared to the cross section for DM annihilation to fermions,

$$\begin{aligned} \sigma(\chi\chi \rightarrow f\bar{f}) = & \frac{g_\chi^2 g_{Z'}^4 N_c^f}{3\pi s ((s - m_{Z'}^2)^2 + \Gamma_{Z'}^2 m_{Z'}^2)} \sqrt{\frac{s - 4m_f^2}{s - 4m_\chi^2}} \left\{ g_V^{f2} (s - 4m_\chi^2)(s + 2m_f^2) \right. \\ & \left. + g_A^{f2} \left[s(s - 4m_\chi^2) + 4m_f^2 \left(m_\chi^2 \left(7 - 6 \frac{s}{m_{Z'}^2} + 3 \frac{s^2}{m_{Z'}^4} \right) - s \right) \right] \right\}. \quad (3.24) \end{aligned}$$

The key difference between these cross sections is that the annihilation to photons (if the anomaly coefficient is not vanishing) remains constant with increasing centre-of-mass energy, unlike the annihilation to fermions which eventually falls as $1/s$.

We calculate the form factors for the annihilations into the rest of the gauge bosons, using exactly the machinery that we have shown here. The starting point in order to guarantee the invariance under the SM gauge group is the imposition of the Ward identities, which we derive in Appendix 3.A. After having fixed the momentum shift, following the procedure sketched in Sec. 3.3, one can compute explicitly the diagrams, with the results collected in Appendix 3.B. For simplicity we take the Z' width to be $\Gamma_{Z'} = m_{Z'}/10$ throughout our calculations. This choice only affects the extent of the influence of resonant effects in our results.

Before we present the results, it is instructive to see how the annihilation cross sections σv scale with the kinetic energy of the fermions for fixed DM mass. We show this scaling within

⁸Notice that, in order to get the expression in Eq. (3.22) without spurious effects on the Z' resonance, one needs to properly apply the complex mass scheme to treat the cross sections. The replacement of the mass $m_{Z'}^2 \rightarrow m_{Z'}^2 - im_{Z'}\Gamma_{Z'}$ must be performed in all occurrences of $m_{Z'}^2$ at the amplitude level [277]. In particular, the Z' propagator (with a momentum p flowing along its virtual line) in the unitary gauge reads

$$\frac{-i}{p^2 - (m_{Z'}^2 - im_{Z'}\Gamma_{Z'})} \left(\eta^{\mu\nu} - \frac{p^\mu p^\nu}{(m_{Z'}^2 - im_{Z'}\Gamma_{Z'})} \right). \quad (3.21)$$

This ensures the needed cancellations to recover the expression of Eq. (3.22) with a contact interaction $Z'\gamma\gamma$ [278, 279]. The physical reason why there is no feature corresponding to the physical production of a Z' is that the Landau-Yang theorem [280, 281] forbids the decay of an on-shell massive vector boson into two identical massless vector bosons, due to Bose and Lorentz symmetry.

the EFT on Fig. 3.3 (we use for this illustration the $U(1)'_{\text{ax}}{}^{c_V^t}$ model). While the cross sections into the fermions fall at the high energies as $1/s$ (as one would expect), the annihilations into the gauge bosons stay constant as a function of s , signalling an inevitable breakdown of unitarity at high energies. This breakdown is expected from the way we have formulated our EFT in Sec. 3.2, in particular because of the higher dimensional interactions that we were forced to introduce. Of course these cross sections are tamed at the scale where the spectator fermions show up. This can in turn happen at or below the scale Λ as defined in Eq. (3.5) (modulo replacing the Abelian anomaly by a mixed one).

Note also that unitarity will often dominate the exact bound on the cutoff Λ , although it will often be of order (3.5). For example, a simple back-of-the-envelope estimation leads us to the conclusion that the unitarity of the model depicted on Fig. 3.3 will break down at a scale ~ 100 TeV. In this sense the very right side of this plot is not meaningful and the physics there should be described by a full UV complete theory rather than the EFT.

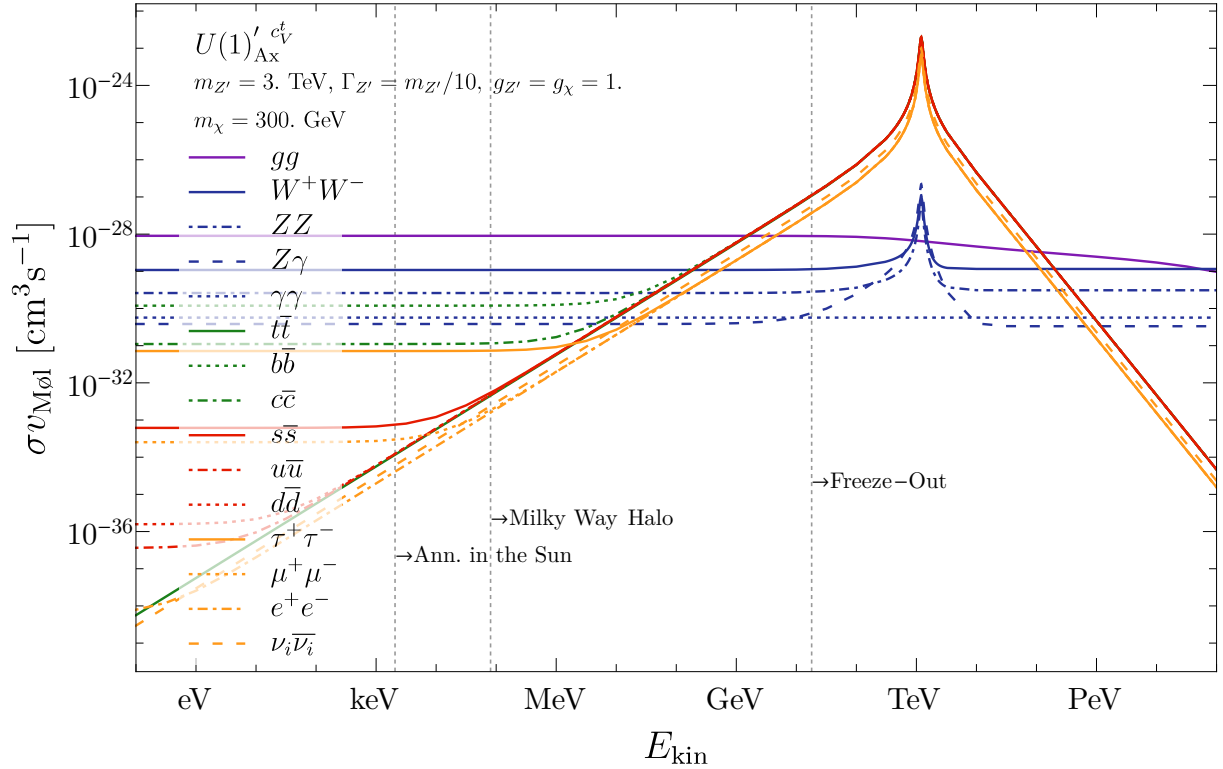


Figure 3.3: Annihilation cross sections in the $U(1)'_{\text{ax}}{}^{c_V^t}$ model as a function of the DM kinetic energy within the EFT that we describe. The blue curves indicate gauge boson final states that receive contributions from anomalies. Annihilations into heavy quarks, light quarks, and leptons are shown in green, red, and yellow, respectively. Kinetic energies corresponding to DM in the Sun, the Milky Way halo, and at freezeout are indicated. Note that above the scale ~ 100 TeV the EFT cannot give the correct solution due to the inevitable unitarity breakdown.

Note also the difference between the fermions that couple axially and ones that couple vectorially to the Z' . While annihilations into the former final states (in this particular example, all the SM fermions except the top) are constant at low energies, the latter in this range scale as v^2 , and therefore linearly with the kinetic energy. This can also be clearly observed in Eq. (3.24).

Another important lesson that we learn from Fig. 3.3 is the dominance of the various chan-

nels in different physical situations. For example, the velocity is still high enough during the thermal freeze-out to render the annihilation into the gauge bosons unimportant, such that the relic abundance is determined almost completely by the annihilations into the fermions. However at lower velocities (annihilation in the Galactic halo or at the centre of the Sun) the entire signal is essentially determined by the radiative annihilations into the gauge bosons.

Finally let us notice, that even in the models where the respective mixed anomaly vanishes, the annihilation channels into the gauge bosons are induced by finite radiative corrections. However, because these contributions do not grow with energy, they are much smaller than the anomaly-augmented annihilations, and can be neglected.

3.4.2 Relic abundance

We first briefly comment on the DM relic abundance, if we assume that the DM is the thermal relic (which might or might not be the case). WIMP freezeout typically happens near $x = m_\chi/T \approx 25$, with the particular decoupling temperature only logarithmically sensitive to the annihilation cross section. The annihilation channels which determine the relic abundance are thus the modes which dominate at a DM velocity of $\sqrt{3/x} \sim 1/3$. From Fig. 3.3, we see that DM annihilation to fermions is primarily responsible for setting the relic abundance. Consequently, the impact of anomalies in the DM relic density calculation is minimal. We thus expect the values of the couplings and masses that reproduce the observed DM abundance to be similar to previous calculations in the literature, see e.g. [282].

3.4.3 Indirect detection

Today very little kinetic energy is available for DM annihilation because the typical velocity of a DM particle in the Milky Way halo is $\sim 10^{-3}$. In our models the gauge boson modes can dominate the annihilations, and so the DM can be probed through searches for annihilation to $gg, W^+W^-, \gamma\gamma, Z\gamma$ and ZZ .

We illustrate this point in Fig. 3.4, where we show the cross sections for the various annihilation channels of DM in our galaxy as a function of the DM mass m_χ .⁹ If the DM is relatively light, $m_\chi \lesssim 10$ GeV, the BRs are dominated by the fermionic channels, particularly $b\bar{b}$. However at sufficiently high DM masses the gg (if the mixed anomaly of the $U(1)'$ with the SM does not vanish) and W^+W^- channels dominate the annihilations at such low DM velocities, and therefore the indirect detection signatures. We also point out the importance of the $\gamma\gamma$ (when present) and $Z\gamma$ annihilation channels. Although the latter channels are suppressed compared to the W^+W^- , the photon emission is monochromatic, leading to the prediction of a γ ray line.

3.4.3.1 Gamma ray continuum searches

We first consider limits from the continuum γ ray spectrum, where the strongest current bound comes from dSph Fermi-LAT observations [143, 283] and, for TeV scale DM masses, from HESS observation of the continuum emission from the Galactic Centre [284].

These bounds depend on the products of DM annihilation, as different SM particles yield distinct photon spectra. In order to apply the γ ray limits, we thus consider the annihilation branching ratios to different final states. At low DM mass, the fermionic annihilation channels are dominant, as seen in Fig. 3.4.

⁹The absence of enhancement in the gauge boson BRs on the Z' resonance is due to the Landau-Yang theorem, which implies a suppression factor $\sim m_V^2/m_{Z'}^2$, in the amplitude for an on-shell vector boson $V \sim W, Z$.

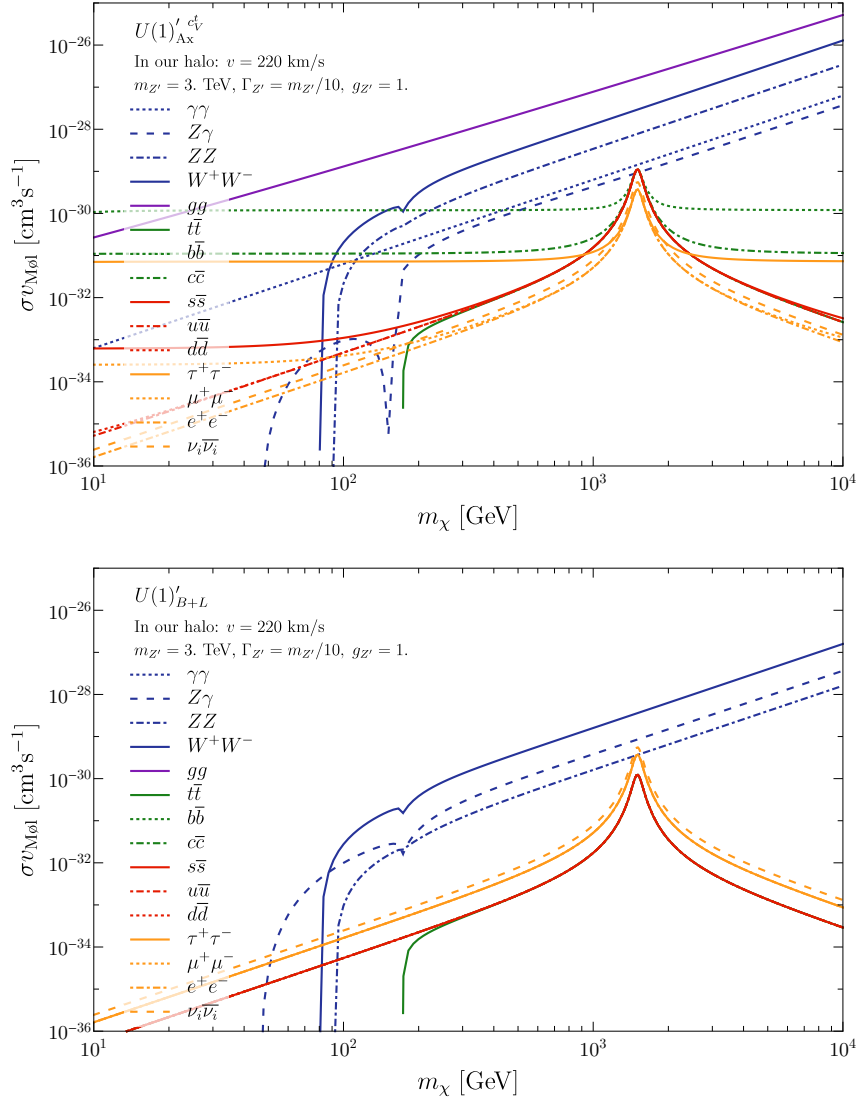


Figure 3.4: *Top:* Annihilation cross sections of DM into all the SM channels as a function of the DM mass m_χ in the $U(1)'_{Ax}$ model. The DM velocity is taken to be 220 km/s, characteristic of the Milky Way halo. The curves are coloured as in Fig. 3.3. *Bottom:* same for the $U(1)'_{B+L}$ model. The quark lines all overlap on the red line. The branching ratios of the $U(1)'_L$ model are analogous to the ones of $U(1)'_{B+L}$, without the quark channels.

We start by discussing the $U(1)'_{Ax}$ model, where all fermionic channels are chirally suppressed (except $t\bar{t}$, which is velocity suppressed), and the $b\bar{b}$ and $\tau^+\tau^-$ annihilations are more common than those into light fermions. In practice, the limits on annihilations to $b\bar{b}$ and $\tau^+\tau^-$ are quite close to one another [143]. Similarly, DM annihilations to charm quarks produce similar photon spectra as to up quarks [285], for which the limits are in turn close to those for annihilations to $b\bar{b}$. We thus choose to compare the total fermionic annihilation cross section to the Fermi-LAT limit on DM annihilating to bottom quarks for DM masses below approximately 200 GeV.

At larger DM masses, the gg , W^+W^- and ZZ channels take over. Again, since the resulting γ ray spectra from these annihilation modes are similar, we simply compare the total bosonic

annihilation cross section to the Fermi-LAT limit on DM annihilations to W^+W^- (which gives a slightly weaker bound than gg). Finally, in the resonance region $m_\chi \approx m_{Z'}/2$, fermionic annihilations take over again and we switch back to comparing the total annihilation cross section to the $b\bar{b}$ limit from Fermi-LAT once more. Throughout, we assume that χ makes up all of the observed DM.

In the $U(1)'_{B+L}$ and $U(1)'_L$ models the procedure is analogous, with the notable difference that the gg channel disappears. At low DM masses the annihilations to fermions, which now couple vectorially to the Z' , are velocity suppressed.

We show the bounds on the suppression scale $m_{Z'}/\sqrt{g_{Z'}g_\chi}$ in the three models as a function of the DM mass in Fig. 3.5. These bounds are insensitive to the choice of DM profile [143]. The bound on the $U(1)'_{ax}$ model is significantly stronger than those on the $B+L$ and L models because of the dominance of the gg annihilation channel, which is prolific in γ rays due to its secondary production of pions. As the mixed anomaly of the latter two $U(1)$ s with the colour group vanishes, the annihilations into gg in these models are much more modest.

The mediator mass by itself has little effect on the bounds except in the resonance region: what matters is the effective scale $m_{Z'}/\sqrt{g_{Z'}g_\chi}$. Note that if the DM is significantly heavier than the mediator mass, the coupling g_χ should be sufficiently small to avoid unitarity constraints on the DM self-scattering [247].

We show the HESS continuum Galactic Centre bounds in Fig. 3.5, assuming three different DM profiles (see Sec. 3.4.3.2 for more details). For each profile we compute the integrated J factor between 0.3° and 1° around the direction of the Galactic Centre using the tables from [285] and scale the HESS bound appropriately.

3.4.3.2 Gamma ray line searches

Given the potential for annihilation to $\gamma\gamma$ or $Z\gamma$ through anomalies, we now discuss the impact of γ ray line searches on our benchmark models, as performed by Fermi-LAT [286] and HESS [287]. Fermi-LAT is typically sensitive to photons below several hundred GeV in energy, while HESS, being a terrestrial telescope, has the best sensitivity for much more energetic γ rays.

The bounds from line searches generally depend on the DM halo profile, and so we will show their variation when different profiles are considered; for an overview of DM halo profiles see for instance Ref. [19]. Fermi-LAT optimises the signal region of interest to maximise the bound depending on the profile, for several different halo shape choices. For instance, the optimal bound is obtained for a region subtending 16° around the Galactic Centre for the Einasto profile, but 90° for an isothermal profile. HESS only shows limits for the Einasto profile, using a signal region of radius 1° . We choose to show bounds for Einasto, isothermal and Burkert DM halo profiles, by rescaling the Fermi-LAT and HESS limits using the ratios of J factors for different profiles over the signal regions of interest [285]. In the case of Fermi-LAT, we obtain the limit for a Burkert profile by rescaling the constraint for an isothermal profile, as these halo shapes are both relatively cored.

We further calculate the expected annihilation cross section to photons and compare with the Fermi-LAT and HESS γ ray line search bounds, computed as described above for different halo profiles. We notice that even if the $\gamma\gamma$ channel is absent (up to finite terms that we neglect here) because of the vanishing mixed anomaly with the $U(1)_{EM}$, as is the case for $U(1)'_{B+L}$ and $U(1)'_L$, the $Z\gamma$ channel can be present, because it is controlled by the mixed anomaly with the hypercharge. Most monochromatic photons come from DM annihilation to $\gamma\gamma$ when it is present, as the $Z\gamma$ mode is less common and provides half as many photons per annihilation.

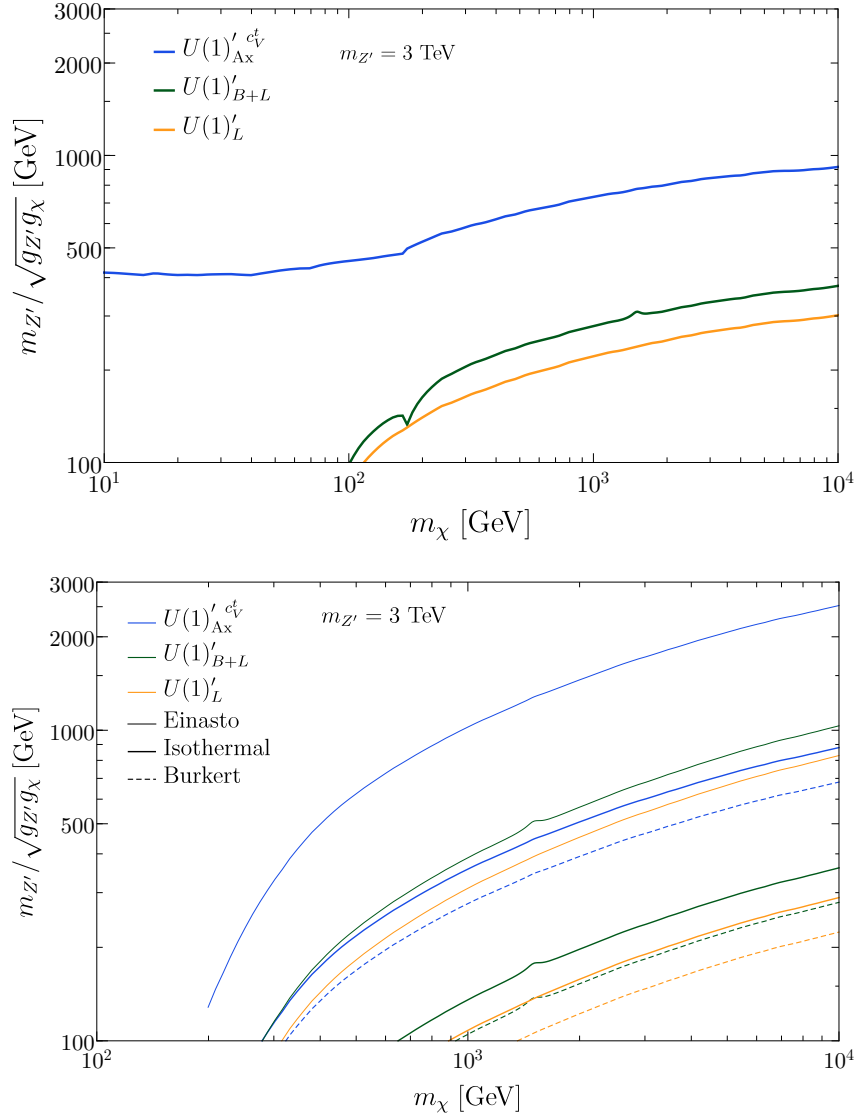


Figure 3.5: Limits from continuum γ ray emission on the three models we consider. *Top:* bounds from Fermi-LAT observations of dSphs [143, 283]. *Bottom:* bounds from HESS observation of the Galactic Centre [284], for three choices of the DM profile distribution.

In the $U(1)'_{ax} c_V^t$ we include the $Z\gamma$ channel above $m_\chi \gtrsim 140$ GeV, where the difference in energies between photons from $\gamma\gamma$ and $Z\gamma$ annihilations is expected to be below the resolution of Fermi-LAT; that of HESS is worse. For simplicity, below this threshold we ignore annihilations to $Z\gamma$, which should not significantly affect our final results due to the lower cross section for this channel.

The resulting constraints are presented in Fig. 3.6, and they illustrate the impact of the anomalies on indirect detection constraints. Conversely, anomaly-free models often do not face strong limits from γ ray line searches, due to suppressed annihilation cross sections to photons. In the two models $U(1)'_{B+L}$ and $U(1)'_L$, where only $Z\gamma$ contributes to the signal, the final bound is weaker, but still non-negligible for a DM mass of a few TeV. The limits are quite sensitive to the choice of halo profile, particularly for HESS which presents limits for a γ ray line search in a very narrow region around the Galactic Centre. As expected, the best limits are

obtained for the cuspy Einasto profile.

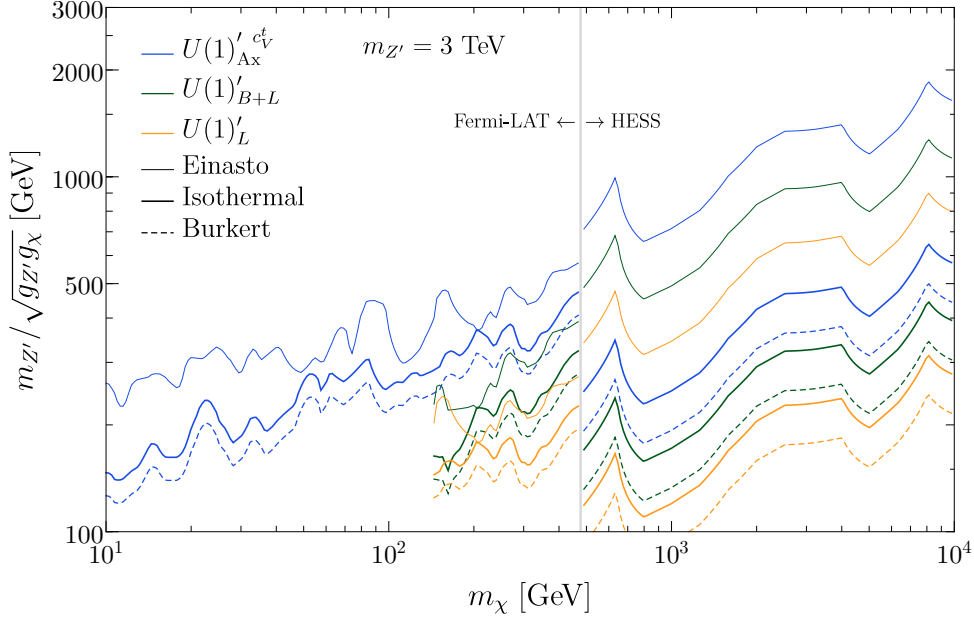


Figure 3.6: Limits from Fermi-LAT [286] and HESS [287] searches for γ ray lines. Below (above) DM masses of 500 GeV, Fermi-LAT (HESS) provides the constraint. The choice of mediator mass affects only the resonance region $m_\chi \approx m_{Z'}/2$.

3.4.3.3 Neutrino telescopes

We finally consider DM annihilation to neutrinos in the Sun, and the associated bounds from three years of observations of IceCube [288]. In particular, annihilations to W^+W^- , ZZ and $\tau^+\tau^-$ produce high-energy neutrinos which are tightly constrained, while annihilations to $b\bar{b}$ are less strongly limited because of the softer neutrino spectrum. To obtain the limit on the overall annihilation cross section, and hence on the scale of DM-SM interactions, we must convolve the various IceCube limits on different annihilation channels with the annihilation branching ratios in the model, as we did above for the continuum γ ray bounds.

For DM that is captured in the Sun, the typical kinetic energy is of the same order as the temperature at the centre of the Sun, $10^7 \text{ K} \sim \text{keV}$, which corresponds to negligible velocity for DM heavier than the MeV scale. This velocity is typically slightly smaller than the DM velocity in the Milky Way halo, and the annihilation cross sections are similar to those shown in Fig. 3.4.

The IceCube bounds on annihilations into $b\bar{b}$ are weaker than the bounds on annihilations into $\tau^+\tau^-$ by 2-3 orders of magnitude. Therefore at low DM mass $\tau^+\tau^-$ annihilations always provide the most constrained source of neutrinos, even in the $U(1)'_{ax} c_V^t$ model when bottom quarks are the main products of DM annihilation.

At higher masses, W^+W^- and ZZ annihilations face bounds from IceCube that are nearly as strong as $\tau^+\tau^-$ [288], and annihilations to $Z\gamma$ produce half as many neutrinos as ZZ . Thus we use the stronger of the bounds on annihilations to $\tau^+\tau^-$ and W^+W^- , ZZ , $Z\gamma$, scaling the IceCube limits by the appropriate branching ratios and assuming that the neutrino spectra for these channels are all similar to that for W^+W^- .

The translation of the IceCube bounds on the SD DM-proton scattering cross section σ_p^{SD}

to bounds on the EFT scale $m_{Z'}/\sqrt{g_{Z'}g_\chi}$ requires some care about the form factor assumed for DM capture in the Sun. When providing a bound on σ_p^{SD} , IceCube assumes that DM and the SM interact through the NR operator $\mathcal{O}_4^{\text{NR}}$ (according to the standard notation, see e. g. [73, 289]). This is indeed the operator that arises in the $U(1)'_{\text{ax}^c_V}$ model, but for the $U(1)'_{B+L}$ model, the leading interaction is the SI velocity-suppressed operator $\mathcal{O}_8^{\text{NR}}$. To convert between bounds on these operators, we use the capture form factors provided by [289]. In the leptophilic model $U(1)'_L$ the DM capture rate is negligible, given the small momentum exchange between DM and free electrons in the Sun, and the suppressed loop interaction with nucleons, so IceCube bounds do not apply.

The results are shown in Fig. 3.7. Because the IceCube bounds are sensitive to the branching ratios of DM annihilations rather than to the absolute annihilation cross sections, in the $U(1)'_{\text{ax}^c_V}$ model the bounds are weakened due to the large branching ratio into gluons, which yield a negligible neutrino spectrum. In the $U(1)'_{B+L}$ model, while there are no annihilations into gluons, the velocity-suppressed capture rate results in an even looser bound. We will see in the next section that in this model, direct detection bounds are much stronger due to coherent enhancement of the spin-independent scattering cross section.

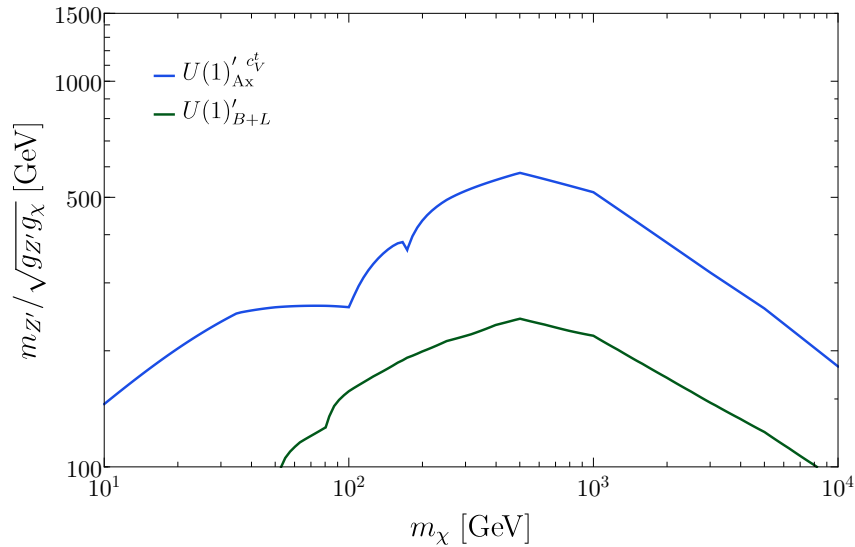


Figure 3.7: Bounds due to IceCube [288] searches for neutrinos originating from DM annihilations in the Sun, on the models we consider.

3.4.4 Colliders and direct detection

In addition to the above indirect detection searches which can be significantly affected by the presence of anomalies, simplified models of DM face complementary constraints from collider and direct detection experiments. In order to present a complete account of the limits on the models we consider, here we discuss these bounds and compare them to the exclusions derived previously that rely on anomalies.

At the LHC, the main probes of simplified DM models are missing energy-based searches, such as monojets and monophotons, and direct searches for the mediator decaying to SM particles.

The stronger constraints from direct Z' searches come from searches for dilepton resonances. We use the combined 8 + 13 TeV CMS dilepton analysis [290]. Because the resonant mediator searches do not involve the DM-mediator coupling, their reach cannot be presented in terms of the DM-SM interaction suppression scale without additional assumptions. Instead, we choose to show in Fig. 3.8 the upper limit on the $U(1)'$ coupling as a function of the mediator mass. The bound on the $U(1)'_{B+L}$ model is rescaled to account for the different charge of light quarks in this model. In the leptophilic model $U(1)'_L$ the LHC bound does not apply, since the production of Z' at the LHC is absent at tree level. The conclusion is that, if the Z' is kinematically accessible at LHC (couples to both light quarks and leptons), the bound from the dilepton searches would push us to very low Z' couplings to SM fermions.

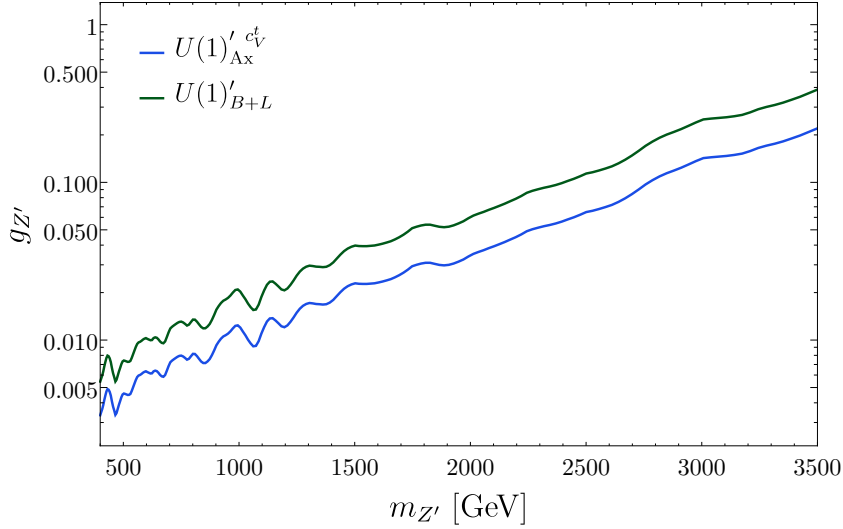


Figure 3.8: Bounds from resonant dilepton searches on a Z' at LHC from the 8 + 13 TeV combined analysis [290], presented in the $g_{Z'}-m_{Z'}$ plane for $U(1)'_{ax} c_V^t$ and $U(1)'_{B+L}$ (whereas $U(1)'_L$ is practically unconstrained at an hadronic collider).

We also rescale the limits of the 8 TeV CMS monojet search [291] for Majorana DM and show the results in Fig. 3.9.¹⁰ For DM below the TeV scale, monojets provide the dominant bound on the models that we consider.

The LHC monojet analysis clearly does not apply in the $U(1)'_L$ model, for which we rely on the recast done in [187] of the monophoton + missing transverse energy searches performed by the DELPHI collaboration at LEP [292, 293]. Due to the lower energy reach of LEP, the exclusion limit extends up to $m_\chi \sim 100$ GeV.

Two models, out the three we consider, also produce direct detection signatures. The $U(1)'_{ax} c_V^t$ model mainly produces spin-dependent interactions because of the axial couplings¹¹. The most powerful direct detection bound for our purposes comes from PICO [114], and is shown in Fig. 3.10. The bound is comparable to the monojet exclusion limit, and is superseded by Fermi-LAT observations of dSph at DM masses around 500 GeV.

The $U(1)'_{B+L}$ model induces instead a spin-independent and velocity-suppressed interac-

¹⁰While more recent searches are available, they are more difficult to recast for our purposes. The inclusion of 13 TeV results would improve the monojet limits at light DM mass in Fig. 3.9, while leaving the situation unchanged for DM heavier than several hundred GeV.

¹¹Spin-independent direct detection is in principle induced at loop level [106]. However, for typical DM and mediator masses in our region of interest the associated cross section is small enough to be safely ignored.

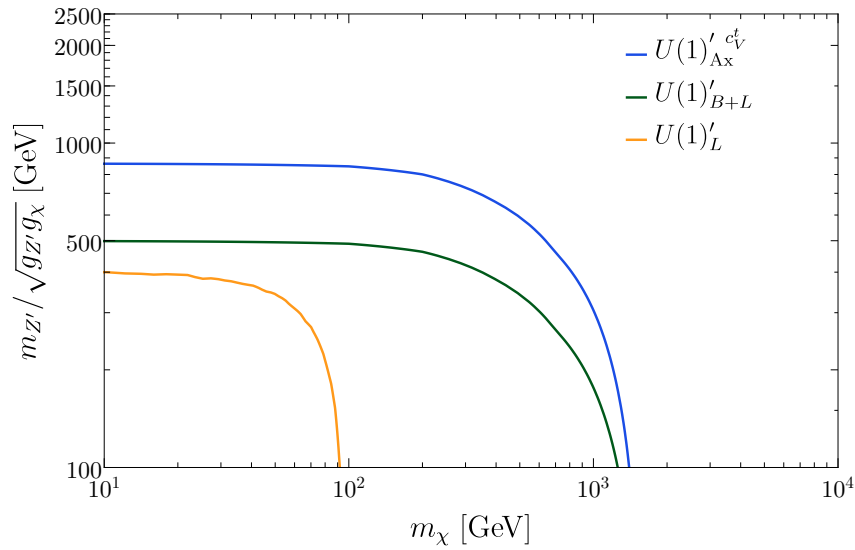


Figure 3.9: Bounds from the CMS monojet search [291] (for the models $U(1)'_{Ax}{}^{ct_V}$ and $U(1)'_{B+L}$), and the monophoton search performed by DELPHI and recast in [187] for the $U(1)'_L$ model.

tion. The most recent experimental bound comes from XENON-1T [294]. The collaboration provides a limit obtained assuming that the interaction between DM and nuclei occurs via the canonical spin-independent operator $\mathcal{O}_1^q = (\bar{\chi}\chi)(\bar{q}q)$ in the EFT of the DM. In our case the dominant interaction is $\mathcal{O}_6^q = (\bar{\chi}\gamma^\mu\gamma_5\chi)(\bar{q}\gamma_\mu q)$ rather than \mathcal{O}_1^q [104, 295, 296]. We perform a recast by means of the tables provided by [73]. The result is shown in Fig. 3.11. The exclusion limit from direct detection is the most powerful for m_χ up to a few TeV, where it is superseded by γ ray line searches only if we assume a cuspy profile of the DM density distribution like Einasto.

3.4.5 Summary of results

The combinations of all the constraints described above are shown in Figs. 3.10, 3.11 and 3.12 respectively for the three models $U(1)'_{Ax}{}^{ct_V}$, $U(1)'_{B+L}$ and $U(1)'_L$.

Indirect detection provides the strongest bounds at large DM mass, driven by loop annihilations of DM to gauge bosons. Depending on the choice of halo profile, either the HESS γ ray line search or the Fermi-LAT dSph continuum γ ray spectrum analysis is most constraining in this regime, depending in ultimate analysis on whether the gg channel is anomaly-induced or not. For models where there is no mixed anomaly between the Z' and $U(1)_{EM}$, the γ ray line searches are only weakly constraining. For lighter DM, monojets and/or direct searches still provide the tightest bound on the interaction scale. Notice that in the leptophilic model $U(1)'_L$ these constraints are absent, as is the IceCube bound, and the monophoton searches performed at LEP have a lower reach in m_χ . In this model, the only limits above LEP are provided by γ ray searches.

The limits are practically independent of the mediator mass. Consequently, the dilepton searches presented on Fig. 3.8 should be considered as an orthogonal bound to those in Fig. 3.10. For very heavy mediators, on the other hand, only large couplings can currently be constrained. However, future experiments will probe regions of our model which can more naturally accommodate a Z' weighing several TeV, and at such mass scales resonant LHC searches

lose sensitivity quite rapidly.

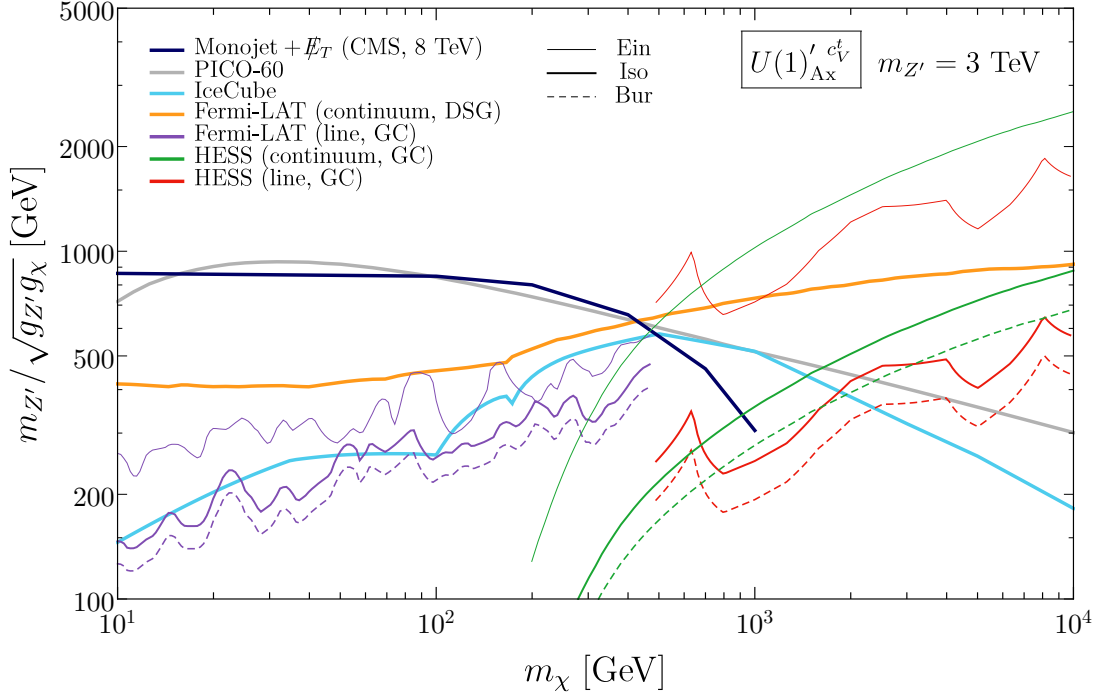


Figure 3.10: Combined limits from indirect detection, collider, and direct detection bounds on the $U(1)'_{Ax}$ model with a 3 TeV mediator. For heavy DM, the anomaly-induced annihilations to gauge bosons lead to strong indirect detection bounds. Some of the indirect detection limits are sensitive to the halo profile, and for these the impact of choosing different halo profiles is shown.

3.5 Comments on the Validity of Our Results

Throughout our discussion, we have assumed that anomalies are cancelled by fermions that are sufficiently decoupled so as to be effectively infinitely heavy for the processes that they mediate. Since the main effects of the Wess-Zumino terms are in DM annihilation, this corresponds to $m_f \gg m_\chi$. It is instructive to ask how our results change as the anomaly-cancelling fermions are brought closer to the DM mass.

Let us illustrate this point with the particular example of DM annihilation in a $U(1)'$ model where the charge of every SM fermion is equal to its usual hypercharge. Above the scale of the heaviest SM fermion, the top quark, there are no mixed $U(1)'$ -SM anomalies. Below the top mass, however, anomalies should appear and induce Wess-Zumino terms. At some point, where the DM becomes sufficiently lighter than the top mass, the EFT should give a good approximation to the full anomaly-free theory.

We compare these two calculation methods in Fig. 3.13, by varying the mass of the DM. The solid curve in Fig. 3.13 shows the annihilation cross section, calculated in the full UV complete theory, while the dashed line stands for the EFT calculation. By comparing the two curves, we see that the anomaly-cancelling fermions can be treated as having infinite mass so long as they are at least 2-3 times heavier than the centre-of-mass energy of the process being studied. In

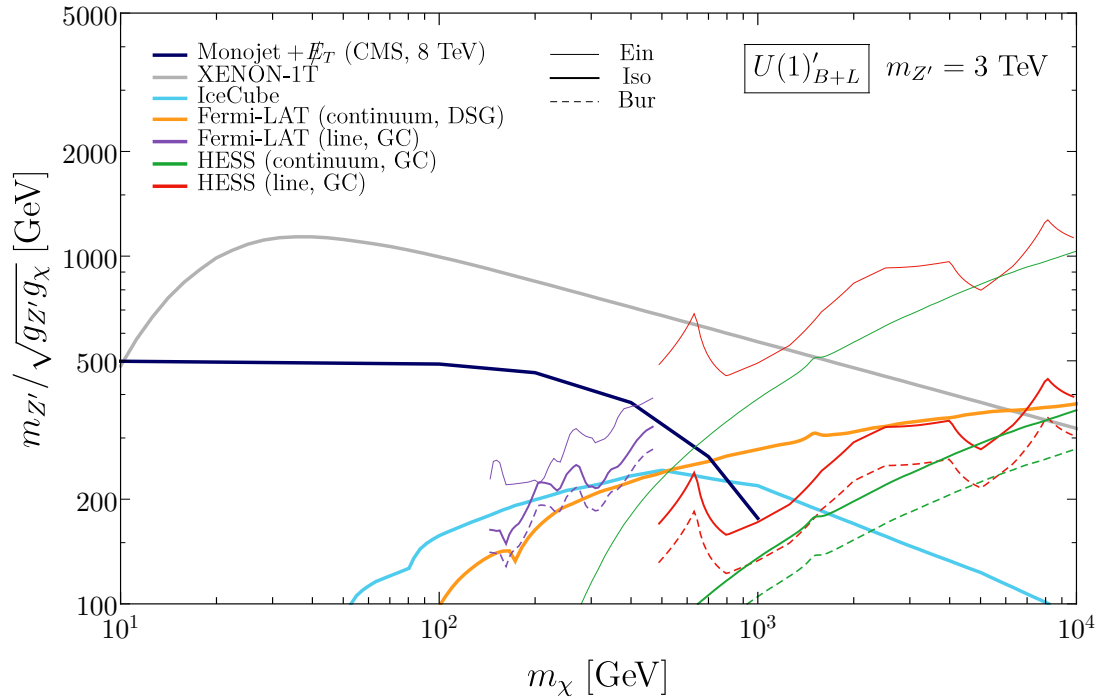


Figure 3.11: The same as in Fig. 3.10, shown for the $U(1)'_{B+L}$ model.

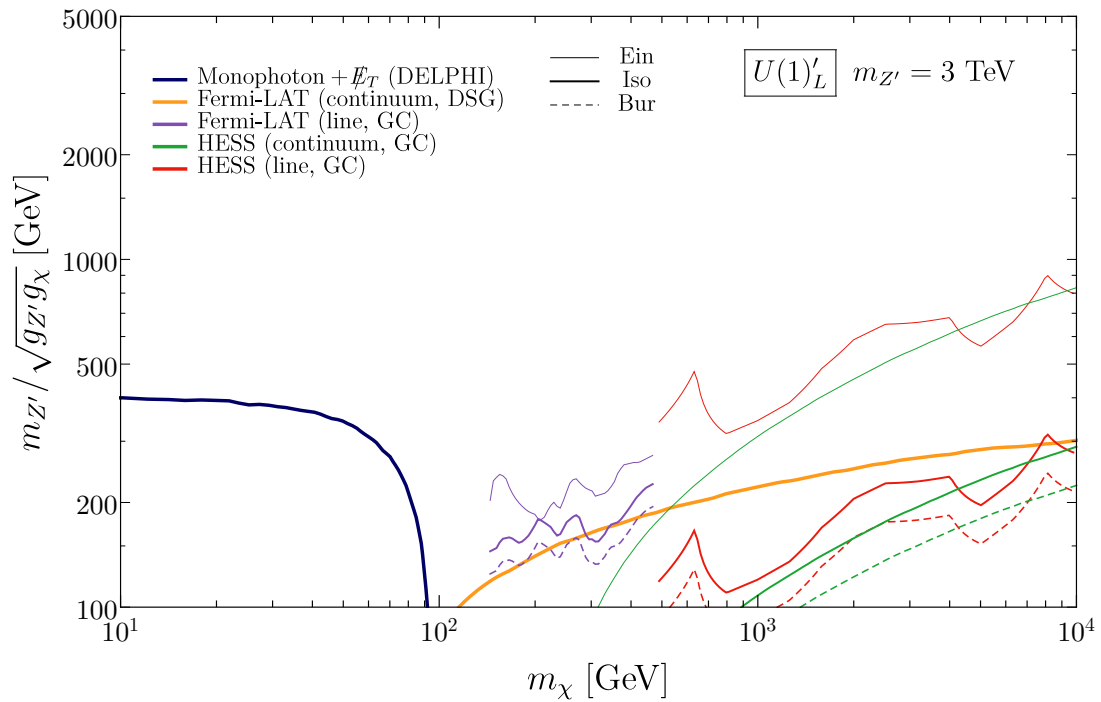


Figure 3.12: The same as in Fig. 3.10, shown for the $U(1)'_L$ model.

principle it is a very optimistic conclusion, that suggests that as long as the spectator fermions are not at the scale of the DM, our results are valid.

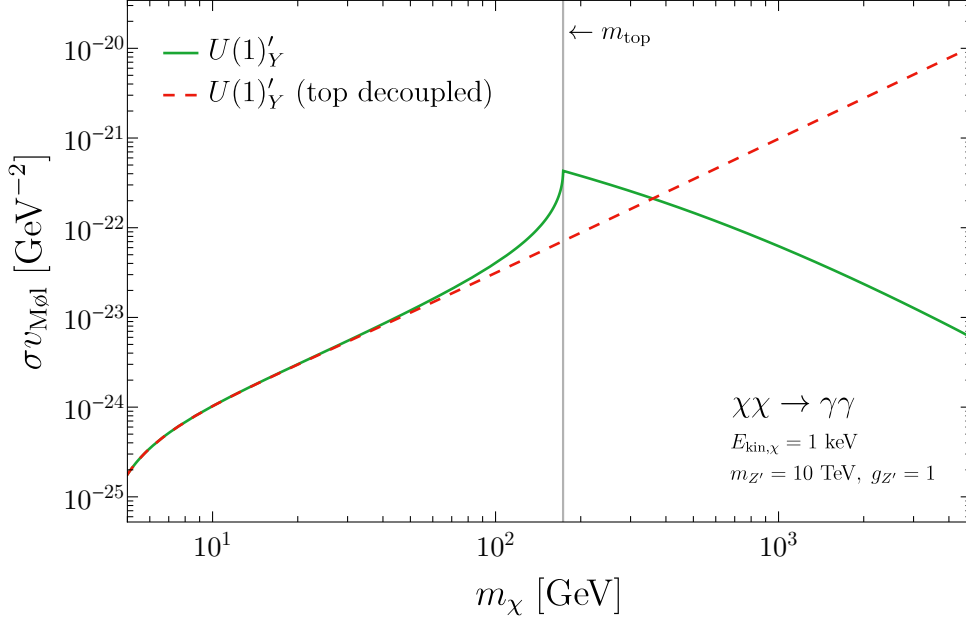


Figure 3.13: The effect of decoupling the top quark in a sequential hypercharge model. The green (solid) curve shows the cross section for DM annihilation to photons with $m_t = 175$ GeV, while the red (dashed) curve shows the same cross section with an infinite top quark mass. In general, anomaly-induced effects rise with energy until the mass scale where the anomaly is resolved.

We also notice that in this particular example we have chosen the mass of the Z' to be very high, 10 TeV. The scale of validity of the effective “anomalous” theory, which lies around $2 - 3 m_{\text{top}}$ if the DM is light, is quite uncorrelated with $m_{Z'}$, showing again that the scale of the Z' plays no role in setting the validity range of the effective theory.

3.6 Conclusions

Simplified models of DM are frequently used to present experimental results, yet the most common spin-1 mediator models often contain anomalies. While these may be resolved at high scales through the introduction of additional chiral fermions, in this work we have demonstrated that this is not without consequence. Integrating out heavy fermions generates Wess-Zumino and generalised Chern-Simons terms, whose derivative couplings can create significant effects at high energies despite the loop suppression.

In particular, mixed anomalies cause couplings between the Z' and the SM gauge bosons. These interactions affect DM annihilation through the Z' , and mostly impact on indirect detection probes of DM. We have evaluated the resulting bounds for a selection of $U(1)'$ possibilities. If a new $U(1)'$ has vector couplings, the only anomaly-induced terms involve the $SU(2)_L$ bosons, and so the annihilation cross sections tend to be smaller. This leads to weaker constraints from indirect detection searches involving photons.

We have compared bounds from indirect detection with those from direct detection and colliders. We find that γ -ray searches can often provide the most stringent limits on heavy DM, with either continuum or line searches being more constraining depending on the choice of halo profile. For intermediate masses between a few hundred GeV and 1 TeV, IceCube can

provide bounds comparable to direct searches if the scattering cross section with protons is SD. At small DM mass, direct detection is more effective at limiting a Z' which couples to quarks. Monojet and monophoton bounds can also constrain lighter DM, and while resonance searches are not directly comparable, dileptons still provide the best bounds if the mediator is kinematically accessible at the LHC and couples to quarks and leptons.

While most of our calculations assumed that the fermions which cancel anomalies are completely decoupled, we also considered the effect of restoring gauge invariance at smaller scales. As long as the anomalies persist up to energies that are a few times higher than the DM mass, which is the relevant energy scale for annihilation, our results remain completely valid.

In our study we have assumed that DM is a Majorana fermion, in part to emphasise our new indirect detection limits over the usual direct detection bounds, which are strong for spin-independent interactions that arise when the DM and quarks both couple vectorially to the Z' . It would nevertheless be interesting to examine the interplay between direct and indirect detection bounds in more general models. For instance, if the DM is a Dirac fermion with a vector $U(1)'$ coupling but the SM quarks couple axially under $U(1)'$, the leading spin-independent direct detection interaction is velocity-suppressed. Dressing such an interaction with Higgses yields a pure vector interaction, but as the main effect involves a top loop, it can be avoided if the top does not couple to the Z' . On the other hand, if the top does carry $U(1)'$ charge but the light quarks do not, the $SU(3)_c^2 \times U(1)'$ anomaly could be relevant for collider searches as there is no tree-level DM production from light quark initial states.

In characterizing the sensitivities of DM searches, models that are employed to show experimental results should be consistent with theoretical considerations. In addition to the recently well-studied requirement that such models provide unitary scattering amplitudes, we have shown here how gauge invariance necessitates the inclusion of additional interactions beyond the minimal Lagrangian of generic simplified DM models. We look forward to future developments in this direction as searches for DM continue.

3.A Ward Identities for non-Abelian spontaneously broken gauge theories

In this Appendix, we derive the Ward identities (more properly called Ward-Takahashi identity for Abelian groups and Slavnov-Taylor identities for non-Abelian groups) for the SM gauge bosons. For a more rigorous derivation, see [297].

We specialise to the calculation of the effective vertex $Z'VV$ (V being a SM gauge boson) at one loop, in order to fix the value of the momentum shift a^μ of the loop momentum between the two diagrams as shown in Fig. 3.2. In Fig. 3.14 we show with Feynman diagrams the final results for the Ward identities we are interested in.

Preliminary definitions We are interested in the three-point functions $\Gamma_{A^a A^b A^c}^{\mu\nu\rho}$ for three gauge bosons $A^{a\mu}(x), A^{b\nu}(y), A^{c\rho}(z)$:

$$\Gamma_{A^a A^b A^c}^{\mu\nu\rho} = \frac{\delta}{\delta A_\mu^a(x)} \frac{\delta}{\delta A_\nu^b(y)} \frac{\delta}{\delta A_\rho^c(z)} \mathcal{W} \Big|_{V=0}, \quad (3.25)$$

where by $V = 0$ we mean that all the fields have to be set to 0 after taking the functional derivatives.

The procedure to derive the Ward identities for the EW bosons is the following: we write an infinitesimal $SU(2)_L \times U(1)_Y$ transformation, and we impose the invariance of the generating

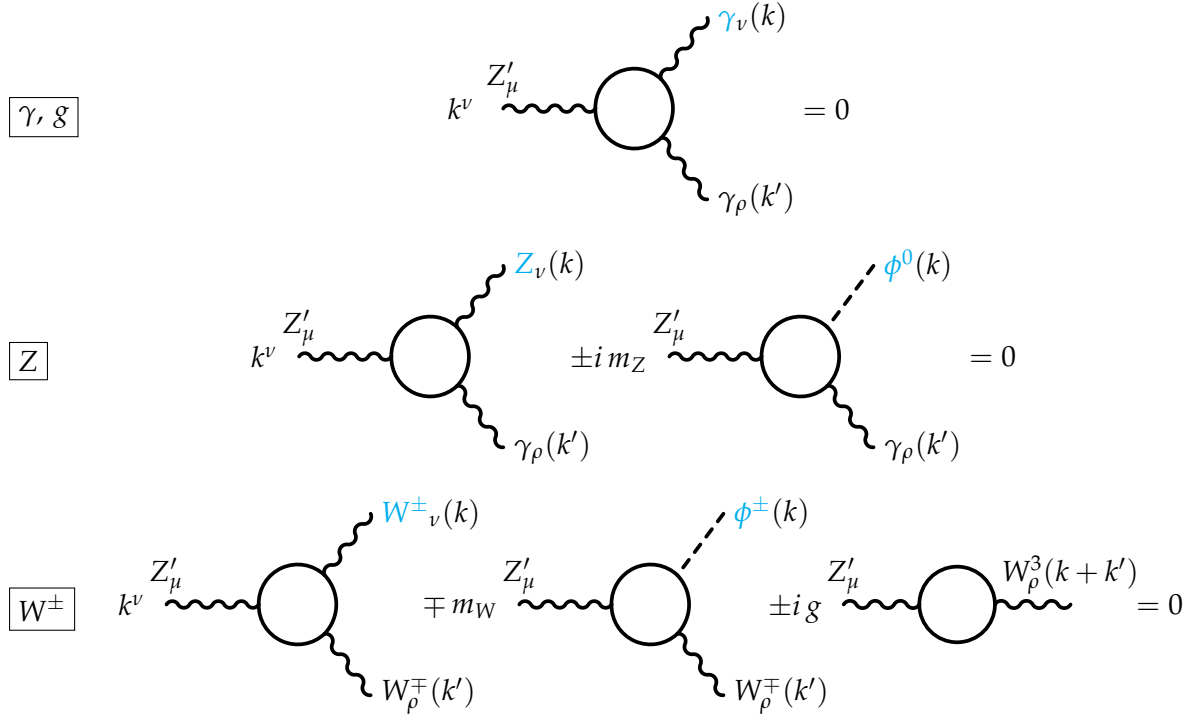


Figure 3.14: Ward Identities for the calculation of the one-loop vertices of the Z' with the SM vector bosons. The ϕ^i fields are the Goldstone bosons. In the fermion loops, we understand the sum of the diagrams with the propagators in clockwise and counter-clockwise directions.

functional of the connected Green functions \mathscr{W} for a transformation along one of the generators of the gauge symmetry. We further take functional derivatives with respect to Z'^μ and to the third vector boson of the amplitude.

$SU(2)_L \times U(1)_Y$ infinitesimal gauge transformations We want to express infinitesimal $SU(2)_L \times U(1)_Y$ transformations in terms of the mass eigenstate basis. Let us denote the bases for the gauge bosons and the generators before the EW symmetry breaking as

$$\{W^1, W^2, W^3, B\}, \quad \{\omega^1, \omega^2, \omega^3, \omega^B\} \quad (3.26)$$

and in the mass basis as

$$\{W^+, W^-, Z, A\}, \quad \{\omega^+, \omega^-, \omega^Z, \omega^A\}, \quad (3.27)$$

with the usual relations between the bosons in the unbroken and broken phases:

$$\begin{aligned} W^\pm &= \frac{W^1 \mp iW^2}{\sqrt{2}}, \quad Z = c_W W^3 - s_W B, \quad A = s_W W^3 + c_W B, \\ \omega^\pm &= \frac{\omega^1 \mp i\omega^2}{\sqrt{2}}, \quad \omega^Z = c_W \omega^3 - s_W \omega^B, \quad \omega^A = s_W \omega^3 + c_W \omega^B, \end{aligned} \quad (3.28)$$

where c_W and s_W are cosine and sine of the Weinberg angle.

Let us consider first the effect of a $SU(2)_L \times U(1)_Y$ transformation on the electroweak gauge bosons. The effect of an infinitesimal $SU(2)_L$ gauge transformation is $\delta W^a = \partial \omega^a - g f^{abc} \omega^b W^c$, where g is the $SU(2)_L$ coupling constant f^{abc} are the structure constants of the gauge group, which in the basis (3.26) are given by the Levi-Civita tensor, $f^{abc} = i\epsilon^{abc}$. We now rewrite

these transformations in the basis (3.27). As an intermediate step, we express them in the basis $\{W^+, W^-, W^3, B\}$ in order to highlight some terms containing ω^+ which will be relevant later:

$$\delta W^+ = \partial\omega^+ + g\omega^+W^3 - g\omega^3W^+ \quad (3.29a)$$

$$\delta W^- = \partial\omega^- - g\omega^-W^3 + g\omega^3W^- \quad (3.29b)$$

$$\delta W^3 = \partial\omega^3 - g\omega^+W^- + g\omega^-W^+ \quad (3.29c)$$

$$\delta B = \partial\omega^B \quad (3.29d)$$

The final result in the mass basis of Eq. (3.27) is

$$\delta W^+ = \partial\omega^+ + \omega^+(gc_WZ + eA) - gc_W\omega^ZW^+ - e\omega^AW^+ \quad (3.30a)$$

$$\delta W^- = \partial\omega^- - \omega^-(gc_WZ + eA) + gc_W\omega^ZW^- + e\omega^AW^- \quad (3.30b)$$

$$\delta Z = \partial\omega^Z - gc_W\omega^+W^- + gc_W\omega^-W^+ \quad (3.30c)$$

$$\delta A = \partial\omega^A - e\omega^+W^- + e\omega^-W^+ \quad (3.30d)$$

where $e = g_{\text{SW}}$ is the electric charge.

We now turn our attention to the transformation of the Higgs doublet, which we parametrise as

$$\Phi = \begin{pmatrix} \phi^+ \\ \frac{v+h+i\phi^0}{\sqrt{2}} \end{pmatrix}. \quad (3.31)$$

Under an infinitesimal $SU(2)_L \times U(1)_Y$ transformation it becomes

$$\Phi' = \exp \left\{ ig\omega^a \frac{\sigma^a}{2} + ig' \frac{1}{2} \omega^B \right\} \Phi \simeq \left[\mathbb{1} + i \begin{pmatrix} \frac{1}{2}(gc_W - g's_W)\omega^Z + e\omega^A & \frac{1}{\sqrt{2}}\omega^+ \\ \frac{1}{\sqrt{2}}\omega^- & -\frac{1}{2}g_Z\omega^Z \end{pmatrix} \right] \Phi, \quad (3.32)$$

where g' is the $U(1)_Y$ coupling constant and $g_Z = \sqrt{g^2 + g'^2} = g/c_W$. The result for the variations of the components of the Higgs doublet is

$$\delta\phi^+ = \frac{i}{2}(gc_W - g's_W)\omega^Z\phi^+ + ie\omega^A\phi^+ + \frac{i}{2}g\omega^+\omega^+ + \frac{i}{2}g(h + i\phi^0)\omega^+ \quad (3.33a)$$

$$\delta h = -g \text{Im}(\omega^- \phi^+) + \frac{1}{2}g_Z\omega^Z\phi^0 \quad (3.33b)$$

$$\delta\phi^0 = g \text{Re}(\omega^- \phi^+) - \frac{1}{2}g_Z\omega^Z\phi^0 - \frac{1}{2}g_Z\omega^Z h \quad (3.33c)$$

Also the fermion doublets of the SM transform under $SU(2)_L \times U(1)_Y$, but they are not contributing to the Ward identities for the $Z'VV$ vertices.

Ward identity for the photon in the $Z'\gamma\gamma$, $Z'Z\gamma$ vertex We start from the standard case of the Ward identity for the photon, associated to the unbroken $U(1)_{\text{EM}}$ gauge symmetry. We perform a $SU(2)_L \times U(1)_Y$ transformation in the $\omega^A(y)$ direction, and we write all the terms arising from the variation of the generating functional \mathcal{W} :

$$\delta_{\omega^A} \mathcal{W} = \int d^4y \omega^A(y) \left[-\partial_\nu \frac{\delta \mathcal{W}}{\delta A_\nu} - eW_\nu^+ \frac{\delta \mathcal{W}}{\delta W_\nu^+} + eW_\nu^- \frac{\delta \mathcal{W}}{\delta W_\nu^-} + \left(ie\phi^+ \frac{\delta \mathcal{W}}{\delta \phi^+} + \text{h.c.} \right) + [\text{fermions}] \right], \quad (3.34)$$

where the last term includes the contribution from fermions, and we understand the dependence on y of all the functions in the integrand. If we impose the invariance of the Lagrangian under $SU(2)_L \times U(1)_Y$, the integrand in Eq. (3.34) vanishes. We now take two functional derivatives with respect to Z'_μ and A_ρ , and we set all the fields to 0. In the final result containing the three-point function for $Z'\gamma\gamma$, only the first term of Eq. (3.34) survives and gives the familiar Ward-Takahashi identity

$$\frac{\partial}{\partial y^\nu} \Gamma_{Z'\gamma\gamma}^{\mu\nu\rho} = 0. \quad (3.35)$$

The same identity holds for the photon in the $Z'Z\gamma$ vertex. Thus, only the term highlighted in yellow in Eq. (3.30d) from the variation δA contributes to the Ward identity for this amplitude.

Ward identity for the Z boson in the $Z'ZZ, Z'Z\gamma$ vertices The procedure is the same outlined for the photon. In this case, in the final result there is another non-vanishing contribution, apart from the familiar one originating from the term highlighted in red in Eq. (3.30c). Due to the EW symmetry breaking and the non-vanishing vev $v/\sqrt{2}$ of the Higgs, there is a term (highlighted in red) in Eq. (3.33c) proportional to v and containing the function ω^Z with no other fields. This leads to an extra term in the Ward identity for the Z boson, proportional to the Z mass. By a calculation completely analogous to the one of Eq. (3.34) one finds

$$\frac{\partial}{\partial y^\nu} \Gamma_{Z'Z\gamma}^{\mu\nu\rho} + im_Z \Gamma_{Z'\phi^0\gamma}^{\mu\rho} = 0, \quad (3.36)$$

where $\Gamma_{Z'\phi^0\gamma}^{\mu\rho}$ is the three-point function of $Z'^\mu(x)\phi^0(y)A^\rho(z)$. The Feynman rule for the 1-loop fermion contribution in Fig. 3.14 contains a \pm sign in front of this Goldstone term because of the Feynman rule for the vertex $\bar{f}\gamma_5 f\phi^0$, which has a $+$ ($-$) sign for upper (lower) components of the $SU(2)_L$ doublet. The same Ward identity of Eq. (3.36) holds also for the $Z'ZZ$ vertex.

Ward identity for the W^\pm boson in the $Z'W^+W^-$ vertex Let us consider now the Ward identity for W^+ boson in the $Z'W^+W^-$ vertex. The standard term coming from the variation δW^+ is highlighted in blue in Eq. (3.29b). A term containing the Goldstone boson contribution and proportional to m_W comes from the term highlighted in Eq. (3.33a). Moreover, in this case, there is also another term: the contribution in blue in Eq. (3.29c) for the variation δW^3 is proportional to ω^+W^- , so that when we derive with respect to $W^{-\rho}$ we cancel the field and we get a non-vanishing piece in the Ward identity. This is a two-point function $\Gamma_{Z'W^3}^{\mu\rho}$ of the Z'^μ and the $W^{3\rho}$ boson:

$$\frac{\partial}{\partial y^\nu} \Gamma_{Z'W^+W^-}^{\mu\nu\rho} - m_Z \Gamma_{Z'\phi^+W^-}^{\mu\rho} - g \Gamma_{Z'W^3}^{\mu\rho} = 0. \quad (3.37)$$

A completely analogous equation holds for the W^- boson, with an opposite sign for the Goldstone boson contribution and the two-point function.

Ward identity for the gluon in the $Z'gg$ vertex In the 3-point function $Z'gg$ of the Z' with gluons, by imposing the $SU(3)_c$ invariance with the same procedure described before, one gets a Ward-Takahashi identity equal to the standard one for photons:

$$\frac{\partial}{\partial y^\nu} \Gamma_{Z'G^aG^a}^{\mu\nu\rho} = 0. \quad (3.38)$$

Of course, given that $SU(3)_c$ is unbroken there is no Goldstone boson piece. The non-Abelianity of $SU(3)_c$ does not introduce extra terms in 3-point function for $Z'gg$: the reason ultimately

relies on the fact the two final gluons carry the same colour index, and the structure constants are completely antisymmetric, so that no pieces survive in the derivation in the Ward identity for $Z'^{\mu}G^{a\nu}G^{a\rho}$. Notice that in the basis $\{W^+, W^-, W^3\}$ the $SU(2)_L$ structure constants are not completely antisymmetric, so that there is no inconsistency between the two results.

3.B Effective triple gauge boson couplings

Eq. (3.19) gives the effective Z' - γ - γ vertex. Here, we provide the form of this vertex for other gauge boson channels.

The calculation of the Z' - g - g vertex is the same as for Z' - γ - γ up to a colour factor and coupling constants:

$$\Gamma_{Z'gg}^{\mu\nu\rho} = \frac{2}{N_c} \left(\frac{g_s}{eQ_f^{\text{em}}} \right)^2 \Gamma_{Z'\gamma\gamma}^{\mu\nu\rho} \quad (3.39)$$

The final cross section for $\chi\chi \rightarrow gg$ is then multiplied by the number of gluons $N_c^2 - 1$.

For massive gauge bosons, we include the Goldstone amplitude in the Ward identities, as described in Sec. 3.2. Unlike the photon and gluon cases, a triangle vertex arises even if the $U(1)'$ coupling of the loop fermion is vector-like, because the weak interactions violate parity. Similarly to the Z' coupling to fermions, we write the Z -fermion-fermion vertex as $i\frac{g}{c_W}\gamma^\rho(g_V^Z + g_A^Z\gamma^5)$. Then, the Z' - Z - γ vertex is given by

$$\begin{aligned} \Gamma_{Z'Z\gamma}^{\mu\nu\rho} = & \frac{g_{Z'}N_c^2 g e Q_f^{\text{em}} (g_V^f g_A^Z + g_A^f g_V^Z)}{\pi^2 c_W} \left(I_1^{Z\gamma} \epsilon^{\alpha\nu\rho\mu} (p_2)_\alpha + I_2^{Z\gamma} \epsilon^{\alpha\nu\rho\mu} (p_3)_\alpha \right. \\ & + I_3^{Z\gamma} \epsilon^{\alpha\beta\nu\mu} (p_2)^\rho (p_2)_\alpha (p_3)_\beta + I_4^{Z\gamma} \epsilon^{\alpha\beta\nu\mu} (p_3)^\rho (p_2)_\alpha (p_3)_\beta \\ & \left. + I_5^{Z\gamma} \epsilon^{\alpha\beta\rho\mu} (p_2)^\sigma (p_2)_\alpha (p_3)_\beta + I_6^{Z\gamma} \epsilon^{\alpha\beta\rho\mu} (p_3)^\sigma (p_2)_\alpha (p_3)_\beta \right) \end{aligned} \quad (3.40)$$

where the form factors, in terms of those in Eq. (3.20), are

$$\begin{aligned} I_1^{Z\gamma}(p_2, p_3; m_f) &= (p_2 \cdot p_3) I_3^{Z\gamma}(p_2, p_3; m_f) + p_3^2 I_4^{Z\gamma}(p_2, p_3; m_f) \\ I_2^{Z\gamma}(p_2, p_3; m_f) &= p_2^2 I_5^{Z\gamma}(p_2, p_3; m_f) + (p_2 \cdot p_3) I_6^{Z\gamma}(p_2, p_3; m_f) \\ &\quad - \frac{g_V^f g_A^Z}{g_V^f g_A^Z + g_A^f g_V^Z} m_f^2 C_0(p_3^2, p_1^2, p_2^2, m_f^2, m_f^2, m_f^2) \\ I_3^{Z\gamma}(p_2, p_3; m_f) &= -I_3^{\gamma\gamma}(p_2, p_3; m_f) \\ I_4^{Z\gamma}(p_2, p_3; m_f) &= -I_4^{\gamma\gamma}(p_2, p_3; m_f) \\ I_5^{Z\gamma}(p_2, p_3; m_f) &= -I_5^{\gamma\gamma}(p_2, p_3; m_f) \\ I_6^{Z\gamma}(p_2, p_3; m_f) &= -I_6^{\gamma\gamma}(p_2, p_3; m_f) \end{aligned} \quad (3.41)$$

The Z' - Z - Z vertex is

$$\begin{aligned} \Gamma_{Z'ZZ}^{\mu\nu\rho} = & \frac{g_{Z'}N_c^2 g^2 \left[2g_V^f g_V^Z g_A^Z + g_A^f \left((g_V^Z)^2 + (g_A^Z)^2 \right) \right]}{\pi^2 c_W^2} \left(I_1^{ZZ} \epsilon^{\alpha\nu\rho\mu} (p_2)_\alpha + I_2^{ZZ} \epsilon^{\alpha\nu\rho\mu} (p_3)_\alpha \right. \\ & + I_3^{ZZ} \epsilon^{\alpha\beta\nu\mu} (p_2)^\rho (p_2)_\alpha (p_3)_\beta + I_4^{ZZ} \epsilon^{\alpha\beta\nu\mu} (p_3)^\rho (p_2)_\alpha (p_3)_\beta \\ & \left. + I_5^{ZZ} \epsilon^{\alpha\beta\rho\mu} (p_2)^\sigma (p_2)_\alpha (p_3)_\beta + I_6^{ZZ} \epsilon^{\alpha\beta\rho\mu} (p_3)^\sigma (p_2)_\alpha (p_3)_\beta \right) \end{aligned} \quad (3.42)$$

where the form factors are

$$\begin{aligned}
I_1^{ZZ}(p_2, p_3; m_f) &= (p_2 \cdot p_3) I_3^{ZZ}(p_2, p_3; m_f) + p_3^2 I_4^{ZZ}(p_2, p_3; m_f) - m_f^2 C_0(p_3^2, p_1^2, p_2^2, m_f^2, m_f^2, m_f^2) \\
I_2^{ZZ}(p_2, p_3; m_f) &= p_2^2 I_5^{ZZ}(p_2, p_3; m_f) + (p_2 \cdot p_3) I_6^{ZZ}(p_2, p_3; m_f) - m_f^2 C_0(p_3^2, p_1^2, p_2^2, m_f^2, m_f^2, m_f^2) \\
I_3^{ZZ}(p_2, p_3; m_f) &= -I_3^{\gamma\gamma}(p_2, p_3; m_f) \\
I_4^{ZZ}(p_2, p_3; m_f) &= -I_4^{\gamma\gamma}(p_2, p_3; m_f) \\
I_5^{ZZ}(p_2, p_3; m_f) &= -I_5^{\gamma\gamma}(p_2, p_3; m_f) \\
I_6^{ZZ}(p_2, p_3; m_f) &= -I_6^{\gamma\gamma}(p_2, p_3; m_f)
\end{aligned} \tag{3.43}$$

For the $Z'-W^+-W^-$ vertex, we assume that two fermions run in the loop whose left-handed components are related by $SU(2)_L$, with the up-type fermion having mass m_f and coupling vectorially to the Z' , $-ig_{Z'}\gamma^\nu$. Then, regardless of whether the down-type fermion coupling to the Z' is vector or axial, i.e. $-ig_{Z'}\gamma^\nu$ or $ig_{Z'}\gamma^\nu\gamma^5$, the vertex is given by

$$\begin{aligned}
\Gamma_{WW}^{\mu\nu\rho} &= \frac{g_{Z'} N_c^2 g^2}{4\pi^2} \left(I_1^{WW} \epsilon^{\alpha\nu\rho\mu} (p_2)_\alpha + I_2^{WW} \epsilon^{\alpha\nu\rho\mu} (p_3)_\alpha \right. \\
&\quad + I_3^{WW} \epsilon^{\alpha\beta\nu\mu} (p_2)^\rho (p_2)_\alpha (p_3)_\beta + I_4^{WW} \epsilon^{\alpha\beta\nu\mu} (p_3)^\rho (p_2)_\alpha (p_3)_\beta \\
&\quad \left. + I_5^{WW} \epsilon^{\alpha\beta\rho\mu} (p_2)^\sigma (p_2)_\alpha (p_3)_\beta + I_6^{WW} \epsilon^{\alpha\beta\rho\mu} (p_3)^\sigma (p_2)_\alpha (p_3)_\beta \right)
\end{aligned} \tag{3.44}$$

where the form factors are

$$\begin{aligned}
I_1^{WW}(p_2, p_3; m_f) &= (p_2 \cdot p_3) I_3^{WW}(p_2, p_3; m_f) + p_3^2 I_4^{WW}(p_2, p_3; m_f) - \frac{m_f^2}{4} \left(C_0(p_3^2, p_1^2, p_2^2, m_f^2, 0, 0) \right. \\
&\quad + C_1(p_3^2, p_1^2, p_2^2, m_f^2, 0, 0) + C_1(p_3^2, p_1^2, p_2^2, 0, m_f^2, m_f^2) \\
&\quad \left. + C_2(p_3^2, p_1^2, p_2^2, m_f^2, 0, 0) + C_2(p_3^2, p_1^2, p_2^2, 0, m_f^2, m_f^2) \right) \\
I_2^{WW}(p_2, p_3; m_f) &= p_2^2 I_5^{WW}(p_2, p_3; m_f) + (p_2 \cdot p_3) I_6^{WW}(p_2, p_3; m_f) + \frac{m_f^2}{4} \left(C_0(p_3^2, p_1^2, p_2^2, m_f^2, 0, 0) \right. \\
&\quad + C_1(p_3^2, p_1^2, p_2^2, m_f^2, 0, 0) + C_1(p_3^2, p_1^2, p_2^2, 0, m_f^2, m_f^2) \\
&\quad \left. + C_2(p_3^2, p_1^2, p_2^2, m_f^2, 0, 0) + C_2(p_3^2, p_1^2, p_2^2, 0, m_f^2, m_f^2) \right) \\
I_3^{WW}(p_2, p_3; m_f) &= \frac{1}{2} \left(C_{12}(p_2^2, p_1^2, p_3^2, m_f^2, 0, 0) + C_{12}(p_2^2, p_1^2, p_3^2, 0, m_f^2, m_f^2) \right) \\
I_4^{WW}(p_2, p_3; m_f) &= -I_5^{WW}(p_3, p_2; m_f) \\
I_5^{WW}(p_2, p_3; m_f) &= \frac{1}{2} \left(C_{11}(p_2^2, p_1^2, p_3^2, m_f^2, 0, 0) + C_{11}(p_2^2, p_1^2, p_3^2, 0, m_f^2, m_f^2) \right. \\
&\quad \left. + C_1(p_2^2, p_1^2, p_3^2, m_f^2, 0, 0) + C_1(p_2^2, p_1^2, p_3^2, 0, m_f^2, m_f^2) \right) \\
I_6^{WW}(p_2, p_3; m_f) &= -I_3^{WW}(p_2, p_3; m_f)
\end{aligned} \tag{3.45}$$

Part III

Cosmological signatures of the Higgs instability

A cosmological signature of the Higgs instability: Primordial Black Holes as Dark Matter

The potential of the Standard Model Higgs boson develops an instability at large scales for the central measured values of the top and Higgs masses. This remarkable feature has spurred a lot of investigation on its possible impact on the early universe, with the hope to get insight on Physics at scale inaccessible at colliders through cosmological considerations. A cosmological signature of this instability could be that the dark matter is under the form of Primordial Black Holes (PBH) seeded by Higgs fluctuations during inflation. This chapter, based on the papers [3] and [4] and on further material contained in [5], illustrates this mechanism.

Section 4.1 summarises the results about the instability of the Higgs vacuum and its impact on the Early Universe, and sketches the mechanism we describe in the rest of the chapter. Section 4.2 describes in detail the dynamics of the mechanism we envisage during and after inflation. Section 4.3 contains analytical estimates of the curvature perturbations. In Section 4.4 we offer a general discussion of PBHs, starting from their motivation and describing their formation, experimental constraints and giving an overview of the models in the literature. In Section 4.5 we resume the illustration of the mechanism we propose, showing the mass function of PBHs that can be generated with this mechanism, and sections 4.6 and 4.7 address the issues of homogeneity and fine tuning. Section 4.8 contains the conclusions, and the final appendices contain additional material.

4.1 Instability of the Standard Model Higgs vacuum

It has been known for a long time that the Standard Model (SM) Higgs potential develops an instability at large field values [298–309]. For the current central values of the Higgs and top masses, the quartic coupling λ in the Higgs potential becomes negative for Higgs field values $\gtrsim 10^{11}$ GeV,¹ making our electroweak (EW) vacuum not the one of minimum energy. The running of λ up to the Planck scale was updated with the input of the measured Higgs mass $m_{\text{Higgs}} = 125.15 \pm 0.24$ GeV in [309] and is shown in Fig. 4.1.

Despite the metastability condition of our present electroweak vacuum, its lifetime against decay both via quantum tunnelling in flat spacetime or thermal fluctuations in the early Universe

¹For a discussion on how to assess the instability scale in a gauge-independent way, see Ref. [310].

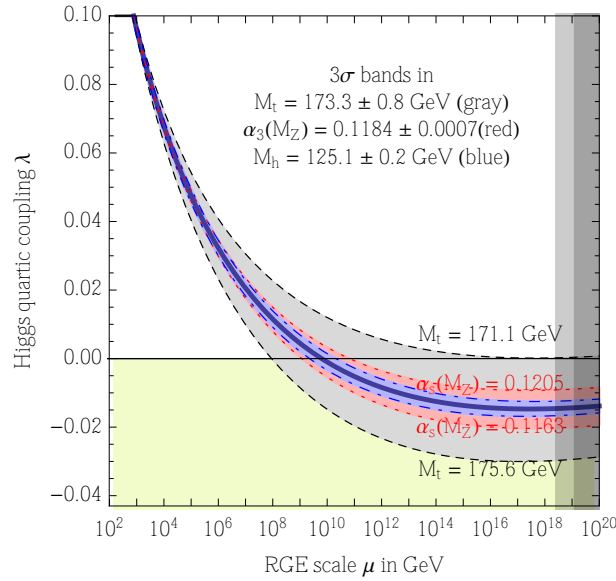


Figure 4.1: Running of the quartic coupling λ for the central measured values of m_{top} , m_{Higgs} and α_S reported in the legend, with bands corresponding to $(\pm 3\sigma)$ deviations in these values (from [309]).

is by far longer than the age of the Universe [307–309, 311]. Fig. 4.2 shows in the $(m_{\text{Higgs}}, m_{\text{top}})$ plane the lifetime of the EW vacuum for each point in the parameter space.

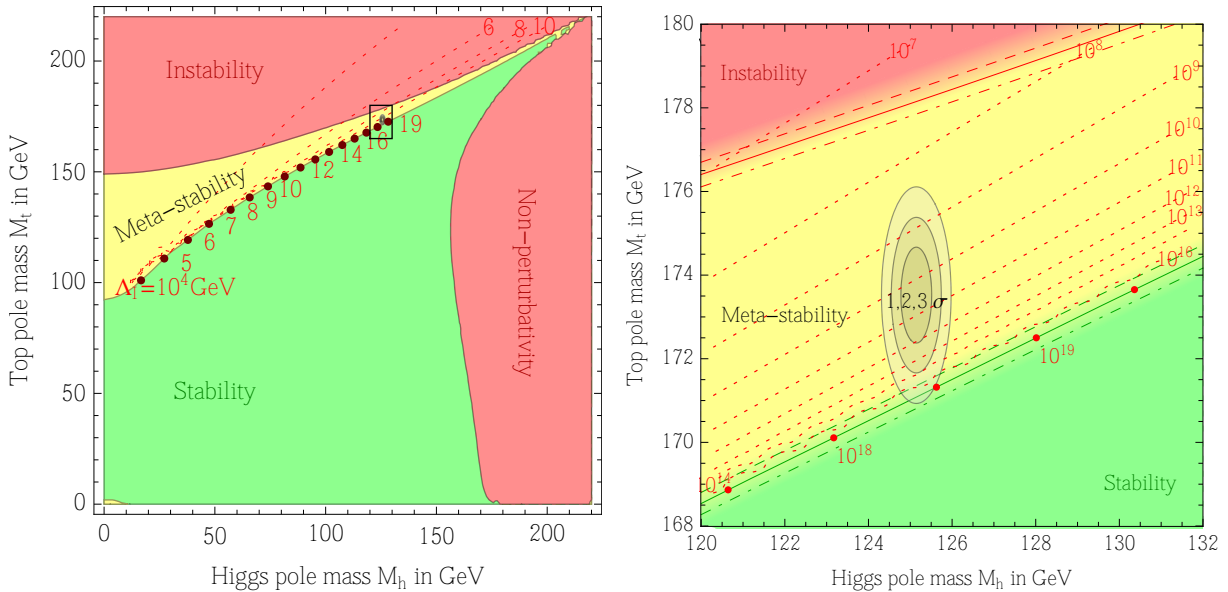


Figure 4.2: Phase space diagrams of the SM in the plane $(m_{\text{Higgs}}, m_{\text{top}})$, with shadings between the different regions corresponding to $(\pm 1\sigma)$ variations in α_S . The green region features an absolutely stable vacuum. In the unstable red region, λ turns negative at a scale low enough to make the lifetime of the EW vacuum shorter than the age of the Universe, whereas the yellow region corresponds to metastable vacua with a lifetime longer than the age of the Universe. The red lines and labels mark the value of the instability scale Λ at which $V(h)$ becomes negative (from [309]).

It is remarkable that we happen to live precisely in the metastable region, the narrow strip dividing the stable and unstable regions of the parameter space. This picture can change of course in presence of Physics Beyond the Standard Model (BSM) interacting with the EW sector. Still, given the current lack of evidence for such states, it is worth considering the SM valid up to the Planck scale and asking what are the implications of the instability during the early universe.

We have seen that the risk of tunnelling beyond the barrier today is completely negligible. The situation is different during primordial inflation [312], the early stage during which the Universe expands exponentially and light fields may be quantum mechanically excited. Assuming that the inflationary stage starts with a vanishing vacuum expectation value of the SM Higgs, if the effective mass of the Higgs field is smaller than the Hubble rate H during inflation, quantum excitations of the Higgs field push it away from its minimum [313]. The classical value (the long wavelength mode) of the Higgs field randomly walks receiving kicks of the order of $\sim \pm(H/2\pi)$ each Hubble time and can surmount the potential barrier and fall deep into the unstable side of the potential [313–323].

At the end of inflation, patches where this happened will be anti-de Sitter regions, and they are lethal for our universe as they grow at the speed of light [324]. From this result, one can derive upper bounds on H , which depend on the reheating temperature T_{RH} and on the Higgs coupling to the scalar curvature or to the inflaton [324–332].

The upper bound on H depends on T_{RH} because, for sufficiently large values of T_{RH} , patches in which the Higgs field probes the unstable part of the potential can be recovered thanks to the thermal effects after inflation. Indeed, the mass squared of the Higgs field receives a positive correction proportional to T^2 in such a way that in those would-be dangerous regions the Higgs field can roll back down to the origin and be safe. This happens because, thanks to the thermal interactions with the surrounding plasma, the Higgs potential receives a correction of the form [324]

$$V_T \simeq \frac{1}{2} m_T^2 h_c^2, \quad m_T^2 \simeq 0.12 T^2 e^{-|h_c|/(2\pi T)} \quad (4.1)$$

(a fit that is accurate for $h \lesssim 10 T$ in the region of interest and includes the effect of ring resummation). If the temperature at reheating is large enough, $T_{\text{RH}}^2 \gtrsim \lambda h_e^2$, where h_e is the value of the Higgs when inflation ends, then the patch is rescued and the Higgs starts oscillating (with a relativistic equation of state) around the current electroweak vacuum where it will settle after a while.

While some take this as motivation for the presence of new physics to change this feature, this is not necessarily a drawback of the SM. The physical implications of living in a metastable electroweak vacuum are fascinating and have far-reaching consequences for cosmology. This has triggered much activity in a field that involves inflationary dynamics, the physics of preheating, the interplay between Higgs properties and observables of cosmological interest, etc. In spite of this richness, a word of warning is in order: the energy scale of this physics is very high and we have no smoking-gun signature (comparable to proton decay for GUTs) that the electroweak vacuum metastability is actually realised in nature (with the exception of the vacuum decay itself!).

One reasonable question to ask is how can we probe, even if indirectly, the SM Higgs vacuum instability. In this chapter we argue that there might be a cosmological signature of this feature: the very presence of dark matter (DM) in our universe. We argue that the origin of DM does not need physics beyond the SM: DM may be due to primordial black holes seeded by the perturbations of the Higgs field generated during the last stages of inflation. The black holes may provide the seeds for structure formation [333, 334].

The picture we envisage is the following. During inflation there are patches where the Higgs has been pushed by quantum fluctuations beyond the potential barrier and is classically rolling down the slope. Higgs fluctuations do not contribute significantly to the total curvature perturbation ζ which is ultimately responsible for the anisotropies in the Cosmic Microwave Background (CMB). Higgs perturbations instead grow to relatively large values in the last e -folds of inflation, which are irrelevant for observations in the CMB. When inflation ends and reheating takes place, these regions are rescued by thermal effects and the Higgs rolls down to the origin of its potential. At later times, the Higgs perturbations reenter inside the Hubble radius and, if they are large enough, they provide high peaks in the matter power spectrum which give rise to PBHs. We show that these PBHs can provide the DM we see in the universe today. A schematic representation of the evolution of the Higgs background throughout the whole mechanism is shown in Fig. 4.3.

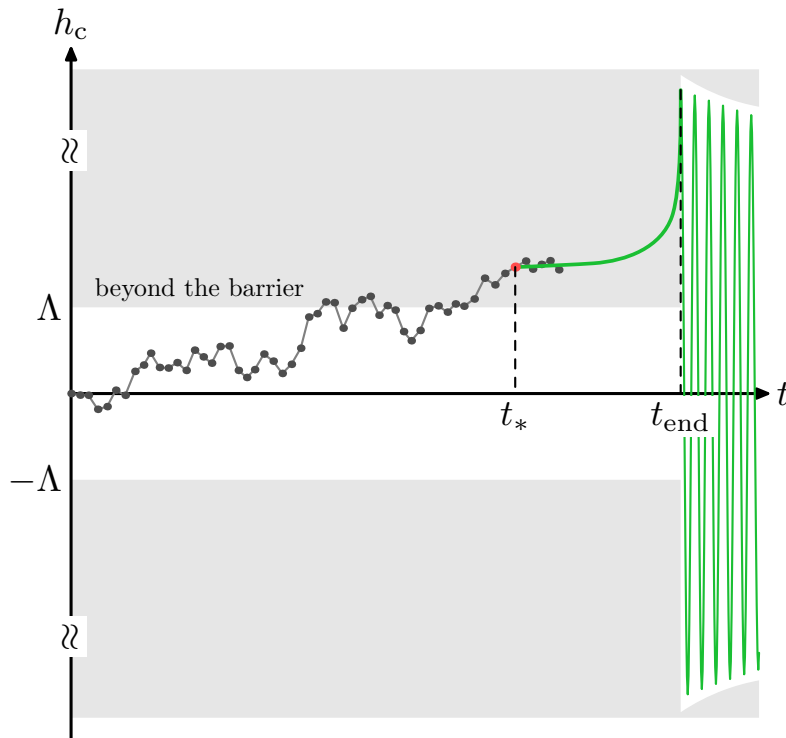


Figure 4.3: Evolution of the Higgs field background h_c during inflation and reheating.

Within an anthropic attitude, one could say that the electroweak SM instability is beneficial to our own existence as DM is necessary to form structures. In the absence of other DM candidates, the SM would be able to provide the right DM abundance. As discussed below, although the parameter choices needed for PBH formation might seem finetuned, they would be motivated anthropically. In particular, this mechanism offers an anthropic explanation of why the electroweak vacuum is metastable (but near-critical, very close to being stable).

4.2 Dynamics of the Higgs background and fluctuations

4.2.1 Quantum fluctuations during inflation

During inflation, which is necessary to explain the anisotropies in the cosmic microwave background radiation as well as to provide the seeds for the large-scale structure, the Higgs field is

subject to quantum fluctuations as any other field lighter than the Hubble rate H [313]. We are agnostic about the details of the model of inflation and the origin of the curvature perturbation responsible for the CMB anisotropies, which we call ζ_{st} . This ζ_{st} might be caused by a single degree of freedom [312] or by another mechanism such as the curvaton [335]. Also, we take a constant Hubble rate H during inflation and suppose that it ends going through a period of reheating characterised by a reheating temperature T_{RH} . Of course, one can repeat our calculations for a preferred model of inflation. We suppose that H is large enough to have allowed the SM Higgs to randomly walk above the barrier of its potential to probe the potentially dangerous unstable region. As a representative value we take $H \simeq 10^{12}$ GeV, and the running of $\lambda(h)$ that we assume, corresponding to the parameters listed in Eq. (4.43), is shown in Fig. 4.4. We postpone to section 4.5 the discussion about our choice for the running of λ .

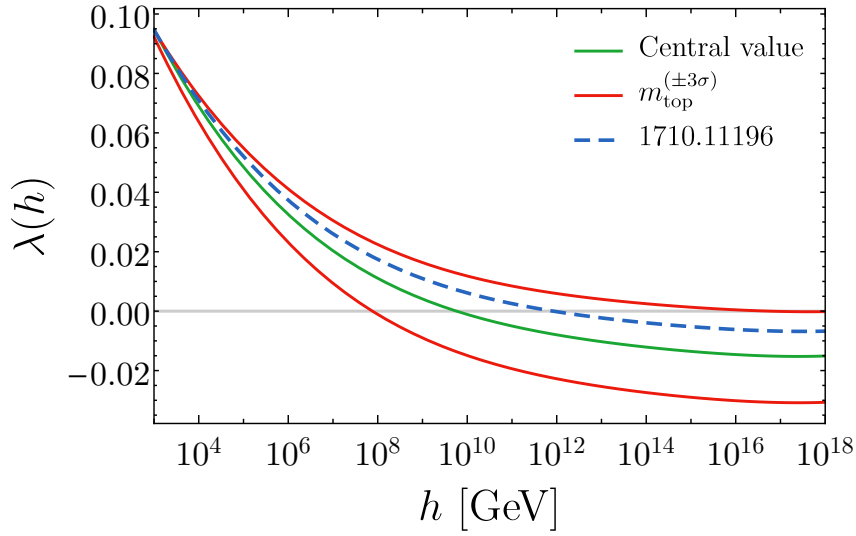


Figure 4.4: Running of λ that we consider in [3] (blue dashed line), together with its central and extremal values [307–309].

In the first phase the Higgs has an initial value much smaller than the instability scale Λ . However, if it is lighter than the Hubble rate H , the background value h_c of the Higgs field keeps receiving each Hubble time kicks of the order of $\pm(H/2\pi)$ and walks randomly. This dynamics is described by the Langevin stochastic equation [313]

$$\ddot{h}_c + 3H\dot{h}_c + V'(h_c) = 3H\eta, \quad V(h_c) \simeq -\frac{1}{4}\lambda h_c^4, \quad (4.2)$$

where dots represent time derivatives and primes field derivatives, η is a Gaussian random noise with

$$\langle \eta(t)\eta(t') \rangle = \frac{H^3}{4\pi^2} \delta(t-t') \quad (4.3)$$

and $\lambda > 0$ runs logarithmically with the field scale. During inflation, λ should in fact be evaluated at a scale μ given by $\mu^2 \simeq h_c^2 + H^2$ [323], but this is not particularly relevant for our scenario where $h_c \gtrsim H$. A typical value (for $h_c \gtrsim 10^{12}$ GeV) is $\lambda \simeq 10^{-2}$.

The Langevin equation (4.2) can be rewritten in a more transparent way by introducing the derivatives with respect to the number of e -folds $N = \ln a/a_i$, so that $dN = Hdt$ and

$$\frac{d^2 h_c}{dN^2} + 3 \frac{dh_c}{dN} + V'(h_c) = 3\bar{\eta}, \quad \langle \bar{\eta}(t)\bar{\eta}(t') \rangle = \left(\frac{H}{2\pi}\right)^2 \delta(t-t'), \quad (4.4)$$

from which it is clear that the stochastic jumps are of order $H/2\pi$ and happen on average every Hubble time.

4.2.2 Quantum to classical transition of the Higgs background

If the Hubble rate is large enough, the Higgs field can climb over the maximum of the potential [313–324]. The Higgs background continues its random walk as long as the quantum diffusion is not counterbalanced by the classical drift, that is the displacement predicted by the equations of motion (4.2) without classical noise:

$$\ddot{h}_c + 3H\dot{h}_c + V'(h_c) = 0, \quad (4.5)$$

In order to make any prediction deterministic and not subject to probability arguments, we are interested in the regime in which the dynamics of the zero mode of the Higgs is dominated by the classical motion rather than by the randomness of the fluctuations. We require therefore that in a Hubble time, $\Delta t = 1/H$, the classical displacement of the Higgs

$$\Delta_{\text{cl}} h_c \simeq \dot{h}_c \Delta t \simeq -\frac{V'(h_c)}{3H^2}, \quad (4.6)$$

is larger (in absolute value) than the quantum jumps

$$\Delta_{\text{q}} h \simeq \pm \left(\frac{H}{2\pi} \right). \quad (4.7)$$

This implies that, inside the inflating region, h_c must be bounded from below for the classical regime to take over:

$$h_c^3 \gtrsim \frac{3H^3}{2\pi\lambda}. \quad (4.8)$$

We call t_* the initial time at which the Higgs starts its classical evolution. In this estimate we assume that the motion of the Higgs is friction dominated, that is $\ddot{h}_c \lesssim 3H\dot{h}_c$. This is true as long as $h_c^2 \lesssim 3H^2/\lambda$. If so, the Higgs is slowly moving for a sufficient number of e -folds.

In our numerical solution of the equations of motion, we take as initial value $h_* \equiv h_c(t_*)$ the value which satisfies Eq. (4.8) with an equality sign, and we assume the initial velocity to be zero, $\dot{h}_c(t_*) = 0$. In reality, both of these quantities have a probability distribution around these central values. We assume these specific values as illustrative for our mechanism. The issue of initial conditions is further discussed in Section 4.6.

The evolution of the classical value of the Higgs can be obtained from Eq. (4.5) if we assume a constant λ and neglect the second derivative term, and reads

$$h_c(t) \simeq \frac{h_*}{[1 - 2\lambda h_*^2(t - t_*)/3H]^1/2}. \quad (4.9)$$

When h_c starts to accelerate and friction gets subdominant, h_c rapidly increases. If we neglect the friction term, we get a solution (see Appendix 4.A for more details) which goes as

$$h_c(t) \simeq \frac{\sqrt{2}}{\sqrt{\lambda}} \frac{1}{(t_p - t)}, \quad (4.10)$$

where t_p is the time when the Higgs hits the pole, something that happens in a finite time. We can rewrite the solution (4.9) in terms of the number N of e -folds till the end of inflation and the final value h_e of the classical Higgs field at the end of inflation:

$$h_c(N) \simeq \frac{h_e}{(1 + 2\lambda h_e^2 N / 3H^2)^{1/2}}, \quad (4.11)$$

We focus on those patches where classicality takes over during the last stages of inflation, say the last 20 e -folds or so. Despite the Higgs negative potential energy, these regions keep inflating as long as the total vacuum energy during inflation is larger, that is, for

$$3H^2 M_{\text{P}}^2 \gtrsim \frac{\lambda}{4} h_c^4, \quad (4.12)$$

where $M_{\text{P}} = 2.4 \cdot 10^{18}$ GeV is the reduced Planck mass.

4.2.3 Excitation of the Higgs fluctuations

Meanwhile, Higgs fluctuations are generated. Perturbing around the slowly-rolling classical value of the Higgs field and accounting for metric perturbations as well, the Fourier transform of the perturbations of the Higgs field satisfy the equation of motion (in the flat gauge)

$$\delta \ddot{h}_k + 3H \delta \dot{h}_k + \frac{k^2}{a^2} \delta h_k + V''(h_c) \delta h_k = \frac{\delta h_k}{a^3 m_{\text{P}}^2} \frac{d}{dt} \left(\frac{a^3}{H} \dot{h}_c^2 \right), \quad (4.13)$$

where a is the scale factor and the last term accounts for the backreaction of the metric perturbations [335, 336]. We have numerically checked that this term in Eq. (4.13) is negligible.

The term proportional to $V''(h_c)$ in Eq. (4.13) has a negative sign, and acts as a driving term for the Higgs fluctuations. In other words, the Higgs background excites a tachyonic instability for its fluctuation. For each given mode, as soon as its physical wavelength becomes larger than the Hubble radius in the last e -folds of inflation, δh_k rapidly grows driven by the rolling down of the Higgs field.

The perturbations are born in the Bunch-Davies vacuum, so we take as an initial value the corresponding solution in the sub-Hubble regime, and a vanishing initial velocity:

$$\delta h_k = \frac{1}{a\sqrt{2k}} e^{ik\eta} \left(1 + \frac{i}{k\eta} \right) \quad \eta \simeq -\frac{1}{aH}, k \gg aH \quad \delta h_k = \frac{1}{a\sqrt{2k}} e^{-\frac{ik}{aH}}. \quad (4.14)$$

The Higgs perturbations will be responsible for the formation of PBHs. In fact, we should deal with the comoving curvature perturbation ζ which is gauge-invariant and reads (still in the flat gauge)

$$\zeta = H \frac{\delta \rho_{\text{tot}}}{\dot{\rho}_{\text{tot}}}. \quad (4.15)$$

We can rewrite this expression in terms of the Higgs perturbation $\zeta_h \equiv H \delta \rho_h / \dot{\rho}_h$, with $\delta \rho_h = \rho(h_c + \delta h) - \rho(h_c)$, and the inflaton perturbation $\zeta_{\text{st}} \equiv H \delta \rho_{\text{infl}} / \dot{\rho}_{\text{infl}}$, where the superscript st stands for standard:

$$\zeta = H \frac{\delta \rho_{\text{infl}} + \delta \rho_h}{\dot{\rho}_{\text{tot}}} = \frac{\dot{\rho}_{\text{infl}}}{\dot{\rho}_{\text{tot}}} \zeta_{\text{st}} + \frac{\dot{\rho}_h}{\dot{\rho}_{\text{tot}}} \zeta_h. \quad (4.16)$$

We assume ζ_{st} is conserved during inflation on super-Hubble scales and, for simplicity, that there is no energy transfer with Higgs fluctuations. The splitting of Eq. (4.16) highlights that

on large scales the dominant contribution is the standard one, whereas for the wavelengths leaving the Hubble radius the last 20 e -folds or so of inflation, the gauge-invariant comoving curvature perturbation $\zeta(\mathbf{x})$ is dominated by the Higgs perturbations.

The dimensionless power spectrum of the curvature perturbation is then defined as

$$\mathcal{P}_\zeta = \frac{k^3}{2\pi^2} |\zeta_k|^2. \quad (4.17)$$

This is the crucial quantity for the computation of the PBH mass function. In the next subsections we solve numerically the system of coupled equations of motion for h_c and δh_k , whereas in Section 4.3 we estimate analytically $\mathcal{P}_\zeta(k)$.

4.2.4 Dynamics after inflation: reheating

At the end of inflation at the time t_e , the vacuum energy which has driven inflation gets converted into thermal relativistic degrees of freedom, a process dubbed reheating. For simplicity, we suppose that this conversion is instantaneous (*instantaneous reheating*), in such a way that the reheating temperature is $T_{\text{RH}} \simeq 0.5 \cdot (H M_{\text{P}})^{1/2}$, obtained by energy conservation and taking the number of relativistic degrees of freedom to be about 10^2 . For our representative value of $H = 10^{12}$ GeV, we obtain $T_{\text{RH}} \simeq 10^{15}$ GeV. Again, one can redo the computation within a favourite model of inflation. Generically, the mechanism we describe tends to require a rather fast reheating process, in order for the thermal corrections to help rescuing quickly the Higgs field.

As we have seen in Section 4.1, due to the thermal effects, the Higgs potential receives thermal corrections such that the potential is quickly augmented by the thermal contribution of Eq. (4.1) [324]. This is due to the energy transfer between the long wavelength Higgs perturbations and the thermal plasma, as the effective Higgs mass suddenly jumps to its thermal value induced by the interactions with the plasma.

If the maximum temperature is larger than the value of the Higgs $h_e \equiv h_c(t_e)$ at the end of inflation, or more precisely if

$$T_{\text{RH}}^2 \gtrsim \lambda h_e^2, \quad (4.18)$$

the corresponding patch is thermally rescued and the initial value of the Higgs immediately after the end of inflation coincides with h_e . The classical value of the Higgs field starts oscillating around the origin, see Fig. 4.5. The Higgs fluctuations oscillate as well with the average value remaining constant and the amplitude slowly increasing for a fraction of e -folds.

After the end of inflation, the long wavelength Higgs perturbations decay after several oscillations into radiation curvature perturbation which, being radiation now the only component, will stay constant on super-Hubble scales (see section 4.3 for a more detailed discussion).

The Higgs damping rate is negligible during the inflationary phase. At zero temperature the Higgs width can be roughly estimated by the decay in the $b\bar{b}$ channel, so that $\gamma_h \sim y_b^2 m_h / (8\pi) \sim y_b^2 \sqrt{\lambda} h_c / (8\pi) \lesssim 10^{-2} H \ll H$. The Higgs damping rate at finite temperature is instead [337]

$$\gamma_h \sim \frac{3g^4 T^2}{256\pi m_T} \sim 10^{-3} T, \quad (4.19)$$

where g is the $SU(2)_L$ coupling constant. This value has been derived by noticing that for a thermal Higgs mass $m_T \simeq 0.34 T$, the one-loop absorption and direct decay channels for quarks and gauge bosons are forbidden, and the damping occurs through two-loop diagrams involving gauge bosons.

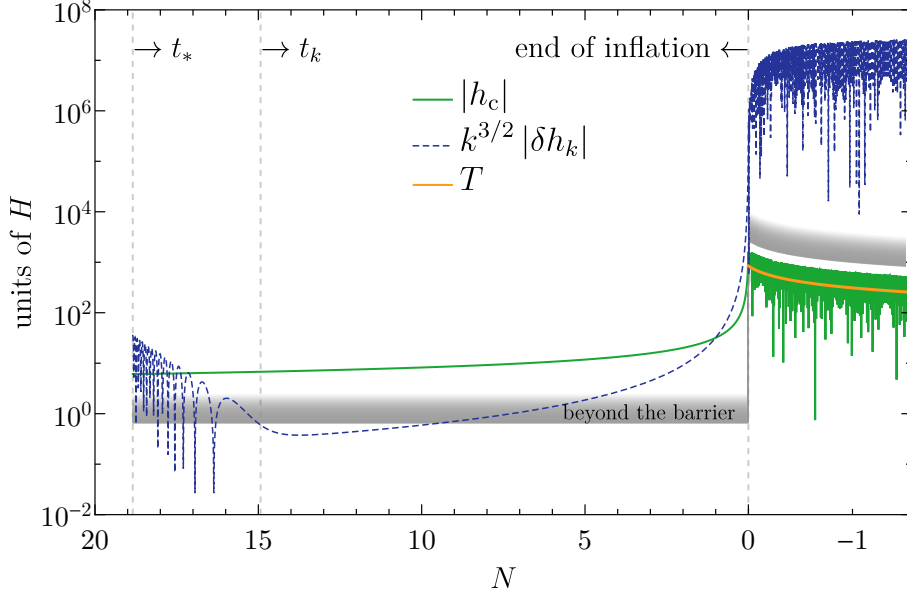


Figure 4.5: Evolution of H , T , h_c , δh_k during the last e -folds of inflation, for $k = 50 k_*$. The region of h_c beyond the top of the potential barrier is shaded gray.

A proper inclusion of the Higgs damping rate would be rather simple for the background (by including a factor $+\gamma_h \dot{h}_c$ in the equations of motion), whereas the study of perturbations by properly accounting for the damping rate is much more complicated [338]. It is reasonable to apply the *sudden decay approximation*, which amounts to assuming that the Higgs field decays instantaneously after a time γ_h^{-1} into radiation. Therefore, we have evaluated the value of the curvature perturbation a small fraction of e -fold after t_e .

The final outcome of this mechanism are large adiabatic perturbations on small scales ($k > k_* = a(t_*)H$).

4.3 Analytical estimates of the comoving curvature perturbations

In this section we offer some analytical insight of the numerical results presented in Fig. 4.5 and 4.8. We analyse the dynamics of the Higgs background and fluctuations first during inflation, and then during the subsequent thermal phase. The main results are that the fluctuations δh_k , during their tachyonic excitation in the inflationary phase, grow as the speed of the background \dot{h}_c , and the formula (4.33) for the final power spectrum of curvature perturbations, which eventually determines the PBH mass function.

4.3.1 Curvature perturbations during inflation

In order to estimate analytically ζ_k (Eq. 4.15) and then \mathcal{P}_ζ , it is useful to find a relation between the behaviour of the Higgs fluctuations δh_k and the background h_c . If we consider for δh_k the super-Hubble regime, where the term proportional to k^2 in Eq. (4.13) is negligible, and we take

the time derivative of the Eq. (4.5) assuming a constant Hubble rate, we get

$$\begin{aligned} (\dot{h}_c)'' + 3H(\dot{h}_c)' + V''(h_c)\dot{h}_c &= 0, \\ \delta\ddot{h}_k + 3H\delta\dot{h}_k + V''(h_c)\delta h_k &= 0. \end{aligned} \quad (\text{inflation, super-Hubble}) \quad (4.20)$$

We see that \dot{h}_c and δh_k solve the same equation on scales larger than the Hubble radius $k \ll aH$. Therefore the two quantities must be proportional to each other during the evolution and on super-Hubble scales:

$$\delta h_k(t) = C(k) \dot{h}_c(t). \quad (\text{inflation, super-Hubble}) \quad (4.21)$$

The growth of δh_k is therefore dictated by the growth of \dot{h}_c . To find the function $C(k)$ we can start from the solution for δh_k : perturbations are born with the standard Bunch-Davies vacuum, and deep in the sub-Hubble regime we find the solution (4.14). By matching this sub-Hubble solution at Hubble crossing $k = a(t_k)H$ with the ansatz of Eq. (4.21) for the super-Hubble regime we find

$$C(k) = \frac{H}{\dot{h}_c(t_k)\sqrt{2k^3}}, \quad (4.22)$$

where t_k is the time when the mode with wavelength $1/k$ leaves the Hubble radius.

Using Eq. (4.5) and (4.13) (again with the negligible last term dropped), one then obtains

$$\delta\rho_h(k \ll aH) = \dot{h}_c\delta\dot{h}_k + V'(h_c)\delta h_k = C(k)\dot{h}_c \left[\ddot{h}_c + V'(h_c) \right] = -3HC(k)\dot{h}_c^2. \quad (4.23)$$

Since $\dot{\rho}_h = \dot{h}_c(\ddot{h}_c + V'(h_c)) = -3H\dot{h}_c^2$, one can easily show (and we have checked it numerically) that during inflation and on super-Hubble scales ζ_h reaches the plateau

$$\zeta_{h_k}(k \ll aH) = H \frac{\delta\rho_{h_k}}{\dot{\rho}_h} = HC(k) = \frac{H^2}{\sqrt{2k^3}\dot{h}_c(t_k)}. \quad (4.24)$$

This is the quantity which gives the largest contribution to ζ in the last few e -folds before the end of inflation.

Within our approximation of constant energy density of the inflaton, $\dot{\rho}_{\text{infl}} = 0$ and $\dot{\rho}_{\text{tot}} = \dot{\rho}_h$, so that $\zeta = \zeta_h$ and (to avoid a heavy notation, we denote $\mathcal{P}_\zeta \equiv \mathcal{P}_{\zeta_k}, \mathcal{P}_{\zeta_h} \equiv \mathcal{P}_{\zeta_{h_k}}$)

$$\mathcal{P}_\zeta(t_e) = \mathcal{P}_{\zeta_h}(t_e) = \frac{k^3}{2\pi^2} |\zeta_k(t_e)|^2 = \left(\frac{H}{2\pi} \right)^2 \left(\frac{H}{\dot{h}_c(t_k)} \right)^2. \quad (\text{inflation}) \quad (4.25)$$

4.3.2 Curvature perturbations during reheating

Similarly to what we have done in the previous subsection, we would like to derive a relation between δh_k and h_c or its derivatives in order to estimate analytically \mathcal{P}_ζ . The derivation of Eq. (4.20) used the constancy of the Hubble rate during inflation, which does not hold during the reheating phase. Nevertheless, given that the leading term in the Higgs potential is the thermal correction of Eq. (4.1) which is quadratic in h_c , we can see that during this phase δh_k is directly proportional to h_c (we write explicitly $H(t)$ in the following to distinguish it from the

constant Hubble parameter H during inflation, and we neglect the decay term as explained in Section 4.2.4):

$$\begin{aligned} \ddot{h}_c + 3H(t)\dot{h}_c + m_T^2 h_c &= 0, \\ \ddot{\delta h}_k + 3H(t)\dot{\delta h}_k + m_T^2 \delta h_k &= 0. \end{aligned} \quad (\text{reheating, super-Hubble}) \quad (4.26)$$

Therefore during the reheating phase $\delta h_k(t)$ tracks $h_c(t)$,

$$\delta h_k(t) = D(k) h_c(t). \quad (\text{reheating, super-Hubble}) \quad (4.27)$$

To estimate the constant $D(k)$ we can apply Eq. (4.27) at the time t_e , and by continuity we can use the relation (4.21) to get

$$D(k) = \frac{\delta h_k(t_e)}{h_c(t_e)} = C(k) \frac{\dot{h}_c(t_e)}{h_c(t_e)} = \frac{H}{\sqrt{2k^3}} \frac{\dot{h}_c(t_e)}{h_c(t_e)\dot{h}_c(t_k)}. \quad (4.28)$$

The perturbations in the energy density come from the Higgs sector, and we can rewrite them as

$$\delta\rho_{\text{tot}} = \delta\rho_h = \dot{h}_c\delta\dot{h}_k + m_T^2 h_c \delta h_k = D(k)(\dot{h}_c^2 + m_T^2 h_c^2) = 2D(k)\rho_h. \quad (4.29)$$

Another important observation is that the Higgs field during the thermal phase and before decaying follows the equation of state of a radiation component, $\dot{\rho}_h = -4H(t)\rho_h$, because of the time dependence of the time dependence of the Higgs mass through the temperature. Indeed, up to fast oscillations of frequency T , the classical Higgs field scales like $h_c(a) \sim 1/a \sim T$, and one can check that, when averaging over some oscillations,

$$\langle \dot{h}_c^2 \rangle = \langle m_T^2 h_c^2 \rangle, \quad (4.30)$$

and therefore

$$\begin{aligned} m_T(t) \sim T(t) \sim a^{-1}(t) &\implies \dot{m}_T/m_T = -H(t), \\ \dot{\rho}_h = \dot{h}_c\ddot{h}_c + m_T^2\dot{h}_c h_c + m_T\dot{m}_T h_c^2 &= -3H(t)\dot{h}_c^2 - H(t)m_T^2 h_c^2 \xrightarrow{\text{averaging}} \dot{\rho}_h = -4H(t)\rho_h. \end{aligned} \quad (4.31)$$

With the use of Eqs. (4.28), (4.29), (4.31) we obtain the total curvature perturbation:

$$\begin{aligned} \zeta(t_{\text{dec}}) &= H(t) \frac{\delta\rho_{\text{tot}}(t_{\text{dec}})}{\dot{\rho}_{\text{tot}}(t_{\text{dec}})} = H(t) \frac{\dot{\rho}_h(t_{\text{dec}})}{\dot{\rho}_{\text{tot}}(t_{\text{dec}})} \frac{\delta\rho_h(t_{\text{dec}})}{\dot{\rho}_h(t_{\text{dec}})} = H(t) \frac{\rho_h(t_{\text{dec}})}{\rho_{\text{tot}}(t_{\text{dec}})} \frac{\delta\rho_h(t_{\text{dec}})}{\dot{\rho}_h(t_{\text{dec}})} = \\ &= -\frac{r_h(t_{\text{dec}})}{4} \frac{\delta\rho_h(t_{\text{dec}})}{\rho_h(t_{\text{dec}})} = -\frac{r_h(t_{\text{dec}})}{2} D(k) = -\frac{r_h(t_{\text{dec}})}{2} \frac{H}{\sqrt{2k^3}} \frac{\dot{h}_c(t_e)}{h_c(t_e)\dot{h}_c(t_k)} \end{aligned} \quad (4.32)$$

where we have introduced the energy fraction of the Higgs field $r_h = \rho_h/\rho_{\text{tot}}$.

In particular, notice that ζ_h during inflation does not coincide with the value during reheating (Eq. 4.24), signalling that ζ_h is not conserved during the transition. This is not surprising, as the Higgs interacts with the hot plasma to suddenly acquire a plasma mass and therefore is not an isolated fluid. The final power spectrum reads

$$\mathcal{P}_\zeta(t_{\text{dec}}) = \frac{k^3}{2\pi^2} |\zeta_k(t_{\text{dec}})|^2 = \frac{r_h^2(t_{\text{dec}})}{4} \left(\frac{H}{2\pi} \right)^2 \left(\frac{\dot{h}_c(t_e)}{h_c(t_e)\dot{h}_c(t_k)} \right)^2. \quad (\text{reheating}) \quad (4.33)$$

4.4 Primordial Black Holes as Dark Matter

Primordial Black Holes (PBH) constitute a class of DM candidates which was proposed many decades ago but was rather overlooked until recently, when they have attracted more attention at the dawn of the Gravitational Wave (GW) era. They are Black Holes (BH) which originated not from the latest stages of collapse of stars in recent epochs, but in the early history of the Universe from overdensities of the matter fluid. Their phenomenology would be rather similar to the one of MACHOs (discussed in Section 1.2.2), but with some other important peculiar features and a much wider (a priori) possible mass range. Today PBHs represent a testable candidate for DM with many prospects for their detection through various phenomena, and the existence of light PBHs could allow the detection of the Hawking-Bekenstein radiation.

Section 4.4.1 introduces PBHs and highlights the motivations for their study. In Section 4.4.2 we summarise their formation process, and in Section 4.4.3 we discuss the current constraints. Section 4.4.4 briefly collects the main proposed models for the generation of a PBH population.

4.4.1 Motivations and prospects for Primordial Black Holes

The first proposals for PBH date back to the early history of Cosmology: in 1966 Zel'dovich and Novikov discussed the fate of regions with large overfluctuations in the density contrast [339, 340], and in 1971 Hawking discussed properties of PBHs of Planckian mass [341]. Curiously, Hawking's paper predates his proposal of BH evaporation of 1974, which gave immediately another motivation for the study of PBH: the evaporation process (by the emission of the so-called Hawking-Bekenstein radiation) is completely negligible unless the BH mass is $\lesssim 10^{-17} M_{\odot}$, a mass range which is only attainable if the BH is of primordial origin. Then, in 1975, Chapline advanced the idea that PBHs could be a DM candidate [342].

The phenomenology of PBHs and the collapse of relativistic fluids in a FLRW universe have been studied in the last decades, with alternate phases of interest, until the recent dawn of the GW era, when they attracted a big deal of attention. The direct observation by the LIGO collaboration of the GWs emitted during the merging of two BHs of masses $\sim 30 M_{\odot}$ in 2015 [343] has opened many new exciting directions for the exploration of BHs through the detection of GWs, reviving the activity in the field of PBHs. For recent comprehensive reviews on PBHs, see [344–346].

The existing observational bounds on PBH populations in the Universe, exposed in Section 4.4.3, are conspicuous in many mass ranges, but leave still some windows open for PBHs to constitute the totality of DM. In the forecoming years we can expect significant progress in the reconsideration and improvement of observational constraints in various mass ranges, and in the study of the formation of Large Scale Structures seeded by PBHs [347]. These efforts could allow us to definitively exclude PBHs as a DM candidate, or to accumulate soon a significant amount of evidence in their favour.

We can identify at least two clear smoking gun signatures of the existence of PBHs. As a first possibility, BH at a redshift $z \gtrsim 30$ would have arisen before the formation of the first stars. Alternatively, a BH with mass $\lesssim 1 M_{\odot}$ (at any epoch) cannot have originated from stellar evolution because of the Chandrasekar limit for the minimum mass required for the gravitational attraction to overcome the electron degeneracy pressure. Observing BHs with one of these features would be an indisputable evidence for PBH.

Currently, an arguable hint in favour of PBHs comes from the observations of SuperMassive Black Holes (SMBH), with masses around $10^5 - 10^{10} M_{\odot}$, located in the centre of galaxies at redshifts up to around 10. SMBH with masses of the order of billions of solar masses are considered too heavy to form within the age of the universe from the collapse of matter at the

centre of galaxies, unless one can explain how to get heavy enough seeds for their formation. The observation of SMBHs so back in the past (at $z \lesssim 6$) further corroborates the hypothesis that they could seed from heavy PBHs, although the issue is far from being settled. In particular, Intermediate Mass Black Holes (IMBH) with masses $10 - 10^4 M_\odot$ could act as seeds for SMBHs in galactic nuclei [347] (see [348] for a review on IMBH).

The (progenitor) BHs observed by LIGO and Virgo so far lie between 8 and $40 M_\odot$, which approximately coincides with the sensitivity window of the instruments. This mass range is expected for astrophysical BHs [349], so that we cannot claim so far that the BHs observed by LIGO are primordial, although it is an intriguing possibility [350]. A possible evidence for PBHs could be the observation of merging bodies with mass in the ranges $[2, 5] M_\odot$ or $[50, 130] M_\odot$, which do not comprise neutron stars and astrophysical BHs [351]. Objects within these mass ranges would be either primordial or the outcome of mergers of astrophysical BHs, and in the latter case they should display a high spin on average (due to the conservation of angular momentum). PBHs, on the contrary, are generically expected to have a nearly vanishing spin, having arisen from the collapse of a distribution of matter without a significant vorticity.

We refer to Section 4.4.3 for other prospects for the detection of PBH through other physical mechanisms.

4.4.2 Formation of Primordial Black Holes

PBHs form from overdensities of order one of the density contrast on small scales, much larger than its average value 10^{-5} on the scales that we probe through the Cosmic Microwave Background (CMB). For an overview of some proposals for the amplifications of perturbations on small scales, see Section 4.4.4. Once these large perturbations are generated during the inflationary phase, they remain outside the Hubble radius until the corresponding mode crosses again the Hubble radius during the radiation dominated epoch following the reheating phase. After inflation, the Hubble radius grows and the perturbations generated during the last e -folds of inflation are the first to reenter the horizon. If they are large enough, they collapse to form PBHs almost immediately after horizon reentry, as sketched in Fig. 4.6. A region of the size of the Hubble radius then decouples from the background expansion, and due to the large spatial curvature the matter contained within that region collapses to form a PBH.

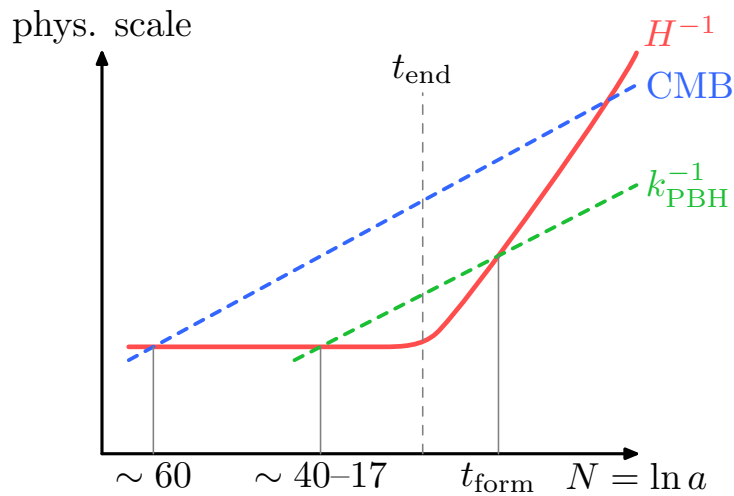


Figure 4.6: PBH form when the corresponding scale enters the Hubble radius during the RD era.

The assessment of the criterion for collapse involves a study of the evolution of perturbations in a FLRW universe filled by a relativistic fluid [344, 345], and a full treatment has to include to shape in the physical space of the density profile of the perturbation [352, 353].

As a simplified rule of thumb for collapse, which approximates reasonably the results of a more detailed analysis, current literature sets a critical threshold Δ_c to be overstepped by the density contrast $\Delta(\mathbf{x}) \equiv (\rho(\mathbf{x}) - \bar{\rho})/\bar{\rho}$, $\bar{\rho}$ being the average energy density. The density contrast expressed on comoving slices can be written in terms of the gauge invariant comoving curvature perturbation $\zeta(\mathbf{x})$ (defined in Eq. 4.15) as (at linear order in ζ , and during the radiation era)

$$\Delta(\mathbf{x}) = \frac{4}{9a^2H^2} \nabla^2 \zeta(\mathbf{x}), \quad (4.34)$$

where a is the scale factor and H is the Hubble rate. Typically $\Delta_c \sim 0.45$ [354]. The emergence of a rather sharp threshold is a result of the balance between the gravity force needed for the collapse and the pressure of radiation: an overdense region just below threshold will eventually lose most of its matter if there is no collapse [355].

The mass of a PBH at formation is then computed as the mass contained within a sphere of radius H^{-1} , up to an efficiency factor γ , which is estimated analytically to be 0.2 [356]:

$$M_{\text{PBH}} = \gamma \frac{4\pi}{3} \rho H^{-3}, \quad (4.35)$$

ρ being the energy density at the collapse time. This can be rewritten in terms of the comoving wavenumber k corresponding to the scale of the collapse, or the number N of e -folds before the end of inflation when k leaves the Hubble radius as [357, 358]

$$\begin{aligned} M_{\text{PBH}} &= 5 \cdot 10^{-16} M_{\odot} \left(\frac{\gamma}{0.2} \right) \left(\frac{g(T_f)}{106.75} \right)^{-\frac{1}{6}} \left(\frac{k}{7 \cdot 10^{13} \text{ Mpc}^{-1}} \right)^{-2} = \\ &= \left(\frac{\gamma}{0.2} \right) \frac{10^{13} \text{ GeV} \cdot H_e}{H_k^2} e^{2(N-37.9)} M_{\odot} \end{aligned} \quad (4.36)$$

where $g(T_f)$ is the number of relativistic degrees of freedom at the temperature of the formation time of the PBH, H_k is the Hubble rate at the time when the mode k exits the Hubble radius (that is $a(t_k)H_k = k$) and H_e is the Hubble rate at the end of inflation. From Fig. 4.6 and Eq. (4.36) we can see that a PBH generated at a scale k^{-1} is more massive if the mode k re-enters the horizon later at RD, or equivalently if it left earlier the Hubble radius during inflation.

The number of PBHs which are generated depends on the probability of exceeding the threshold Δ_c . For simplicity, we assume that the probability distribution for Δ is Gaussian, although non-Gaussian deviations usually play an important role given that we look at the tail of the distribution [359]. We define the formation rate $\beta(M)$, which is the mass fraction of the universe which ends up into PBHs at the time of formation, as the probability that the density contrast $\Delta(k)$ exceeds Δ_c (the one-to-one correspondence between M and k is established by Eq. 4.36):

$$\beta(M) = \int_{\Delta_c}^{\infty} \frac{d\Delta}{\sqrt{2\pi} \sigma_{\Delta}} e^{-\Delta^2/2\sigma_{\Delta}^2} \simeq \frac{\sigma_{\Delta}}{\Delta_c \sqrt{2\pi}} e^{-\Delta_c^2/2\sigma_{\Delta}^2}, \quad (4.37)$$

where in the last step we have taken the limit $\Delta_c \gg \sigma_{\Delta}$ (typically, for the formation of PBHs, $\sigma_{\Delta} \sim \mathcal{O}(10^{-2})$).

Within the Gaussian approximation, the only parameter involved in the distribution function of Δ is the variance σ_{Δ} , the variance of the density contrast smoothed with a Gaussian

window function $W(q, R) = \exp[(qR)^2/2]$ at a scale $R = k^{-1}$:

$$\sigma_{\Delta}^2(M(k)) = \int_0^{\infty} d \ln q W^2(q, R) \mathcal{P}_{\Delta}(q) = \int_0^{\infty} d \ln q \frac{16}{81} \left(\frac{q}{k}\right)^4 e^{-(q/k)^2} \mathcal{P}_{\zeta}(q), \quad (4.38)$$

where the last step follows from Eq. (4.34).

After their formation, PBHs behave as matter and their energy density scales just as a^{-3} , whereas the average energy density in the rest of the universe decreases as a^{-4} until the time t_{eq} of matter-radiation equality. After t_{eq} , the energy fraction of PBHs stays constant. The resulting abundance of PBHs per logarithmic mass interval ($d \ln M$) is [360] (the value of $\Omega_m h^2$ is replaced by the value (1.1) measured by Planck)

$$\begin{aligned} f_{\text{PBH}}(M) &= \frac{\Omega_{\text{PBH}}(M)}{\Omega_{\text{CDM}}} = \frac{\rho_{\text{PBH}}}{\rho_m} \Big|_{t_{\text{eq}}} \frac{\Omega_m h^2}{\Omega_{\text{CDM}} h^2} = \\ &= \frac{\beta(M)}{1.6 \cdot 10^{-16}} \left(\frac{\Omega_{\text{CDM}} h^2}{0.12}\right)^{-1} \left(\frac{\gamma}{0.2}\right)^{\frac{3}{2}} \left(\frac{g(T_f)}{106.75}\right)^{-\frac{1}{4}} \left(\frac{M}{5.0 \cdot 10^{-16} M_{\odot}}\right)^{-\frac{1}{2}}. \end{aligned} \quad (4.39)$$

The total contribution of PBHs to the energy density of the universe is (without accounting for the PBHs lighter than $\sim 10^{-18} M_{\odot}$ which have completely evaporated, see Sec. 4.4.3)

$$\Omega_{\text{PBH}} = \Omega_{\text{CDM}} \int d \ln M f_{\text{PBH}}(M). \quad (4.40)$$

Apart from evaporation, which is completely negligible for $M_{\text{PBH}} \gtrsim 10^{-16} M_{\odot}$, there are two phenomena which transform the PBH mass function at late times. The first effect is the merging of BHs, which shifts and spreads to higher values the mass function without changing the total abundance. Another important phenomenon is the accretion of radiation and matter into BHs, which increases the abundance (and shifts to higher values the mass function). These two effects can affect importantly the mass function, with an increase of the abundance and a shift to higher masses up to a few orders of magnitude, but accounting for them seems hardly feasible without numerical simulations.

4.4.3 Constraints on Primordial Black Holes

In this section we quickly review the main current constraints on the PBH mass function, collected in Fig. 4.7. See also [345] for a recent review.

The bounds of Fig. 4.7 refer to a monochromatic PBH mass function: for the realistic case of an extended mass function, the constraints are slightly modified by a slight attenuation of the dips, and a moderate increase in the transition regions between adjacent bounds [344, 361, 362]. Moreover, PBHs are expected to be created in clusters, given that they arise from rare peaks of the density contrast, and an overdense region on a large scale hosts more easily many higher subpeaks which can form PBHs. As long as observational constraints are concerned, clustering of PBHs could alleviate many bounds [363].

Evaporation The evaporation of BHs through the Hawking-Bekenstein radiation is described semiclassically as the physical emission of particles generated through virtual pair creation around the event horizon at the expenses of the BH mass. The emitted radiation has a black-body spectrum with a temperature going as $1/M_{\text{BH}}$, corresponding to a peak at a wavelength of about 16 times the Schwarzschild radius. The emitted power is proportional to $1/M_{\text{BH}}^2$, so

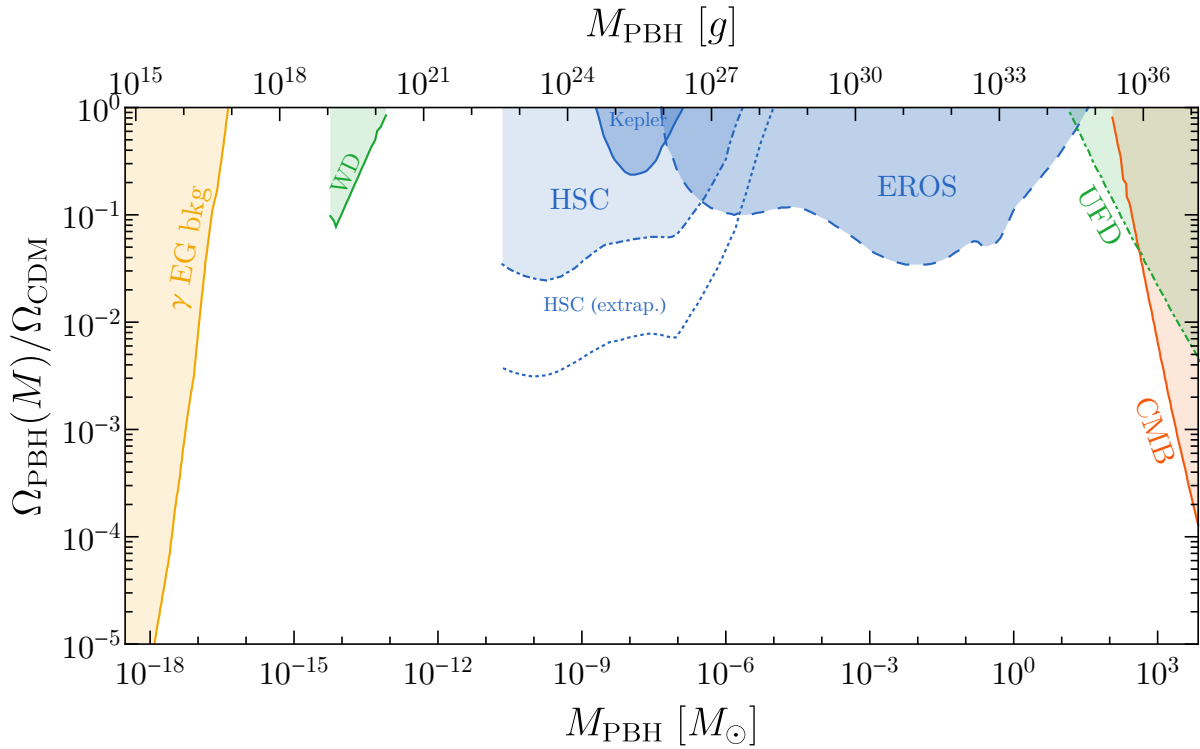


Figure 4.7: Experimental constraints on monochromatic PBH spectra (see the text for details): In yellow, the observations of extra-galactic γ -ray background; in blue, micro- and milli-lensing observations from Eros, Kepler, Subaru HSC; in green, dynamical constraints from White Dwarves and Ultra-Faint Dwarf galaxies; in orange, constraints from the CMB (adapted from [360]).

this process turns out to be completely negligible unless $M_{\text{BH}} \lesssim 10^{-16} M_{\odot}$, corresponding to a wavelength $\lesssim 10^{-13}$ m, in the γ -ray band for emitted photons. As mentioned in Section 4.4.1, because of the tiny emittance power, the evaporation process is observable only for extremely light BHs, whose origin can only be primordial.

The evaporation time (proportional to M_{BH}^3) is shorter than the age of the universe for $M_{\text{PBH}} \lesssim 10^{-19} M_{\odot}$: PBHs below this mass wouldn't exist any more today. In the range $10^{-19} M_{\odot} \lesssim M_{\text{PBH}} \lesssim 10^{-16} M_{\odot}$ the emitted power would be sizeable today, and we could detect a contribution to the extragalactic γ -ray background. The null results in this direction from the observations of EGRET and Fermi-LAT were recast in [364]. Ref. [365] obtained similar bounds from the analysis of the e^{\pm} fluxes measured by the satellites Voyager-1 and AMS.

In principle, the collapse of an overdense region could lead to a final exotic GR configuration different from a Schwarzschild BH, in particular without an event horizon, so that the evaporation process would be suppressed [366]. Apart from this speculative scenario, given the robustness of the theoretical prediction of the Hawking-Bekenstein radiation, we can consider this constraint very solid.

CMB constraints If PBHs were affecting their environment significantly between their formation time and recombination, they could have influenced the CMB that we observe. During the RD epoch though, PBHs do not accrete much due to the radiation pressure, unless the PBH is a few orders of magnitude heavier than M_{\odot} . Updated analyses of the effects due to the interference of the PBH accretion activity on the CMB were performed in [367–370] and yield the

bound shown in Fig. 4.7, which identifies an upper mass $\sim 10^2 M_\odot$ for the PBHs to constitute the totality of DM. This and other constraints reinforce the upper limit of about $10^3 M_\odot$ for the PBHs to constitute a significant fraction of DM.

Lensing A phenomenological signature that PBHs share with MACHOs (discussed in Section 1.2.2) is the lensing of light coming from background objects. During the passage of a PBH close to the line of sight to a distant object, it gravitationally deflects the light rays so that more of them reach the observer. The result is an amplification of the apparent magnitude of the object, which reaches a peak when the PBH gets closest to the line of sight and then gradually decreases, until the lensed object reaches its normal magnitude. The time dependence of the apparent magnitude takes the name of Alcock-Paczynski curve.

The time duration of this process is directly proportional to the Einstein radius $r_E \sim \sqrt{r_S D}$ where $r_S = 2GM_{\text{PBH}}$ is the Schwarzschild radius of the lens and D is the distance to the lens (assumed to be comparable to the distances to the lens and between lens and source). Indeed, only light rays within r_E from the lens are deflected appreciably. Therefore, the observation time (together with the distance of the survey) determines the mass range probed by experiments aiming at observing lensing events. To give an idea of the orders of magnitude, PBHs with $M_{\text{PBH}} \sim (10^{-5} - 1) M_\odot$ require an observation time ranging between seconds and weeks, and for $M_{\text{PBH}} \sim 10 - 100 M_\odot$, years of observation are required.

In Fig. 4.7 we show the main lensing constraints. Two of these experiments had a sensitivity for millisecond lensing events. The EROS experiment, designed for the search for MACHOs, observed stars in the Large and Small Magellanic clouds (at 50 – 60 kpc from us) [371], and Kepler aimed at near stars within 1 kpc [372]. The (unfortunately short) observations of the satellite Subaru HSC of microsecond lensing of stars in M31, at 770 kpc from us, were used in [373] to constrain the range $10^{-11} - 10^{-6} M_\odot$. The dot-dashed line blue in Fig. 4.7 is a more conservative bound, and the dotted blue line comes from an extrapolation from the Panchromatic Hubble Andromeda Treasury (PHAT) catalogues [374] in the disk region. Another lensing bound that we do not show in Fig. 4.7 comes from the observation of type IA supernovae, and constrains the abundance of PBHs above $1 M_\odot$ [375, 376]

All of the previous observations were performed in the optical light window. The observations of the Fermi-GRB (Gamma-Ray Burst monitor) of γ -ray bursts of known redshift look for femtosecond lensing events, and were used in [377] to constrain the low mass range $10^{-15} - 10^{-17} M_\odot$. Recently, this derivation has been questioned by Ref. [378]. They analyse in detail two effects; the finite size of the sources, and the breakdown of geometrical optics when assuming that light rays follows two paths around the lens. As a result, current measurements do not constraint the PBH abundance, but we could achieve the required sensitivity in the future [378].

An important phenomenon which was unaccounted for in the recast of the constraints by Subaru is the so called wave effect [379, 380]. If the wavelength λ of the observed light is smaller than the Schwarzschild radius r_S of the lenses, then geometrical optics ceases to be a good approximation, and the diffraction of light from the small lens gives small or vanishing magnification of the source. One could wonder why r_S is a relevant quantity in this context, given that the deflected images of the source travel at a distance $r_E \gg r_S$ from the lens. The reason is the following, and has to do with the expression of the Einstein radius $r_E \sim \sqrt{r_S D}$. We denote by D the distance from us to the lens, which we assume for simplicity to be of the same order as the distance between lens and source. The lensed rays travelling at opposite sides of the lens, can be seen as a double slit interference experiment. The first maxima of the diffracted pattern are at angles $\theta_1 \sim \lambda/r_E$, r_E being the distance of the slits. The deflected rays

form an angle $\theta_S \sim r_E/D$ with respect to the line to the PBH. If this angle is much larger than θ_1 , then the interference pattern is not resolvable, the wave effects of light diffusion are negligible and the background objects are magnified by the PBH. If instead $\theta_S < \theta_1$, then the interference pattern is appreciable, and the geometrical optics approximation breaks down. The condition for magnification $\theta_S \gtrsim \theta_1$ implies $\lambda \lesssim r_E^2/D \sim r_S$. For the Subaru HSC observations, the wavelength of visible light corresponds to the Schwarzschild radius for $M_{\text{PBH}} \sim 10^{-11} M_\odot$, and therefore we remove the constraint below that value.

Dynamical constraints The presence of PBHs in the galaxy could interfere with the life cycle of stars. PBHs would be rather sparse in the galaxy: even for PBHs as light as $10^{-16} M_\odot$ (the mass of an asteroid, or of Mount Everest), whose $r_S \sim 10^{-13}$ m is of subnuclear size, there would be a few in our Solar system. The heavier they were, the sparser they would be.

In the low mass range, PBHs could be dense enough to encounter along their motion White Dwarves (WD), compact stars which could be dynamically heated by PBHs and explode as supernovae too often to account for the observed WD density [381]. This prevents PBHs of mass $10^{-14} - 10^{-13} M_\odot$ from forming all of DM.

Neutron Stars (NS), much denser than WD, would trap PBHs within a longer time through multiple oscillation around the NS. This happens more easily if the velocity of the PBHs is small. It was suggested [382] that NS could offer a probe of the presence of PBHs in the cores of globular clusters, where the velocity dispersion is typically $\mathcal{O}(10)$ km/s. The bound obtained in [382], falling in the range $10^{-14} - 10^{-10} M_\odot$, assumed a DM density in globular cluster which 10^2 to 10^4 larger than the average 0.3 GeV/cm^3 in the halo. For more conservative estimates this bound would disappear, so we do not show it in Fig. 4.7.

For PBHs heavier than stars, another constraint comes from the observed properties of stars in Ultra-Faint Dwarf (UFD) galaxies around the Milky Way and Andromeda. Stars in UFD would intermittently interact gravitationally with PBHs, gaining kinetic energy. From the study of their kinematic properties of stars in known UFD, Ref. [383] obtained exclusion limits above $\mathcal{O}(10) M_\odot$.

4.4.4 Models for the generation of Primordial Black Holes

As mentioned in Section 4.4.2, PBHs require a large power spectrum (of order 10^{-2}) of the co-moving curvature perturbations on small scales. The most recent measurements from Planck [33] of the power spectrum at CMB scales ($k \sim 10^{-4} - 10^{-1} \text{ Mpc}^{-1}$) constrain it rather accurately to be nearly flat and slightly red-tilted (in excellent agreement with the inflationary prediction): at 68% confidence level, and with a pivot scale $k_* = 0.05 \text{ Mpc}^{-1}$, we parametrise it as

$$\begin{aligned} \mathcal{P}_\zeta &= A_s \left(\frac{k}{k_*} \right)^{n_s - 1 + \frac{1}{2} \alpha_s \ln(k/k_*)}, \\ A_s &= 2.1 \cdot 10^{-9}, \\ n_s &= 0.968 \pm 0.006, \\ \alpha_s &= -0.003 \pm 0.007. \end{aligned} \tag{4.41}$$

In order to enhance the curvature perturbations generated by the inflaton field within a slow-roll regime, one would need to deviate consistently from the flatness of the power spectrum, in particular with a large α_s at large k , in a way which is incompatible with the standard simplest inflationary models. Therefore, the models proposed for PBH formation either introduce a

feature in the inflaton potential to deviate from the slow-roll prediction during some interval of time, or rely on other fields to generate the curvature perturbation on smaller scales.

In the following we briefly review the proposals along these directions. It is worth stressing that the final PBH abundance, being so sensitive to the tail of the probability distribution of the density contrast (and exponentially sensitive to σ_Δ , see Eq. 4.37), has to be fine-tuned as a function of the parameters or initial conditions of the model. This is a generic feature of all of the models presented in the following.

Higgs instability In this Chapter 4 we illustrate in detail the proposal of Ref. [3], which exploits a mechanism already built in the SM to produce large perturbations: the instability of the vacuum of the Higgs potential. If the Higgs field probed the unstable region towards the end of the inflationary epoch (sourced by some other field), and was rescued back in time during the thermal phase (in the sense explained in Section 4.2.4), then a tachyonic instability of the Higgs perturbation is excited. The risk of creating through this mechanism some undesired anti-de Sitter regions close to our observable universe is avoided by the proposal of Ref. [4], illustrated in Section 4.7. This proposal has the attractive feature that its basic ingredient is already present within the SM extrapolated to high energies.

Inflection point in the inflaton potential Another direction in the model building scenario is introducing an inflection point in the inflaton potential. When ϕ approaches that point, in the equations of motion of the inflaton field

$$\ddot{\phi} + 3H\dot{\phi} + V'(\phi) = 0, \quad (4.42)$$

the last term becomes negligible: $\dot{\phi}$ becomes very small, and the slow-roll regime temporarily ceases. This phase is also called ultra-slow roll regime. During this phase the curvature perturbations grow importantly. The physical quantity to look at after inflation are the energy perturbations $\delta\rho/\rho$, which are properly rewritten as a gauge invariant quantity through the comoving curvature perturbation $\zeta = H\delta\rho_{\text{tot}}/\dot{\rho}_{\text{tot}}$ (in the flat gauge). ζ is not conserved on super-Hubble scales, and if the inflaton ϕ is the main component for both $\delta\rho_{\text{tot}}$ and ρ_{tot} we can rewrite $\zeta \simeq H\delta\phi/\dot{\phi} \sim H^2/\ddot{\phi}$. It is clear then that, if the inflaton velocity decreases, the gauge invariant curvature perturbations are amplified.

Various models have been proposed to realise this inflection point. One of them relies on Higgs inflation [384, 385], where a non-minimal coupling of the Higgs to gravity determines in the Einstein frame a Higgs potential suitable for slow-roll inflation (for the non-unitarity issues of this theory see [386–388]). Ref. [389] studies the case of Higgs critical inflation [390–392], arising when the SM parameters yield an inflection point in the Higgs potential (although the parameters needed for this to happen would deviate of about 3 standard deviations from their central measured values [393]).

Alternatively, inflection points were obtained by coupling the inflaton to the Ricci scalar [357]. Other inflationary models displaying inflection points in the inflaton potential are motivated within string theory (see for example [394, 395]) and supergravity [396].

Impact of quantum diffusion An important specification about the predicted mass functions within all the models discussed so far concerns the impact of the quantum diffusion. Quantum fluctuations of any (effectively massless) scalar field during the inflationary epoch can affect the initial conditions, or the evolution of the inflaton during the ultra-slow roll phase (when by definition the classical evolution becomes subleading). The result is that the mass function

has itself a probability distribution, and nearby patches in the universe display a different PBH abundance [397]. This is not a problem by itself, since in any case the PBH distribution is generally clustered on large scales [398], but it is an important ingredient for an accurate estimate of the final PBH abundance.

Double inflation Another possibility for violating temporarily the slow roll conditions is to have two stages of inflation.

This can be achieved with a single field, if this starts at large values with chaotic inflation, and then reaches the origin where a small negative mass term allows a second new inflationary phase [399].

With multi-scalar inflation, various possibilities arise for building models of double inflation. One of the first models proposed involves hybrid inflation: after a first inflationary phase driven by the inflaton field, its effective mass becomes negative due to the coupling with the curvaton field, and the trajectory in the field space starts to bend in the direction of the latter. Between these two phases of inflation, if the potential is flat enough, the slow roll conditions are violated and the seeds for PBHs could be generated [400]. Similar models of double inflation have been proposed also in the framework of supergravity and were dubbed hybrid new inflation [401–403].

Alternatively, the curvature perturbations can be the sum of a flat contribution on all scales from the inflaton field (which is the sole responsible for the inflationary epoch) and a larger contribution at small scales from a curvaton field [404, 405].

Other proposals Finally, we mention some proposals going in different directions.

The seeds for PBHs could come from localised solutions of a scalar field, called oscillons. These long lived configurations can arise at the end of the inflationary era, and the denser ones can eventually collapse into a PBH. The scalar field responsible for the oscillons could be the inflaton itself [406] or another scalar field, as any of the ones appearing for example in supersymmetry [407].

If the SM is extended by axions (in order to solve the strong CP problem, see Sec. 1.4.4) and the corresponding Peccei-Quinn $U(1)$ symmetry is broken after inflation, then the collapse of domain walls could seed the generation of a small population of PBHs with masses $10^4 - 10^7 M_{\odot}$ [408]. The DM in this case would be constituted of axions, but the presence of these massive PBHs could explain the issues about SMBH exposed in Sec. 4.4.1.

Another proposal discusses the effects induced by a long-range attractive force, stronger than the gravitational force in the early universe, mediated by a light scalar. The interactions between heavy particles interacting through these force could lead to nonlinear dynamics, and eventually to their collapse and the generation of PBHs [409].

4.5 Generation of Primordial Black Holes through the Higgs instability

After having introduced the subject of Primordial Black Holes in the previous Sec. 4.4, we resume from Sec. 4.3 the illustration of the mechanism for the generation of PBHs through the SM Higgs instability. The Higgs contributes to the curvature perturbation with a peak at small scales, when there are about 20 e -folds to go till the end of inflation. During the radiation phase that immediately follows the end of inflation, the Higgs decays communicating its

perturbations to the curvature perturbation now in the form of radiation. The final curvature perturbation is therefore flat on large scales, but has a peak at small scales.

The numerical result for the power spectrum computed for the case showed in Fig. 4.5 is in agreement with the analytical estimate of Eq. (4.33) and is shown in Fig. 4.8.

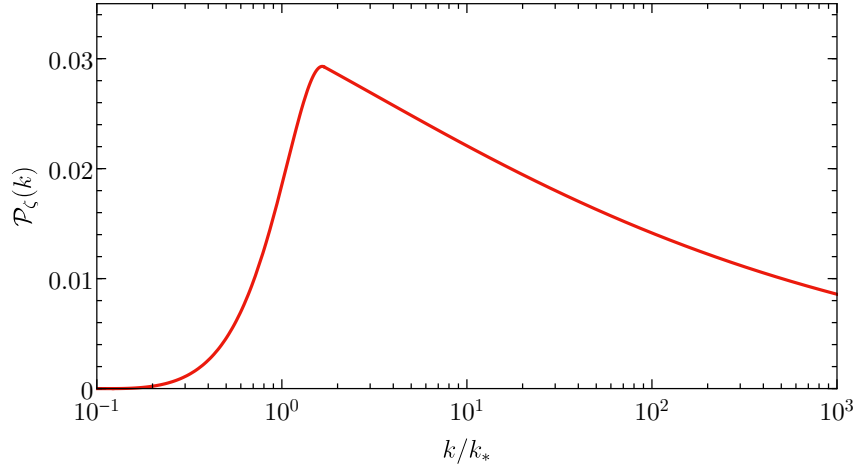


Figure 4.8: The power spectrum $\mathcal{P}_\zeta(k)$ defined in Eq. (4.17), where k is expressed in units of $k_* = a(t_*)H$.

As illustrated in section 4.4, from the power spectrum we can compute with Eq. (4.38) the variance of the density contrast $\sigma_\Delta(k)$ which is the key ingredient to compute the abundance of PBHs (Eq. 4.39) generated when the corresponding modes re-enter the Hubble radius during the radiation dominated era. The variance of the density contrast σ_Δ is shown in Fig. 4.9.

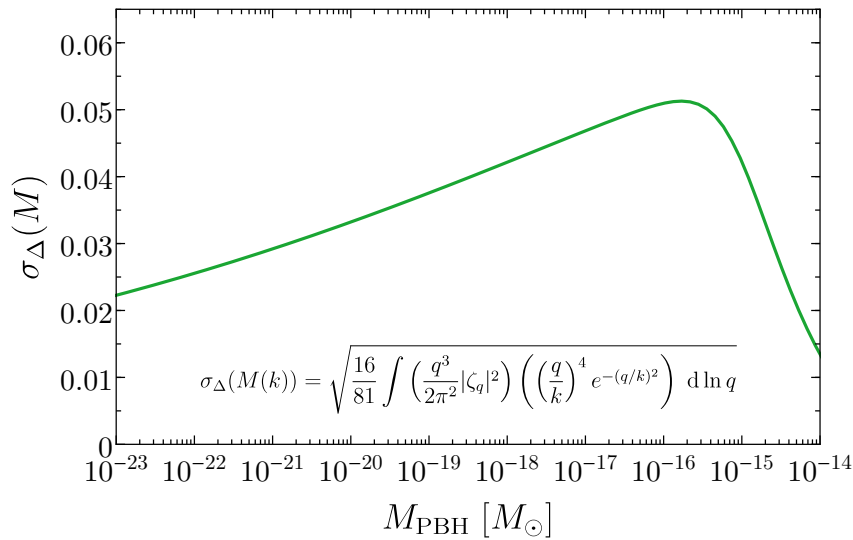


Figure 4.9: Variance of the density contrast as a function of the mass of the PBH generated at the corresponding scale k (Eq. 4.36), for the case considered in [3].

Fig. (4.10) shows the resulting mass spectrum of PBHs today, computed with the Eqs. (4.37) and (4.39).

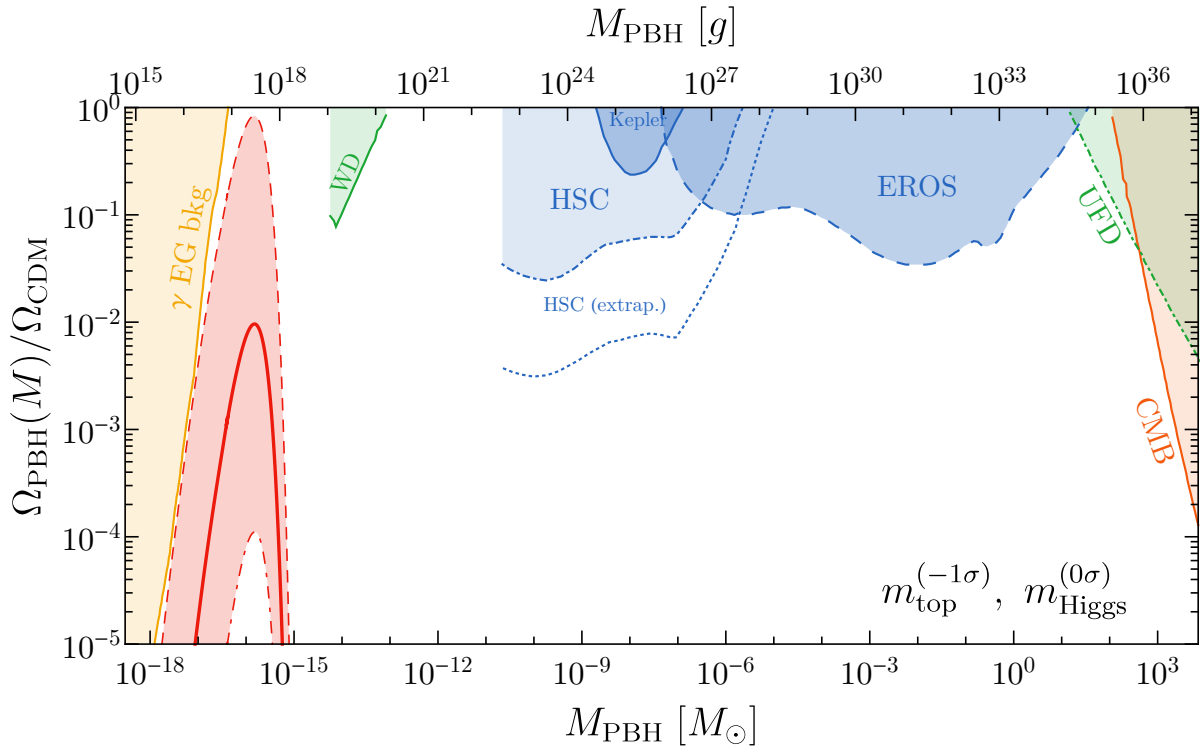


Figure 4.10: Spectrum of PBHs at formation generated by the mechanism we discuss (solid red refers to $S_3 = 0$ in Eq. (4.44), and dashed lines to $S_3 = \pm 1$), superimposed with the experimental constraints on PBHs (see Fig. 4.7 for details).

The position of the peak in the PBH mass spectrum is set by the mode k_* that exits the Hubble radius during inflation when the Higgs zero mode starts its classical evolution. To be on the safe side we ask that the interesting range of PBH masses is large enough to avoid the bounds from evaporating PBHs by the present time. This requires the dynamics to last about 18 e -folds before the Higgs field hits the pole in Eq. (4.10). Interestingly this can be achieved in the SM for realistic values of the Higgs and top masses and α_s : In our numerical example we use

$$m_{\text{Higgs}} = 125.09 \text{ GeV}, \quad m_{\text{top}} = 172 \text{ GeV}, \quad \alpha_s = 0.1184 \quad (4.43)$$

and we choose correspondingly $N_* = 18.8435$, whereas $h_* = 6.11 H$ is fixed by requiring the classical and quantum jumps in Eq. (4.8) to be equal.

In our findings we have not included the fact that the mass of the PBH is not precisely the mass contained in the corresponding horizon volume, but in fact obeys a scaling relation with initial perturbations [410] or the fact that the threshold is shape-dependent [411]. Furthermore, we have not accounted for the fact that the threshold amplitude and the final black hole mass depend on the initial density profile of the perturbation [352, 353, 412]. We estimate that the first two effects change the abundance by order unity. The third effect would require a thorough study of the spatial correlation of density fluctuations. Nevertheless, we have included in Fig. (4.10) the possible effect of non-Gaussianity in the PBH mass function. To estimate the impact of non-Gaussianity is not an easy task, as one needs to evaluate the second-order contribution to the comoving curvature perturbation ζ_2 . Some steps towards the calculation of the non-Gaussian contributions are collected in section 4.C. A rough estimate based on Ref. [413] gives $\zeta_2 = \mathcal{O}(1)\zeta_1^2$ and therefore we include in Fig. (4.10) two bands corresponding to $S_3 = \pm 1$, where $S_3 = \langle \Delta^3 \rangle / \sigma_\Delta^4$ is the skewness which appears in the modification of the arguments of the

exponential in Eq. (4.37) via the shift [414]

$$v^2 \rightarrow v^2 \left[1 - S_3 \frac{\sigma_\Delta}{3} \left(v - 2 - \frac{1}{v^2} \right) \right], \quad v \equiv \Delta_c / \sigma_\Delta. \quad (4.44)$$

The shift in the final abundance is not negligible, but we stress that there will be a set of parameters in our model which can provide the right final abundance. We also stress that the primordial abundance of PBHs depends in a very sensitive way on the value of t_* , keeping fixed all the other parameters. This does not come as a surprise as the function $\beta(M)$ is exponentially sensitive to v . In this sense the anthropic argument based on the necessity of having DM would justify a tuned initial PBH abundance. As a final warning, one should keep in mind that (as in any model for the generation of PBHs) splitting the metric into background and perturbations might be questionable for large perturbations.

From the time of equality to now, the PBH mass distribution will slide to larger masses due to merging. While the final word can only be said through N-body simulations, one can expect merging to shift the spectrum to higher masses even by orders of magnitude [364, 415] and to spread the spectrum, but maintaining the abundance. Accretion, on the other hand, increases both the masses and the abundance of PBHs as DM. On the other side, both merging and accretion help to render the PBHs more long-living. To roughly account for an increase of the current abundance by a representative factor 10^2 because of accretion, we have properly set the abundance at formation time to be $\Omega_{\text{PBH}} / \Omega_{\text{DM}} \sim 10^{-2}$ (higher values can be achieved). It would be certainly interesting to analyse these issues in more detail and account for the fact that the abundance of PBH has to be of the right magnitude during standard Big Bang Nucleosynthesis.

The choice of parameters of Eq. (4.43) allows the slow roll of the Higgs beyond the barrier to last enough time so that the corresponding PBH mass function lying above the bounds from black hole evaporation. For a different choice of the parameters related to the running of λ , it is possible to shift the PBH mass distribution even to a window of sublunar masses $10^{-14} - 10^{-11} M_\odot$, unbounded by current observations (see Section 4.4.3). This is achieved for example for $m_{\text{top}}^{(-2\sigma)}$ and $m_{\text{Higgs}}^{(+1\sigma)}$, where the superscripts denote the number of standard deviations from the current LHC combination [416–418]

$$m_{\text{top}} = 172.47 \pm 0.5 \text{ GeV}, \quad m_{\text{Higgs}} = 125.09 \pm 0.24 \text{ GeV}. \quad (4.45)$$

The corresponding PBH mass function is shown in Fig. 4.11.

4.6 Homogeneity of the Higgs field and fine-tuning

As any other model of inflation which creates PBHs out of spiked perturbations at small scales, the scenario we have described is fine-tuned. Indeed, the mass fraction (4.37) is exponentially sensitive to the variance of the density contrast. Small variations of it lead to too small or too large PBH abundances. Moreover, the mechanism needs fine-tuning to avoid the overshooting of the Higgs into the dangerous AdS vacuum. In Ref. [3] the fine-tuned choice of the parameters has been motivated anthropically. Structures can form through the dark matter under the form of PBHs and life can develop only in those regions which survive the AdS catastrophe and are saved by the thermal effects. In this sense, the electroweak SM instability is a bonus.

A natural question to ask is how large is the patch for which we can assume exact homogeneity, that is the same initial conditions. The Higgs field is subject to quantum fluctuations during the inflationary epoch, so that its evolution is a random walk at temporal and *spatial*

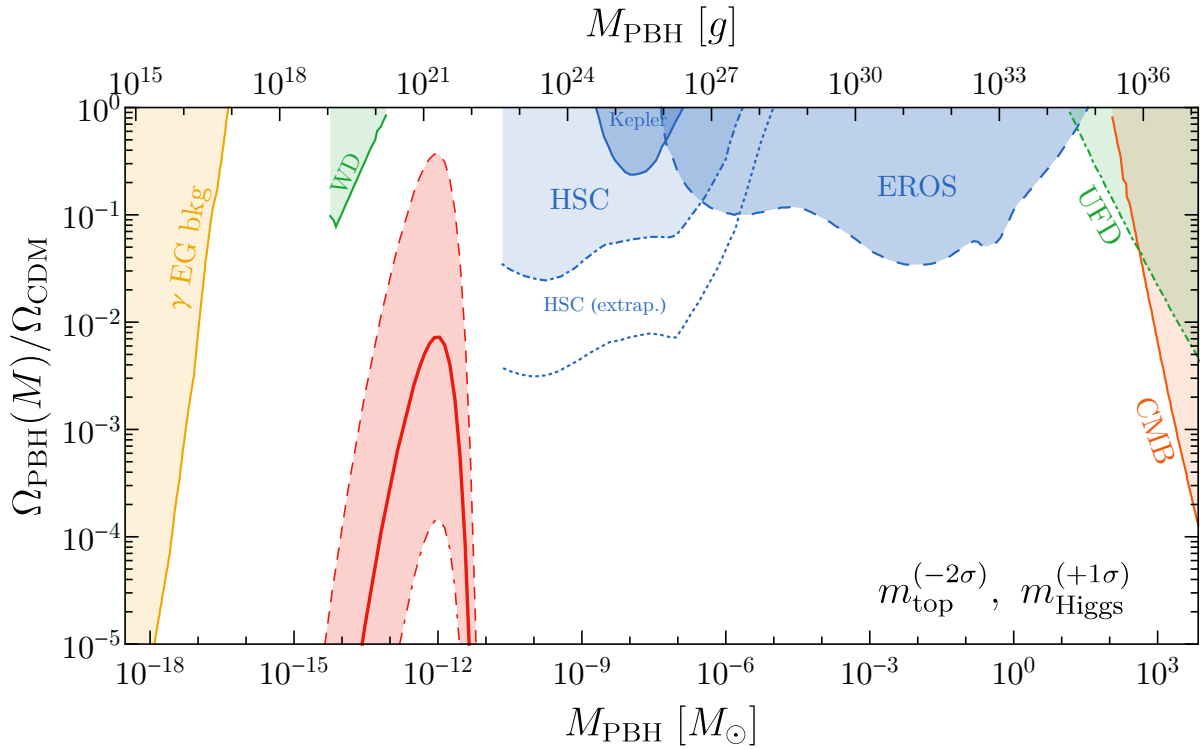


Figure 4.11: Spectrum of PBHs for $m_{\text{top}}^{(-2\sigma)}$ and $m_{\text{Higgs}}^{(+1\sigma)}$ (see Figs. 4.10 and 4.7 for details).

steps of order H^{-1} . At each Hubble time, a region of the size of the Hubble radius H^{-1} makes a jump whose amplitude is distributed according to a Gaussian with average zero and deviation $H/(2\pi)$. In the meanwhile these regions get stretched by the expansion, and within the next Hubble time new fluctuations on the same physical scale H^{-1} will arise on top of the previous ones, whose typical scale has now become $e \cdot H^{-1}$.

Regions which start this random walk together at the beginning of inflation will eventually display uncorrelated values, but this process takes time after their separation scale exits the horizon. The correlation length ℓ is then of the order of the particle horizon [419]:

$$H^{-1} \ll \ell \ll H^{-1} e^{Ht_i}, \quad (4.46)$$

where t_i is the time from the beginning of inflation. This is shown schematically in Fig. 4.12. Therefore it is correct to assume that the Higgs background has approximately the same initial conditions on an exponentially large region. On scales of order of the Hubble radius, though, h_c displays small inhomogeneities of order $H/(2\pi) \simeq 0.16 H$.

The abundance of PBHs is sensitive to the initial condition of the Higgs field h_* at the time when classicality takes over, that is ~ 20 e-folds before the end of inflation. Small deviations from h_* , $\delta h_* \simeq (10^{-3} - 10^{-2})H$ lead to a too tiny value of the PBH abundance or to a fall into anti de Sitter. This variation is smaller than the quantum fluctuations $\sim 0.16 H$ which arise on length scales $\sim H^{-1}$ during the first e -folds of evolution of the Higgs field. This gives a small probability $\sim 10^{-2}$ for each Hubble volume that the initial condition stays close to h_* .

Since our observed universe (corresponding to a number of e-folds of about 60) contained at that time about $\sim [\exp(60 - 20)]^3 = \exp(120)$ Hubble volumes, one might naively think that the total probability will be therefore $\sim 10^{-2} \exp(120)$. This is not correct as one is not interested

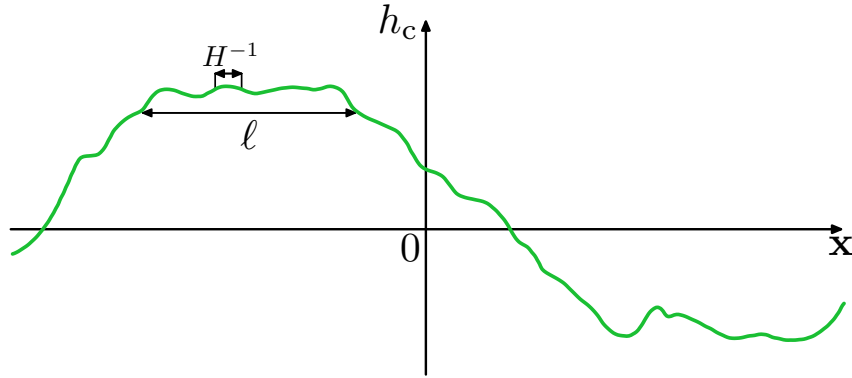


Figure 4.12: Fluctuations of the background value of a scalar field in de Sitter space (adapted from [420]).

in the probability of simultaneous production of PBHs in all Hubble size domains². The probability though applies to the counting of regions with might end up not being saved by the thermal effects. If one of those $\sim \exp(120)$ regions is not saved, it will expand after inflation and eventually engulf our entire universe. For each of these regions, in Ref. [421] (which repeated, confirmed and reported the results of Ref. [3]) it was argued that the probability for the Higgs to be saved is of order $1/2$. The reason is that, in the regions that give an abundance of PBHs of the order of Ω_{DM} , the Higgs field reaches a final value $h_c(t_e)$ very close to the critical value not to create a dangerous AdS bubble. A small overfluctuation of h_* or its initial velocity $\dot{h}_c(t_*)$ would push then $h_c(t_e)$ into the AdS regime. Thus, in Ref. [421] it is argued that the probability that none of the $\sim \exp(120)$ regions makes an AdS bubble is $2^{-\exp(120)}$.

In [3], it was already explicitly stated that the choice of parameters needed for PBH formation, although fine-tuned, would be motivated anthropically. The relevant issue is then the following: is $\sim 2^{-\exp(120)}$ really a small number from the point of view of the multiverse and anthropic argument? In fact, once one accepts the anthropic principle, the reasonable question is what one should multiply the tiny probability for? Within the eternal inflation/multiverse, one should use the volume-weighted physical probability which, unlike the comoving probability distribution, takes into account the overall growth of the volume of the universe: inflationary growth rewards parts of the universe with respect to others. If one assumes a comoving probability point of view, a sample is assumed to be typical and then general properties are deduced. However, distributions looking atypical from an analysis based on the comoving probability, can be common when using the physical probability (and vice versa). We might well live in a region of the global universe which looks unusual if judged so using the comoving probability [422]. In other words, there might be a number of universes much bigger than $\sim 2^{\exp(120)}$ to probe.

As an example, we can refer to Ref. [423] where it is estimated that the number of universes in eternal inflation is proportional to the exponent of the entropy of inflationary perturbations, $\exp(\exp(3N))$, where N is the number of e -folds of slow-roll post-eternal inflation. If we assume that our observed universe originates from only 60 e -folds of exponential expansion, one gets [423]

$$\mathcal{N} = \text{number of universes} \sim 10^{10^{77}}. \quad (4.47)$$

²In this sense, the production of PBHs as dark matter through our mechanism suffers from a fine-tuning of the order of $\delta h_*/(\sqrt{2\pi}(H/2\pi)) = \sqrt{2\pi}(\delta h_*/H) \simeq (10^{-3} - 10^{-2})$ obtained assuming a Gaussian distribution for the Higgs field. This fine-tuning is typical of all mechanisms giving rise to PBHs through inflation.

This is incomparably larger than the number \mathcal{N} of universes needed to find, with a probability of order one, $n = \exp(120)$ adjacent regions which have not fallen into AdS. This probability can be approximated as $2^{-n}\mathcal{N}$, which gives $\mathcal{N} \gtrsim 2^{\exp(120)} \sim 10^{4 \cdot 10^{51}}$. In chaotic inflation where the number of e -folds is typically 10^{12} one gets [423]

$$\mathcal{N} \sim 10^{10^{10^7}}. \quad (4.48)$$

As scary as it might seem, the small probability quoted in Ref. [421] takes an (exponentially) enormous advantage of this number of universes and what seems unnatural in fact might turn out to be natural.

Furthermore, if one wishes to estimate the probability of survival of our universe, it should also be remembered that luckily we live again in a period when the cosmological constant dominates. It can be easily calculated that the particle horizon in our universe from now until infinity will expand by just one third with respect to its current value. From that moment on, our universe will be screened against AdS bubbles.

Leaving aside these considerations which might render the reader (and us) uncomfortable for the lack of any firm quantitative arguments, in the following Section 4.7 we propose a natural solution to the fine-tuning problem. As mentioned above, the fine-tuning caused demanding the right abundance of PBHs is only $\sim (10^{-3} - 10^{-2})$. The problem arises when discussing the fine-tuning needed to save all the Hubble volumes when there are about 20 e -folds to go. So, one just needs a (reasonable) solution which will eliminate the presence of the AdS regions altogether without altering the attractive properties of the scenario, i.e. that the PBHs are generated by the SM Higgs and that dark matter is made of SM particles. This is what we will discuss in the next Section.

4.7 Getting rid of the AdS regions altogether

As stressed in [3] the mechanism to produce PBHs, which today form the dark matter without resorting to any dark matter particle beyond the Standard Model, relies on the instability of the electroweak vacuum, so that the Higgs perturbations can grow during inflation. This dynamics is totally built within the Standard Model. On the other hand, to get rid of the fine-tuning caused by the dangerous AdS vacua, one can simply alter the form of the Higgs potential at energies much larger than the instability scale, thus without altering the nice features of the mechanism [4].

Let us then suppose that at energy scales much larger than the instability scale $\sim 10^{11}$ GeV, there are new particles whose interaction with the Higgs can change the sign of the quartic coupling from negative to positive again, thus stabilising the Higgs potential. As a simple case, add a complex scalar field S with potential [424]

$$V = \lambda_S \left(|S|^2 - \frac{\omega^2}{2} \right)^2 + 2\lambda_{HS} \left(|S|^2 - \frac{\omega^2}{2} \right) \left(|\varphi_H|^2 - \frac{v^2}{2} \right), \quad (4.49)$$

where S is the additional singlet (with vacuum expectation ω) and φ_H the SM Higgs doublet (with vacuum expectation v). The interaction term in Eq. (4.49), generates a threshold contribution $\delta\lambda = -\lambda_{HS}^2/\lambda_S$ to the Higgs quartic $\lambda(h)$ above a scale $\sim m_S$ [424]. Moderate values of λ_{HS} and λ_S can produce a $\delta\lambda$ large enough to bring $\lambda(h)$ to be positive for $h \gtrsim m_S = \sqrt{\lambda_S}\omega$. In such case the Higgs potential displays a true minimum at $h \sim m_S$.

For our purposes we consider the case $m_S \sim \mathcal{O}(T_{\text{RH}})$. In this way, even if the Higgs jumps beyond the barrier early during inflation, it will stop at its true minimum and thermal effects at reheating rescue the Higgs, bringing it back towards the electroweak vacuum.

We show in Fig. 4.13 the running of λ corresponding to $m_S = 2 \cdot 10^{15}$ GeV, and $\lambda_{SH} = 0.05$, $\lambda_S = 0.3$. We stress that there is no fine-tuning here: we can allow relative variations of order (10 – 20)% for m_S , and the only requirement for λ_{SH} and λ_S is that they yield $\lambda(h \gtrsim m_S) > 0$, corresponding to $|\delta\lambda| \gtrsim 0.008$.

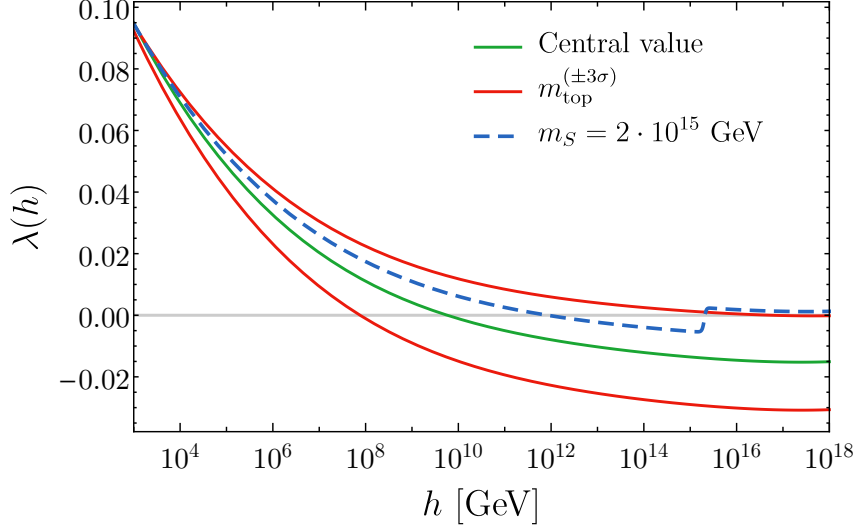


Figure 4.13: Running of the Higgs quartic coupling λ with the introduction of an extra scalar (dashed blue line), together with the central and marginal values within the SM [307–309].

We repeat the analysis performed in the previous sections [3], with the same choice of the Hubble rate $H = 10^{12}$ GeV and parameters in Eq. (4.43). The Higgs field starts its classical evolution beyond the barrier at 10^{11} GeV from a value h_* at the time t_* (corresponding to N_* e -folds till the end of inflation). We solve the equations of motion for the Higgs background h_c and its perturbations δh_k , and compute the power spectrum \mathcal{P}_ζ of the comoving curvature perturbation ζ .

The outcome is the following. Let us fix for the moment h_* , and denote by \bar{N}_* the initial time which would give the right abundance of PBHs without the presence of S . By including S , the Higgs potential does not change for $h < m_S$, so that for $N_* \leq \bar{N}_*$ the evolution of the Higgs is not altered with respect to what was discussed in the previous sections [3]: for $N_* < \bar{N}_*$, the final \mathcal{P}_ζ is too small to seed PBHs. For $N_* > \bar{N}_*$, the Higgs field reaches its minimum at m_S before the end of inflation, and starts oscillating around it³. In the meantime, the tachyonic excitation of the Higgs fluctuations ceases, and δh_k oscillates around zero with the same frequency as h_c . The evolution for this case $N_* > \bar{N}_*$ is shown in Fig. 4.14.

The redshift of δh_k during this phase (in which the Higgs behaves as a matter fluid) slowly reduces the amplitude of ζ as $a^{-3/2}$, and \mathcal{P}_ζ decreases as a^{-3} during the oscillation of h_c around its true minimum.⁴ The final value of \mathcal{P}_ζ for the mode $k_* = a(t_*)H$ (which exits the Hubble radius at N_*) is shown in Fig. 4.15.

³The Higgs mass in this true minimum is typically larger than H .

⁴Throughout this Chapter we assume for simplicity a constant Hubble rate during inflation, in order not to specify an inflation model. This implies $\dot{\rho}_{\text{tot}} = \dot{\rho}_h$ during inflation. This approximation works less well during the

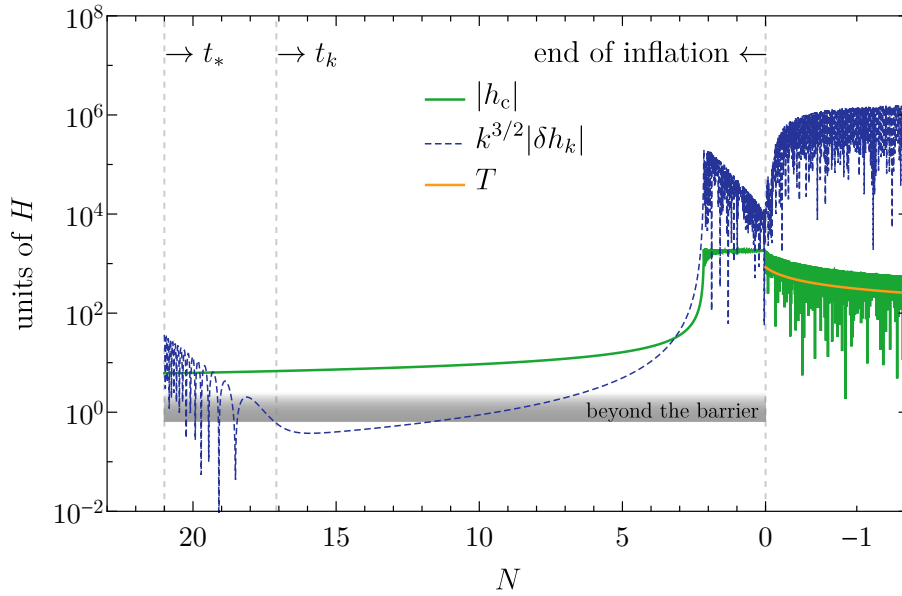


Figure 4.14: Evolution of h_c and its perturbation δh_k for the case $N_* > \bar{N}_*$ (or equivalently $h_* > \bar{h}_*$; see the text for details).

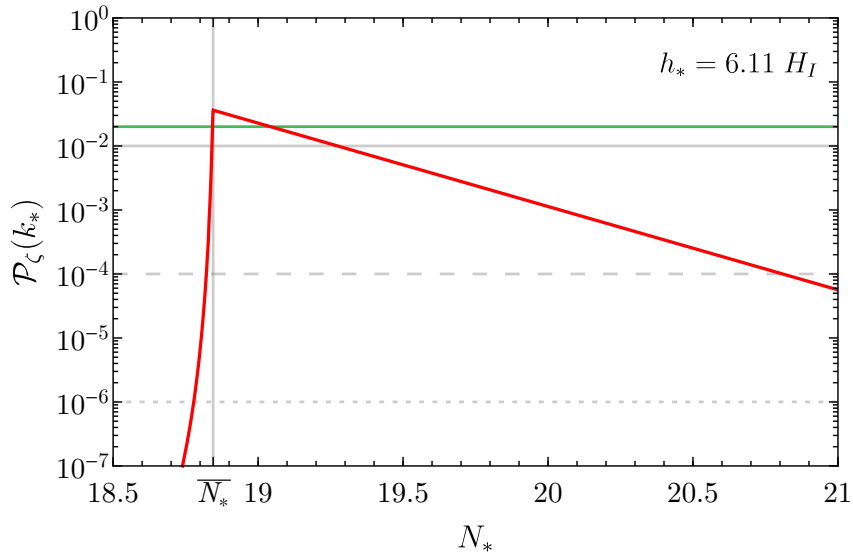


Figure 4.15: Power spectrum \mathcal{P}_ζ as a function of the starting value N_* , for a fixed $h_* = 6.11 H_I$. The green line corresponds to a PBH abundance roughly of order unity, and the grey lines, yielding no PBHs, correspond to the cases shown in Fig. 4.16.

Notice that the previous discussion proceeds in the same way if we fix a generic N_* and identify what \bar{h}_* leads to the right PBH abundance without the presence of S . For $h_* \leq \bar{h}_*$ the evolution is the same described in Ref. [3], whereas for $h_* > \bar{h}_*$ the curvature perturbation is slowly

oscillating phase in which the Higgs behaves as matter, and $\rho_h \sim a^{-3}$. In any case the qualitative behaviour of \mathcal{P}_ζ shown in Fig. 4.15 and 4.16 would be the same: the slope of \mathcal{P}_ζ for $N_* > \bar{N}_*$ in Fig. 4.15 would be steeper, without altering our conclusions.

reduced at the end of inflation.

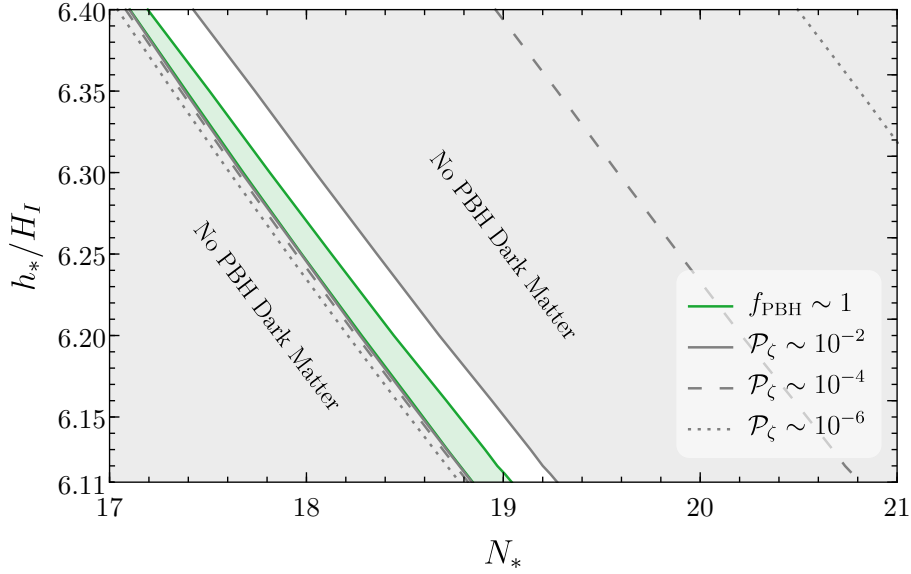


Figure 4.16: Power spectrum \mathcal{P}_ζ as a function of the starting values N_* , h_* . The grey regions do not yield PBHs, and the green region corresponds to a non-negligible PBH abundance.

Fig. 4.16 shows the final power spectrum \mathcal{P}_ζ in the plane of the initial values (N_*, h_*) . On the lower left corner of the plot we have the same situation as in the previous sections [3], with a strong variation of the final \mathcal{P}_ζ even for per mille variations of N_* and h_* . On the right and upper side of the plot we find the region which would have fallen into AdS without the threshold correction on λ at m_S . If λ is pushed to positive values at a scale close to T_{RH} , then the Higgs is always rescued and there are no AdS regions which could form. Moreover, the dependence of \mathcal{P}_ζ on N_* is much milder on the right side of Fig. 4.16, and a second region leading to the right PBH abundance is found. We highlight all the region corresponding to $\mathcal{P}_\zeta(k_*) \sim (0.02 - 0.04)$: although values larger than ~ 0.02 yield a too large PBH abundance, we recall the argument exposed previously. The formation rate of PBH is a probabilistic quantity and says nothing about the distribution of such BHs in space. Even if some patches lead to a larger abundance they could be compensated by regions without PBH. These inhomogeneities occur at very small scales and do not constitute a problem as the PBHs are generated anyway strongly clustered [415].

4.8 Conclusions

For the current central values of the Higgs and top masses, the Standard Model Higgs potential develops an instability at a scale of the order of 10^{11} GeV. We show that a cosmological signature of such instability could be dark matter in the form of primordial black holes seeded by Higgs fluctuations during inflation.

We can highlight three points as the most relevant, were this scenario realised in nature. First, the SM would be capable of explaining DM by itself (supplemented by a period of inflation that is well motivated by other reasons). This has a double side: the SM provides a DM candidate in the form of PBHs and also provides the mechanism necessary to create the PBH seeds during inflation via the quantum fluctuations of the Higgs field in the unstable part of the

Higgs potential. Both aspects (DM candidate and PBH generation mechanism) go against the common lore that physics beyond the SM is needed to explain DM. In fact, if this scenario were correct, the Higgs field would not only be responsible for the masses of elementary particles but also for the DM content of our universe.

Second, the PBH generation mechanism gives an anthropic handle on Higgs near-criticality which would be explained as needed to get sufficient DM so that large enough structures can grow in the universe.

Finally, the PBHs responsible for DM would represent a conspicuous cosmological signature of the actual existence of an unstable range in the Higgs potential at large field values.

In this scenario, no physics beyond the Standard Model should be invoked to explain the dark matter in our observed Universe, but anthropic arguments are necessary to explain the fine-tuning on the initial conditions. We show then how such fine-tuning can be naturally avoided by coupling the Higgs to a very heavy scalar with mass $\gg 10^{11}$ GeV that stabilises the potential in the deep ultraviolet, but preserving the basic feature of the mechanism which is built within the Standard Model.

4.A Dynamics of the Higgs hitting the pole

To understand Eq. (4.10) one solves the equation

$$\ddot{h}_c - \lambda h_c^3 = 0, \quad (4.50)$$

Taking the initial conditions $h_c(0) = h_0$ and $\dot{h}_c(0) = \dot{h}_0$, and using the fact that there is an integral of motion

$$\frac{1}{2}\dot{h}_c^2 - \frac{\lambda}{4}h_c^4 = -E = \frac{1}{2}\dot{h}_0^2 - \frac{\lambda}{4}h_0^4, \quad (4.51)$$

one finds the solution

$$h_c(t) = h_0 \alpha_0 \operatorname{cn} \left(i\sqrt{\lambda} h_0 \alpha_0 t + \operatorname{cn}^{-1}(1/\alpha_0, 1/2), 1/2 \right), \quad (4.52)$$

where $\operatorname{cn}(z, k)$ is one of the Jacobian elliptic functions and

$$\alpha_0 \equiv \left(1 - \frac{2\dot{h}_0^2}{\lambda h_0^4} \right)^{1/4}. \quad (4.53)$$

The function $\operatorname{cn}(ix, 1/2)$ has poles at $x = K(1/2)$ with residue $-i\sqrt{2}$, where

$$K(k) = \int_0^{\pi/2} \frac{d\theta}{\sqrt{1 - k \sin^2 \theta}}. \quad (4.54)$$

Around the pole the classical value of the Higgs can therefore be approximated by Eq. (4.10) with

$$t_p = \frac{1}{\sqrt{\lambda} h_0 \alpha_0} \left[K(1/2) + i \operatorname{cn}^{-1}(1/\alpha_0, 1/2) \right]. \quad (4.55)$$

4.B Energy densities and their perturbations in the thermal phase

In this Appendix we follow the evolution of the perturbations during the reheating phase, which we consider for simplicity to be instantaneous (happening for instance in hybrid models in which a heavy waterfall field releases its vacuum energy providing a fast transition from inflation to radiation), and the subsequent radiation phase. To model the sudden transition from inflation to radiation one can imagine that the equations of motion of the Higgs and its perturbations possess a time-dependent term taking care of the fast appearance of the plasma correction to the potential under the form of the $m_T^2 h^2$ term. By continuity, $h_c(t_e) = h_c(T_{\text{RH}})$, $\dot{h}_c(t_e) = \dot{h}_c(T_{\text{RH}})$, $\delta h(t_e) = \delta h(T_{\text{RH}})$, and $\delta \dot{h}(t_e) = \delta \dot{h}(T_{\text{RH}})$, where t_e is the time at the end of inflation and T_{RH} is the time at the beginning of reheating. Assuming a fast reheating essentially amounts to saying that $t_e \simeq T_{\text{RH}}$. Across this time boundary, energy is also conserved. At the end of inflation the energy density is

$$\rho_e = \rho_{\text{inf}} + \rho_{h,e}, \quad (4.56)$$

with

$$\rho_{\text{inf}} = 3H^2 M_{\text{P}}^2 \quad \rho_{h,e} = \frac{1}{2} \dot{h}_c(t_e)^2 + V_0(h_e). \quad (4.57)$$

During the instantaneous reheating, ρ_{inf} is used up in reheating the plasma (populated through the inflaton decays). The total energy density at T_{RH} is

$$\rho_{\text{RH}} = \rho_{\text{pl}} + \rho_{h,\text{RH}}. \quad (4.58)$$

In the plasma rest-frame

$$\rho_{\text{pl}} = \omega - P, \quad (4.59)$$

where P is the plasma pressure (equal to minus the free-energy density [29, p. 66]) and

$$\omega = T \frac{\partial P}{\partial T} \quad (4.60)$$

is the enthalpy density. We also have $\rho_{h,\text{RH}} = \dot{h}_{c,\text{RH}}^2/2 + V_0(h_{c,\text{RH}})$, with $h_{c,\text{RH}} \equiv h_c(T_{\text{RH}})$. It is more convenient to arrange the splitting between plasma and Higgs background energies in a different way, by first separating a pure radiation part in ρ_{pl} by writing

$$P = P_\gamma - V_T(h_c, T) \quad (4.61)$$

and

$$\omega = \omega_\gamma - T \frac{\partial V_T}{\partial T}, \quad (4.62)$$

where $P_\gamma = \pi^2 g_* T^4/90$, $\omega_\gamma = 2\pi^2 g_* T^4/45$ and $V_T(h_c, T)$ is the field-dependent thermal contribution of the plasma to the Higgs potential. Then, we assign this potential term to the Higgs energy density and write

$$\rho_{\text{pl}} = \frac{\pi^2}{30} g_* T^4 - T \frac{\partial V_T}{\partial T}, \quad \rho_{h,\text{RH}} = \frac{1}{2} \dot{h}_{c,\text{RH}}^2 + V_0(h_{c,\text{RH}}) + V_T(h_{c,\text{RH}}, T). \quad (4.63)$$

The reheating temperature can be obtained from $\rho_e = \rho_{\text{RH}}$, which gives (neglecting ρ_h with respect to ρ_{inf})

$$T_{\text{RH}} \simeq \left(\frac{90}{\pi^2 g_*} \right)^{1/4} \sqrt{H M_{\text{P}}}. \quad (4.64)$$

The small fluctuations in the Higgs background cause small fluctuations in T_{RH} :

$$V_T \simeq \frac{1}{2}m_T^2 h_c^2 = \frac{1}{2}\kappa T^2 h_c^2 \implies \delta T \simeq \frac{15\kappa h_c}{2\pi^2 g_* T} \delta h \ll \delta h. \quad (4.65)$$

By matching the fluctuations in the energy density across $t_e \simeq T_{\text{RH}}$, that is, $\delta\rho_e = \delta\rho_{\text{RH}}$, we obtain

$$\begin{aligned} \delta \left[\frac{1}{2} \dot{h}_{c,e}^2 + V_0(h_{c,e}) \right]_h &= \left[\frac{2\pi^2}{15} g_* T^3 \delta T - 2\kappa T^2 h_{c,\text{RH}} \delta h_{\text{RH}} \right]_{\text{pl}} + \delta \left[\frac{1}{2} \dot{h}_{c,\text{RH}}^2 + V_0(h_{c,\text{RH}}) + \frac{1}{2} \kappa T^2 h_{c,\text{RH}}^2 \right]_h \\ &= \delta \left[\frac{1}{2} \dot{h}_{c,\text{RH}}^2 + V_0(h_{c,\text{RH}}) \right]_h, \end{aligned} \quad (4.66)$$

where in the last equality we have used the result for δT above, which leads to a cancellation of the $\kappa T^2 h_c \delta h$ terms. This consistency check confirms that the splitting between the radiation and Higgs energy density of Eq. (4.63) holds also at the perturbation level:

$$\delta\rho_{h,e} = \delta\rho_{\text{pl}} + \delta\rho_{h,\text{RH}}. \quad (4.67)$$

Leaving aside Hubble friction, the energy density of plasma and Higgs background field are not conserved separately. We can still split the energy conservation equation $\dot{\rho}_{\text{tot}} = 0$ in a plasma and a Higgs one, taking into account Higgs decays into the plasma and write

$$\dot{\rho}_h = (\partial\rho_h/\partial h_c) \dot{h}_c = (\square h_c + V') \dot{h}_c = -\gamma_h \dot{h}_c^2, \quad (4.68)$$

with $V = V_0 + V_T$, and $\gamma_h \simeq 10^{-3}T$ the Higgs decay width, while $\dot{\rho}_{\text{pl}} = +\gamma_h \dot{h}_c^2$. The right-hand side in Eq. (4.68) introduces a friction term in the equation of motion for the Higgs field that is initially subleading in comparison with the Hubble friction term that it should also include, but is important for the late time behaviour of the Higgs condensate.

4.C Some considerations about the Non-Gaussianity

In this appendix we offer some considerations about the non-Gaussianity of the perturbations.

To evaluate the non-Gaussianity at the instant at which the perturbations re-enter the Hubble radius we proceed as follows. During the radiation phase, we have

$$\rho_h = \rho_h + \delta\rho_{h,1} + \frac{1}{2}\delta\rho_{h,2} = m_T^2 h_c^2 + 2m_T^2 h_c \delta h_1 + m_T^2 \delta h_1^2, \quad (4.69)$$

so that

$$\frac{\delta\rho_{h,2}}{\rho_h} = \frac{1}{2} \left(\frac{\delta\rho_{h,1}}{\rho_h} \right)^2 = 8\zeta_{h,1}^2, \quad (4.70)$$

where we have used again the fact that (in the flat gauge)

$$-\zeta_{h,1} = H \frac{\delta\rho_{h,1}}{\dot{\rho}_h} = H \frac{\delta\rho_{h,1}}{-4H\rho_h} = -\frac{1}{4} \frac{\delta\rho_{h,1}}{\rho_h}. \quad (4.71)$$

The total gauge-invariant curvature perturbation at second-order is [338, 413, 425, 426]

$$-\zeta_2 = \psi_2 - 2 \frac{\delta\rho_{h,1}}{\dot{\rho}} (\psi_1 + 2H\dot{\psi}_1) + H \frac{\delta\rho_{h,2}}{\dot{\rho}} - 2 \frac{H}{\dot{\rho}} \delta\dot{\rho}_{h,1} \delta\rho_{h,1}$$

$$+ H^2 \frac{(\delta\rho_{h,1})^2}{\dot{\rho}^2} \left(\frac{\ddot{\rho}}{H\dot{\rho}} - \frac{\dot{H}}{H^2} - 2 \right), \quad (4.72)$$

where we have assumed that on small scales only the perturbation of the Higgs field is relevant. Having defined $r_h = \rho_h/\rho = \dot{\rho}_h/\dot{\rho}$ and using the fact that during the radiation phase $\dot{H} = -2H^2$, $\dot{\rho} = -4H\dot{\rho}$ and $\ddot{\rho} = -6H\dot{\rho}$, we find (using again the flat gauge)

$$- \zeta_2 = -2r_h(1 - r_h)\zeta_{h,1}^2 = -2\frac{1}{r_h}(1 - r_h)\zeta_1^2, \quad (4.73)$$

where we have used the relation $\delta\dot{\rho}_{h,1} = -4H\delta\rho_{h,1}$. A similar computation gives

$$- \zeta_{2,h} = (-2 + 8 - 6)\zeta_{h,1}^2 = 0 \quad (4.74)$$

and therefore the Higgs perturbation is Gaussian. This is important for what comes later on.

One can ask about the non-Gaussianity during inflation. Writing $h = h_c + \delta h_1 + \delta h_2/2$, the equation for δh_2 on super-Hubble scales is

$$\delta\ddot{h}_2 + 3H\delta\ddot{h}_2 + V''\delta h_2 + V''(\delta h_1)^2 = 0, \quad (4.75)$$

from which one deduces that, if $\delta h_1(t, \mathbf{x}) = C(\mathbf{x})\dot{h}_c(t)$, then

$$\delta h_2(t, \mathbf{x}) = C^2(\mathbf{x})\ddot{h}_c(t). \quad (4.76)$$

During inflation the gauge-invariant second-order Higgs curvature perturbation is

$$- \zeta_{h,2} = \psi_2 - 2\frac{\delta h_1}{\dot{h}_c}(\psi_1 + 2H\dot{\psi}_1) + H\frac{\delta h_2}{\dot{h}_c} - 2\frac{H}{\dot{h}_c^2}\delta\dot{h}_1\delta h_1 + H^2\frac{(\delta h_1)^2}{\dot{h}_c^2} \left(\frac{\ddot{h}_c}{H\dot{h}_c} - \frac{\dot{H}}{H^2} - 2 \right), \quad (4.77)$$

In the flat gauge one finds

$$- \zeta_{h,2} = -2\zeta_{h,1}^2 \quad (\text{during inflation}). \quad (4.78)$$

Another way of finding the result (4.73) is the following. In the absence of interactions, the Higgs and radiation have a conserved curvature perturbation [427]

$$\zeta_i(\mathbf{x}) = -\psi(t, \mathbf{x}) + \frac{1}{3} \int_{\rho_i(t)}^{\rho_i(t, \mathbf{x})} \frac{d\tilde{\rho}_i}{\tilde{\rho}_i + \bar{P}(\tilde{\rho}_i)}, \quad (i = \gamma, h). \quad (4.79)$$

Let us assume that the Higgs decays on a uniform (total) density hypersurface corresponding to $\gamma_h = H$, being γ_h the decay rate of the Higgs. On this hypersurface one has

$$\rho_\gamma(t_{\text{dec}}, \mathbf{x}) + \rho_h(t_{\text{dec}}, \mathbf{x}) = \rho(t_{\text{dec}}) \quad (4.80)$$

and also $\zeta = -\psi$ given that $\delta\rho_{\text{tot}} = 0$ in this gauge. On the other hand, the local Higgs and radiation densities on such decay surface are inhomogeneous (we understand the arguments (t, \mathbf{x}) of ζ, ζ_i)

$$\zeta_\gamma = \zeta + \frac{1}{4} \ln \frac{\rho_\gamma(t, \mathbf{x})}{\rho_\gamma(t)},$$

$$\tilde{\zeta}_h = \zeta + \frac{1}{4} \ln \frac{\rho_h(t, \mathbf{x})}{\rho_h(t)}, \quad (4.81)$$

and therefore

$$\begin{aligned} \rho_\gamma(t, \mathbf{x}) &= \rho_\gamma(t) e^{-4(\zeta - \zeta_\gamma)}, \\ \rho_h(t, \mathbf{x}) &= \rho_h(t) e^{-4(\zeta - \zeta_h)}. \end{aligned} \quad (4.82)$$

Since the total density is uniform on the decay surface one finds

$$(1 - r_h) e^{-4\zeta} + r_h e^{-4(\zeta - \zeta_h)} = 1, \quad (4.83)$$

where we have assumed that on small scales $\zeta_\gamma = 0$. Solving for ζ one finds

$$\zeta_\pm = \pm \frac{1}{4} \ln \left(1 - r_h + r_h e^{4\zeta_h} \right). \quad (4.84)$$

In practice, the solution corresponding to ζ_- can be disregarded as one is interested in large values of ζ when dealing with the primordial black holes. Expanding at first order ζ_+ one finds $\zeta = r_h \zeta_h$ and at second-order one recovers the relation (4.73).

Now, the relation (4.84) allows to compute the non-perturbative probability function for the quantity ζ , by using the relation $P(\zeta_+) d\zeta_+ = P(\zeta_h) d\zeta_h$. One can first find $P(\zeta_h)$ and then integrate it from a critical value

$$\zeta_h(\zeta_c) = \frac{1}{4} \ln \left(\frac{r_h - 1 + e^{4\zeta_c}}{r_h} \right) \quad (4.85)$$

in order to find the mass fraction of the primordial black holes at formation time. Typical values in the literature for ζ_c go from 0.1 to 1.3 [428]. The fact that $P(\zeta_h)$ is Gaussian considerably simplifies the computation: the primordial mass fraction $\beta_{\text{prim}}(M)$ of the universe occupied by primordial black holes formed at the time t_M is therefore given by

$$P(\zeta > \zeta_c) = \beta_{\text{prim}}(M) = \int_{\zeta_c} d\zeta P(\zeta) = \int_{\zeta_h(\zeta_c)} \frac{d\zeta_h}{\sqrt{2\pi} \sigma_{\zeta_h}} e^{-\zeta_h^2/2\sigma_{\zeta_h}^2} = \int_{\zeta_h(\zeta_c)} \frac{d\zeta_1}{\sqrt{2\pi} \sigma_{\zeta_1}} e^{-\zeta_1^2/2\sigma_{\zeta_1}^2}, \quad (4.86)$$

where in the last step we have introduced the Gaussian order of the total curvature perturbation $\zeta_1 = r_h \zeta_h$. The last formula, which is an exact result, gives an improvement of the usual approximated Gaussian formula by the simple replacement of the threshold from ζ_c to $\zeta_h(\zeta_c)$. For $\zeta_c \simeq 0.5$ and $r_h \simeq 0.01$, one finds the new threshold to be $\zeta_h(\zeta_c) \simeq 1.6$, which seems to signal that non-Gaussianity makes more difficult to produce PBHs. We write ‘‘seems’’ because it is by now accepted in the literature that $\zeta(\mathbf{x})$ is not the best variable to describe the PBH mass fraction at formation [428]. The density contrast $\Delta(\mathbf{x})$ is more suitable. This however makes more difficult to gauge the importance of the non-Gaussianity due to the presence of the Laplacian operator. One might evaluate the density contrast at Hubble crossing, so that $\Delta(\mathbf{x}) \simeq (4/9a^2H^2)\nabla^2\zeta(\mathbf{x}) \simeq 4/9\zeta(\mathbf{x})$ and then use the relation among $\zeta(\mathbf{x})$ and the Gaussian $\zeta_h(\mathbf{x})$. Another approach might be to compute the Laplacian identifying the PBHs with the peaks of the distribution and therefore dropping the gradients of the fields.

Notice that one should also include another source of non-Gaussianity coming from the non-linear mapping between $h(T_{\text{RH}})$ and $h(t_e)$. This certainly calls for a more thorough analysis to assess the impact of the non-Gaussianity onto the PBH mass distribution.

A cosmological signature of the Higgs instability: Gravitational Waves

In Chapter 4 we have illustrated a possible cosmological signature of the instability of the Higgs potential in the Standard Model. If the Higgs field probed the unstable region towards the end of inflation, then its fluctuations on small scales grew considerably and, if large enough, they could have sourced the creation of Primordial Black Holes.

In this chapter, based on [5], we discuss another independent signature of this phenomenon: the production of gravitational waves sourced by Higgs fluctuations generated during inflation. We fully characterise the two-point correlator of such gravitational waves by computing its amplitude, the frequency at peak, the spectral index, as well as their three-point correlators for various polarisations. We show that, depending on the Higgs and top masses, either LISA or the Einstein Telescope and Advanced-Ligo, could detect such stochastic background of gravitational waves. In this sense, collider and gravitational wave physics can provide fundamental and complementary informations. Furthermore, the consistency relation among the three- and the two-point correlators could provide an efficient tool to ascribe the detected gravitational waves to the Standard Model itself. Since the mechanism described in this chapter might also be responsible for the generation of dark matter under the form of primordial black holes, this latter hypothesis may find its confirmation through the detection of gravitational waves.

For an introduction to the instability of the Higgs potential in the Standard Model and its implications in the Early Universe, together with a summary of the mechanism we envisage, we refer the reader to Section 4.1. In Section 5.1 we summarise the content of this chapter. Section 5.2 introduces the equation of motion and its solution for gravitational waves sourced at second order by the scalar perturbations. These results are used in Sections 5.3 and 5.4 to compute the power spectrum and bispectrum of this stochastic background of gravitational waves. Section 5.5 collects our numerical results for the power spectra generated by the Higgs instability. In Section 5.6 we conclude, and the final appendices contain further details of our calculations.

5.1 Gravitational waves as a signature of the Higgs instability

The recent detection of gravitational waves sourced by a spiralling binary system made of two $\sim 30M_{\odot}$ black holes [343] has initiated the era of Gravitational Wave (GW) cosmology [345] and opened a new window to investigate the very early stages of the evolution of the

Universe [429]. In particular, the Laser Interferometer Space Antenna (LISA) project [430], as well as the Einstein Telescope (ET) [431], Advanced-Ligo [432], and the Cosmic Explorer [433] at larger frequencies, will search for the stochastic gravitational wave background produced from different mechanisms, possibly identifying a primordial origin.

In Chapter 4 we discussed the generation of Primordial Black Holes (PBH) as a possible probe of one of the most fundamental properties of the Standard Model (SM) of weak interactions: the SM Higgs instability at high energies [3]. In this chapter we propose that a second signature of the SM instability might be a stochastic background of gravitational waves potentially detectable by the space-based interferometer LISA. Indeed, if there are large Higgs perturbations generated during the last stages of inflation, responsible or not for the PBHs as dark matter, they inevitably act as a (second-order) source of primordial gravitational waves at horizon reentry. The goal of this chapter is therefore to:

1. characterize the two-point correlator (power spectrum \mathcal{P}_h , its tilt as well as the frequency at the peak) of gravitational waves induced by the first-order Higgs perturbations. Parametrically one expects $\mathcal{P}_h \sim \mathcal{P}_\zeta^2$ at Hubble crossing and therefore one can reach values of \mathcal{P}_h as large as 10^{-4} ; the spectral tilt is also particularly interesting as the GW spectrum usually covers a large range of frequencies. The study of the detectability of the spectral index of a generic GW background with energy density $\Omega_{\text{GW}}(f) = A(f/f_*)^{n_T}$ can be found in Ref. [430] as a function of the frequency at the peak. For a signal peaked at $f_* \sim 0.05$ Hz and $A \sim 10^{-12}$ one could constrain $n_T \lesssim \mathcal{O}(1)$ and $n_T \gtrsim \mathcal{O}(7)$ ¹;
2. calculate the three-point correlator (bispectrum B_h) of the gravitational waves induced by the first-order Higgs perturbations. Parametrically one expects $B_h \sim \mathcal{P}_\zeta^3$ at Hubble crossing. The detectability of a non-Gaussian signal in the primordial gravitational waves at interferometers is discussed in Ref. [434] and LISA should be sensitive to it. This is of fundamental importance since a consistency relation between the three-point and the two-point correlators may represent a way to distinguish the origin of the signal.

We will see that

1. the energy density Ω_{GW} of the GWs generated by the Higgs fluctuations is typically of the order of 10^{-8} at the peak. The latter is reached at frequencies ranging from 10^{-2} to 10 Hz. This should allow either LISA or ET and Advanced-Ligo to detect the signal. Furthermore, as the frequency at the peak depends sensitively on the Higgs and top mass, this will provide complementary and fundamental information to be crossed with the ones provided by colliders with the possibility of either confirming or ruling out the origin of the GW signal;
2. the spectral index of the signal will have a characteristic behaviour: blue with $n_T \simeq 3$ for frequencies below the peak, and red with $n_T \simeq -0.6$ for frequencies above the peak frequency;
3. the bispectrum, in the case in which the two-point correlator is detectable by LISA, is mainly peaked in the so-called folded and equilateral configurations. Summing up all polarisations we find the characteristic consistency relation $(k_1 k_2 k_3)^2 B_h \sim 10^3 \mathcal{P}_h^{3/2}$. This

¹For a frequency at the peak of $f_{\text{CMB}} \sim 7.7 \cdot 10^{-17}$ Hz, present CMB data already provide an upper bound on the amount of GWs, $\Omega_{\text{GW}}^{\text{CMB}}$, generated during inflation and one can write the GW energy density $\Omega_{\text{GW}} = \Omega_{\text{GW}}^{\text{CMB}} (f/f_{\text{CMB}})^{n_T}$, being n_T the spectral tilt. A limit of $n_T \lesssim 0.35$ can be obtained for the best LISA configuration with six links, five million km arm length and a five year mission [430].

consistency relation should be relevant when identifying the origin of a detected signal and possibly give the chance to connect it to the idea that the very same Higgs fluctuations have originated the dark matter under the form of PBHs.

5.2 Equation of motion and its solution for Gravitational Waves

Our goal is to evaluate the amount of gravitational waves produced during the radiation phase by the SM Higgs perturbations which in turn owe their origin to the previous period of inflation. The correct formalism to evaluate the contribution to the generation at second-order of tensor modes from first-order scalar perturbations has been first discussed in [435–438]. The first two parts of this section follow quite closely the notation of Appendix A of [405]. Our convention for the signature of the metric is $(-+++)$, so that the perturbed metric in the conformal Newtonian gauge reads

$$ds^2 = -a^2(1 + 2\Phi)d\eta^2 + a^2 \left[(1 - 2\Psi)\delta_{ij} + \frac{1}{2}h_{ij} \right] dx^i dx^j, \quad (5.1)$$

where Φ, Ψ are the Bardeen potentials and the tensor perturbations h_{ij} are transverse and traceless: $\partial_i h_{ij} = h_{ii} = 0$. In absence of anisotropy in the stress-energy tensor, we have $\Phi = \Psi$ (including stress gives only a small correction [438]). Furthermore, one can rewrite h_{ij} in terms of the basis $\{e_{ij}^{(+)}, e_{ij}^{(\times)}\}$ of polarisation tensors as follows

$$h_{ij}(\eta, \mathbf{x}) = \int \frac{d^3k}{(2\pi)^3} \left[h_{\mathbf{k}}^{(+)}(\eta) e_{ij}^{(+)}(\mathbf{k}) + h_{\mathbf{k}}^{(\times)}(\eta) e_{ij}^{(\times)}(\mathbf{k}) \right] e^{i\mathbf{k}\cdot\mathbf{x}}. \quad (5.2)$$

The polarisation basis is given by

$$e_{ij}^{(+)}(\mathbf{k}) = \frac{1}{\sqrt{2}} [e_i(\mathbf{k})e_j(\mathbf{k}) - \bar{e}_i(\mathbf{k})\bar{e}_j(\mathbf{k})], \quad (5.3)$$

$$e_{ij}^{(\times)}(\mathbf{k}) = \frac{1}{\sqrt{2}} [e_i(\mathbf{k})\bar{e}_j(\mathbf{k}) + \bar{e}_i(\mathbf{k})e_j(\mathbf{k})], \quad (5.4)$$

where $e_i(\mathbf{k})$ and $\bar{e}_i(\mathbf{k})$ are two three-dimensional vectors orthonormal to \mathbf{k} , and the normalisation factor guarantees that $e_{ij}^{(+)}e_{ij}^{(+)} = e_{ij}^{(\times)}e_{ij}^{(\times)} = 1, e_{ij}^{(+)}e_{ij}^{(\times)} = 0$.

5.2.1 Equation of motion of GWs

The equation of motion for the GWs is obtained by extracting the tensor component of the Einstein equations expanded up to second order in perturbations

$$h''_{ij} + 2\mathcal{H}h'_{ij} - \nabla^2 h_{ij} = -4\mathcal{T}_{ij}{}^{lm}\mathcal{S}_{lm}, \quad (5.5)$$

where $'$ denotes the derivative with respect to conformal time, $\mathcal{H} = a'/a$ is the conformal Hubble parameter, \mathcal{S}_{lm} is the source term defined below in Eq. (5.11). The projector $\mathcal{T}_{ij}{}^{lm}$ acting on the source term selects its transverse and traceless part. We define it in Fourier space (and use $\hat{}$, when needed, to denote quantities in the conjugate space) as

$$\hat{\mathcal{T}}_{ij}{}^{lm}(\mathbf{k}) = e_{ij}^{(+)}(\mathbf{k})e^{(+)lm}(\mathbf{k}) + e_{ij}^{(\times)}(\mathbf{k})e^{(\times)lm}(\mathbf{k}). \quad (5.6)$$

Our convention for the Fourier transform is the following:

$$\mathcal{S}_{lm}(\eta, \mathbf{x}) = \int \frac{d^3k}{(2\pi)^3} \widehat{\mathcal{S}}_{lm}(\eta, \mathbf{k}) e^{i\mathbf{k}\cdot\mathbf{x}}, \quad (5.7)$$

so that the equation of motion (5.5) reads, for each polarisation mode $s = (+), (\times)$,

$$h_{\mathbf{k}}^{s''}(\eta) + 2\mathcal{H} h_{\mathbf{k}}^{s'}(\eta) + k^2 h_{\mathbf{k}}^s(\eta) = \widehat{\mathcal{S}}^s(\eta, \mathbf{k}), \quad (5.8)$$

where $\widehat{\mathcal{S}}^s(\eta, \mathbf{k}) \equiv -4 e^{s,lm}(\mathbf{k}) \widehat{\mathcal{S}}_{lm}(\eta, \mathbf{k})$. The method of the Green function yields the solution

$$h_{\mathbf{k}}^s(\eta) = \frac{1}{a(\eta)} \int^{\eta} d\tilde{\eta} g_{\mathbf{k}}(\eta, \tilde{\eta}) a(\tilde{\eta}) \widehat{\mathcal{S}}^s(\tilde{\eta}, \mathbf{k}), \quad (5.9)$$

where the Green function $g_{\mathbf{k}}(\eta, \tilde{\eta})$ for a radiation-dominated (RD) Universe is

$$g_{\mathbf{k}}(\eta, \tilde{\eta}) = \frac{\sin[k(\eta - \tilde{\eta})]}{k} \theta(\eta - \tilde{\eta}), \quad (5.10)$$

θ being the Heaviside step function.

5.2.2 The source term for GWs

The source term $\widehat{\mathcal{S}}_{ij}$ for GWs appearing in Eq. (5.5) arises at second order in the scalar perturbation Ψ [435]

$$\mathcal{S}_{ij} = 4\Psi\partial_i\partial_j\Psi + 2\partial_i\Psi\partial_j\Psi - \frac{4}{3(1+w)}\partial_i\left(\frac{\Psi'}{\mathcal{H}} + \Psi\right)\partial_j\left(\frac{\Psi'}{\mathcal{H}} + \Psi\right), \quad (5.11)$$

where w is the equation of state of the fluid permeating the Universe at a given epoch. Since the generation of GWs occurs mainly when the relevant modes re-enter the Hubble radius, which for the modes of our interest happens deeply into the RD era, we specialise to $w = 1/3$. We rewrite the source in Fourier space, introducing

$$\widehat{\Psi}(\eta, \mathbf{k}) = \int d^3x \Psi(\eta, \mathbf{x}) e^{-i\mathbf{k}\cdot\mathbf{x}} \quad (5.12)$$

so the right hand side of Eq. (5.8) becomes (we omit the temporal dependence for brevity)

$$\begin{aligned} \widehat{\mathcal{S}}^s(\eta, \mathbf{k}) = 4 \int \frac{d^3p}{(2\pi)^3} e^{s,ij}(\mathbf{k}) p_i p_j & \left[2\widehat{\Psi}(\mathbf{p})\widehat{\Psi}(\mathbf{k}-\mathbf{p}) + \right. \\ & \left. + \left(\widehat{\Psi}(\mathbf{p}) + \frac{1}{\mathcal{H}}\widehat{\Psi}'(\mathbf{p}) \right) \left(\widehat{\Psi}(\mathbf{k}-\mathbf{p}) + \frac{1}{\mathcal{H}}\widehat{\Psi}'(\mathbf{k}-\mathbf{p}) \right) \right]. \end{aligned} \quad (5.13)$$

The expression inside squared brackets is explicitly symmetric under the exchange of \mathbf{p} and $\mathbf{k}-\mathbf{p}$.

The scalar perturbation $\Psi(\eta, \mathbf{k})$ is directly related to the gauge invariant comoving curvature perturbation by $\Psi = \frac{2}{3}\zeta$ [312]. We define then the transfer function $T(\eta, k)$ through the relation

$$\widehat{\Psi}(\eta, \mathbf{k}) = \frac{2}{3}T(\eta, k)\zeta(\mathbf{k}), \quad (5.14)$$

and its expression is given in the RD era by

$$T(\eta, k) = \mathcal{T}(k\eta), \quad \mathcal{T}(z) = \frac{9}{z^2} \left[\frac{\sin(z/\sqrt{3})}{z/\sqrt{3}} - \cos(z/\sqrt{3}) \right]. \quad (5.15)$$

We can rewrite the source term (5.13) as

$$\widehat{\mathcal{S}}^s(\eta, \mathbf{k}) = \frac{4}{9} \int \frac{d^3p}{(2\pi)^3} e^s(\mathbf{k}, \mathbf{p}) f(p, |\mathbf{k} - \mathbf{p}|, \eta) \zeta(\mathbf{p}) \zeta(\mathbf{k} - \mathbf{p}), \quad (5.16)$$

where we have introduced

$$e^s(\mathbf{k}, \mathbf{p}) \equiv e^{s,ij}(\mathbf{k}) p_i p_j = \begin{cases} \frac{1}{\sqrt{2}} p^2 \sin^2 \theta \cos 2\phi & \text{for } s = (+), \\ \frac{1}{\sqrt{2}} p^2 \sin^2 \theta \sin 2\phi & \text{for } s = (\times), \end{cases} \quad (5.17)$$

where (p, θ, ϕ) are the coordinates of \mathbf{p} in a spherical coordinate system whose $(\hat{x}, \hat{y}, \hat{z})$ axes are aligned with $(e(\mathbf{k}), \bar{e}(\mathbf{k}), \mathbf{k})$, and

$$f(k_1, k_2, \eta) \equiv 4 \left[2T(\eta, k_1)T(\eta, k_2) + \left(T(\eta, k_1) + \frac{1}{\mathcal{H}} T'(\eta, k_1) \right) \left(T(\eta, k_2) + \frac{1}{\mathcal{H}} T'(\eta, k_2) \right) \right]. \quad (5.18)$$

5.2.3 A compact expression for GWs with a numerical integration over time

Let us rewrite the solution for the GWs $h_{\mathbf{k}}^s(\eta)$ by collecting the results of (5.9), (5.10), (5.16)

$$\begin{aligned} h_{\mathbf{k}}^s(\eta) &= \frac{1}{a(\eta)} \int^{\eta} d\tilde{\eta} \frac{\sin(k\eta) \cos(k\tilde{\eta}) - \cos(k\eta) \sin(k\tilde{\eta})}{k} a(\tilde{\eta}) \cdot \\ &\quad \cdot \frac{4}{9} \int \frac{d^3p}{(2\pi)^3} e^s(\mathbf{k}, \mathbf{p}) f(p, |\mathbf{k} - \mathbf{p}|, \tilde{\eta}) \zeta(\mathbf{p}) \zeta(\mathbf{k} - \mathbf{p}) = \\ &= \frac{4}{9} \int \frac{d^3p}{(2\pi)^3} \frac{1}{k^3 \eta} e^s(\mathbf{k}, \mathbf{p}) \zeta(\mathbf{p}) \zeta(\mathbf{k} - \mathbf{p}) \cdot \\ &\quad \cdot \left[\int^{\eta} k d\tilde{\eta} (k\tilde{\eta}) \left(\sin(k\eta) \cos(k\tilde{\eta}) - \cos(k\eta) \sin(k\tilde{\eta}) \right) f(p, |\mathbf{k} - \mathbf{p}|, \tilde{\eta}) \right], \end{aligned} \quad (5.19)$$

where we have expressed the scale factor in terms of conformal time during RD, $a(\tilde{\eta})/a(\eta) = \tilde{\eta}/\eta$.

The tensor modes begin to be generated at the time at which the wavelength $1/k$ re-enters the comoving Hubble radius. The transfer function (5.15) decays as η^{-2} , so that the generation of tensor modes is completed within a time which is a few orders of magnitude larger than k^{-1} , around $\eta \sim \mathcal{O}(10^3)k^{-1}$. Therefore the extrema of the integral over $\tilde{\eta}$ in Eq. (5.19) are $\tilde{\eta} = k^{-1}$ and the current time $\eta \gg \mathcal{O}(10^3)k^{-1}$, so that we can approximate it to $\tilde{\eta} \rightarrow \infty$.

The dimensionless expression contained in square brackets in Eq. (5.19) can be computed analytically, in order to facilitate the calculation of the two- and three-point functions. We denote

$$x = \frac{p}{k}, \quad y = \frac{|\mathbf{k} - \mathbf{p}|}{k}, \quad (5.20)$$

and we use the dimensionless time variable $\tau \equiv k\tilde{\eta}$, and we input the Hubble rate $\mathcal{H} = aH = \eta^{-1}$ during RD. We can then rewrite Eq. (5.19) as

$$h_{\mathbf{k}}^s(\eta) = \frac{4}{9} \int \frac{d^3p}{(2\pi)^3} \frac{1}{k^3 \eta} e^s(\mathbf{k}, \mathbf{p}) \zeta(\mathbf{p}) \zeta(\mathbf{k} - \mathbf{p}) \left[\mathcal{I}_c(x, y) \cos(k\eta) + \mathcal{I}_s(x, y) \sin(k\eta) \right], \quad (5.21)$$

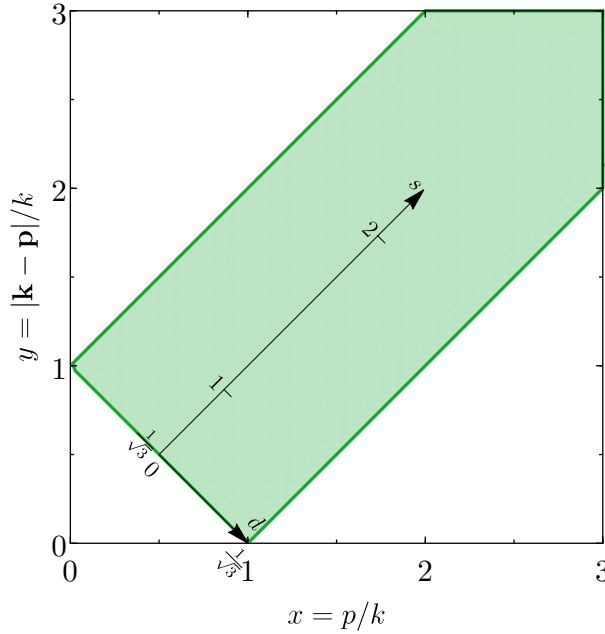


Figure 5.1: Domain for the variables $x = p/k$, $y = |\mathbf{k} - \mathbf{p}|/k$ allowed by the triangular inequality, superimposed with the (d, s) coordinates defined in Eq. (5.24).

where we have introduced two functions, \mathcal{I}_c and \mathcal{I}_s , that can be computed analytically (the reader can find the analytical result in Appendix 5.A)

$$\begin{aligned}\mathcal{I}_c(x, y) &= \int_1^\infty d\tau \tau (-\sin \tau) \cdot 4 \left\{ 2\mathcal{T}(x\tau)\mathcal{T}(y\tau) + \left[\mathcal{T}(x\tau) + x\tau \mathcal{T}'(x\tau) \right] \left[\mathcal{T}(y\tau) + y\tau \mathcal{T}'(y\tau) \right] \right\}, \\ \mathcal{I}_s(x, y) &= \int_1^\infty d\tau \tau (\cos \tau) \cdot 4 \left\{ 2\mathcal{T}(x\tau)\mathcal{T}(y\tau) + \left[\mathcal{T}(x\tau) + x\tau \mathcal{T}'(x\tau) \right] \left[\mathcal{T}(y\tau) + y\tau \mathcal{T}'(y\tau) \right] \right\}.\end{aligned}\quad (5.22)$$

The domain in the (x, y) plane is shown in Fig. 5.1: it consists of the configurations allowed by the triangular inequality applied to the triangle formed by the vectors \mathbf{k} , \mathbf{p} , $\mathbf{k} - \mathbf{p}$, and is given by

$$(x + y \geq 1) \wedge (x + 1 \geq y) \wedge (y + 1 \geq x). \quad (5.23)$$

It is useful to introduce two auxiliary variables (d, s) in terms of (x, y) , which simplify the expression of $\mathcal{I}_c, \mathcal{I}_s$ for the purpose of an analytical integration,

$$d = \frac{1}{\sqrt{3}}|x - y|, \quad s = \frac{1}{\sqrt{3}}(x + y), \quad (d, s) \in [0, 1/\sqrt{3}] \times [1/\sqrt{3}, +\infty) \quad (5.24)$$

This redefinition of domain is illustrated in Fig. 5.1.

The result for the analytical calculation of the integrals $\mathcal{I}_c, \mathcal{I}_s$ for each point (d, s) is shown in Figs. 5.2 and 5.3.

We observe that the numerical value of $\mathcal{I}_c(d, s), \mathcal{I}_s(d, s)$ is nearly independent of $d = |x - y|/\sqrt{3}$. More interestingly, the integrals $\mathcal{I}_c, \mathcal{I}_s$ are spiked for a value of $s \sim 1$ corresponding to $p + |\mathbf{k} - \mathbf{p}| \sim \sqrt{3}k$. The reason for this is that the integrands of \mathcal{I}_c and \mathcal{I}_s are products of trigonometric functions of τ times a rational function of τ , and the oscillating behaviour determines cancellations in the final result. Only for $p + |\mathbf{k} - \mathbf{p}| \sim \sqrt{3}k$ there appear some

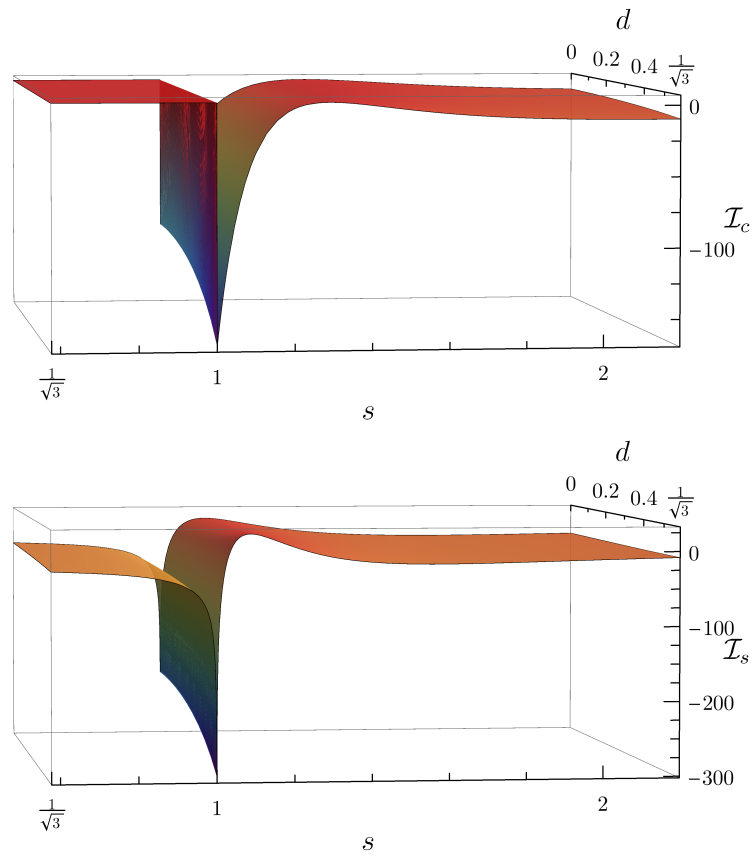


Figure 5.2: 3D plots of \mathcal{I}_c (upper plot) and \mathcal{I}_s (lower plot), defined in Eq. (5.22), as a function of (d, s) (Eq. (5.24)).

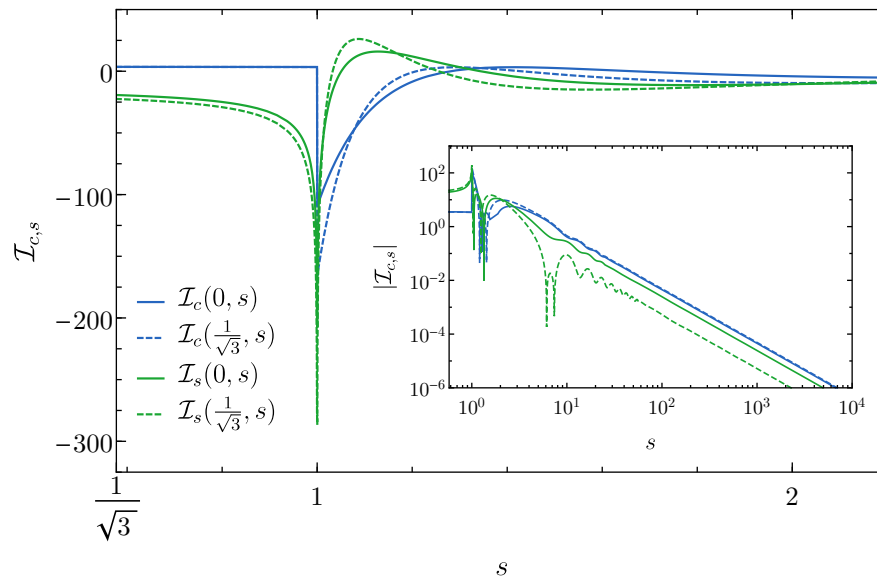


Figure 5.3: Behaviour of the integrals $\mathcal{I}_c, \mathcal{I}_s$, defined in Eq. (5.22), as a function of s (Eq. (5.24)), for the two extremal values of $d = |x - y|/\sqrt{3}$.

terms in the integrand with the square of a trigonometric function and thus with a definite sign, and this increases the final result. Notice that the factor $\sqrt{3}$ is simply due to the factor \sqrt{w} appearing in the arguments of the transfer function of Eq. (5.15), and not to geometrical reasons.

5.3 The Power Spectrum of Gravitational Waves

In this section we present the generic derivation of the two-point function and the power spectrum of gravitational waves. This result has been already derived and exposed in Refs. [435–438]. The goal of the present section is to match it with our notation, and to prepare an analogous derivation of the three-point function of GWs in the next section. In Sec. 5.5 we will use the formulæ obtained here to calculate the power spectrum and the three-point function of GWs generated in our scenario.

5.3.1 Two-point function of GWs

We begin by writing the definition of two-point function, with the use of Eq. (5.21)

$$\begin{aligned} \langle h^r(\eta, \mathbf{k}_1) h^s(\eta, \mathbf{k}_2) \rangle &= \\ &= \left(\frac{4}{9}\right)^2 \int \frac{d^3 p_1}{(2\pi)^3} \int \frac{d^3 p_2}{(2\pi)^3} \frac{1}{k_1^3 k_2^3 \eta^2} e^{r(\mathbf{k}_1, \mathbf{p}_1)} e^{s(\mathbf{k}_2, \mathbf{p}_2)} \langle \zeta(\mathbf{p}_1) \zeta(\mathbf{k}_1 - \mathbf{p}_1) \zeta(\mathbf{p}_2) \zeta(\mathbf{k}_2 - \mathbf{p}_2) \rangle \cdot \\ &\cdot [\cos(k_1 \eta) \mathcal{I}_c(x_1, y_1) + \sin(k_1 \eta) \mathcal{I}_s(x_1, y_1)] [\cos(k_2 \eta) \mathcal{I}_c(x_2, y_2) + \sin(k_2 \eta) \mathcal{I}_s(x_2, y_2)], \end{aligned} \quad (5.25)$$

where $x_i = p_i/k_i$, $y_i = |\mathbf{k}_i - \mathbf{p}_i|/k_i$. To evaluate the four-point function of the curvature perturbation ζ we proceed as usual, noting that at leading order it is a Gaussian variable defined by the dimensionless power spectrum \mathcal{P}_ζ

$$\langle \zeta(\mathbf{k}_1) \zeta(\mathbf{k}_2) \rangle \equiv (2\pi)^3 \delta^{(3)}(\mathbf{k}_1 + \mathbf{k}_2) \frac{2\pi^2}{k_1^3} \mathcal{P}_\zeta(k_1), \quad (5.26)$$

and the four-point function of ζ of the first line of (5.25) has two possible non-vanishing contractions for $\mathbf{k}_1, \mathbf{k}_2 \neq 0$. The two contributions give the same result, given that they correspond to each other up to a shift $\mathbf{p}_2 \rightarrow (\mathbf{k}_2 - \mathbf{p}_2)$, which is a symmetry of Eq. (5.25), see Appendix 5.B for details. We can evaluate then Eq. (5.25) for any of the two configurations, and multiply the final result by 2. After integrating over \mathbf{p}_2 one gets

$$\begin{aligned} \langle h^r(\eta, \mathbf{k}_1) h^s(\eta, \mathbf{k}_2) \rangle &= \\ &= (2\pi)^3 \delta^{(3)}(\mathbf{k}_1 + \mathbf{k}_2) \cdot 2 \left(\frac{4}{9}\right)^2 \int \frac{d^3 p_1}{(2\pi)^3} \frac{1}{k_1^3 \eta^2} e^{r(\mathbf{k}_1, \mathbf{p}_1)} e^{s(\mathbf{k}_1, \mathbf{p}_1)} \frac{2\pi^2}{p_1^3} \frac{2\pi^2}{|\mathbf{k}_1 - \mathbf{p}_1|^3} \mathcal{P}_\zeta(p_1) \mathcal{P}_\zeta(|\mathbf{k}_1 - \mathbf{p}_1|) \cdot \\ &\cdot [\cos^2(k_1 \eta) \mathcal{I}_c(x_1, y_1)^2 + \sin^2(k_1 \eta) \mathcal{I}_s(x_1, y_1)^2 + \sin(2k_1 \eta) \mathcal{I}_c(x_1, y_1) \mathcal{I}_s(x_1, y_1)]. \end{aligned} \quad (5.27)$$

Let us refer to a system of spherical coordinates (p_1, θ, ϕ) oriented around the axis \mathbf{k}_1 , and denote $x \equiv x_1 = p_1/k_1$, $y \equiv y_1 = |\mathbf{k}_1 - \mathbf{p}_1|/k_1$. In these variables one has

$$\mathbf{p}_1 = (k_1 x, \cos^{-1}((1 + x^2 - y^2)/2x), \phi). \quad (5.28)$$

We perform the following change of integration variables

$$\int d^3 p_1 \longrightarrow k_1^3 \iint_{\mathcal{S}} dx dy x^2 \frac{y}{x} \int_0^{2\pi} d\phi, \quad (5.29)$$

where \mathcal{S} is the infinite strip shown in Fig. 5.1. The integral over ϕ can be easily solved analytically, and selects only some of the possible couples of polarisations (r, s) to give a non-vanishing result. With the use of Eq. (5.17) we obtain

$$\int_0^{2\pi} d\phi e^{r(\mathbf{k}_1, \mathbf{p}_1)} e^{s(\mathbf{k}_1, \mathbf{p}_1)} = \frac{k_1^4}{2} x^4 \left[1 - \frac{(1+x^2-y^2)^2}{4x^2} \right]^2 \cdot \pi \delta^{rs}. \quad (5.30)$$

By collecting the results of the last three equations we get the final expression for the two-point function of GWs:

$$\begin{aligned} \langle h^r(\eta, \mathbf{k}_1) h^s(\eta, \mathbf{k}_2) \rangle &= \\ &= (2\pi)^3 \delta^{(3)}(\mathbf{k}_1 + \mathbf{k}_2) \delta^{rs} \frac{2\pi^2}{k_1^3} \cdot 2 \left(\frac{4}{9} \right)^2 \frac{1}{k_1^2 \eta^2} \iint_{\mathcal{S}} dx dy \frac{x^2}{8y^2} \left[1 - \frac{(1+x^2-y^2)^2}{4x^2} \right]^2 \cdot \\ &\quad \mathcal{P}_\zeta(k_1 x) \mathcal{P}_\zeta(k_1 y) [\cos^2(k_1 \eta) \mathcal{I}_c^2 + \sin^2(k_1 \eta) \mathcal{I}_s^2 + \sin(2k_1 \eta) \mathcal{I}_c \mathcal{I}_s], \end{aligned} \quad (5.31)$$

where for brevity we do not write the arguments of the functions $\mathcal{I}_c(x, y)$ and $\mathcal{I}_s(x, y)$, defined in Eq. (5.22) and plotted in Figs. 5.2 and 5.3. The integrand is explicitly symmetric under exchange of x and y . From Eq. (5.31) and the definition of the power spectrum of GWs

$$\langle h^r(\eta, \mathbf{k}_1) h^s(\eta, \mathbf{k}_2) \rangle \equiv (2\pi)^3 \delta^{(3)}(\mathbf{k}_1 + \mathbf{k}_2) \delta^{rs} \frac{2\pi^2}{k_1^3} \mathcal{P}_h(k_1) \quad (5.32)$$

we can extract $\mathcal{P}_h(\eta, k)$:

$$\begin{aligned} \mathcal{P}_h(\eta, k) &= \frac{4}{81} \frac{1}{k^2 \eta^2} \iint_{\mathcal{S}} dx dy \frac{x^2}{y^2} \left[1 - \frac{(1+x^2-y^2)^2}{4x^2} \right]^2 \mathcal{P}_\zeta(kx) \mathcal{P}_\zeta(ky) \cdot \\ &\quad \cdot [\cos^2(k\eta) \mathcal{I}_c^2 + \sin^2(k\eta) \mathcal{I}_s^2 + \sin(2k\eta) \mathcal{I}_c \mathcal{I}_s]. \end{aligned} \quad (5.33)$$

5.3.2 The energy density of GWs

In this section we derive the expression for the energy density of GWs, and its fraction Ω_{GW} relative to the critical energy density. The energy density of GWs is [439]

$$\rho_{\text{GW}}(\eta, \mathbf{x}) = \frac{M_{\text{P}}^2}{16a^2(\eta)} \left\langle \frac{1}{2} \overline{(h'_{ij})^2} + \frac{1}{2} \overline{(\nabla h_{ij})^2} \right\rangle \simeq \frac{M_{\text{P}}^2}{16a^2(\eta)} \left\langle \overline{(\nabla h_{ij})^2} \right\rangle, \quad (5.34)$$

where the overlines denote an average over time. This expression for the energy density can be rewritten in terms of the power spectrum of GWs as follows

$$\rho_{\text{GW}}(\eta) = \int d \ln k \rho_{\text{GW}}(\eta, k), \quad (5.35)$$

$$\rho_{\text{GW}}(\eta, k) = \frac{M_{\text{P}}^2}{8} \left(\frac{k}{a(\eta)} \right)^2 \overline{\mathcal{P}_h(\eta, k)}. \quad (5.36)$$

We can then define the density parameter of GWs per logarithmic interval of k ,

$$\Omega_{\text{GW}}(\eta, k) = \frac{\rho_{\text{GW}}(\eta, k)}{\rho_{\text{cr}}(\eta)} = \frac{1}{24} \left(\frac{k}{\mathcal{H}(\eta)} \right)^2 \overline{\mathcal{P}_h(\eta, k)}. \quad (5.37)$$

The expression for the power spectrum that we have computed in the previous section holds only during the RD era. The energy density of GWs decays as radiation, so we can easily estimate the fraction of energy density of GWs in terms of the current energy density of radiation $\Omega_{r,0}$ and $\Omega_{\text{GW}}(\eta_f, k)$ at a generic time η_f towards the end of the RD era:

$$\Omega_{\text{GW}}(\eta_0, k) = \Omega_{r,0} \Omega_{\text{GW}}(\eta_f, k) = \frac{\Omega_{r,0}}{24} \frac{k^2}{\mathcal{H}(\eta_f)^2} \overline{\mathcal{P}_h(\eta_f, k)}. \quad (5.38)$$

We can collect the results of Eqs. (5.33) and (5.38), plug $\mathcal{H}(\eta_f) = 1/\eta_f$ (valid through RD), and perform a simplification for the average over time justified by the fact that $k\eta \gg 1$

$$\frac{\overline{\cos^2(k\eta)}}{\eta^2} \sim \frac{\overline{\sin^2(k\eta)}}{\eta^2} \sim \frac{1}{2} \frac{1}{\eta^2}, \quad \frac{\overline{\sin(2k\eta)}}{\eta^2} \sim 0. \quad (5.39)$$

We finally obtain the current energy density of GWs

$$\Omega_{\text{GW}}(\eta_0, k) = \frac{\Omega_{r,0}}{972} \iint_{\mathcal{S}} dx dy \frac{x^2}{y^2} \left[1 - \frac{(1+x^2-y^2)^2}{4x^2} \right]^2 \mathcal{P}_\zeta(kx) \mathcal{P}_\zeta(ky) [\mathcal{I}_c(x, y)^2 + \mathcal{I}_s(x, y)^2]. \quad (5.40)$$

5.4 Bispectrum of Gravitational Waves

In this section we compute the bispectrum (three-point function) of GWs. Let us start from the solution (5.21) for GWs, and write the three-point function as

$$\begin{aligned} & \langle h^r(\eta, \mathbf{k}_1) h^s(\eta, \mathbf{k}_2) h^t(\eta, \mathbf{k}_3) \rangle = \\ & = \left(\frac{4}{9} \right)^3 \int \frac{d^3 p_1}{(2\pi)^3} \int \frac{d^3 p_2}{(2\pi)^3} \int \frac{d^3 p_3}{(2\pi)^3} \frac{1}{k_1^3 k_2^3 k_3^3 \eta^3} e^r(\mathbf{k}_1, \mathbf{p}_1) e^s(\mathbf{k}_2, \mathbf{p}_2) e^t(\mathbf{k}_3, \mathbf{p}_3) \cdot \\ & \cdot \langle \zeta(\mathbf{p}_1) \zeta(\mathbf{k}_1 - \mathbf{p}_1) \zeta(\mathbf{p}_2) \zeta(\mathbf{k}_2 - \mathbf{p}_2) \zeta(\mathbf{p}_3) \zeta(\mathbf{k}_3 - \mathbf{p}_3) \rangle [\cos(k_1 \eta) \mathcal{I}_c(x_1, y_1) + \sin(k_1 \eta) \mathcal{I}_s(x_1, y_1)] \cdot \\ & \cdot [\cos(k_2 \eta) \mathcal{I}_c(x_2, y_2) + \sin(k_2 \eta) \mathcal{I}_s(x_2, y_2)] [\cos(k_3 \eta) \mathcal{I}_c(x_3, y_3) + \sin(k_3 \eta) \mathcal{I}_s(x_3, y_3)], \quad (5.41) \end{aligned}$$

where $x_i = p_i/k_i$ and $y_i = |\mathbf{k}_i - \mathbf{p}_i|/k_i$. The details of the calculation of the six-point function of the curvature perturbation ζ are given in Appendix 5.B. We have eight possible contractions for $\mathbf{k}_i \neq 0$ that yield the same contribution to the bispectrum. We can evaluate the three-point function for any of these configurations and multiply by eight the result: we choose the configuration shown in Fig. 5.4. The three-point function (5.41) becomes then (we understand that $\mathbf{p}_2 = \mathbf{p}_1 - \mathbf{k}_1$, $\mathbf{p}_3 = \mathbf{p}_1 + \mathbf{k}_3$, and $y_1 = x_2$, $y_2 = x_3$, $y_3 = x_1$):

$$\begin{aligned} & \langle h^r(\eta, \mathbf{k}_1) h^s(\eta, \mathbf{k}_2) h^t(\eta, \mathbf{k}_3) \rangle = \quad (5.42) \\ & = (2\pi)^3 \delta^{(3)}(\mathbf{k}_1 + \mathbf{k}_2 + \mathbf{k}_3) 8 \left(\frac{4}{9} \right)^3 \pi^3 \int d^3 p_1 \frac{1}{k_1^3 k_2^3 k_3^3 \eta^3} \cdot \\ & \cdot e^r(\mathbf{k}_1, \mathbf{p}_1) e^s(\mathbf{k}_2, \mathbf{p}_2) e^t(\mathbf{k}_3, \mathbf{p}_3) \frac{\mathcal{P}_\zeta(p_1)}{p_1^3} \frac{\mathcal{P}_\zeta(p_2)}{p_2^3} \frac{\mathcal{P}_\zeta(p_3)}{p_3^3} \left[\cos(k_1 \eta) \mathcal{I}_c \left(\frac{p_1}{k_1}, \frac{p_2}{k_1} \right) + \sin(k_1 \eta) \mathcal{I}_s \left(\frac{p_1}{k_1}, \frac{p_2}{k_1} \right) \right] \cdot \\ & \cdot \left[\cos(k_2 \eta) \mathcal{I}_c \left(\frac{p_2}{k_2}, \frac{p_3}{k_2} \right) + \sin(k_2 \eta) \mathcal{I}_s \left(\frac{p_2}{k_2}, \frac{p_3}{k_2} \right) \right] \left[\cos(k_3 \eta) \mathcal{I}_c \left(\frac{p_3}{k_3}, \frac{p_1}{k_3} \right) + \sin(k_3 \eta) \mathcal{I}_s \left(\frac{p_3}{k_3}, \frac{p_1}{k_3} \right) \right]. \end{aligned}$$

The polarisation tensors defined in Eq. (5.17) involve the angles θ_i , ϕ_i (shown in Fig. 5.4 for $i = 1$) which identify \mathbf{p}_i in spherical coordinates around the axis \mathbf{k}_i .

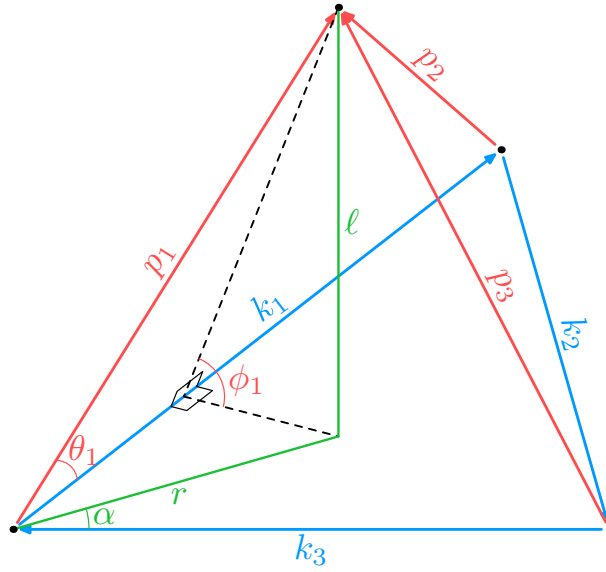


Figure 5.4: Geometrical configuration for the contraction (i) of the 6-point function of ζ written in Eq. (5.63).

With reference to Fig. 5.4, the vectors \mathbf{k}_i in blue are given and we can choose a reference frame such that

$$\mathbf{k}_1 = (k_{1x}, k_{1y}, 0), \quad \mathbf{k}_2 = (k_{2x}, k_{2y}, 0), \quad \mathbf{k}_3 = (-k_3, 0, 0); \quad (5.43)$$

the quantities ℓ , r , and α in green are a convenient choice of cylindrical coordinates as integration variables,

$$\int d^3 p_1 \longrightarrow \int_{-\infty}^{+\infty} d\ell \int_0^{+\infty} r dr \int_0^{2\pi} d\alpha; \quad (5.44)$$

the quantities marked in red give the expressions to plug in Eq. (??),

$$\begin{aligned} \mathbf{p}_1 &= (r \cos \alpha, r \sin \alpha, \ell), \\ \mathbf{p}_2 &= (-k_{1x} + r \cos \alpha, -k_{1y} + r \sin \alpha, \ell), \\ \mathbf{p}_3 &= (k_3 + r \cos \alpha, r \sin \alpha, \ell), \end{aligned} \quad (5.45)$$

$$p_i^2 \sin^2 \theta_i = p_i^2 - \frac{|\mathbf{p}_i \cdot \mathbf{k}_i|^2}{k_i^2}, \quad \sin \phi_i = \frac{\ell k_i}{|\mathbf{p}_i \times \mathbf{k}_i|}.$$

Eqs. (??), (5.17), and (5.22), with the replacements listed in (5.43), (5.44), (5.45), contain all the ingredients for the numerical calculation of the bispectrum B_h^{rst} of GWs, defined as

$$\langle h^r(\eta, \mathbf{k}_1) h^s(\eta, \mathbf{k}_2) h^t(\eta, \mathbf{k}_3) \rangle \equiv (2\pi)^3 \delta^{(3)}(\mathbf{k}_1 + \mathbf{k}_2 + \mathbf{k}_3) B_h^{rst}(\mathbf{k}_1, \mathbf{k}_2, \mathbf{k}_3). \quad (5.46)$$

Out of the eight possible polarisations (r, s, t) of the three-point function, four of them vanish due to parity arguments applied to the polarisation tensors, in analogy to what happens for the two-point function, see Eq. (5.30). Among the terms contained in Eq. (??), the only ones which are odd under the parity transformation $\ell \rightarrow -\ell$ (that is, a parity transformation with respect to the plane containing $\mathbf{k}_1, \mathbf{k}_2, \mathbf{k}_3$) are the polarisation tensors e^\times , and all other terms are even. This implies that the only four non-vanishing polarisation combinations for the three-point functions are

$$(+++), \quad (+\times\times), \quad (\times+\times), \quad (\times\times+). \quad (5.47)$$

5.5 Numerical results for the Energy Density and Bispectrum of GWs

5.5.1 Energy density of GWs

We devote this section to the results of the numerical integration for the scalar power spectra $\mathcal{P}_\zeta(k)$ obtained for a few illustrative cases of the mechanism discussed in Chapter 4. We rewrite for convenience the energy density of GWs of Eq. (5.40) in terms of the variables (d, s) defined in Eq. (5.24) as

$$\Omega_{\text{GW}}(\eta_0, k) = \frac{\Omega_{r,0}}{36} \int_0^{\frac{1}{\sqrt{3}}} dd \int_{\frac{1}{\sqrt{3}}}^{\infty} ds \left[\frac{(d^2 - 1/3)(s^2 - 1/3)}{s^2 - d^2} \right]^2 \cdot \mathcal{P}_\zeta \left(\frac{k\sqrt{3}}{2}(s+d) \right) \mathcal{P}_\zeta \left(\frac{k\sqrt{3}}{2}(s-d) \right) [\mathcal{I}_c(d,s)^2 + \mathcal{I}_s(d,s)^2], \quad (5.48)$$

where the functions $\mathcal{I}_c, \mathcal{I}_s$ are defined in Eq. (5.22) and are plotted in Figures 5.2 and 5.3.

We consider the running of the quartic Higgs coupling λ for some sample points in the parameter space $(m_{\text{top}}, m_{\text{Higgs}})$ denoted by the number of standard deviations from the measured central values. We have taken the current LHC combination [416–418]

$$m_{\text{top}} = 172.47 \pm 0.5 \text{ GeV}, \quad m_{\text{Higgs}} = 125.09 \pm 0.24 \text{ GeV}. \quad (5.49)$$

The corresponding running of the quartic Higgs coupling λ is shown in Fig. 5.5.

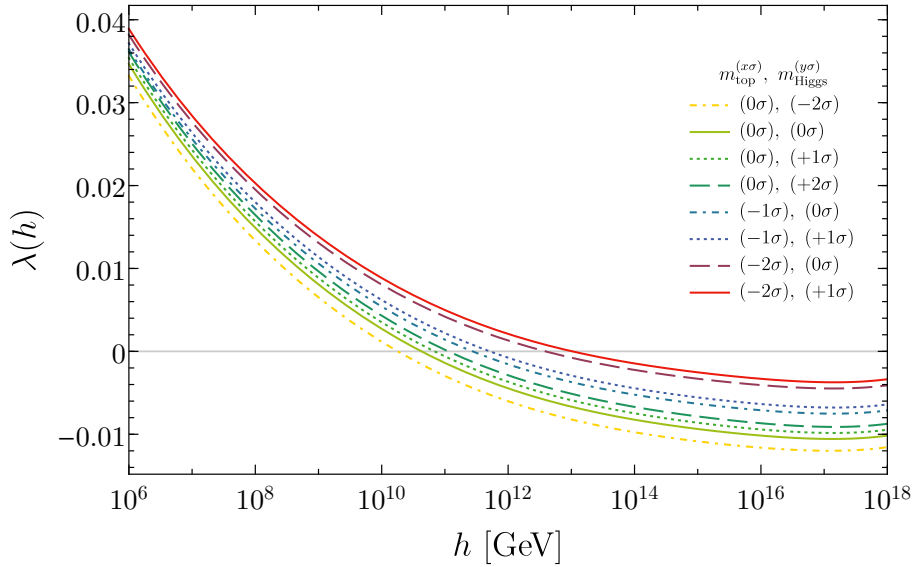


Figure 5.5: Running of the quartic Higgs coupling λ for the masses $m_{\text{top}}, m_{\text{Higgs}}$ listed in Eq. (5.49).

Each of these points defines therefore a different Higgs potential, for which we run an evolution of the Higgs field completely analogous to what was described in Chapter 4, by keeping a fixed Hubble rate $H = 10^{12}$ GeV. This evolution leads to the creation of PBH during the radiation dominated era, with a peak in the mass function for scales of the order of k_* , the mode that leaves the Hubble radius at the time t_* when the classical evolution of the Higgs field starts, as described in the Introduction. The corresponding \mathcal{P}_ζ has basically the same shape in all these

cases, and what changes is the reference scale k_* for the enhancement of the power spectrum as we show in Fig. 5.6.²

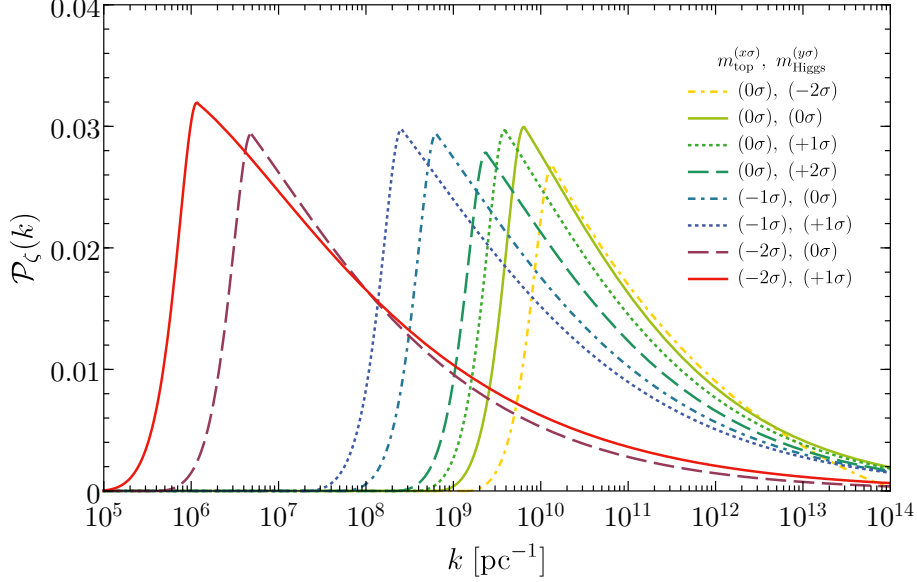


Figure 5.6: The power spectrum of the comoving curvature perturbation during the radiation phase obtained in Ref. [3] for the masses $m_{\text{top}}, m_{\text{Higgs}}$ listed in Eq. (5.49).

The final result for the power spectra of GW is shown in Fig. 5.7, together with the comparison with the projected sensitivity of proposed future experiments. The sensitivity curve for LISA is estimated on the basis of the proposal [440]: the proposed design (4y, 2.5 Gm of length, 6 links) is expected to yield a sensitivity in between the ones dubbed C1 and C2 in Ref. [441]³. We also include the projected design sensitivity for Advanced LIGO + Virgo from Ref. [442], and the estimated sensitivity for the proposed Einstein Telescope (ET) [443, 444].

The GW power spectra are shown for different combinations of the values of the Higgs and top masses where the symbols $m_{\text{Higgs}}^{(\pm n\sigma)}$ and $m_{\text{top}}^{(\pm n\sigma)}$ indicate their values $\pm n\sigma$ away from their central values. A GW power spectrum for values of the Higgs boson mass $m_{\text{Higgs}} = 125.09$ GeV (the current central value) and $m_{\text{top}} = 171.47$ GeV, is well within the reach of LISA. To relate the amount of GWs and the PBH abundance at formation following the proposal of Chapter 4, one can use the relation $M_{\text{PBH}} \simeq 50M_{\odot} (10^{-9}\text{Hz}/f)^2$. In Fig. 5.7, we have used that relation to translate the frequencies of the GW signal in terms of the peak mass of the PBH distribution.

One fundamental information to be drawn from Fig. 5.7 is that the frequency at the peak depends in a sensitive way on the Higgs and top masses, ranging from 10^{-2} to about 10 Hz, see Table 5.1. Therefore, according to the Higgs and top masses, the signal falls either within the LISA or the ET and Advanced-Ligo sensitivity curves. This implies that a detected signal can be cross-checked with the information obtained through colliders, thus either confirming or ruling out its Standard Model origin.

We draw the attention of the reader that our results for the GW power spectra in Fig. 5.7 are sensitive to the value of the Higgs field at the beginning of its classical dynamics. A per mille change in such a value can lead to variations of the power spectrum of the curvature

²If the same mechanism is supposed to give rise to PBHs, then these power spectra yield a final abundance $\Omega_{\text{PBH}}/\Omega_{\text{CDM}}$ ranging between 10^{-3} and 10^{-1} when no accretion is included [3].

³We thank G. Nardini for clarifying discussions about this point.

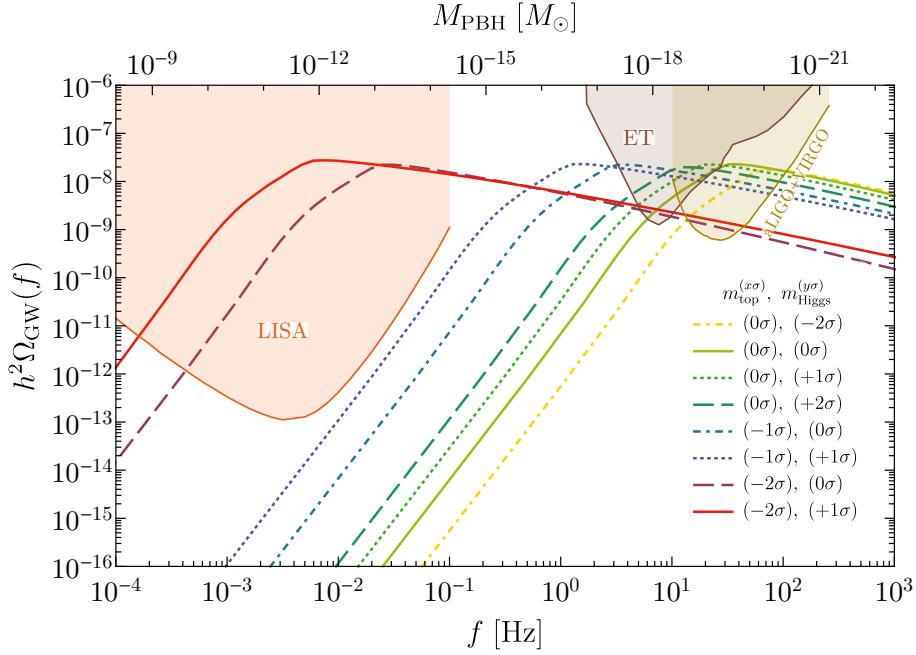


Figure 5.7: Power spectra of GWs for the scalar power spectra generated by the mechanism discussed in Chapter 4, compared with the estimated sensitivities for LISA, the Einstein Telescope, and the design sensitivity of Advanced LIGO + Virgo. The Higgs and top mass values are $m_{\text{Higgs}} = 125.09 \pm 0.24$ GeV and $m_{\text{top}} = 172.47 \pm 0.5$ GeV.

perturbation by (2 – 4) orders of magnitude. However, from Fig. 5.7 it is clear that we can still afford a change in \mathcal{P}_ζ of three orders of magnitude.

5.5.2 The spectral tilt of GWs at low and high frequencies

As we have mentioned in the introduction, the spectral tilt of the GW spectrum is a very interesting observable as GWs cover a large range of frequencies. For instance, writing the GW energy density as $\Omega_{\text{GW}} = \Omega_{\text{GW}}^{\text{CMB}} (f/f_{\text{CMB}})^{n_T}$, being n_T the spectral tilt and $f_{\text{CMB}} \sim 7.7 \cdot 10^{-17}$ Hz the CMB frequency, a limit of $n_T \lesssim 0.35$ can in principle be obtained for the best LISA configuration with six links, five million km arm length and a five year mission [430].

If the scalar power spectrum $\mathcal{P}_\zeta(k)$ is vanishing or negligible for k smaller than some scale k_* , and approximately constant for $k > k_*$ as in our case, then at small k we have $\Omega_{\text{GW}} \sim k^3$. Indeed, in this case $\mathcal{P}_\zeta(kx)$ in Eq. (5.48) for $k \ll k_*$ selects $s \gtrsim 1/k$ in the integral over s , so that the tail at high s of $\mathcal{I}_{c,s}(d, s)$ is picked up and it goes as $1/s^2$ (see Fig. 5.3). The resulting overall integral is therefore of order

$$\int_{1/k} ds \frac{ds}{s^4} \sim k^3. \quad (5.50)$$

As for the spectral tilt at $k \gg k_*$, the integral over s in Eq. (5.48) is peaked at $s \sim \sqrt{3}$ due to the spike in $\mathcal{I}_{c,s}(d, s)$ (see Fig. 5.3) and the dependence on k comes from $\mathcal{P}_\zeta(kx)\mathcal{P}_\zeta(k(\sqrt{3}-x))$ which has a spectral tilt equal roughly to twice the spectral index of \mathcal{P}_ζ . In our case, $\mathcal{P}_\zeta(k) \sim k^{-0.35}$ and $\Omega_{\text{GW}}(k)$ turns out to go as $\sim k^{-0.6}$. For a narrow scalar power spectrum $\mathcal{P}_\zeta(k)$, we would expect by similar arguments a spectral index $\sim +4$ at small k and a quite sharp cutoff at high k .

The final parametrisation of the GW spectrum induced by the Higgs fluctuations is therefore

$$\Omega_{\text{GW}}(f) \simeq 3 \cdot 10^{-8} \left(\frac{f}{f_*} \right)^{n_T} \quad \text{with} \quad n_T = \begin{cases} 3 & \text{for } f < f_*, \\ -0.6 & \text{for } f > f_*. \end{cases} \quad (5.51)$$

$m_{\text{top}}^{(x\sigma)}$	$m_{\text{Higgs}}^{(y\sigma)}$	f_* (Hz)
(0 σ)	(-2 σ)	40.0
(0 σ)	(0 σ)	21.8
(0 σ)	(+1 σ)	13.0
(0 σ)	(+2 σ)	7.74
(-1 σ)	(0 σ)	2.02
(-1 σ)	(+1 σ)	0.80
(-2 σ)	(0 σ)	0.015
(-2 σ)	(+1 σ)	0.0038

Table 5.1: Values of f_* defined in Eq. (5.51) for each of the cases considered in Fig. 5.7.

The values of f_* for the cases we consider are listed in Table 5.1. The parametrisation of Eq. (5.51) is useful to deduce its detectability by LISA. The investigation of a generic GW background whose energy density is parametrised as $\Omega_{\text{GW}}(f) = A(f/f_*)^{n_T}$ can be found in Ref. [430] where it was imposed that the signal-to-noise ratio is larger than 10, see Fig. 2 of Ref. [430]. It seems that for the case of Higgs mass $m_{\text{Higgs}} = 125.09$ GeV and $m_{\text{top}} = 171.47$ GeV not only the amplitude of the gravitational waves from Higgs perturbations, but also its spectral index can be measured with accuracy, opening the possibility of a full identification of the underlying mechanism.

Were GWs found, the value of the frequency f_* would allow to identify the approximate position of the instability scale Λ_I of the Higgs potential, defined by $V(\Lambda_I) = 0$. The instability scale Λ_I can be identified by the relation

$$\Lambda_I \simeq 3 \cdot 10^{11} \left(\frac{f_*}{\text{Hz}} \right)^{-0.65} \text{ GeV}, \quad (5.52)$$

obtained by the numerical fit shown in Fig. 5.8.

We stress that this relation is robust in the sense that the frequency changes very little even when the overall amplitude of the GW signal decreases due to a variation of the initial condition of the classical Higgs field. It is remarkable that a measurement of the frequency of the GW signal can be directly related to such a high energy scale.

5.5.3 The three-point correlator of GWs and its consistency relations

In this subsection we present our findings for the three-point correlator of the GWs. As mentioned in the introduction, the community has already started discussing the detectability of such non-Gaussian signal at interferometers [434]. The ultimate reason for measuring the GW bispectrum is to exploit the correspondence between the three-point and the two-point correlators in order to discriminate the different mechanisms which give rise to a GW signal hopefully measured by LISA.

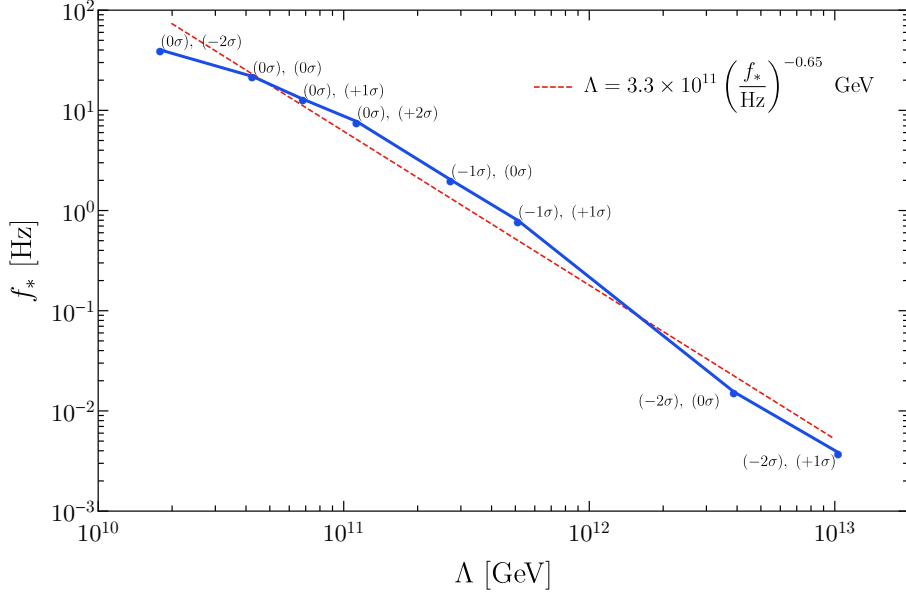


Figure 5.8: Instability scale Λ of the Higgs potential as a function of the peak frequency of the GW power spectrum f_* .

We defined the bispectrum $B_h^{rst}(\mathbf{k}_1, \mathbf{k}_2, \mathbf{k}_3)$ (the temporal dependence on η is understood) in Eq. (5.46). We also define a dimensionless normalised shape $S_h^{rst}(\mathbf{k}_1, \mathbf{k}_2, \mathbf{k}_3)$ in order to cancel the time scaling of GWs as $1/\eta$ [see Eq. (5.21)]:

$$S_h^{rst}(\mathbf{k}_1, \mathbf{k}_2, \mathbf{k}_3) = k_1^2 k_2^2 k_3^2 \frac{B_h^{rst}(\mathbf{k}_1, \mathbf{k}_2, \mathbf{k}_3)}{\sqrt{\mathcal{P}_h(k_1)\mathcal{P}_h(k_2)\mathcal{P}_h(k_3)}}, \quad (5.53)$$

where $\mathcal{P}_h(k)$ is the dimensionless power spectrum defined in Eq. (5.32). As for the oscillatory behaviour of the two- and three-point functions, we consider their envelope in time. We replace then the oscillating function in squared brackets in the solution (5.21) by its envelope

$$\mathcal{I}_c(x, y) \cos(k\eta) + \mathcal{I}_s(x, y) \sin(k\eta) \rightarrow \sqrt{\mathcal{I}_c(x, y)^2 + \mathcal{I}_s(x, y)^2}, \quad (5.54)$$

both for B_h and \mathcal{P}_h in Eq. (5.53).

We show the numerical results for the bispectrum by fixing the value of k_3 and by ordering the momenta as $k_1 \leq k_2 \leq k_3$. Figs. 5.9 and 5.10 show contours of $S_h(\mathbf{k}_1, \mathbf{k}_2, \mathbf{k}_3)$ in the plane $(k_1/k_3, k_2/k_3)$ for two values of k_3 close to the maximum of $\mathcal{P}_\zeta(k)$ (shown in Fig. 5.6). We choose the case $(m_{\text{top}}^{(-2\sigma)}, m_{\text{higgs}}^{(0\sigma)})$, as it falls into the window detectable by LISA, but we notice that the result is identical for the other cases, given that the shape of the power spectrum is identical, up to a rescaling of the momenta (k_1, k_2, k_3) . We also notice that the normalised shape defined in Eq. (5.53) is invariant under rescaling of the scalar power spectrum $\mathcal{P}_\zeta(k)$. In Fig. 5.9, together with the separate plots for each polarisation, we also show their sum in the lower two plots, both with contours and with a three-dimensional plot.

From these numerical results we observe several features. First of all, we remind the reader that there are traditionally several configurations one can analyse:

- the local one where the signal is peaked for squeezed configurations $k_1 \ll k_2 \simeq k_3$;

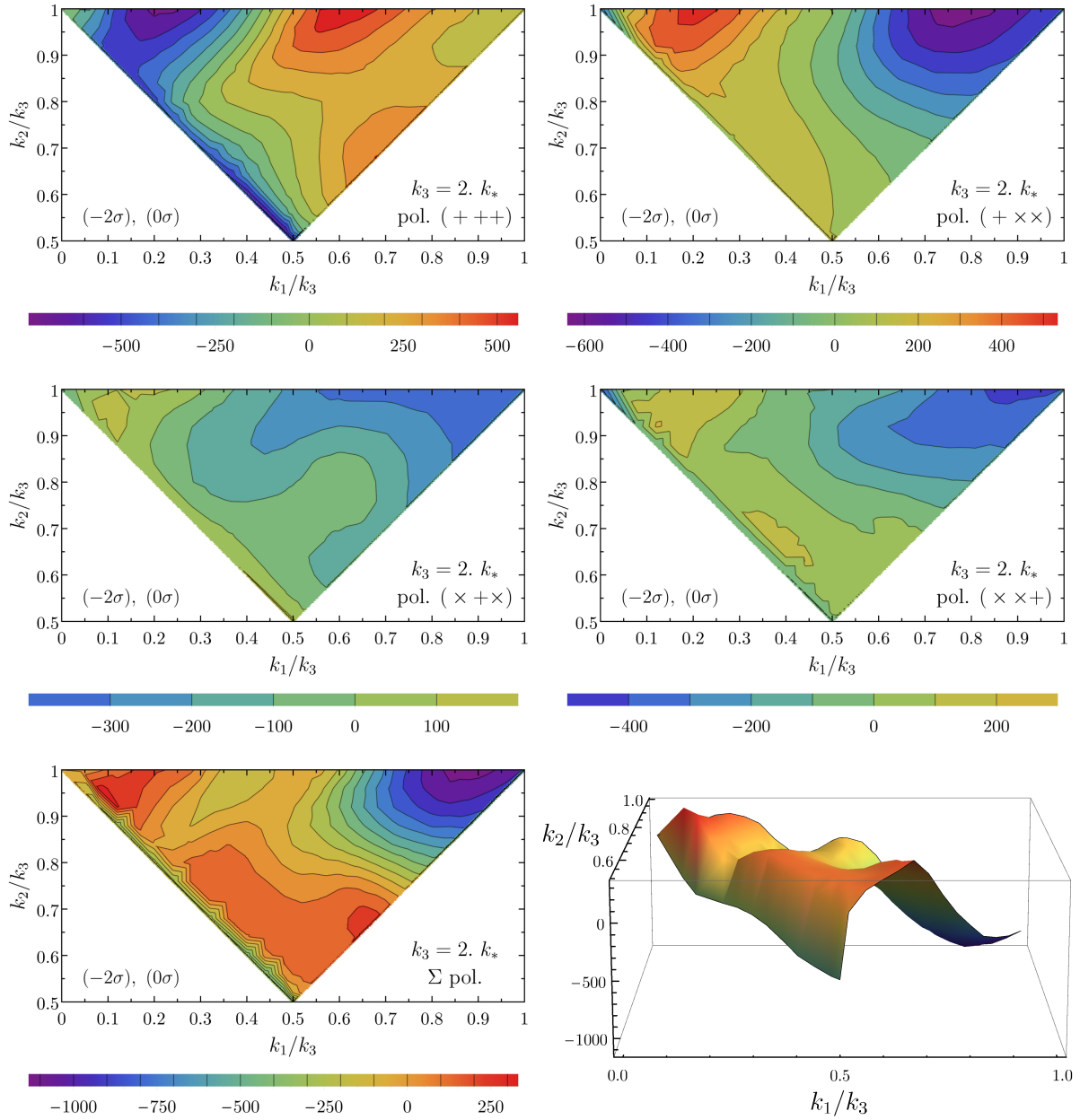


Figure 5.9: Normalised shapes of GWs [defined in Eq. (5.53)] for the spectrum in the case $(m_{\text{top}}^{(-2\sigma)}, m_{\text{higgs}}^{(0\sigma)})$. Here k_3 is fixed to be $2k_*$, corresponding to 0.04 Hz. The upper four plots show the four non-vanishing polarisations listed in Eq. (5.47). The two plots at the bottom show the sum over all the polarisations.

- the equilateral configuration peaks for equilateral configurations $k_1 \simeq k_2 \simeq k_3$ for which the strongest correlations between fluctuation modes happen when they cross the horizon approximately at the same time;
- the folded configuration for which the signal is boosted for $k_1 + k_2 \simeq k_3$;
- the orthogonal configuration ($k_1 \simeq k_2$) which creates a signal with a positive peak at the equilateral configuration and a negative peak at the folded configuration.

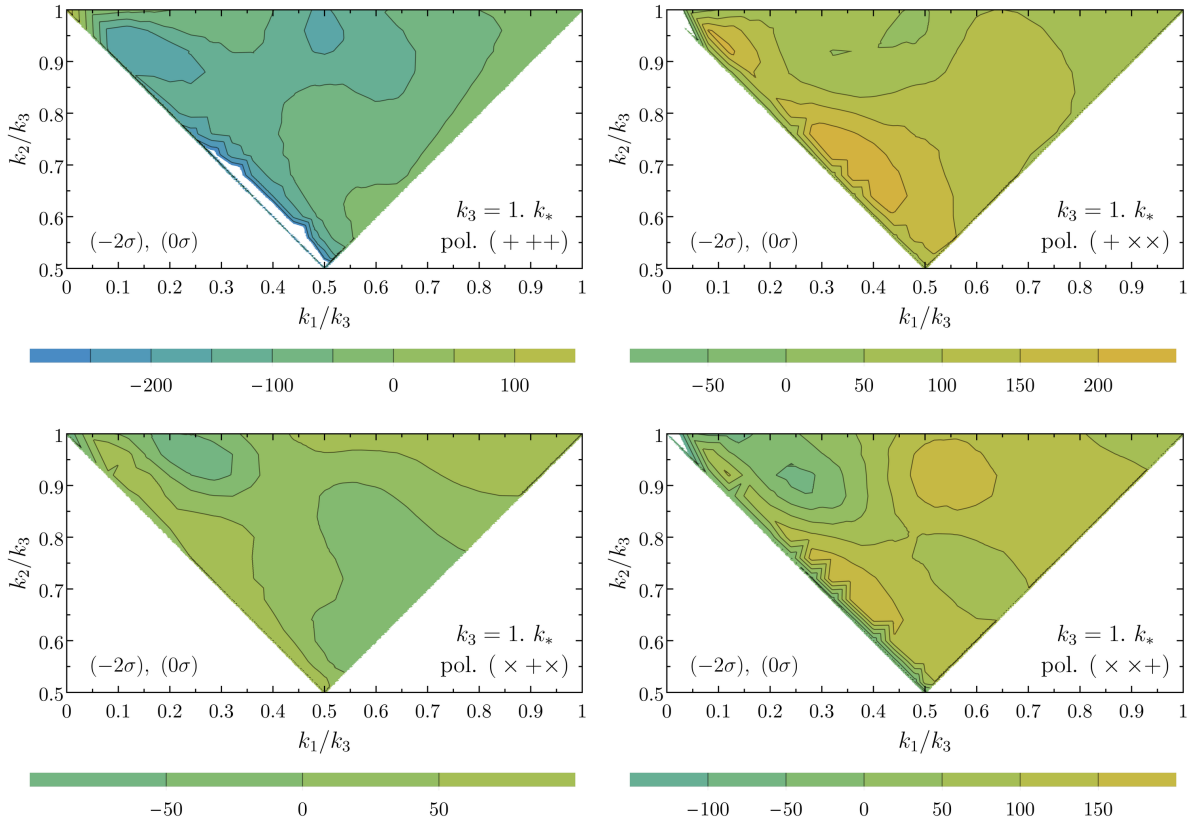


Figure 5.10: Same as Fig. 5.9, for $k_3 = k_*$, corresponding to 0.02 Hz.

The signal is peaked in different configurations according to the polarizations. There seems to be however a tendency of the signal to peak for folded and equilateral configurations. This does not come as a surprise as the GWs are generated at Hubble crossing and the source depends on spatial gradients of the comoving curvature perturbations and this tends to enhance the signal when the scales involved are not too different. As a rule of thumb we can propose the following consistency relation for the largest signals

$$\begin{aligned}
 S_h^{+++} &= \mathcal{O}(-600) \text{ for folded configurations,} \\
 S_h^{+xx} &= \mathcal{O}(-600) \text{ for equilateral configurations.}
 \end{aligned}
 \tag{5.55}$$

As for the signal summed for all the polarizations, the results are presented in the lower plot of Fig. (5.9). From it we can estimate

$$\sum_{\text{pol}} S_h = \mathcal{O}(-1000) \text{ for equilateral configurations.}
 \tag{5.56}$$

The bispectrum therefore offers a distinct tool to confirm the nature of the origin of the GW signal, once the two-point correlation is measured by LISA (or other experiments).

5.6 Conclusions

In this Chapter we have characterized the GW signal possibly originated by physics of the Standard Model and its inherent instability scale appearing in the Higgs scalar sector. In this sense, GW physics allows a test, albeit indirect, of the behaviour of the Standard Model at large field values. The source of the GWs is generated by the Higgs perturbations created during a primordial epoch of inflation and amplified during the phase in which the Higgs probes the unstable part of the potential.

The energy density Ω_{GW} can be as large as 10^{-8} and therefore measurable either by LISA or by the ET and Advanced-Ligo, the amplitude being sensitive to the initial conditions of the Higgs classical dynamics. Which experiment turns out to be relevant is dictated by the frequency at the peak of the signal, which in turn depends on the Higgs and top masses. This is indeed a bonus. The more knowledge from collider physics is collected on these masses, the more one could confirm or disprove the hypothesis that these GWs come from Standard Model physics.

We have also characterized the signal in terms of its spectral index as well as three-point correlator. The latter is particularly relevant as it allows to check the consistency between the three- and the two-point correlators and thus offers a way to discriminate among the primordial mechanisms generating the stochastic background of GWs.

We close with some comments. The mechanism described in this paper makes use of the fact that we identify our observed Universe as one of those regions which have been thermally saved during the reheating stage following inflation after the Higgs has probed the unstable part of its potential during inflation. The choice of the parameters might therefore seem fine-tuned. However, anthropic arguments come to the rescue as the very same dynamics might create the dark matter of the Universe under the form of PBHs [3]. Put in other words, if the dark matter has to be ascribed to the Standard Model, then one should also detect the corresponding GW signal.

5.A Analytical results for the functions $\mathcal{I}_c, \mathcal{I}_s$

We write down the analytical formulæ for the integrals $\mathcal{I}_c, \mathcal{I}_s$ defined in Eq. (5.22):

$$\begin{aligned} I_c(d, s) = & \frac{288}{(s^2 - d^2)^3} \left\{ [2c_1 + (5 + d^2)s_1] s \sin s - [2c_1 + (5 + s^2)s_1] d \sin d \right. \\ & + [(1 + d^2)c_1 + (5 + d^2 - 2s^2)s_1] \cos s - [(1 + s^2)c_1 + (5 + s^2 - 2d^2)s_1] \cos d \\ & \left. + \frac{1}{8}(s^2 + d^2 - 2)^2 [\text{Si}(1 + d) + \text{Si}(1 - d) - \text{Si}(1 - s) - \text{Si}(1 + s) - \pi\theta(s - 1)] \right\}, \quad (5.57) \end{aligned}$$

where $c_1 \equiv \cos(1) \simeq 0.54$, $s_1 \equiv \sin(1) \simeq 0.84$ and $\text{Si}(x)$ is the sine integral function;

$$\begin{aligned} I_s(d, s) = & \frac{288}{(d^2 - s^2)^3} \left\{ [-2s_1 + (5 + d^2)c_1] s \sin s - [-2s_1 + (5 + s^2)c_1] d \sin d \right. \\ & + [-(1 + d^2)s_1 + (5 + d^2 - 2s^2)c_1] \cos s - [-(1 + s^2)s_1 + (5 + s^2 - 2d^2)c_1] \cos d \\ & \left. + \frac{1}{8}(s^2 + d^2 - 2)^2 [\text{Ci}(1 + d) + \text{Ci}(1 - d) - \text{Ci}(|1 - s|) - \text{Ci}(1 + s)] \right\}, \quad (5.58) \end{aligned}$$

where $\text{Ci}(x)$ is the cosine integral function.

5.B Four and Six-Point Functions of the Curvature Perturbation

5.B.1 Four-point function of the curvature perturbation

The four-point function of the curvature perturbation ζ in the first line of Eq. (5.25) has two possible non-vanishing contractions for $\mathbf{k}_1, \mathbf{k}_2 \neq 0$:

$$\begin{aligned} (i) \quad & \left\langle \zeta(\mathbf{p}_1) \zeta(\mathbf{k}_1 - \mathbf{p}_1) \zeta(\mathbf{p}_2) \zeta(\mathbf{k}_2 - \mathbf{p}_2) \right\rangle \\ (ii) \quad & \left\langle \zeta(\mathbf{p}_1) \zeta(\mathbf{k}_1 - \mathbf{p}_1) \zeta(\mathbf{p}_2) \zeta(\mathbf{k}_2 - \mathbf{p}_2) \right\rangle \quad (\text{obtained from (i) by } \mathbf{p}_2 \rightarrow (\mathbf{k}_2 - \mathbf{p}_2)) \end{aligned} \quad (5.59)$$

The two contractions (i), (ii) correspond to the configuration of momenta shown in Fig. 5.11. The sum of the contractions (i) and (ii) gives

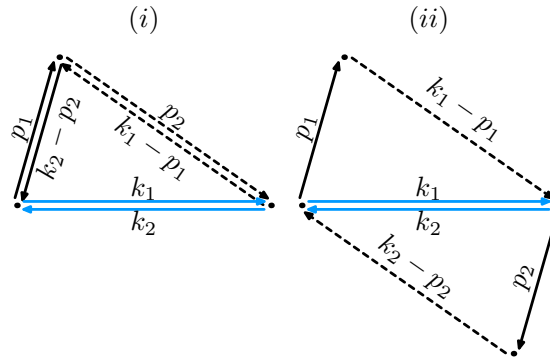


Figure 5.11: Geometrical configurations for the non-vanishing contractions of the two-point function listed in Eq. (5.59).

$$\begin{aligned} & \left\langle \zeta(\mathbf{p}_1) \zeta(\mathbf{k}_1 - \mathbf{p}_1) \zeta(\mathbf{p}_2) \zeta(\mathbf{k}_2 - \mathbf{p}_2) \right\rangle = \\ & = (2\pi)^6 \delta^{(3)}(\mathbf{k}_1 + \mathbf{k}_2) \left[\delta^{(3)}(\mathbf{k}_2 + \mathbf{p}_1 - \mathbf{p}_2) + \delta^{(3)}(\mathbf{p}_1 + \mathbf{p}_2) \right] \frac{2\pi^2}{p_1^3} \frac{2\pi^2}{|\mathbf{k}_1 - \mathbf{p}_1|^3} \mathcal{P}_\zeta(p_1) \mathcal{P}_\zeta(|\mathbf{k}_1 - \mathbf{p}_1|). \end{aligned} \quad (5.60)$$

The two contributions give the same result, given that they correspond to each other up to a shift $\mathbf{p}_2 \rightarrow (\mathbf{k}_2 - \mathbf{p}_2)$, which is a symmetry of Eq. (5.25). To check the symmetry of the whole integral under the exchange of $\mathbf{p}, \mathbf{k} - \mathbf{p}$, it is important to observe that, for a generic function f ,

$$\begin{aligned} \int d^3 p e^{s,ij}(\mathbf{k}) p_i p_j f(\mathbf{k} - \mathbf{p}) f(\mathbf{p}) &= \int d^3 \tilde{p} e^{s,ij}(\mathbf{k}) (k_i - \tilde{p}_i) (k_j - \tilde{p}_j) f(\tilde{\mathbf{p}}) f(\mathbf{k} - \tilde{\mathbf{p}}) = \\ &= \int d^3 \tilde{p} e^{s,ij}(\mathbf{k}) \tilde{p}_i \tilde{p}_j f(\tilde{\mathbf{p}}) f(\mathbf{k} - \tilde{\mathbf{p}}), \end{aligned} \quad (5.61)$$

since $e^{s,ij}(\mathbf{k})$ is transverse to \mathbf{k} .

We can evaluate then Eq. (5.25) for any of the two configurations, and multiply the final result by 2, to get Eq. (5.27) after integration over \mathbf{p}_2 with a Dirac delta so that $\mathbf{p}_2 = \mathbf{p}_1 - \mathbf{k}_1$, and $\mathbf{k}_2 = -\mathbf{k}_1$.

5.B.2 Six-point function of the curvature perturbation

To calculate the six-point function of ζ that appears in (5.41) we have eight possible contractions for $\mathbf{k}_i \neq 0$, listed in Eq. (5.62). This total number of eight can be understood as the product of four choices for the contraction of $\zeta(\mathbf{p}_1)$ times the number of contractions for the remaining four ζ 's, that is two. All these contractions yield the same contribution to the bispectrum, thanks to the invariance of Eq. (5.41) under the exchange of the subscripts 1 and 2 and under $\mathbf{p}_i \rightarrow \mathbf{k}_i - \mathbf{p}_i$, as shown in Eq. (5.61) and (5.22).

$$\begin{aligned}
 (i) \quad & \left\langle \zeta(\mathbf{p}_1)\zeta(\mathbf{k}_1 - \mathbf{p}_1)\zeta(\mathbf{p}_2)\zeta(\mathbf{k}_2 - \mathbf{p}_2)\zeta(\mathbf{p}_3)\zeta(\mathbf{k}_3 - \mathbf{p}_3) \right\rangle & (5.62) \\
 (ii) \quad & \left\langle \zeta(\mathbf{p}_1)\zeta(\mathbf{k}_1 - \mathbf{p}_1)\zeta(\mathbf{p}_2)\zeta(\mathbf{k}_2 - \mathbf{p}_2)\zeta(\mathbf{p}_3)\zeta(\mathbf{k}_3 - \mathbf{p}_3) \right\rangle & \text{(obtained from (i) by } \mathbf{p}_1 \rightarrow (\mathbf{k}_1 - \mathbf{p}_1) \text{)} \\
 (iii) \quad & \left\langle \zeta(\mathbf{p}_1)\zeta(\mathbf{k}_1 - \mathbf{p}_1)\zeta(\mathbf{p}_2)\zeta(\mathbf{k}_2 - \mathbf{p}_2)\zeta(\mathbf{p}_3)\zeta(\mathbf{k}_3 - \mathbf{p}_3) \right\rangle & \text{(obtained from (i) by } \mathbf{p}_3 \rightarrow (\mathbf{k}_3 - \mathbf{p}_3) \text{)} \\
 (iv) \quad & \left\langle \zeta(\mathbf{p}_1)\zeta(\mathbf{k}_1 - \mathbf{p}_1)\zeta(\mathbf{p}_2)\zeta(\mathbf{k}_2 - \mathbf{p}_2)\zeta(\mathbf{p}_3)\zeta(\mathbf{k}_3 - \mathbf{p}_3) \right\rangle & \text{(obtained from (i) by } \mathbf{p}_2 \rightarrow (\mathbf{k}_2 - \mathbf{p}_2) \text{)} \\
 (v) \quad & \left\langle \zeta(\mathbf{p}_1)\zeta(\mathbf{k}_1 - \mathbf{p}_1)\zeta(\mathbf{p}_2)\zeta(\mathbf{k}_2 - \mathbf{p}_2)\zeta(\mathbf{p}_3)\zeta(\mathbf{k}_3 - \mathbf{p}_3) \right\rangle & \text{(obtained from (i) by } 1 \leftrightarrow 2 \text{)} \\
 (vi) \quad & \left\langle \zeta(\mathbf{p}_1)\zeta(\mathbf{k}_1 - \mathbf{p}_1)\zeta(\mathbf{p}_2)\zeta(\mathbf{k}_2 - \mathbf{p}_2)\zeta(\mathbf{p}_3)\zeta(\mathbf{k}_3 - \mathbf{p}_3) \right\rangle & \text{(obtained from (i) by } \mathbf{p}_1 \rightarrow (\mathbf{k}_1 - \mathbf{p}_1) \text{ and } 1 \leftrightarrow 2 \text{)} \\
 (vii) \quad & \left\langle \zeta(\mathbf{p}_1)\zeta(\mathbf{k}_1 - \mathbf{p}_1)\zeta(\mathbf{p}_2)\zeta(\mathbf{k}_2 - \mathbf{p}_2)\zeta(\mathbf{p}_3)\zeta(\mathbf{k}_3 - \mathbf{p}_3) \right\rangle & \text{(obtained from (i) by } \mathbf{p}_3 \rightarrow (\mathbf{k}_3 - \mathbf{p}_3) \text{ and } 1 \leftrightarrow 2 \text{)} \\
 (viii) \quad & \left\langle \zeta(\mathbf{p}_1)\zeta(\mathbf{k}_1 - \mathbf{p}_1)\zeta(\mathbf{p}_2)\zeta(\mathbf{k}_2 - \mathbf{p}_2)\zeta(\mathbf{p}_3)\zeta(\mathbf{k}_3 - \mathbf{p}_3) \right\rangle & \text{(obtained from (i) by } \mathbf{p}_2 \rightarrow (\mathbf{k}_2 - \mathbf{p}_2) \text{ and } 1 \leftrightarrow 2 \text{)}
 \end{aligned}$$

In Fig. 5.12 we show the resulting geometrical configurations for the six momenta $\mathbf{p}_i, (\mathbf{k}_i - \mathbf{p}_i)$, projected on the plane of the triangle formed by the \mathbf{k}_i . Notice indeed that all the contractions result in a common factor $\delta^{(3)}(\mathbf{k}_1 + \mathbf{k}_2 + \mathbf{k}_3)$. The labels of the vectors are printed only for the contraction (i) to facilitate the reading.

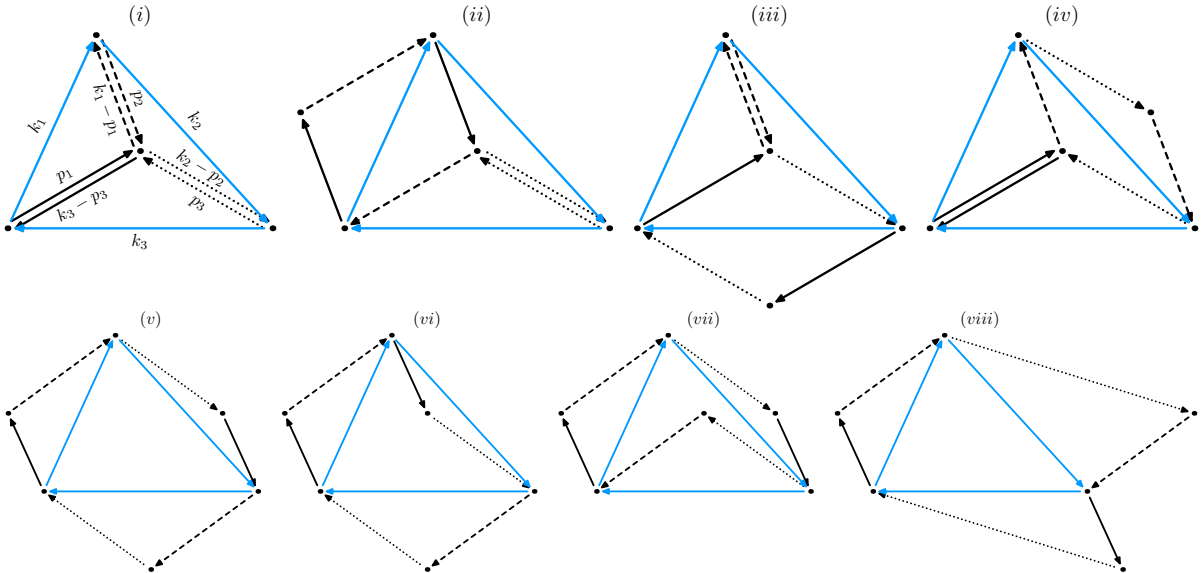


Figure 5.12: Geometrical configurations for the eight non-vanishing contractions of the three-point function listed in Eq. (5.62).

We can evaluate the three-point function for any of these configurations and multiply by eight

the result. We choose the contraction (i), which is equal to

$$\begin{aligned} \left\langle \underbrace{\zeta(\mathbf{p}_1)\zeta(\mathbf{k}_1 - \mathbf{p}_1)\zeta(\mathbf{p}_2)\zeta(\mathbf{k}_2 - \mathbf{p}_2)\zeta(\mathbf{p}_3)\zeta(\mathbf{k}_3 - \mathbf{p}_3)}_i \right\rangle &= (2\pi)^9 \delta^{(3)}(\mathbf{k}_1 + \mathbf{k}_2 + \mathbf{k}_3) \cdot \\ &\cdot (2\pi^2)^3 \frac{\mathcal{P}_\zeta(p_1)}{p_1^3} \frac{\mathcal{P}_\zeta(p_2)}{p_2^3} \frac{\mathcal{P}_\zeta(p_3)}{p_3^3} \delta^{(3)}(\mathbf{p}_1 + \mathbf{k}_3 - \mathbf{p}_3) \delta^{(3)}(\mathbf{k}_1 - \mathbf{p}_1 + \mathbf{p}_2). \end{aligned} \quad (5.63)$$

We then proceed to the integration of the three-point function over the conjugate momenta. The Dirac deltas in Eq. (5.63) fix the geometrical configuration of the six momenta $\mathbf{k}_i, \mathbf{p}_i$ as shown in Fig. 5.4. We can integrate over d^3p_2 and d^3p_3 in Eq. (5.41) with the last two Dirac deltas in (5.63). The result is (??) and the remaining integral in d^3p_1 has to be evaluated numerically.

Bibliography

- [1] D. Racco, A. Wulzer, and F. Zwirner, *Robust collider limits on heavy-mediator Dark Matter*, *JHEP* 05 (2015), p. 009, arXiv: [1502.04701 \[hep-ph\]](#) (pp. [ix](#), [32](#), [37](#), [41](#)).
- [2] A. Ismail, A. Katz, and D. Racco, *On Dark Matter Interactions with the Standard Model through an Anomalous Z'* , *JHEP* 10 (2017), p. 165, arXiv: [1707.00709 \[hep-ph\]](#) (pp. [ix](#), [63](#), [64](#)).
- [3] J. R. Espinosa, D. Racco, and A. Riotto, *A Cosmological Signature of the Standard Model Higgs Vacuum Instability: Primordial Black Holes as Dark Matter*, *Phys. Rev. Lett.* 120.12 (2018), p. 121301, arXiv: [1710.11196 \[hep-ph\]](#) (pp. [ix](#), [97](#), [101](#), [115](#), [117](#), [119](#), [121](#), [122](#), [123](#), [124](#), [125](#), [132](#), [143](#), [149](#)).
- [4] J. R. Espinosa, D. Racco, and A. Riotto, *Primordial Black Holes from Higgs Vacuum Instability: Avoiding Fine-tuning through an Ultraviolet Safe Mechanism*, (2018). To appear in *JCAP*, arXiv: [1804.07731 \[hep-ph\]](#) (pp. [ix](#), [97](#), [115](#), [122](#)).
- [5] J. R. Espinosa, D. Racco, and A. Riotto, *A Cosmological Signature of the SM Higgs Instability: Gravitational Waves*, (2018). Submitted to *Eur. Phys. Jour. C*, arXiv: [1804.07732 \[hep-ph\]](#) (pp. [ix](#), [97](#), [131](#)).
- [6] M. Biagetti, V. Desjacques, A. Kehagias, D. Racco, and A. Riotto, *The Halo Boltzmann Equation*, *JCAP* 1604.04 (2016), p. 040, arXiv: [1508.07330 \[astro-ph.CO\]](#) (p. [ix](#)).
- [7] E. Morgante, D. Racco, M. Rameez, and A. Riotto, *The 750 GeV Diphoton excess, Dark Matter and Constraints from the IceCube experiment*, *JHEP* 07 (2016), p. 141, arXiv: [1603.05592 \[hep-ph\]](#) (p. [ix](#)).
- [8] T. Jacques, A. Katz, E. Morgante, D. Racco, M. Rameez, and A. Riotto, *Complementarity of DM searches in a consistent simplified model: the case of Z'* , *JHEP* 10 (2016), p. 071, arXiv: [1605.06513 \[hep-ph\]](#) (pp. [ix](#), [71](#)).
- [9] F. Farakos, A. Kehagias, D. Racco, and A. Riotto, *Scanning of the Supersymmetry Breaking Scale and the Gravitino Mass in Supergravity*, *JHEP* 06 (2016), p. 120, arXiv: [1605.07631 \[hep-th\]](#) (p. [ix](#)).
- [10] J. Abdallah et al., *Simplified Models for Dark Matter Searches at the LHC*, *Phys. Dark Univ.* 9-10 (2015), pp. 8–23, arXiv: [1506.03116 \[hep-ph\]](#) (pp. [ix](#), [32](#), [73](#)).
- [11] D. Abercrombie et al., *Dark Matter Benchmark Models for Early LHC Run-2 Searches: Report of the ATLAS/CMS Dark Matter Forum*. Ed. by A. Boveia, C. Doglioni, S. Lowette, S. Malik, and S. Mrenna. 2015, arXiv: [1507.00966 \[hep-ex\]](#) (pp. [ix](#), [32](#)).
- [12] D. Racco, *Robust Collider Limits on Heavy-mediator Dark Matter*, *Frascati Phys. Ser.* 61 (2016), pp. 133–140 (pp. [x](#), [32](#)).
- [13] G. Bertone and D. Hooper, *A History of Dark Matter*, Submitted to: *Rev. Mod. Phys.* (2016), arXiv: [1605.04909 \[astro-ph.CO\]](#) (p. [3](#)).
- [14] G. Jungman, M. Kamionkowski, and K. Griest, *Supersymmetric dark matter*, *Phys. Rept.* 267 (1996), pp. 195–373, arXiv: [hep-ph/9506380 \[hep-ph\]](#) (pp. [3](#), [16](#)).
- [15] J. Silk et al., *Particle Dark Matter: Observations, Models and Searches*. Ed. by G. Bertone. Cambridge Univ. Press (Cambridge), 2010 (p. [3](#)).
- [16] L. E. Strigari, *Galactic Searches for Dark Matter*, *Phys. Rept.* 531 (2013), pp. 1–88, arXiv: [1211.7090 \[astro-ph.CO\]](#) (pp. [3](#), [10](#), [28](#)).
- [17] S. Profumo, “Astrophysical Probes of Dark Matter”, *Proceedings, Theoretical Advanced Study Institute in Elementary Particle Physics: Searching for New Physics at Small*

- and Large Scales (TASI 2012): Boulder, Colorado, June 4-29, 2012. 2013, pp. 143–189, arXiv: [1301.0952 \[hep-ph\]](#) (p. 3).
- [18] G. B. Gelmini, “The Hunt for Dark Matter”, *Proceedings, Theoretical Advanced Study Institute in Elementary Particle Physics: Journeys Through the Precision Frontier: Amplitudes for Colliders (TASI 2014): Boulder, Colorado, June 2-27, 2014*. 2015, pp. 559–616, arXiv: [1502.01320 \[hep-ph\]](#) (p. 3).
- [19] M. Lisanti, “Lectures on Dark Matter Physics”, *Proceedings, Theoretical Advanced Study Institute in Elementary Particle Physics: New Frontiers in Fields and Strings (TASI 2015): Boulder, CO, USA, June 1-26, 2015*. 2017, pp. 399–446, arXiv: [1603.03797 \[hep-ph\]](#) (pp. 3, 79).
- [20] S. Profumo, *An Introduction to Particle Dark Matter*. World Scientific (Singapore), 2017 (p. 3).
- [21] G. Bertone, D. Hooper, and J. Silk, *Particle dark matter: Evidence, candidates and constraints*, *Phys. Rept.* 405 (2005), pp. 279–390, arXiv: [hep-ph/0404175 \[hep-ph\]](#) (p. 3).
- [22] J. L. Feng, *Dark Matter Candidates from Particle Physics and Methods of Detection*, *Ann. Rev. Astron. Astrophys.* 48 (2010), pp. 495–545, arXiv: [1003.0904 \[astro-ph.CO\]](#) (p. 3).
- [23] K. G. Begeman, A. H. Broeils, and R. H. Sanders, *Extended rotation curves of spiral galaxies: Dark haloes and modified dynamics*, *Mon. Not. Roy. Astron. Soc.* 249 (1991), p. 523 (p. 5).
- [24] A. Bosma, *The distribution and kinematics of neutral hydrogen in spiral galaxies of various morphological types*. Ph.D. Thesis, Groningen University. [Online; accessed 18-June-2018]. 1978, URL: <http://ned.ipac.caltech.edu/level5/March05/Bosma/TOC.html> (p. 5).
- [25] S. M. Faber and J. S. Gallagher, *Masses and mass-to-light ratios of galaxies*, *Ann. Rev. Astron. Astrophys.* 17 (1979), pp. 135–183 (p. 5).
- [26] D. Clowe, M. Bradac, A. H. Gonzalez, M. Markevitch, S. W. Randall, C. Jones, and D. Zaritsky, *A direct empirical proof of the existence of dark matter*, *Astrophys. J.* 648 (2006), pp. L109–L113, arXiv: [astro-ph/0608407 \[astro-ph\]](#) (pp. 4, 5).
- [27] D. Harvey, R. Massey, T. Kitching, A. Taylor, and E. Tittley, *The non-gravitational interactions of dark matter in colliding galaxy clusters*, *Science* 347 (2015), pp. 1462–1465, arXiv: [1503.07675 \[astro-ph.CO\]](#) (p. 6).
- [28] **Planck** collaboration, P. A. R. Ade et al., *Planck 2015 results. XX. Constraints on inflation*, *Astron. Astrophys.* 594 (2016), A20, arXiv: [1502.02114 \[astro-ph.CO\]](#) (p. 6).
- [29] E. W. Kolb and M. S. Turner, *The Early Universe*, *Front. Phys.* 69 (1990), pp. 1–547 (pp. 6, 11, 60, 127).
- [30] S. Dodelson, *Modern Cosmology*. Academic Press (Amsterdam), 2003 (p. 6).
- [31] R. Durrer, *The Cosmic Microwave Background*. Cambridge University Press (Cambridge), 2008 (p. 6).
- [32] D. S. Gorbunov and V. A. Rubakov, *Introduction to the theory of the early universe: Cosmological perturbations and inflationary theory*. World Scientific (Singapore), 2011 (pp. 6, 7).
- [33] **Planck** collaboration, P. A. R. Ade et al., *Planck 2015 results. XIII. Cosmological parameters*, *Astron. Astrophys.* 594 (2016), A13, arXiv: [1502.01589 \[astro-ph.CO\]](#) (pp. 7, 28, 29, 59, 114).
- [34] D. Baumann, *Cosmology, Part III Mathematical Tripos*. <http://www.damtp.cam.ac.uk/user/db275/Cosmology/Lectures.pdf>. 2015 (pp. 7, 8).
- [35] V. J. Martinez, *The Large Scale Structure in the Universe: From Power-Laws to Acoustic Peaks*, *Lect. Notes Phys.* 665 (2009), p. 269, arXiv: [0804.1536 \[astro-ph\]](#) (p. 8).
- [36] M. Milgrom, *A Modification of the Newtonian dynamics as a possible alternative to the hidden mass hypothesis*, *Astrophys. J.* 270 (1983), pp. 365–370 (p. 9).
- [37] M. Kaplinghat and M. S. Turner, *How cold dark matter theory explains Milgrom’s law*, *Astrophys. J.* 569 (2002), p. L19, arXiv: [astro-ph/0107284 \[astro-ph\]](#) (p. 9).
- [38] S. McGaugh, F. Lelli, and J. Schombert, *Radial Acceleration Relation in Rotationally Supported Galaxies*, *Phys. Rev. Lett.* 117.20 (2016), p. 201101, arXiv: [1609.05917 \[astro-ph.GA\]](#) (p. 9).

- [39] J. D. Bekenstein, *Relativistic gravitation theory for the MOND paradigm*, *Phys. Rev. D* 70 (2004). [Erratum: *Phys. Rev. D* 71, 069901(2005)], p. 083509, arXiv: [astro-ph/0403694](#) [[astro-ph](#)] (p. 9).
- [40] S. Dodelson, *The Real Problem with MOND*, *Int. J. Mod. Phys. D* 20 (2011), pp. 2749–2753, arXiv: [1112.1320](#) [[astro-ph.CO](#)] (pp. 9, 10).
- [41] P. Gondolo and G. Gelmini, *Cosmic abundances of stable particles: Improved analysis*, *Nucl. Phys. B* 360 (1991), pp. 145–179 (pp. 11, 60).
- [42] K. Griest and D. Seckel, *Three exceptions in the calculation of relic abundances*, *Phys. Rev. D* 43 (1991), pp. 3191–3203 (p. 11).
- [43] J. McDonald, *Thermally generated gauge singlet scalars as selfinteracting dark matter*, *Phys. Rev. Lett.* 88 (2002), p. 091304, arXiv: [hep-ph/0106249](#) [[hep-ph](#)] (p. 13).
- [44] L. J. Hall, K. Jedamzik, J. March-Russell, and S. M. West, *Freeze-In Production of FIMP Dark Matter*, *JHEP* 03 (2010), p. 080, arXiv: [0911.1120](#) [[hep-ph](#)] (pp. 13, 14).
- [45] N. Bernal, M. Heikinheimo, T. Tenkanen, K. Tuominen, and V. Vaskonen, *The Dawn of FIMP Dark Matter: A Review of Models and Constraints*, *Int. J. Mod. Phys. A* 32, 27 (2017), p. 1730023, arXiv: [1706.07442](#) [[hep-ph](#)] (p. 13).
- [46] S. Nussinov, *Technoc cosmology: Could a Technibaryon Excess Provide a 'Natural' Missing Mass Candidate?*, *Phys. Lett.* 165B (1985), pp. 55–58 (p. 15).
- [47] G. B. Gelmini, L. J. Hall, and M. J. Lin, *What Is the Cosmion?*, *Nucl. Phys. B* 281 (1987), p. 726 (p. 15).
- [48] D. B. Kaplan, *A Single explanation for both the baryon and dark matter densities*, *Phys. Rev. Lett.* 68 (1992), pp. 741–743 (p. 15).
- [49] D. E. Kaplan, M. A. Luty, and K. M. Zurek, *Asymmetric Dark Matter*, *Phys. Rev. D* 79 (2009), p. 115016, arXiv: [0901.4117](#) [[hep-ph](#)] (p. 15).
- [50] A. Falkowski, J. T. Ruderman, and T. Volansky, *Asymmetric Dark Matter from Leptogenesis*, *JHEP* 05 (2011), p. 106, arXiv: [1101.4936](#) [[hep-ph](#)] (p. 15).
- [51] K. Petraki and R. R. Volkas, *Review of asymmetric dark matter*, *Int. J. Mod. Phys. A* 28 (2013), p. 1330028, arXiv: [1305.4939](#) [[hep-ph](#)] (p. 15).
- [52] K. M. Zurek, *Asymmetric Dark Matter: Theories, Signatures, and Constraints*, *Phys. Rept.* 537 (2014), pp. 91–121, arXiv: [1308.0338](#) [[hep-ph](#)] (p. 15).
- [53] A. Riotto and M. Trodden, *Recent progress in baryogenesis*, *Ann. Rev. Nucl. Part. Sci.* 49 (1999), pp. 35–75, arXiv: [hep-ph/9901362](#) [[hep-ph](#)] (p. 15).
- [54] M. A. Luty, *Baryogenesis via leptogenesis*, *Phys. Rev. D* 45 (1992), pp. 455–465 (p. 15).
- [55] S. Davidson, E. Nardi, and Y. Nir, *Leptogenesis*, *Phys. Rept.* 466 (2008), pp. 105–177, arXiv: [0802.2962](#) [[hep-ph](#)] (p. 15).
- [56] H. P. Nilles, *Supersymmetry, Supergravity and Particle Physics*, *Phys. Rept.* 110 (1984), pp. 1–162 (p. 16).
- [57] H. E. Haber and G. L. Kane, *The Search for Supersymmetry: Probing Physics Beyond the Standard Model*, *Phys. Rept.* 117 (1985), pp. 75–263 (p. 16).
- [58] S. P. Martin, *A Supersymmetry primer*, (1997). *Adv. Ser. Direct. High Energy Phys.* 18, 1 (1998), pp. 1–98, arXiv: [hep-ph/9709356](#) [[hep-ph](#)] (p. 16).
- [59] G. D. Mack, J. F. Beacom, and G. Bertone, *Towards Closing the Window on Strongly Interacting Dark Matter: Far-Reaching Constraints from Earth's Heat Flow*, *Phys. Rev. D* 76 (2007), p. 043523, arXiv: [0705.4298](#) [[astro-ph](#)] (p. 17).
- [60] N. Arkani-Hamed, S. Dimopoulos, and G. R. Dvali, *The Hierarchy problem and new dimensions at a millimeter*, *Phys. Lett. B* 429 (1998), pp. 263–272, arXiv: [hep-ph/9803315](#) [[hep-ph](#)] (p. 17).
- [61] L. Randall and R. Sundrum, *A Large mass hierarchy from a small extra dimension*, *Phys. Rev. Lett.* 83 (1999), pp. 3370–3373, arXiv: [hep-ph/9905221](#) [[hep-ph](#)] (p. 17).
- [62] L. Randall and R. Sundrum, *An Alternative to compactification*, *Phys. Rev. Lett.* 83 (1999), pp. 4690–4693, arXiv: [hep-th/9906064](#) [[hep-th](#)] (p. 17).

- [63] G. F. Giudice, R. Rattazzi, and J. D. Wells, *Quantum gravity and extra dimensions at high-energy colliders*, *Nucl. Phys.* B544 (1999), pp. 3–38, arXiv: [hep-ph/9811291](#) [[hep-ph](#)] (p. 18).
- [64] V. A. Rubakov, *Large and infinite extra dimensions: An Introduction*, *Phys. Usp.* 44 (2001), pp. 871–893, arXiv: [hep-ph/0104152](#) [[hep-ph](#)] (p. 18).
- [65] T. Appelquist, H.-C. Cheng, and B. A. Dobrescu, *Bounds on universal extra dimensions*, *Phys. Rev.* D64 (2001), p. 035002, arXiv: [hep-ph/0012100](#) [[hep-ph](#)] (p. 18).
- [66] D. Hooper and S. Profumo, *Dark matter and collider phenomenology of universal extra dimensions*, *Phys. Rept.* 453 (2007), pp. 29–115, arXiv: [hep-ph/0701197](#) [[hep-ph](#)] (p. 18).
- [67] G. Servant, *Dark matter at the electroweak scale: Non-supersymmetric candidates*. In: *Particle Dark Matter*. Ed. by G. Bertone. Cambridge Univ. Press (Cambridge), 2010, pp. 164–189 (p. 18).
- [68] M. Cirelli, N. Fornengo, and A. Strumia, *Minimal dark matter*, *Nucl. Phys.* B753 (2006), pp. 178–194, arXiv: [hep-ph/0512090](#) [[hep-ph](#)] (p. 18).
- [69] M. Cirelli, A. Strumia, and M. Tamburini, *Cosmology and Astrophysics of Minimal Dark Matter*, *Nucl. Phys.* B787 (2007), pp. 152–175, arXiv: [0706.4071](#) [[hep-ph](#)] (pp. 18, 19).
- [70] M. Cirelli and A. Strumia, *Minimal Dark Matter: Model and results*, *New J. Phys.* 11 (2009), p. 105005, arXiv: [0903.3381](#) [[hep-ph](#)] (p. 18).
- [71] M. Cirelli, T. Hambye, P. Panci, F. Sala, and M. Taoso, *Gamma ray tests of Minimal Dark Matter*, *JCAP* 1510.10 (2015), p. 026, arXiv: [1507.05519](#) [[hep-ph](#)] (pp. 18, 19).
- [72] A. Mitridate, M. Redi, J. Smirnov, and A. Strumia, *Cosmological Implications of Dark Matter Bound States*, *JCAP* 1705.05 (2017), p. 006, arXiv: [1702.01141](#) [[hep-ph](#)] (pp. 18, 19).
- [73] M. Cirelli, E. Del Nobile, and P. Panci, *Tools for model-independent bounds in direct dark matter searches*, *JCAP* 1310 (2013), p. 019, arXiv: [1307.5955](#) [[hep-ph](#)] (pp. 19, 82, 84).
- [74] E. Del Nobile, M. Nardecchia, and P. Panci, *Millicharge or Decay: A Critical Take on Minimal Dark Matter*, *JCAP* 1604.04 (2016), p. 048, arXiv: [1512.05353](#) [[hep-ph](#)] (p. 19).
- [75] T. Asaka, S. Blanchet, and M. Shaposhnikov, *The nuMSM, dark matter and neutrino masses*, *Phys. Lett.* B631 (2005), pp. 151–156, arXiv: [hep-ph/0503065](#) [[hep-ph](#)] (p. 20).
- [76] T. Asaka and M. Shaposhnikov, *The nuMSM, dark matter and baryon asymmetry of the universe*, *Phys. Lett.* B620 (2005), pp. 17–26, arXiv: [hep-ph/0505013](#) [[hep-ph](#)] (p. 20).
- [77] M. Shaposhnikov, *Sterile neutrinos*. In: *Particle Dark Matter*. Ed. by G. Bertone. Cambridge Univ. Press (Cambridge), 2010, pp. 228–248 (p. 20).
- [78] R. D. Peccei and H. R. Quinn, *CP Conservation in the Presence of Instantons*, *Phys. Rev. Lett.* 38 (1977). [[328\(1977\)](#)], pp. 1440–1443 (p. 20).
- [79] S. Weinberg, *A New Light Boson?*, *Phys. Rev. Lett.* 40 (1978), pp. 223–226 (p. 20).
- [80] F. Wilczek, *Problem of Strong p and t Invariance in the Presence of Instantons*, *Phys. Rev. Lett.* 40 (1978), pp. 279–282 (p. 20).
- [81] M. Dine, “TASI lectures on the strong CP problem”, *Flavor physics for the millennium. Proceedings, Theoretical Advanced Study Institute in elementary particle physics, TASI 2000, Boulder, USA, June 4-30, 2000*. 2000, pp. 349–369, arXiv: [hep-ph/0011376](#) [[hep-ph](#)] (p. 21).
- [82] R. D. Peccei, *The Strong CP problem and axions*, *Lect. Notes Phys.* 741 (2008). [[3\(2006\)](#)], pp. 3–17, arXiv: [hep-ph/0607268](#) [[hep-ph](#)] (p. 21).
- [83] P. Sikivie, *Axion Cosmology*, *Lect. Notes Phys.* 741 (2008). [[19\(2006\)](#)], pp. 19–50, arXiv: [astro-ph/0610440](#) [[astro-ph](#)] (p. 21).
- [84] L. D. Duffy and K. van Bibber, *Axions as Dark Matter Particles*, *New J. Phys.* 11 (2009), p. 105008, arXiv: [0904.3346](#) [[hep-ph](#)] (p. 21).
- [85] J. E. Kim and G. Carosi, *Axions and the Strong CP Problem*, *Rev. Mod. Phys.* 82 (2010), pp. 557–602, arXiv: [0807.3125](#) [[hep-ph](#)] (p. 21).

- [86] D. J. E. Marsh, *Axion Cosmology*, *Phys. Rept.* 643 (2016), pp. 1–79, arXiv: [1510.07633 \[astro-ph.CO\]](#) (pp. 21, 22).
- [87] D. J. E. Marsh, “Axions and ALPs: a very short introduction”, *Proceedings, 13th Patras Workshop on Axions, WIMPs and WISPs, (PATRAS 2017): Thessaloniki, Greece, 15 May 2017 - 19, 2017*. 2018, pp. 59–74, arXiv: [1712.03018 \[hep-ph\]](#) (p. 21).
- [88] I. G. Irastorza and J. Redondo, *New experimental approaches in the search for axion-like particles*, *Prog. Part. Nucl. Phys.* 102 (2018), pp. 89–159, arXiv: [1801.08127 \[hep-ph\]](#) (pp. 21, 22, 23).
- [89] L. Hui, J. P. Ostriker, S. Tremaine, and E. Witten, *Ultralight scalars as cosmological dark matter*, *Phys. Rev. D* 95.4 (2017), p. 043541, arXiv: [1610.08297 \[astro-ph.CO\]](#) (p. 21).
- [90] **BICEP2, Keck Array** collaboration, P. A. R. Ade et al., *Improved Constraints on Cosmology and Foregrounds from BICEP2 and Keck Array Cosmic Microwave Background Data with Inclusion of 95 GHz Band*, *Phys. Rev. Lett.* 116 (2016), p. 031302, arXiv: [1510.09217 \[astro-ph.CO\]](#) (p. 23).
- [91] M. W. Goodman and E. Witten, *Detectability of Certain Dark Matter Candidates*, *Phys. Rev. D* 31 (1985). [[325\(1984\)](#)], p. 3059 (p. 24).
- [92] J. Engel, S. Pittel, and P. Vogel, *Nuclear physics of dark matter detection*, *Int. J. Mod. Phys. E* 1 (1992), pp. 1–37 (p. 24).
- [93] J. D. Lewin and P. F. Smith, *Review of mathematics, numerical factors, and corrections for dark matter experiments based on elastic nuclear recoil*, *Astropart. Phys.* 6 (1996), pp. 87–112 (p. 24).
- [94] V. A. Bednyakov and H. V. Klapdor-Kleingrothaus, *Direct Search for Dark Matter - Striking the Balance - and the Future*, *Phys. Part. Nucl.* 40 (2009), pp. 583–611, arXiv: [0806.3917 \[hep-ph\]](#) (p. 24).
- [95] D. G. Cerdeño and A. M. Green, *Direct detection of WIMPs*. In: *Particle Dark Matter*. Ed. by G. Bertone. Cambridge Univ. Press (Cambridge), 2010, pp. 347–369, arXiv: [1002.1912 \[astro-ph.CO\]](#) (p. 24).
- [96] K. Freese, M. Lisanti, and C. Savage, *Colloquium: Annual modulation of dark matter*, *Rev. Mod. Phys.* 85 (2013), pp. 1561–1581, arXiv: [1209.3339 \[astro-ph.CO\]](#) (p. 24).
- [97] A. M. Green, *Astrophysical uncertainties on direct detection experiments*, *Mod. Phys. Lett. A* 27 (2012), p. 1230004, arXiv: [1112.0524 \[astro-ph.CO\]](#) (p. 24).
- [98] M. C. Smith et al., *The RAVE Survey: Constraining the Local Galactic Escape Speed*, *Mon. Not. Roy. Astron. Soc.* 379 (2007), pp. 755–772, arXiv: [astro-ph/0611671 \[astro-ph\]](#) (p. 24).
- [99] M. Fairbairn, T. Douce, and J. Swift, *Quantifying Astrophysical Uncertainties on Dark Matter Direct Detection Results*, *Astropart. Phys.* 47 (2013), pp. 45–53, arXiv: [1206.2693 \[astro-ph.CO\]](#) (p. 24).
- [100] E. Del Nobile, *Halo-independent comparison of direct dark matter detection data: a review*, *Adv. High Energy Phys.* 2014 (2014), p. 604914, arXiv: [1404.4130 \[hep-ph\]](#) (p. 24).
- [101] F. Kahlhoefer and S. Wild, *Studying generalised dark matter interactions with extended halo-independent methods*, *JCAP* 1610.10 (2016), p. 032, arXiv: [1607.04418 \[hep-ph\]](#) (p. 24).
- [102] A. Ibarra, B. J. Kavanagh, and A. Rappelt, *Bracketing the impact of astrophysical uncertainties on local dark matter searches*, (2018), arXiv: [1806.08714 \[hep-ph\]](#) (p. 24).
- [103] J. Fan, M. Reece, and L.-T. Wang, *Non-relativistic effective theory of dark matter direct detection*, *JCAP* 1011 (2010), p. 042, arXiv: [1008.1591 \[hep-ph\]](#) (p. 25).
- [104] A. L. Fitzpatrick, W. Haxton, E. Katz, N. Lubbers, and Y. Xu, *The Effective Field Theory of Dark Matter Direct Detection*, *JCAP* 1302 (2013), p. 004, arXiv: [1203.3542 \[hep-ph\]](#) (pp. 25, 84).
- [105] E. Del Nobile, *A complete Lorentz-to-Galileo dictionary for direct Dark Matter detection*, (2018), arXiv: [1806.01291 \[hep-ph\]](#) (p. 25).
- [106] U. Haisch and F. Kahlhoefer, *On the importance of loop-induced spin-independent interactions for dark matter direct detection*, *JCAP* 1304 (2013), p. 050, arXiv: [1302.4454 \[hep-ph\]](#) (pp. 25, 41, 83).
- [107] A. Crivellin, F. D’Eramo, and M. Procura, *New Constraints on Dark Matter Effective Theories from Standard Model Loops*, *Phys. Rev. Lett.* 112 (2014), p. 191304, arXiv: [1402.1173 \[hep-ph\]](#) (pp. 25, 41).

- [108] F. D’Eramo and M. Procura, *Connecting Dark Matter UV Complete Models to Direct Detection Rates via Effective Field Theory*, *JHEP* 04 (2015), p. 054, arXiv: [1411.3342 \[hep-ph\]](#) (pp. 25, 41).
- [109] F. D’Eramo, B. J. Kavanagh, and P. Panci, *You can hide but you have to run: direct detection with vector mediators*, *JHEP* 08 (2016), p. 111, arXiv: [1605.04917 \[hep-ph\]](#) (pp. 25, 41).
- [110] F. D’Eramo, B. J. Kavanagh, and P. Panci, *Probing Leptophilic Dark Sectors with Hadronic Processes*, *Phys. Lett.* B771 (2017), pp. 339–348, arXiv: [1702.00016 \[hep-ph\]](#) (pp. 25, 41).
- [111] J. Billard, L. Strigari, and E. Figueroa-Feliciano, *Implication of neutrino backgrounds on the reach of next generation dark matter direct detection experiments*, *Phys. Rev.* D89.2 (2014), p. 023524, arXiv: [1307.5458 \[hep-ph\]](#) (p. 26).
- [112] XENON collaboration, E. Aprile et al., *Dark Matter Search Results from a One Tonne×Year Exposure of XENON1T*, (2018), arXiv: [1805.12562 \[astro-ph.CO\]](#) (p. 26).
- [113] T. Marrodán Undagoitia and L. Rauch, *Dark matter direct-detection experiments*, *J. Phys.* G43.1 (2016), p. 013001, arXiv: [1509.08767 \[physics.ins-det\]](#) (p. 26).
- [114] PICO collaboration, C. Amole et al., *Dark Matter Search Results from the PICO-60 C₃F₈ Bubble Chamber*, *Phys. Rev. Lett.* 118.25 (2017), p. 251301, arXiv: [1702.07666 \[astro-ph.CO\]](#) (pp. 26, 83).
- [115] R. Essig, J. Mardon, and T. Volansky, *Direct Detection of Sub-GeV Dark Matter*, *Phys. Rev.* D85 (2012), p. 076007, arXiv: [1108.5383 \[hep-ph\]](#) (p. 25).
- [116] R. Essig, A. Manalaysay, J. Mardon, P. Sorensen, and T. Volansky, *First Direct Detection Limits on sub-GeV Dark Matter from XENON10*, *Phys. Rev. Lett.* 109 (2012), p. 021301, arXiv: [1206.2644 \[astro-ph.CO\]](#) (p. 25).
- [117] S. K. Lee, M. Lisanti, S. Mishra-Sharma, and B. R. Safdi, *Modulation Effects in Dark Matter-Electron Scattering Experiments*, *Phys. Rev.* D92.8 (2015), p. 083517, arXiv: [1508.07361 \[hep-ph\]](#) (p. 25).
- [118] S. Derenzo, R. Essig, A. Massari, A. Soto, and T.-T. Yu, *Direct Detection of sub-GeV Dark Matter with Scintillating Targets*, *Phys. Rev.* D96.1 (2017), p. 016026, arXiv: [1607.01009 \[hep-ph\]](#) (p. 25).
- [119] S. Knapen, T. Lin, M. Pyle, and K. M. Zurek, *Detection of Light Dark Matter With Optical Phonons in Polar Materials*, (2017), arXiv: [1712.06598 \[hep-ph\]](#) (p. 25).
- [120] P. W. Graham, D. E. Kaplan, S. Rajendran, and M. T. Walters, *Semiconductor Probes of Light Dark Matter*, *Phys. Dark Univ.* 1 (2012), pp. 32–49, arXiv: [1203.2531 \[hep-ph\]](#) (p. 25).
- [121] R. Essig, M. Fernandez-Serra, J. Mardon, A. Soto, T. Volansky, and T.-T. Yu, *Direct Detection of sub-GeV Dark Matter with Semiconductor Targets*, *JHEP* 05 (2016), p. 046, arXiv: [1509.01598 \[hep-ph\]](#) (p. 25).
- [122] Y. Hochberg, T. Lin, and K. M. Zurek, *Absorption of light dark matter in semiconductors*, *Phys. Rev.* D95.2 (2017), p. 023013, arXiv: [1608.01994 \[hep-ph\]](#) (p. 25).
- [123] Y. Hochberg, Y. Kahn, M. Lisanti, K. M. Zurek, A. G. Grushin, R. Ilan, et al., *Detection of sub-MeV Dark Matter with Three-Dimensional Dirac Materials*, *Phys. Rev.* D97.1 (2018), p. 015004, arXiv: [1708.08929 \[hep-ph\]](#) (p. 25).
- [124] W. Guo and D. N. McKinsey, *Concept for a dark matter detector using liquid helium-4*, *Phys. Rev.* D87.11 (2013), p. 115001, arXiv: [1302.0534 \[astro-ph.IM\]](#) (p. 26).
- [125] K. Schutz and K. M. Zurek, *Detectability of Light Dark Matter with Superfluid Helium*, *Phys. Rev. Lett.* 117.12 (2016), p. 121302, arXiv: [1604.08206 \[hep-ph\]](#) (p. 26).
- [126] Y. Hochberg, Y. Zhao, and K. M. Zurek, *Superconducting Detectors for Superlight Dark Matter*, *Phys. Rev. Lett.* 116.1 (2016), p. 011301, arXiv: [1504.07237 \[hep-ph\]](#) (p. 26).
- [127] Y. Hochberg, M. Pyle, Y. Zhao, and K. M. Zurek, *Detecting Superlight Dark Matter with Fermi-Degenerate Materials*, *JHEP* 08 (2016), p. 057, arXiv: [1512.04533 \[hep-ph\]](#) (p. 26).
- [128] S. Knapen, T. Lin, and K. M. Zurek, *Light Dark Matter in Superfluid Helium: Detection with Multi-excitation Production*, *Phys. Rev.* D95.5 (2017), p. 056019, arXiv: [1611.06228 \[hep-ph\]](#) (p. 26).

- [129] C. Kouvaris and J. Pradler, *Probing sub-GeV Dark Matter with conventional detectors*, *Phys. Rev. Lett.* 118.3 (2017), p. 031803, arXiv: [1607.01789 \[hep-ph\]](#) (p. 26).
- [130] Y. Hochberg, Y. Kahn, M. Lisanti, C. G. Tully, and K. M. Zurek, *Directional detection of dark matter with two-dimensional targets*, *Phys. Lett. B* 772 (2017), pp. 239–246, arXiv: [1606.08849 \[hep-ph\]](#) (p. 26).
- [131] S. Baum, A. K. Drukier, K. Freese, M. Górski, and P. Stengel, *Searching for Dark Matter with Paleo-Detectors*, (2018), arXiv: [1806.05991 \[astro-ph.CO\]](#) (p. 26).
- [132] P. Ciafaloni, D. Comelli, A. Riotto, F. Sala, A. Strumia, and A. Urbano, *Weak Corrections are Relevant for Dark Matter Indirect Detection*, *JCAP* 1103 (2011), p. 019, arXiv: [1009.0224 \[hep-ph\]](#) (p. 27).
- [133] E. Morgante, *Aspects of WIMP Dark Matter searches at colliders and other probes*. Ph.D. Thesis, University of Geneva. 20 Sep. 2016, URL: <https://archive-ouverte.unige.ch/unige:90529> (pp. 27, 32).
- [134] **AMS** collaboration, M. Aguilar et al., *Electron and Positron Fluxes in Primary Cosmic Rays Measured with the Alpha Magnetic Spectrometer on the International Space Station*, *Phys. Rev. Lett.* 113 (2014), p. 121102 (pp. 27, 29).
- [135] **AMS** collaboration, L. Accardo et al., *High Statistics Measurement of the Positron Fraction in Primary Cosmic Rays of 0.5–500 GeV with the Alpha Magnetic Spectrometer on the International Space Station*, *Phys. Rev. Lett.* 113 (2014), p. 121101 (pp. 27, 29).
- [136] **AMS** collaboration, A. Kounine, *AMS Days at CERN - The Future of Cosmic Ray Physics and Latest Results*. https://indico.cern.ch/event/381134/contributions/900587/attachments/759339/1041605/AMS_positrons_antiprotons.pdf. 15-17 Apr. 2015 (p. 27).
- [137] G. Giesen, M. Boudaud, Y. Génolini, V. Poulin, M. Cirelli, P. Salati, and P. D. Serpico, *AMS-02 antiprotons, at last! Secondary astrophysical component and immediate implications for Dark Matter*, *JCAP* 1509.09 (2015), p. 023, arXiv: [1504.04276 \[astro-ph.HE\]](#) (p. 27).
- [138] D. Hooper, P. Blasi, and P. D. Serpico, *Pulsars as the Sources of High Energy Cosmic Ray Positrons*, *JCAP* 0901 (2009), p. 025, arXiv: [0810.1527 \[astro-ph\]](#) (p. 27).
- [139] **Fermi-LAT** collaboration, D. Grasso et al., *On possible interpretations of the high energy electron-positron spectrum measured by the Fermi Large Area Telescope*, *Astropart. Phys.* 32 (2009), pp. 140–151, arXiv: [0905.0636 \[astro-ph.HE\]](#) (p. 27).
- [140] M. Di Mauro, F. Donato, N. Fornengo, R. Lineros, and A. Vittino, *Interpretation of AMS-02 electrons and positrons data*, *JCAP* 1404 (2014), p. 006, arXiv: [1402.0321 \[astro-ph.HE\]](#) (p. 27).
- [141] M. Di Mauro, F. Donato, N. Fornengo, and A. Vittino, *Dark matter vs. astrophysics in the interpretation of AMS-02 electron and positron data*, *JCAP* 1605.05 (2016), p. 031, arXiv: [1507.07001 \[astro-ph.HE\]](#) (p. 27).
- [142] P. Blasi, *The origin of the positron excess in cosmic rays*, *Phys. Rev. Lett.* 103 (2009), p. 051104, arXiv: [0903.2794 \[astro-ph.HE\]](#) (p. 27).
- [143] **Fermi-LAT** collaboration, M. Ackermann et al., *Searching for Dark Matter Annihilation from Milky Way Dwarf Spheroidal Galaxies with Six Years of Fermi Large Area Telescope Data*, *Phys. Rev. Lett.* 115.23 (2015), p. 231301, arXiv: [1503.02641 \[astro-ph.HE\]](#) (pp. 27, 29, 77, 78, 79, 80).
- [144] **DES, Fermi-LAT** collaboration, A. Albert et al., *Searching for Dark Matter Annihilation in Recently Discovered Milky Way Satellites with Fermi-LAT*, *Astrophys. J.* 834.2 (2017), p. 110, arXiv: [1611.03184 \[astro-ph.HE\]](#) (pp. 27, 29).
- [145] L. Goodenough and D. Hooper, *Possible Evidence For Dark Matter Annihilation In The Inner Milky Way From The Fermi Gamma Ray Space Telescope*, (2009), arXiv: [0910.2998 \[hep-ph\]](#) (p. 28).
- [146] T. Daylan, D. P. Finkbeiner, D. Hooper, T. Linden, S. K. N. Portillo, N. L. Rodd, and T. R. Slatyer, *The characterization of the gamma-ray signal from the central Milky Way: A case for annihilating dark matter*, *Phys. Dark Univ.* 12 (2016), pp. 1–23, arXiv: [1402.6703 \[astro-ph.HE\]](#) (p. 28).

- [147] K. N. Abazajian, *The Consistency of Fermi-LAT Observations of the Galactic Center with a Millisecond Pulsar Population in the Central Stellar Cluster*, JCAP 1103 (2011), p. 010, arXiv: [1011.4275 \[astro-ph.HE\]](#) (p. 28).
- [148] J. Petrović, P. D. Serpico, and G. Zaharijas, *Millisecond pulsars and the Galactic Center gamma-ray excess: the importance of luminosity function and secondary emission*, JCAP 1502.02 (2015), p. 023, arXiv: [1411.2980 \[astro-ph.HE\]](#) (p. 28).
- [149] R. Bartels, S. Krishnamurthy, and C. Weniger, *Strong support for the millisecond pulsar origin of the Galactic center GeV excess*, Phys. Rev. Lett. 116.5 (2016), p. 051102, arXiv: [1506.05104 \[astro-ph.HE\]](#) (p. 28).
- [150] S. K. Lee, M. Lisanti, B. R. Safdi, T. R. Slatyer, and W. Xue, *Evidence for Unresolved γ -Ray Point Sources in the Inner Galaxy*, Phys. Rev. Lett. 116.5 (2016), p. 051103, arXiv: [1506.05124 \[astro-ph.HE\]](#) (p. 28).
- [151] E. Carlson and S. Profumo, *Cosmic Ray Protons in the Inner Galaxy and the Galactic Center Gamma-Ray Excess*, Phys. Rev. D90.2 (2014), p. 023015, arXiv: [1405.7685 \[astro-ph.HE\]](#) (p. 28).
- [152] J. Petrović, P. D. Serpico, and G. Zaharijaš, *Galactic Center gamma-ray "excess" from an active past of the Galactic Centre?*, JCAP 1410.10 (2014), p. 052, arXiv: [1405.7928 \[astro-ph.HE\]](#) (p. 28).
- [153] I. Cholis, C. Evoli, F. Calore, T. Linden, C. Weniger, and D. Hooper, *The Galactic Center GeV Excess from a Series of Leptonic Cosmic-Ray Outbursts*, JCAP 1512.12 (2015), p. 005, arXiv: [1506.05119 \[astro-ph.HE\]](#) (p. 28).
- [154] D. Gaggero, A. Urbano, M. Valli, and P. Ullio, *Gamma-ray sky points to radial gradients in cosmic-ray transport*, Phys. Rev. D91.8 (2015), p. 083012, arXiv: [1411.7623 \[astro-ph.HE\]](#) (p. 28).
- [155] D. Gaggero, M. Taoso, A. Urbano, M. Valli, and P. Ullio, *Towards a realistic astrophysical interpretation of the gamma-ray Galactic center excess*, JCAP 1512 (2015), p. 056, arXiv: [1507.06129 \[astro-ph.HE\]](#) (p. 28).
- [156] E. Carlson, T. Linden, and S. Profumo, *Cosmic-Ray Injection from Star-Forming Regions*, Phys. Rev. Lett. 117.11 (2016), p. 111101, arXiv: [1510.04698 \[astro-ph.HE\]](#) (p. 28).
- [157] A. Boyarsky, O. Ruchayskiy, D. Iakubovskiy, and J. Franse, *Unidentified Line in X-Ray Spectra of the Andromeda Galaxy and Perseus Galaxy Cluster*, Phys. Rev. Lett. 113 (2014), p. 251301, arXiv: [1402.4119 \[astro-ph.CO\]](#) (p. 28).
- [158] E. Bulbul, M. Markevitch, A. Foster, R. K. Smith, M. Loewenstein, and S. W. Randall, *Detection of An Unidentified Emission Line in the Stacked X-ray spectrum of Galaxy Clusters*, Astrophys. J. 789 (2014), p. 13, arXiv: [1402.2301 \[astro-ph.CO\]](#) (p. 28).
- [159] M. E. Anderson, E. Churazov, and J. N. Bregman, *Non-Detection of X-Ray Emission From Sterile Neutrinos in Stacked Galaxy Spectra*, Mon. Not. Roy. Astron. Soc. 452.4 (2015), pp. 3905–3923, arXiv: [1408.4115 \[astro-ph.HE\]](#) (p. 28).
- [160] E. Carlson, T. Jeltema, and S. Profumo, *Where do the 3.5 keV photons come from? A morphological study of the Galactic Center and of Perseus*, JCAP 1502.02 (2015), p. 009, arXiv: [1411.1758 \[astro-ph.HE\]](#) (p. 28).
- [161] T. E. Jeltema and S. Profumo, *Discovery of a 3.5 keV line in the Galactic Centre and a critical look at the origin of the line across astronomical targets*, Mon. Not. Roy. Astron. Soc. 450.2 (2015), pp. 2143–2152, arXiv: [1408.1699 \[astro-ph.HE\]](#) (p. 28).
- [162] A. Boyarsky, J. Franse, D. Iakubovskiy, and O. Ruchayskiy, *Comment on the paper "Dark matter searches going bananas: the contribution of Potassium (and Chlorine) to the 3.5 keV line" by T. Jeltema and S. Profumo*, (2014), arXiv: [1408.4388 \[astro-ph.CO\]](#) (p. 28).
- [163] E. Bulbul, M. Markevitch, A. R. Foster, R. K. Smith, M. Loewenstein, and S. W. Randall, *Comment on "Dark matter searches going bananas: the contribution of Potassium (and Chlorine) to the 3.5 keV line"*, (2014), arXiv: [1409.4143 \[astro-ph.HE\]](#) (p. 28).
- [164] T. Jeltema and S. Profumo, *Reply to Two Comments on "Dark matter searches going bananas the contribution of Potassium (and Chlorine) to the 3.5 keV line"*, (2014), arXiv: [1411.1759 \[astro-ph.HE\]](#) (p. 28).
- [165] R. K. Leane, T. R. Slatyer, J. F. Beacom, and K. C. Y. Ng, *GeV-scale thermal WIMPs: Not even slightly ruled out*, Phys. Rev. D98.2 (2018), p. 023016, arXiv: [1805.10305 \[hep-ph\]](#) (pp. 28, 29).

- [166] G. Steigman, B. Dasgupta, and J. F. Beacom, *Precise Relic WIMP Abundance and its Impact on Searches for Dark Matter Annihilation*, *Phys. Rev. D* 86 (2012), p. 023506, arXiv: [1204.3622 \[hep-ph\]](#) (p. 29).
- [167] **IceCube** collaboration, M. G. Aartsen et al., *Improved limits on dark matter annihilation in the Sun with the 79-string IceCube detector and implications for supersymmetry*, *JCAP* 1604.04 (2016), p. 022, arXiv: [1601.00653 \[hep-ph\]](#) (p. 30).
- [168] **Super-Kamiokande** collaboration, K. Choi et al., *Search for neutrinos from annihilation of captured low-mass dark matter particles in the Sun by Super-Kamiokande*, *Phys. Rev. Lett.* 114.14 (2015), p. 141301, arXiv: [1503.04858 \[hep-ex\]](#) (p. 30).
- [169] **ATLAS** collaboration, M. Aaboud et al., *Search for dark matter and other new phenomena in events with an energetic jet and large missing transverse momentum using the ATLAS detector*, *JHEP* 01 (2018), p. 126, arXiv: [1711.03301 \[hep-ex\]](#) (p. 30).
- [170] **CMS** collaboration, A. M. Sirunyan et al., *Search for new physics in final states with an energetic jet or a hadronically decaying W or Z boson and transverse momentum imbalance at $\sqrt{s} = 13$ TeV*, *Phys. Rev. D* 97.9 (2018), p. 092005, arXiv: [1712.02345 \[hep-ex\]](#) (p. 30).
- [171] **ATLAS** collaboration, M. Aaboud et al., *Search for dark matter at $\sqrt{s} = 13$ TeV in final states containing an energetic photon and large missing transverse momentum with the ATLAS detector*, *Eur. Phys. J. C* 77.6 (2017), p. 393, arXiv: [1704.03848 \[hep-ex\]](#) (p. 30).
- [172] **CMS** collaboration, A. M. Sirunyan et al., *Search for new physics in the monophoton final state in proton-proton collisions at $\sqrt{s} = 13$ TeV*, *JHEP* 10 (2017), p. 073, arXiv: [1706.03794 \[hep-ex\]](#) (p. 30).
- [173] **ATLAS** collaboration, M. Aaboud et al., *Search for dark matter produced in association with a hadronically decaying vector boson in pp collisions at $\sqrt{s} = 13$ TeV with the ATLAS detector*, *Phys. Lett. B* 763 (2016), pp. 251–268, arXiv: [1608.02372 \[hep-ex\]](#) (p. 30).
- [174] **CMS** collaboration, A. M. Sirunyan et al., *Search for new physics in events with a leptonically decaying Z boson and a large transverse momentum imbalance in proton-proton collisions at $\sqrt{s} = 13$ TeV*, *Eur. Phys. J. C* 78.4 (2018), p. 291, arXiv: [1711.00431 \[hep-ex\]](#) (p. 30).
- [175] **ATLAS** collaboration, G. Aad et al., *Search for dark matter in events with heavy quarks and missing transverse momentum in pp collisions with the ATLAS detector*, *Eur. Phys. J. C* 75.2 (2015), p. 92, arXiv: [1410.4031 \[hep-ex\]](#) (p. 30).
- [176] **CMS** collaboration, A. M. Sirunyan et al., *Search for dark matter produced in association with heavy-flavor quark pairs in proton-proton collisions at $\sqrt{s} = 13$ TeV*, *Eur. Phys. J. C* 77.12 (2017), p. 845, arXiv: [1706.02581 \[hep-ex\]](#) (p. 30).
- [177] **CMS** collaboration, A. M. Sirunyan et al., *Search for dark matter in events with energetic, hadronically decaying top quarks and missing transverse momentum at $\sqrt{s} = 13$ TeV*, *JHEP* 06 (2018), p. 027, arXiv: [1801.08427 \[hep-ex\]](#) (p. 30).
- [178] **ATLAS** collaboration, M. Aaboud et al., *Search for dark matter in association with a Higgs boson decaying to b-quarks in pp collisions at $\sqrt{s} = 13$ TeV with the ATLAS detector*, *Phys. Lett. B* 765 (2017), pp. 11–31, arXiv: [1609.04572 \[hep-ex\]](#) (p. 30).
- [179] **CMS** collaboration, A. M. Sirunyan et al., *Search for dark matter produced in association with a Higgs boson decaying to $\gamma\gamma$ or $\tau^+\tau^-$ at $\sqrt{s} = 13$ TeV*, Submitted to: *JHEP* (2018), arXiv: [1806.04771 \[hep-ex\]](#) (p. 30).
- [180] A. Birkedal, K. Matchev, and M. Perelstein, *Dark matter at colliders: A Model independent approach*, *Phys. Rev. D* 70 (2004), p. 077701, arXiv: [hep-ph/0403004 \[hep-ph\]](#) (pp. 31, 38).
- [181] M. Beltran, D. Hooper, E. W. Kolb, and Z. C. Krusberg, *Deducing the nature of dark matter from direct and indirect detection experiments in the absence of collider signatures of new physics*, *Phys. Rev. D* 80 (2009), p. 043509, arXiv: [0808.3384 \[hep-ph\]](#) (pp. 31, 38).
- [182] Q.-H. Cao, C.-R. Chen, C. S. Li, and H. Zhang, *Effective Dark Matter Model: Relic density, CDMS II, Fermi LAT and LHC*, *JHEP* 08 (2011), p. 018, arXiv: [0912.4511 \[hep-ph\]](#) (pp. 31, 38).
- [183] M. Beltran, D. Hooper, E. W. Kolb, Z. A. C. Krusberg, and T. M. P. Tait, *Maverick dark matter at colliders*, *JHEP* 09 (2010), p. 037, arXiv: [1002.4137 \[hep-ph\]](#) (pp. 31, 38).

- [184] J. Goodman, M. Ibe, A. Rajaraman, W. Shepherd, T. M. P. Tait, and H.-B. Yu, *Constraints on Light Majorana dark Matter from Colliders*, *Phys. Lett.* B695 (2011), pp. 185–188, arXiv: [1005.1286 \[hep-ph\]](#) (pp. [31](#), [38](#), [41](#)).
- [185] Y. Bai, P. J. Fox, and R. Harnik, *The Tevatron at the Frontier of Dark Matter Direct Detection*, *JHEP* 12 (2010), p. 048, arXiv: [1005.3797 \[hep-ph\]](#) (pp. [31](#), [38](#), [39](#), [40](#), [52](#)).
- [186] J. Goodman, M. Ibe, A. Rajaraman, W. Shepherd, T. M. P. Tait, and H.-B. Yu, *Constraints on Dark Matter from Colliders*, *Phys. Rev.* D82 (2010), p. 116010, arXiv: [1008.1783 \[hep-ph\]](#) (pp. [31](#), [38](#), [41](#)).
- [187] P. J. Fox, R. Harnik, J. Kopp, and Y. Tsai, *LEP Shines Light on Dark Matter*, *Phys. Rev.* D84 (2011), p. 014028, arXiv: [1103.0240 \[hep-ph\]](#) (pp. [31](#), [38](#), [39](#), [40](#), [49](#), [52](#), [83](#), [84](#)).
- [188] A. Rajaraman, W. Shepherd, T. M. P. Tait, and A. M. Wijangco, *LHC Bounds on Interactions of Dark Matter*, *Phys. Rev.* D84 (2011), p. 095013, arXiv: [1108.1196 \[hep-ph\]](#) (pp. [31](#), [38](#)).
- [189] P. J. Fox, R. Harnik, J. Kopp, and Y. Tsai, *Missing Energy Signatures of Dark Matter at the LHC*, *Phys. Rev.* D85 (2012), p. 056011, arXiv: [1109.4398 \[hep-ph\]](#) (pp. [31](#), [38](#), [39](#), [40](#), [52](#)).
- [190] I. M. Shoemaker and L. Vecchi, *Unitarity and Monojet Bounds on Models for DAMA, CoGeNT, and CRESST-II*, *Phys. Rev.* D86 (2012), p. 015023, arXiv: [1112.5457 \[hep-ph\]](#) (pp. [31](#), [38](#)).
- [191] H. An, X. Ji, and L.-T. Wang, *Light Dark Matter and Z' Dark Force at Colliders*, *JHEP* 07 (2012), p. 182, arXiv: [1202.2894 \[hep-ph\]](#) (pp. [31](#), [38](#), [47](#), [57](#), [64](#)).
- [192] R. C. Cotta, J. L. Hewett, M. P. Le, and T. G. Rizzo, *Bounds on Dark Matter Interactions with Electroweak Gauge Bosons*, *Phys. Rev.* D88 (2013), p. 116009, arXiv: [1210.0525 \[hep-ph\]](#) (pp. [31](#), [38](#), [39](#), [40](#), [52](#)).
- [193] H. Dreiner, M. Huck, M. Krämer, D. Schmeier, and J. Tattersall, *Illuminating Dark Matter at the ILC*, *Phys. Rev.* D87.7 (2013), p. 075015, arXiv: [1211.2254 \[hep-ph\]](#) (pp. [31](#), [38](#), [39](#), [40](#), [52](#)).
- [194] Y. J. Chae and M. Perelstein, *Dark Matter Search at a Linear Collider: Effective Operator Approach*, *JHEP* 05 (2013), p. 138, arXiv: [1211.4008 \[hep-ph\]](#) (pp. [31](#), [38](#)).
- [195] P. J. Fox and C. Williams, *Next-to-Leading Order Predictions for Dark Matter Production at Hadron Colliders*, *Phys. Rev.* D87.5 (2013), p. 054030, arXiv: [1211.6390 \[hep-ph\]](#) (pp. [31](#), [38](#), [39](#), [40](#), [52](#)).
- [196] A. De Simone, A. Monin, A. Thamm, and A. Urbano, *On the effective operators for Dark Matter annihilations*, *JCAP* 1302 (2013), p. 039, arXiv: [1301.1486 \[hep-ph\]](#) (pp. [31](#), [38](#)).
- [197] H. Dreiner, D. Schmeier, and J. Tattersall, *Contact Interactions Probe Effective Dark Matter Models at the LHC*, *EPL* 102.5 (2013), p. 51001, arXiv: [1303.3348 \[hep-ph\]](#) (pp. [31](#), [38](#), [39](#), [40](#), [52](#), [58](#)).
- [198] J.-Y. Chen, E. W. Kolb, and L.-T. Wang, *Dark matter coupling to electroweak gauge and Higgs bosons: an effective field theory approach*, *Phys. Dark Univ.* 2 (2013), pp. 200–218, arXiv: [1305.0021 \[hep-ph\]](#) (pp. [31](#), [38](#), [39](#), [40](#), [52](#)).
- [199] A. Friedland, M. L. Graesser, I. M. Shoemaker, and L. Vecchi, *Probing Nonstandard Standard Model Backgrounds with LHC Monojets*, *Phys. Lett.* B714 (2012), pp. 267–275, arXiv: [1111.5331 \[hep-ph\]](#) (pp. [31](#), [39](#), [40](#), [52](#)).
- [200] O. Buchmueller, M. J. Dolan, and C. McCabe, *Beyond Effective Field Theory for Dark Matter Searches at the LHC*, *JHEP* 01 (2014), p. 025, arXiv: [1308.6799 \[hep-ph\]](#) (pp. [31](#), [39](#), [40](#), [49](#), [50](#), [52](#), [63](#)).
- [201] A. Berlin, T. Lin, and L.-T. Wang, *Mono-Higgs Detection of Dark Matter at the LHC*, *JHEP* 06 (2014), p. 078, arXiv: [1402.7074 \[hep-ph\]](#) (pp. [31](#), [39](#), [40](#), [52](#)).
- [202] C. Englert and M. Spannowsky, *Effective Theories and Measurements at Colliders*, *Phys. Lett.* B740 (2015), pp. 8–15, arXiv: [1408.5147 \[hep-ph\]](#) (pp. [31](#), [39](#), [40](#), [52](#)).
- [203] M. R. Buckley, D. Feld, and D. Goncalves, *Scalar Simplified Models for Dark Matter*, *Phys. Rev.* D91 (2015), p. 015017, arXiv: [1410.6497 \[hep-ph\]](#) (pp. [31](#), [39](#), [40](#), [52](#)).
- [204] G. Busoni, A. De Simone, E. Morgante, and A. Riotto, *On the Validity of the Effective Field Theory for Dark Matter Searches at the LHC*, *Phys. Lett.* B728 (2014), pp. 412–421, arXiv: [1307.2253 \[hep-ph\]](#) (pp. [31](#), [39](#), [40](#), [52](#), [53](#), [63](#)).

- [205] G. Busoni, A. De Simone, J. Gramling, E. Morgante, and A. Riotto, *On the Validity of the Effective Field Theory for Dark Matter Searches at the LHC, Part II: Complete Analysis for the s-channel*, JCAP 1406 (2014), p. 060, arXiv: [1402.1275 \[hep-ph\]](#) (pp. [31](#), [32](#), [39](#), [40](#), [41](#), [52](#), [53](#), [63](#)).
- [206] G. Busoni, A. De Simone, T. Jacques, E. Morgante, and A. Riotto, *On the Validity of the Effective Field Theory for Dark Matter Searches at the LHC Part III: Analysis for the t-channel*, JCAP 1409 (2014), p. 022, arXiv: [1405.3101 \[hep-ph\]](#) (pp. [31](#), [39](#), [40](#), [41](#), [52](#), [53](#), [63](#)).
- [207] E. Dudas, Y. Mambrini, S. Pokorski, and A. Romagnoni, *(In)visible Z-prime and dark matter*, JHEP 08 (2009), p. 014, arXiv: [0904.1745 \[hep-ph\]](#) (pp. [32](#), [64](#)).
- [208] J. Goodman and W. Shepherd, *LHC Bounds on UV-Complete Models of Dark Matter*, (2011), arXiv: [1111.2359 \[hep-ph\]](#) (p. [32](#)).
- [209] M. T. Frandsen, F. Kahlhoefer, A. Preston, S. Sarkar, and K. Schmidt-Hoberg, *LHC and Tevatron Bounds on the Dark Matter Direct Detection Cross-Section for Vector Mediators*, JHEP 07 (2012), p. 123, arXiv: [1204.3839 \[hep-ph\]](#) (pp. [32](#), [64](#)).
- [210] R. C. Cotta, A. Rajaraman, T. M. P. Tait, and A. M. Wijangco, *Particle Physics Implications and Constraints on Dark Matter Interpretations of the CDMS Signal*, Phys. Rev. D90.1 (2014), p. 013020, arXiv: [1305.6609 \[hep-ph\]](#) (p. [32](#)).
- [211] J. Abdallah et al., *Simplified Models for Dark Matter and Missing Energy Searches at the LHC*, (2014), arXiv: [1409.2893 \[hep-ph\]](#) (p. [32](#)).
- [212] S. A. Malik et al., *Interplay and Characterization of Dark Matter Searches at Colliders and in Direct Detection Experiments*, Phys. Dark Univ. 9-10 (2015), pp. 51–58, arXiv: [1409.4075 \[hep-ex\]](#) (p. [32](#)).
- [213] G. Busoni et al., *Recommendations on presenting LHC searches for missing transverse energy signals using simplified s-channel models of dark matter*, (2016). Ed. by A. Boveia, O. Buchmuller, C. Doglioni, K. Hahn, U. Haisch, F. Kahlhoefer, et al., arXiv: [1603.04156 \[hep-ex\]](#) (pp. [32](#), [64](#), [71](#)).
- [214] A. De Simone and T. Jacques, *Simplified models vs. effective field theory approaches in dark matter searches*, Eur. Phys. J. C76.7 (2016), p. 367, arXiv: [1603.08002 \[hep-ph\]](#) (p. [32](#)).
- [215] S. Bruggisser, F. Riva, and A. Urbano, *The Last Gasp of Dark Matter Effective Theory*, JHEP 11 (2016), p. 069, arXiv: [1607.02475 \[hep-ph\]](#) (pp. [32](#), [41](#), [43](#), [54](#), [55](#)).
- [216] S. Bruggisser, F. Riva, and A. Urbano, *Strongly Interacting Light Dark Matter*, SciPost Phys. 3.3 (2017), p. 017, arXiv: [1607.02474 \[hep-ph\]](#) (pp. [32](#), [41](#), [54](#), [55](#)).
- [217] F. Pobbe, A. Wulzer, and M. Zanetti, *Setting limits on Effective Field Theories: the case of Dark Matter*, JHEP 08 (2017), p. 074, arXiv: [1704.00736 \[hep-ph\]](#) (pp. [32](#), [41](#), [55](#), [56](#)).
- [218] ATLAS collaboration, M. Aaboud et al., *Search for new phenomena in events with a photon and missing transverse momentum in pp collisions at $\sqrt{s} = 13$ TeV with the ATLAS detector*, JHEP 06 (2016), p. 059, arXiv: [1604.01306 \[hep-ex\]](#) (p. [32](#)).
- [219] ATLAS collaboration, Exotic Physics Group, *Summary plots from the ATLAS Exotic physics group*. <https://atlas.web.cern.ch/Atlas/GROUPS/PHYSICS/CombinedSummaryPlots/EXOTICS/>. [Online; accessed July 2018] (p. [32](#)).
- [220] A. Biekötter, A. Knochel, M. Krämer, D. Liu, and F. Riva, *Vices and virtues of Higgs effective field theories at large energy*, Phys. Rev. D91 (2015), p. 055029, arXiv: [1406.7320 \[hep-ph\]](#) (p. [40](#)).
- [221] J. Brehmer, A. Freitas, D. Lopez-Val, and T. Plehn, *Pushing Higgs Effective Theory to its Limits*, Phys. Rev. D93.7 (2016), p. 075014, arXiv: [1510.03443 \[hep-ph\]](#) (p. [40](#)).
- [222] R. Contino, A. Falkowski, F. Goertz, C. Grojean, and F. Riva, *On the Validity of the Effective Field Theory Approach to SM Precision Tests*, JHEP 07 (2016), p. 144, arXiv: [1604.06444 \[hep-ph\]](#) (p. [40](#)).
- [223] M. Farina, G. Panico, D. Pappadopulo, J. T. Ruderman, R. Torre, and A. Wulzer, *Energy helps accuracy: electroweak precision tests at hadron colliders*, Phys. Lett. B772 (2017), pp. 210–215, arXiv: [1609.08157 \[hep-ph\]](#) (p. [40](#)).

- [224] A. Falkowski, M. Gonzalez-Alonso, A. Greljo, D. Marzocca, and M. Son, *Anomalous Triple Gauge Couplings in the Effective Field Theory Approach at the LHC*, *JHEP* 02 (2017), p. 115, arXiv: [1609.06312 \[hep-ph\]](#) (p. 40).
- [225] R. Franceschini, G. Panico, A. Pomarol, F. Riva, and A. Wulzer, *Electroweak Precision Tests in High-Energy Diboson Processes*, *JHEP* 02 (2018), p. 111, arXiv: [1712.01310 \[hep-ph\]](#) (p. 40).
- [226] S. Alioli, M. Farina, D. Pappadopulo, and J. T. Ruderman, *Precision Probes of QCD at High Energies*, *JHEP* 07 (2017), p. 097, arXiv: [1706.03068 \[hep-ph\]](#) (p. 40).
- [227] ATLAS collaboration, G. Aad et al., *Search for New Phenomena in Monojet plus Missing Transverse Momentum Final States using 10 fb^{-1} of pp Collisions at $\sqrt{s} = 8 \text{ TeV}$ with the ATLAS detector at the LHC*. ATLAS-CONF-2012-147. 2012, URL: <https://inspirehep.net/record/1230004/files/ATLAS-CONF-2012-147.pdf> (pp. 40, 42, 43, 44, 46, 47, 49, 55, 56).
- [228] J. Alwall, R. Frederix, S. Frixione, V. Hirschi, F. Maltoni, O. Mattelaer, et al., *The automated computation of tree-level and next-to-leading order differential cross sections, and their matching to parton shower simulations*, *JHEP* 07 (2014), p. 079, arXiv: [1405.0301 \[hep-ph\]](#) (pp. 42, 43).
- [229] M. L. Graesser, I. M. Shoemaker, and L. Vecchi, *A Dark Force for Baryons*, (2011), arXiv: [1107.2666 \[hep-ph\]](#) (pp. 47, 57).
- [230] A. Alves, S. Profumo, and F. S. Queiroz, *The dark Z' portal: direct, indirect and collider searches*, *JHEP* 04 (2014), p. 063, arXiv: [1312.5281 \[hep-ph\]](#) (pp. 47, 57).
- [231] O. Lebedev and Y. Mambrini, *Axial dark matter: The case for an invisible Z'* , *Phys. Lett. B* 734 (2014), pp. 350–353, arXiv: [1403.4837 \[hep-ph\]](#) (pp. 47, 57, 64, 71).
- [232] D. Hooper, *Z' Mediated Dark Matter Models for the Galactic Center Gamma-Ray Excess*, *Phys. Rev. D* 91 (2015), p. 035025, arXiv: [1411.4079 \[hep-ph\]](#) (pp. 47, 57).
- [233] S. Chang, R. Edezhath, J. Hutchinson, and M. Luty, *Effective WIMPs*, *Phys. Rev. D* 89.1 (2014), p. 015011, arXiv: [1307.8120 \[hep-ph\]](#) (pp. 47, 58).
- [234] H. An, L.-T. Wang, and H. Zhang, *Dark matter with t -channel mediator: a simple step beyond contact interaction*, *Phys. Rev. D* 89.11 (2014), p. 115014, arXiv: [1308.0592 \[hep-ph\]](#) (pp. 47, 58).
- [235] A. DiFranzo, K. I. Nagao, A. Rajaraman, and T. M. P. Tait, *Simplified Models for Dark Matter Interacting with Quarks*, *JHEP* 11 (2013). [Erratum: *JHEP*01,162(2014)], p. 014, arXiv: [1308.2679 \[hep-ph\]](#) (pp. 47, 58).
- [236] M. Papucci, A. Vichi, and K. M. Zurek, *Monojet versus the rest of the world I: t -channel models*, *JHEP* 11 (2014), p. 024, arXiv: [1402.2285 \[hep-ph\]](#) (pp. 47, 58).
- [237] M. Garny, A. Ibarra, S. Rydbeck, and S. Vogl, *Majorana Dark Matter with a Coloured Mediator: Collider vs Direct and Indirect Searches*, *JHEP* 06 (2014), p. 169, arXiv: [1403.4634 \[hep-ph\]](#) (pp. 47, 58).
- [238] P. Harris, V. V. Khoze, M. Spannowsky, and C. Williams, *Constraining Dark Sectors at Colliders: Beyond the Effective Theory Approach*, *Phys. Rev. D* 91 (2015), p. 055009, arXiv: [1411.0535 \[hep-ph\]](#) (pp. 47, 58).
- [239] B. A. Dobrescu and F. Yu, *Coupling-mass mapping of dijet peak searches*, *Phys. Rev. D* 88.3 (2013). [Erratum: *Phys. Rev. D* 90, no. 7, 079901 (2014)], p. 035021, arXiv: [1306.2629 \[hep-ph\]](#) (p. 50).
- [240] M. de Vries, *Four-quark effective operators at hadron colliders*, *JHEP* 03 (2015), p. 095, arXiv: [1409.4657 \[hep-ph\]](#) (p. 58).
- [241] G. Arcadi, Y. Mambrini, M. H. G. Tytgat, and B. Zaldivar, *Invisible Z' and dark matter: LHC vs LUX constraints*, *JHEP* 03 (2014), p. 134, arXiv: [1401.0221 \[hep-ph\]](#) (p. 64).
- [242] X. Chu, Y. Mambrini, J. Quevillon, and B. Zaldivar, *Thermal and non-thermal production of dark matter via Z' -portal(s)*, *JCAP* 1401 (2014), p. 034, arXiv: [1306.4677 \[hep-ph\]](#) (p. 64).
- [243] E. Dudas, L. Heurtier, Y. Mambrini, and B. Zaldivar, *Extra $U(1)$, effective operators, anomalies and dark matter*, *JHEP* 11 (2013), p. 083, arXiv: [1307.0005 \[hep-ph\]](#) (p. 64).
- [244] M. Fairbairn and J. Heal, *Complementarity of dark matter searches at resonance*, *Phys. Rev. D* 90.11 (2014), p. 115019, arXiv: [1406.3288 \[hep-ph\]](#) (p. 64).

- [245] A. Alves, A. Berlin, S. Profumo, and F. S. Queiroz, *Dark Matter Complementarity and the Z' Portal*, *Phys. Rev. D* **92**, 8 (2015), p. 083004, arXiv: [1501.03490 \[hep-ph\]](#) (p. 64).
- [246] A. Alves, A. Berlin, S. Profumo, and F. S. Queiroz, *Dirac-fermionic dark matter in $U(1)_X$ models*, *JHEP* **10** (2015), p. 076, arXiv: [1506.06767 \[hep-ph\]](#) (p. 64).
- [247] F. Kahlhoefer, K. Schmidt-Hoberg, T. Schwetz, and S. Vogl, *Implications of unitarity and gauge invariance for simplified dark matter models*, *JHEP* **02** (2016), p. 016, arXiv: [1510.02110 \[hep-ph\]](#) (pp. 64, 71, 79).
- [248] M. Bauer, S. Diefenbacher, T. Plehn, M. Russell, and D. A. Camargo, *Dark Matter in Anomaly-Free Gauge Extensions*, (2018), arXiv: [1805.01904 \[hep-ph\]](#) (p. 64).
- [249] J. Ellis, M. Fairbairn, and P. Tunney, *Phenomenological Constraints on Anomaly-Free Dark Matter Models*, (2018), arXiv: [1807.02503 \[hep-ph\]](#) (p. 64).
- [250] A. Albert et al., *Recommendations of the LHC Dark Matter Working Group: Comparing LHC searches for heavy mediators of dark matter production in visible and invisible decay channels*, (2017), arXiv: [1703.05703 \[hep-ex\]](#) (pp. 64, 71).
- [251] A. Ismail, W.-Y. Keung, K.-H. Tsao, and J. Unwin, *Axial vector Z' and anomaly cancellation*, *Nucl. Phys. B* **918** (2017), pp. 220–244, arXiv: [1609.02188 \[hep-ph\]](#) (pp. 64, 71).
- [252] M. B. Green and J. H. Schwarz, *Anomaly Cancellation in Supersymmetric $D=10$ Gauge Theory and Superstring Theory*, *Phys. Lett. B* **149** (1984), pp. 117–122 (p. 64).
- [253] C. Corianò, N. Irges, and E. Kiritsis, *On the effective theory of low scale orientifold string vacua*, *Nucl. Phys. B* **746** (2006), pp. 77–135, arXiv: [hep-ph/0510332 \[hep-ph\]](#) (p. 64).
- [254] R. Armillis, C. Corianò, M. Guzzi, and S. Morelli, *An Anomalous Extra Z Prime from Intersecting Branes with Drell-Yan and Direct Photons at the LHC*, *Nucl. Phys. B* **814** (2009), pp. 156–179, arXiv: [0809.3772 \[hep-ph\]](#) (p. 64).
- [255] J. Ellis, M. Fairbairn, and P. Tunney, *Anomaly-Free Dark Matter Models are not so Simple*, *JHEP* **08** (2017), p. 053, arXiv: [1704.03850 \[hep-ph\]](#) (pp. 64, 71).
- [256] E. D’Hoker and E. Farhi, *Decoupling a Fermion in the Standard Electroweak Theory*, *Nucl. Phys. B* **248** (1984), p. 77 (p. 64).
- [257] E. D’Hoker and E. Farhi, *Decoupling a Fermion Whose Mass Is Generated by a Yukawa Coupling: The General Case*, *Nucl. Phys. B* **248** (1984), pp. 59–76 (p. 64).
- [258] J. Preskill, *Gauge anomalies in an effective field theory*, *Annals Phys.* **210** (1991), pp. 323–379 (pp. 64, 65, 67).
- [259] Y. Mambrini, *A Clear Dark Matter gamma ray line generated by the Green-Schwarz mechanism*, *JCAP* **0912** (2009), p. 005, arXiv: [0907.2918 \[hep-ph\]](#) (p. 64).
- [260] F. Domingo, O. Lebedev, Y. Mambrini, J. Quevillon, and A. Ringwald, *More on the Hypercharge Portal into the Dark Sector*, *JHEP* **09** (2013), p. 020, arXiv: [1305.6815 \[hep-ph\]](#) (p. 64).
- [261] G. Arcadi, P. Ghosh, Y. Mambrini, M. Pierre, and F. S. Queiroz, *Z' portal to Chern-Simons Dark Matter*, *JCAP* **1711.11** (2017), p. 020, arXiv: [1706.04198 \[hep-ph\]](#) (p. 64).
- [262] C.-S. Chu, P.-M. Ho, and B. Zumino, *Non-Abelian anomalies and effective actions for a homogeneous space G/H* , *Nucl. Phys. B* **475** (1996), pp. 484–504, arXiv: [hep-th/9602093 \[hep-th\]](#) (p. 64).
- [263] A. Bilal, *Lectures on Anomalies*, (2008), arXiv: [0802.0634 \[hep-th\]](#) (p. 64).
- [264] J. A. Dror, R. Lasenby, and M. Pospelov, *New constraints on light vectors coupled to anomalous currents*, *Phys. Rev. Lett.* **119**, 14 (2017), p. 141803, arXiv: [1705.06726 \[hep-ph\]](#) (p. 64).
- [265] J. Preskill, *Physics 230 notes*. <http://www.theory.caltech.edu/~preskill/ph230/notes/230Chapter3-Page23-74.pdf>. [Online]. 1983 (pp. 65, 69, 73).
- [266] P. Anastasopoulos, F. Fucito, A. Lionetto, G. Pradisi, A. Racioppi, and Y. S. Stanev, *Minimal Anomalous $U(1)$ -prime Extension of the MSSM*, *Phys. Rev. D* **78** (2008), p. 085014, arXiv: [0804.1156 \[hep-th\]](#) (p. 65).
- [267] A. Racioppi, “Anomalies, $U(1)'$ and the MSSM”. PhD thesis. Rome U., Tor Vergata, 2009, arXiv: [0907.1535 \[hep-ph\]](#), URL: <http://dspace.uniroma2.it/dspace/handle/2108/905> (pp. 65, 69, 73, 74).

- [268] E. D'Hoker and E. Farhi, *Decoupling a Fermion Whose Mass Is Generated by a Yukawa Coupling: The General Case*, *Nucl. Phys. B* 248 (1984), pp. 59–76 (p. 65).
- [269] E. D'Hoker and E. Farhi, *Decoupling a Fermion in the Standard Electroweak Theory*, *Nucl. Phys. B* 248 (1984), p. 77 (p. 65).
- [270] K. Fujikawa, *Path Integral Measure for Gauge Invariant Fermion Theories*, *Phys. Rev. Lett.* 42 (1979), pp. 1195–1198 (p. 66).
- [271] J. Wess and B. Zumino, *Consequences of anomalous Ward identities*, *Phys. Lett. B* 37 (1971), pp. 95–97 (p. 67).
- [272] N. F. Bell, Y. Cai, and R. K. Leane, *Impact of mass generation for spin-1 mediator simplified models*, *JCAP* 1701.01 (2017), p. 039, arXiv: 1610.03063 [hep-ph] (p. 71).
- [273] Y. Cui and F. D'Eramo, *Surprises from complete vector portal theories: New insights into the dark sector and its interplay with Higgs physics*, *Phys. Rev. D* 96.9 (2017), p. 095006, arXiv: 1705.03897 [hep-ph] (p. 71).
- [274] J. Kopp, L. Michaels, and J. Smirnov, *Loopy Constraints on Leptophilic Dark Matter and Internal Bremsstrahlung*, *JCAP* 1404 (2014), p. 022, arXiv: 1401.6457 [hep-ph] (p. 72).
- [275] L. Rosenberg, *Electromagnetic interactions of neutrinos*, *Phys. Rev.* 129 (1963), pp. 2786–2788 (p. 74).
- [276] T. Hahn and M. Perez-Victoria, *Automatized one loop calculations in four-dimensions and D-dimensions*, *Comput. Phys. Commun.* 118 (1999), pp. 153–165, arXiv: hep-ph/9807565 [hep-ph] (p. 74).
- [277] M. Nowakowski and A. Pilaftsis, *On gauge invariance of Breit-Wigner propagators*, *Z. Phys. C* 60 (1993), pp. 121–126, arXiv: hep-ph/9305321 [hep-ph] (p. 75).
- [278] P. Artoisenet et al., *A framework for Higgs characterisation*, *JHEP* 11 (2013), p. 043, arXiv: 1306.6464 [hep-ph] (p. 75).
- [279] C. Garcia-Cely and A. Rivera, *General calculation of the cross section for dark matter annihilations into two photons*, *JCAP* 1703.03 (2017), p. 054, arXiv: 1611.08029 [hep-ph] (p. 75).
- [280] L. D. Landau, *On the angular momentum of a system of two photons*, *Dokl. Akad. Nauk Ser. Fiz.* 60.2 (1948), pp. 207–209 (p. 75).
- [281] C.-N. Yang, *Selection Rules for the Dematerialization of a Particle Into Two Photons*, *Phys. Rev.* 77 (1950), pp. 242–245 (p. 75).
- [282] G. Arcadi, M. Dutra, P. Ghosh, M. Lindner, Y. Mambrini, M. Pierre, et al., *The waning of the WIMP? A review of models, searches, and constraints*, *Eur. Phys. J. C* 78.3 (2018), p. 203, arXiv: 1703.07364 [hep-ph] (p. 77).
- [283] **DES, Fermi-LAT** collaboration, A. Drlica-Wagner et al., *Search for Gamma-Ray Emission from DES Dwarf Spheroidal Galaxy Candidates with Fermi-LAT Data*, *Astrophys. J.* 809.1 (2015), p. L4, arXiv: 1503.02632 [astro-ph.HE] (pp. 77, 80).
- [284] **H.E.S.S.** collaboration, H. Abdallah et al., *Search for dark matter annihilations towards the inner Galactic halo from 10 years of observations with H.E.S.S.*, *Phys. Rev. Lett.* 117.11 (2016), p. 111301, arXiv: 1607.08142 [astro-ph.HE] (pp. 77, 80).
- [285] M. Cirelli, G. Corcella, A. Hektor, G. Hutsi, M. Kadastik, P. Panci, et al., *PPPC 4 DM ID: A Poor Particle Physicist Cookbook for Dark Matter Indirect Detection*, *JCAP* 1103 (2011). [Erratum: *JCAP* 1210, E01 (2012)], p. 051, arXiv: 1012.4515 [hep-ph] (pp. 78, 79).
- [286] **Fermi-LAT** collaboration, M. Ackermann et al., *Updated search for spectral lines from Galactic dark matter interactions with pass 8 data from the Fermi Large Area Telescope*, *Phys. Rev. D* 91.12 (2015), p. 122002, arXiv: 1506.00013 [astro-ph.HE] (pp. 79, 81).
- [287] **H.E.S.S.** collaboration, A. Abramowski et al., *Search for Photon-Lineline Signatures from Dark Matter Annihilations with H.E.S.S.*, *Phys. Rev. Lett.* 110 (2013), p. 041301, arXiv: 1301.1173 [astro-ph.HE] (pp. 79, 81).
- [288] **IceCube** collaboration, M. G. Aartsen et al., *Search for annihilating dark matter in the Sun with 3 years of IceCube data*, *Eur. Phys. J. C* 77.3 (2017), p. 146, arXiv: 1612.05949 [astro-ph.HE] (pp. 81, 82).
- [289] R. Catena and B. Schwabe, *Form factors for dark matter capture by the Sun in effective theories*, *JCAP* 1504.04 (2015), p. 042, arXiv: 1501.03729 [hep-ph] (p. 82).
- [290] **CMS** collaboration, V. Khachatryan et al., *Search for narrow resonances in dilepton mass spectra in proton-proton collisions at $\sqrt{s} = 13$ TeV and combination with 8 TeV data*, *Phys. Lett. B* 768 (2017), pp. 57–80, arXiv: 1609.05391 [hep-ex] (p. 83).

- [291] CMS collaboration, V. Khachatryan et al., *Search for dark matter, extra dimensions, and unparticles in monojet events in proton–proton collisions at $\sqrt{s} = 8$ TeV*, *Eur. Phys. J. C* 75.5 (2015), p. 235, arXiv: [1408.3583 \[hep-ex\]](#) (pp. 83, 84).
- [292] DELPHI collaboration, J. Abdallah et al., *Photon events with missing energy in e^+e^- collisions at $s^{*(1/2)} = 130\text{-GeV}$ to 209-GeV* , *Eur. Phys. J. C* 38 (2005), pp. 395–411, arXiv: [hep-ex/0406019 \[hep-ex\]](#) (p. 83).
- [293] DELPHI collaboration, J. Abdallah et al., *Search for one large extra dimension with the DELPHI detector at LEP*, *Eur. Phys. J. C* 60 (2009), pp. 17–23, arXiv: [0901.4486 \[hep-ex\]](#) (p. 83).
- [294] XENON collaboration, E. Aprile et al., *First Dark Matter Search Results from the XENON1T Experiment*, *Phys. Rev. Lett.* 119.18 (2017), p. 181301, arXiv: [1705.06655 \[astro-ph.CO\]](#) (p. 84).
- [295] A. L. Fitzpatrick, W. Haxton, E. Katz, N. Lubbers, and Y. Xu, *Model Independent Direct Detection Analyses*, (2012), arXiv: [1211.2818 \[hep-ph\]](#) (p. 84).
- [296] N. Anand, A. L. Fitzpatrick, and W. C. Haxton, *Weakly interacting massive particle-nucleus elastic scattering response*, *Phys. Rev. C* 89.6 (2014), p. 065501, arXiv: [1308.6288 \[hep-ph\]](#) (p. 84).
- [297] M. S. Chanowitz and M. K. Gaillard, *The TeV Physics of Strongly Interacting W 's and Z 's*, *Nucl. Phys. B* 261 (1985), pp. 379–431 (p. 88).
- [298] M. Sher, *Electroweak Higgs Potentials and Vacuum Stability*, *Phys. Rept.* 179 (1989), pp. 273–418 (p. 97).
- [299] P. B. Arnold, *Can the Electroweak Vacuum Be Unstable?*, *Phys. Rev. D* 40 (1989), p. 613 (p. 97).
- [300] G. Altarelli and G. Isidori, *Lower limit on the Higgs mass in the standard model: An Update*, *Phys. Lett. B* 337 (1994), pp. 141–144 (p. 97).
- [301] J. A. Casas, J. R. Espinosa, and M. Quiros, *Standard model stability bounds for new physics within LHC reach*, *Phys. Lett. B* 382 (1996), pp. 374–382, arXiv: [hep-ph/9603227 \[hep-ph\]](#) (p. 97).
- [302] T. Hambye and K. Riesselmann, *Matching conditions and Higgs mass upper bounds revisited*, *Phys. Rev. D* 55 (1997), pp. 7255–7262, arXiv: [hep-ph/9610272 \[hep-ph\]](#) (p. 97).
- [303] G. Isidori, G. Ridolfi, and A. Strumia, *On the metastability of the standard model vacuum*, *Nucl. Phys. B* 609 (2001), pp. 387–409, arXiv: [hep-ph/0104016 \[hep-ph\]](#) (p. 97).
- [304] J. Ellis, J. R. Espinosa, G. F. Giudice, A. Hoecker, and A. Riotto, *The Probable Fate of the Standard Model*, *Phys. Lett. B* 679 (2009), pp. 369–375, arXiv: [0906.0954 \[hep-ph\]](#) (p. 97).
- [305] F. Bezrukov, M. Yu. Kalmykov, B. A. Kniehl, and M. Shaposhnikov, *Higgs Boson Mass and New Physics*, *JHEP* 10 (2012). [[275\(2012\)](#)], p. 140, arXiv: [1205.2893 \[hep-ph\]](#) (p. 97).
- [306] A. V. Bednyakov, B. A. Kniehl, A. F. Pikelner, and O. L. Veretin, *Stability of the Electroweak Vacuum: Gauge Independence and Advanced Precision*, *Phys. Rev. Lett.* 115.20 (2015), p. 201802, arXiv: [1507.08833 \[hep-ph\]](#) (p. 97).
- [307] J. Elias-Miro, J. R. Espinosa, G. F. Giudice, G. Isidori, A. Riotto, and A. Strumia, *Higgs mass implications on the stability of the electroweak vacuum*, *Phys. Lett. B* 709 (2012), pp. 222–228, arXiv: [1112.3022 \[hep-ph\]](#) (pp. 97, 98, 101, 123).
- [308] G. Degrassi, S. Di Vita, J. Elias-Miro, J. R. Espinosa, G. F. Giudice, G. Isidori, and A. Strumia, *Higgs mass and vacuum stability in the Standard Model at NNLO*, *JHEP* 08 (2012), p. 098, arXiv: [1205.6497 \[hep-ph\]](#) (pp. 97, 98, 101, 123).
- [309] D. Buttazzo, G. Degrassi, P. P. Giardino, G. F. Giudice, F. Sala, A. Salvio, and A. Strumia, *Investigating the near-criticality of the Higgs boson*, *JHEP* 12 (2013), p. 089, arXiv: [1307.3536 \[hep-ph\]](#) (pp. 97, 98, 101, 123).
- [310] J. R. Espinosa, M. Garny, T. Konstandin, and A. Riotto, *Gauge-Independent Scales Related to the Standard Model Vacuum Instability*, *Phys. Rev. D* 95.5 (2017), p. 056004, arXiv: [1608.06765 \[hep-ph\]](#) (p. 97).
- [311] A. Salvio, A. Strumia, N. Tetradis, and A. Urbano, *On gravitational and thermal corrections to vacuum decay*, *JHEP* 09 (2016), p. 054, arXiv: [1608.02555 \[hep-ph\]](#) (p. 98).

- [312] D. H. Lyth and A. Riotto, *Particle physics models of inflation and the cosmological density perturbation*, *Phys. Rept.* 314 (1999), pp. 1–146, arXiv: [hep - ph / 9807278 \[hep-ph\]](#) (pp. 99, 101, 134).
- [313] J. R. Espinosa, G. F. Giudice, and A. Riotto, *Cosmological implications of the Higgs mass measurement*, *JCAP* 0805 (2008), p. 002, arXiv: [0710 . 2484 \[hep-ph\]](#) (pp. 99, 101, 102).
- [314] A. Kobakhidze and A. Spencer-Smith, *Electroweak Vacuum (In)Stability in an Inflationary Universe*, *Phys. Lett.* B722 (2013), pp. 130–134, arXiv: [1301 . 2846 \[hep-ph\]](#) (pp. 99, 102).
- [315] A. Kobakhidze and A. Spencer-Smith, *The Higgs vacuum is unstable*, (2014), arXiv: [1404.4709 \[hep-ph\]](#) (pp. 99, 102).
- [316] M. Fairbairn and R. Hogan, *Electroweak Vacuum Stability in light of BICEP2*, *Phys. Rev. Lett.* 112 (2014), p. 201801, arXiv: [1403.6786 \[hep-ph\]](#) (pp. 99, 102).
- [317] K. Enqvist, T. Meriniemi, and S. Nurmi, *Higgs Dynamics during Inflation*, *JCAP* 1407 (2014), p. 025, arXiv: [1404 . 3699 \[hep-ph\]](#) (pp. 99, 102).
- [318] A. Hook, J. Kearney, B. Shakya, and K. M. Zurek, *Probable or Improbable Universe? Correlating Electroweak Vacuum Instability with the Scale of Inflation*, *JHEP* 01 (2015), p. 061, arXiv: [1404.5953 \[hep-ph\]](#) (pp. 99, 102).
- [319] K. Kamada, *Inflationary cosmology and the standard model Higgs with a small Hubble induced mass*, *Phys. Lett.* B742 (2015), pp. 126–135, arXiv: [1409 . 5078 \[hep-ph\]](#) (pp. 99, 102).
- [320] A. Shkerin and S. Sibiryakov, *On stability of electroweak vacuum during inflation*, *Phys. Lett.* B746 (2015), pp. 257–260, arXiv: [1503 . 02586 \[hep-ph\]](#) (pp. 99, 102).
- [321] J. Kearney, H. Yoo, and K. M. Zurek, *Is a Higgs Vacuum Instability Fatal for High-Scale Inflation?*, *Phys. Rev.* D91.12 (2015), p. 123537, arXiv: [1503 . 05193 \[hep-th\]](#) (pp. 99, 102).
- [322] W. E. East, J. Kearney, B. Shakya, H. Yoo, and K. M. Zurek, *Spacetime Dynamics of a Higgs Vacuum Instability During Inflation*, *Phys. Rev.* D95.2 (2017), p. 023526, arXiv: [1607.00381 \[hep-ph\]](#) (pp. 99, 102).
- [323] M. Herranen, T. Markkanen, S. Nurmi, and A. Rajantie, *Spacetime curvature and the Higgs stability during inflation*, *Phys. Rev. Lett.* 113.21 (2014), p. 211102, arXiv: [1407 . 3141 \[hep-ph\]](#) (pp. 99, 101, 102).
- [324] J. R. Espinosa, G. F. Giudice, E. Morgante, A. Riotto, L. Senatore, A. Strumia, and N. Tetradis, *The cosmological Higgstory of the vacuum instability*, *JHEP* 09 (2015), p. 174, arXiv: [1505 . 04825 \[hep-ph\]](#) (pp. 99, 102, 104).
- [325] Y. Ema, K. Mukaida, and K. Nakayama, *Fate of Electroweak Vacuum during Preheating*, *JCAP* 1610.10 (2016), p. 043, arXiv: [1602.00483 \[hep-ph\]](#) (p. 99).
- [326] K. Kohri and H. Matsui, *Higgs vacuum metastability in primordial inflation, preheating, and reheating*, *Phys. Rev.* D94.10 (2016), p. 103509, arXiv: [1602 . 02100 \[hep-ph\]](#) (p. 99).
- [327] K. Enqvist, M. Karciauskas, O. Lebedev, S. Rusak, and M. Zatta, *Postinflationary vacuum instability and Higgs-inflaton couplings*, *JCAP* 1611 (2016), p. 025, arXiv: [1608 . 08848 \[hep-ph\]](#) (p. 99).
- [328] M. Postma and J. van de Vis, *Electroweak stability and non-minimal coupling*, *JCAP* 1705.05 (2017), p. 004, arXiv: [1702 . 07636 \[hep-ph\]](#) (p. 99).
- [329] Y. Ema, M. Karciauskas, O. Lebedev, and M. Zatta, *Early Universe Higgs dynamics in the presence of the Higgs-inflaton and non-minimal Higgs-gravity couplings*, *JCAP* 1706.06 (2017), p. 054, arXiv: [1703 . 04681 \[hep-ph\]](#) (p. 99).
- [330] A. Joti, A. Katsis, D. Loupas, A. Salvio, A. Strumia, N. Tetradis, and A. Urbano, *(Higgs) vacuum decay during inflation*, *JHEP* 07 (2017), p. 058, arXiv: [1706 . 00792 \[hep-ph\]](#) (p. 99).
- [331] A. Rajantie and S. Stopyra, *Standard Model vacuum decay in a de Sitter Background*, *Phys. Rev.* D97.2 (2018), p. 025012, arXiv: [1707 . 09175 \[hep-th\]](#) (p. 99).
- [332] D. G. Figueroa, A. Rajantie, and F. Torrenti, *Higgs-curvature coupling and post-inflationary vacuum instability*, (2017), arXiv: [1709.00398 \[astro-ph.CO\]](#) (p. 99).

- [333] S. Clesse and J. García-Bellido, *Massive Primordial Black Holes from Hybrid Inflation as Dark Matter and the seeds of Galaxies*, *Phys. Rev. D* 92.2 (2015), p. 023524, arXiv: [1501.07565 \[astro-ph.CO\]](#) (p. 99).
- [334] J. García-Bellido, *Massive Primordial Black Holes as Dark Matter and their detection with Gravitational Waves*, *J. Phys. Conf. Ser.* 840.1 (2017), p. 012032, arXiv: [1702.08275 \[astro-ph.CO\]](#) (p. 99).
- [335] D. H. Lyth and D. Wands, *Generating the curvature perturbation without an inflaton*, *Phys. Lett. B* 524 (2002), pp. 5–14, arXiv: [hep-ph/0110002 \[hep-ph\]](#) (pp. 101, 103).
- [336] V. F. Mukhanov, H. A. Feldman, and R. H. Brandenberger, *Theory of cosmological perturbations. Part 1. Classical perturbations. Part 2. Quantum theory of perturbations. Part 3. Extensions*, *Phys. Rept.* 215 (1992), pp. 203–333 (p. 103).
- [337] P. Elmfors, K. Enqvist, and I. Vilja, *Thermalization of the Higgs field at the electroweak phase transition*, *Nucl. Phys. B* 412 (1994), pp. 459–478, arXiv: [hep-ph/9307210 \[hep-ph\]](#) (p. 104).
- [338] N. Bartolo, S. Matarrese, and A. Riotto, *Evolution of second - order cosmological perturbations and non-Gaussianity*, *JCAP* 0401 (2004), p. 003, arXiv: [astro-ph/0309692 \[astro-ph\]](#) (pp. 105, 128).
- [339] Y. B. Zel'dovich and I. D. Novikov, *The Hypothesis of Cores Retarded during Expansion and the Hot Cosmological Model*, *Astron. Zh.* 43 (1966), p. 758 (p. 108).
- [340] Y. B. Zel'dovich and I. D. Novikov, *Sov. Astron.* 10 (1967), p. 602 (p. 108).
- [341] S. Hawking, *Gravitationally collapsed objects of very low mass*, *Mon. Not. Roy. Astron. Soc.* 152 (1971), p. 75 (p. 108).
- [342] G. F. Chapline, *Cosmological effects of primordial black holes*, *Nature* 253 (1975), pp. 251–252 (p. 108).
- [343] **Virgo, LIGO Scientific** collaboration, B. P. Abbott et al., *Observation of Gravitational Waves from a Binary Black Hole Merger*, *Phys. Rev. Lett.* 116.6 (2016), p. 061102, arXiv: [1602.03837 \[gr-qc\]](#) (pp. 108, 131).
- [344] B. Carr, F. Kuhnel, and M. Sandstad, *Primordial Black Holes as Dark Matter*, *Phys. Rev. D* 94.8 (2016), p. 083504, arXiv: [1607.06077 \[astro-ph.CO\]](#) (pp. 108, 110, 111).
- [345] M. Sasaki, T. Suyama, T. Tanaka, and S. Yokoyama, *Primordial black holes—perspectives in gravitational wave astronomy*, *Class. Quant. Grav.* 35.6 (2018), p. 063001, arXiv: [1801.05235 \[astro-ph.CO\]](#) (pp. 108, 110, 111, 131).
- [346] L. Barack et al., *Black holes, gravitational waves and fundamental physics: a roadmap*, (2018), arXiv: [1806.05195 \[gr-qc\]](#) (p. 108).
- [347] B. Carr and J. Silk, *Primordial Black Holes as Generators of Cosmic Structures*, (2018), arXiv: [1801.00672 \[astro-ph.CO\]](#) (pp. 108, 109).
- [348] M. Mezcua, *Observational evidence for intermediate-mass black holes*, *Int. J. Mod. Phys. D* 26.11 (2017), p. 1730021, arXiv: [1705.09667 \[astro-ph.GA\]](#) (p. 109).
- [349] K. Belczynski, T. Bulik, C. L. Fryer, A. Ruitter, J. S. Vink, and J. R. Hurley, *On The Maximum Mass of Stellar Black Holes*, *Astrophys. J.* 714 (2010), pp. 1217–1226, arXiv: [0904.2784 \[astro-ph.SR\]](#) (p. 109).
- [350] S. Clesse and J. García-Bellido, *Seven Hints for Primordial Black Hole Dark Matter*, (2017), arXiv: [1711.10458 \[astro-ph.CO\]](#) (p. 109).
- [351] K. Belczynski et al., *The Effect of Pair-Instability Mass Loss on Black Hole Mergers*, *Astron. Astrophys.* 594 (2016), A97, arXiv: [1607.03116 \[astro-ph.HE\]](#) (p. 109).
- [352] C.-M. Yoo, T. Harada, J. Garriga, and K. Kohri, *PBH abundance from random Gaussian curvature perturbations and a local density threshold*, (2018), arXiv: [1805.03946 \[astro-ph.CO\]](#) (pp. 110, 118).
- [353] C. Germani and I. Musco, *The abundance of primordial black holes depends on the shape of the inflationary power spectrum*, (2018), arXiv: [1805.04087 \[astro-ph.CO\]](#) (pp. 110, 118).
- [354] J. R. Chisholm, *Primordial Black Hole Minimum Mass*, *Phys. Rev. D* 74 (2006), p. 043512, arXiv: [astro-ph/0604174 \[astro-ph\]](#) (p. 110).
- [355] I. Musco and J. C. Miller, *Primordial black hole formation in the early universe: critical behaviour and self-similarity*, *Class. Quant. Grav.* 30 (2013), p. 145009, arXiv: [1201.2379 \[gr-qc\]](#) (p. 110).
- [356] B. J. Carr, *The Primordial black hole mass spectrum*, *Astrophys. J.* 201 (1975), pp. 1–19 (p. 110).

- [357] G. Ballesteros and M. Taoso, *Primordial black hole dark matter from single field inflation*, *Phys. Rev. D* 97.2 (2018), p. 023501, arXiv: [1709.05565 \[hep-ph\]](#) (pp. [110](#), [115](#)).
- [358] J. Garcia-Bellido, M. Peloso, and C. Unal, *Gravitational waves at interferometer scales and primordial black holes in axion inflation*, *JCAP* 1612.12 (2016), p. 031, arXiv: [1610.03763 \[astro-ph.CO\]](#) (p. [110](#)).
- [359] G. Franciolini, A. Kehagias, S. Matarrese, and A. Riotto, *Primordial Black Holes from Inflation and non-Gaussianity*, *JCAP* 1803.03 (2018), p. 016, arXiv: [1801.09415 \[astro-ph.CO\]](#) (p. [110](#)).
- [360] K. Inomata, M. Kawasaki, K. Mukaida, Y. Tada, and T. T. Yanagida, *Inflationary Primordial Black Holes as All Dark Matter*, *Phys. Rev. D* 96.4 (2017), p. 043504, arXiv: [1701.02544 \[astro-ph.CO\]](#) (pp. [111](#), [112](#)).
- [361] B. Carr, M. Raidal, T. Tenkanen, V. Vaskonen, and H. Veermäe, *Primordial black hole constraints for extended mass functions*, *Phys. Rev. D* 96.2 (2017), p. 023514, arXiv: [1705.05567 \[astro-ph.CO\]](#) (p. [111](#)).
- [362] A. M. Green, *Microlensing and dynamical constraints on primordial black hole dark matter with an extended mass function*, *Phys. Rev. D* 94.6 (2016), p. 063530, arXiv: [1609.01143 \[astro-ph.CO\]](#) (p. [111](#)).
- [363] J. García-Bellido and S. Clesse, *Constraints from microlensing experiments on clustered primordial black holes*, *Phys. Dark Univ.* 19 (2018), pp. 144–148, arXiv: [1710.04694 \[astro-ph.CO\]](#) (p. [111](#)).
- [364] B. J. Carr, K. Kohri, Y. Sendouda, and J. Yokoyama, *New cosmological constraints on primordial black holes*, *Phys. Rev. D* 81 (2010), p. 104019, arXiv: [0912.5297 \[astro-ph.CO\]](#) (pp. [112](#), [119](#)).
- [365] M. Boudaud and M. Cirelli, *Voyager-1 e^\pm further constrain Primordial Black Holes as Dark Matter*, (2018), arXiv: [1807.03075 \[astro-ph.HE\]](#) (p. [112](#)).
- [366] M. Raidal, S. Solodukhin, V. Vaskonen, and H. Veermäe, *Light Primordial Exotic Compact Objects as All Dark Matter*, *Phys. Rev. D* 97 (2018), p. 123520, arXiv: [1802.07728 \[astro-ph.CO\]](#) (p. [112](#)).
- [367] Y. Ali-Haïmoud and M. Kamionkowski, *Cosmic microwave background limits on accreting primordial black holes*, *Phys. Rev. D* 95.4 (2017), p. 043534, arXiv: [1612.05644 \[astro-ph.CO\]](#) (p. [112](#)).
- [368] D. Aloni, K. Blum, and R. Flauger, *Cosmic microwave background constraints on primordial black hole dark matter*, *JCAP* 1705.05 (2017), p. 017, arXiv: [1612.06811 \[astro-ph.CO\]](#) (p. [112](#)).
- [369] B. Horowitz, *Revisiting Primordial Black Holes Constraints from Ionization History*, (2016), arXiv: [1612.07264 \[astro-ph.CO\]](#) (p. [112](#)).
- [370] V. Poulin, P. D. Serpico, F. Calore, S. Clesse, and K. Kohri, *CMB bounds on disk-accreting massive primordial black holes*, *Phys. Rev. D* 96.8 (2017), p. 083524, arXiv: [1707.04206 \[astro-ph.CO\]](#) (p. [112](#)).
- [371] **EROS-2** collaboration, P. Tisserand et al., *Limits on the Macho Content of the Galactic Halo from the EROS-2 Survey of the Magellanic Clouds*, *Astron. Astrophys.* 469 (2007), pp. 387–404, arXiv: [astro-ph/0607207 \[astro-ph\]](#) (p. [113](#)).
- [372] K. Griest, A. M. Cieplak, and M. J. Lehner, *New Limits on Primordial Black Hole Dark Matter from an Analysis of Kepler Source Microlensing Data*, *Phys. Rev. Lett.* 111.18 (2013), p. 181302 (p. [113](#)).
- [373] H. Niihura, M. Takada, N. Yasuda, R. H. Lupton, T. Sumi, S. More, et al., *Microlensing constraints on primordial black holes with the Subaru/HSC Andromeda observation*, (2017), arXiv: [1701.02151 \[astro-ph.CO\]](#) (p. [113](#)).
- [374] J. J. Dalcanton et al., *The Panchromatic Hubble Andromeda Treasury*, *Astrophys. J. Suppl.* 200 (2012), p. 18, arXiv: [1204.0010 \[astro-ph.CO\]](#) (p. [113](#)).
- [375] M. Zumalacarregui and U. Seljak, *No LIGO MACHO: Primordial Black Holes, Dark Matter and Gravitational Lensing of Type Ia Supernovae*, (2017), arXiv: [1712.02240 \[astro-ph.CO\]](#) (p. [113](#)).
- [376] J. Garcia-Bellido, S. Clesse, and P. Fleury, *Primordial black holes survive SN lensing constraints*, *Phys. Dark Univ.* 20 (2018), pp. 95–100, arXiv: [1712.06574 \[astro-ph.CO\]](#) (p. [113](#)).

- [377] A. Barnacka, J. F. Glicenstein, and R. Moderski, *New constraints on primordial black holes abundance from femtolensing of gamma-ray bursts*, *Phys. Rev. D* 86 (2012), p. 043001, arXiv: [1204.2056 \[astro-ph.CO\]](#) (p. 113).
- [378] A. Katz, J. Kopp, S. Sibiryakov, and W. Xue, *Femtolensing by Dark Matter Revisited*, Submitted to: *JCAP* (2018), arXiv: [1807.11495 \[astro-ph.CO\]](#) (p. 113).
- [379] A. Gould, *Femto microlensing of gamma-ray bursters*, *Astrophys. J. Lett.* 386 (1992), p. L5 (p. 113).
- [380] T. T. Nakamura, *Gravitational lensing of gravitational waves from inspiraling binaries by a point mass lens*, *Phys. Rev. Lett.* 80 (1998), pp. 1138–1141 (p. 113).
- [381] P. W. Graham, S. Rajendran, and J. Varela, *Dark Matter Triggers of Supernovae*, *Phys. Rev. D* 92.6 (2015), p. 063007, arXiv: [1505.04444 \[hep-ph\]](#) (p. 114).
- [382] F. Capela, M. Pshirkov, and P. Tinyakov, *Constraints on primordial black holes as dark matter candidates from capture by neutron stars*, *Phys. Rev. D* 87.12 (2013), p. 123524, arXiv: [1301.4984 \[astro-ph.CO\]](#) (p. 114).
- [383] T. D. Brandt, *Constraints on MACHO Dark Matter from Compact Stellar Systems in Ultra-Faint Dwarf Galaxies*, *Astrophys. J.* 824.2 (2016), p. L31, arXiv: [1605.03665 \[astro-ph.GA\]](#) (p. 114).
- [384] F. L. Bezrukov and M. Shaposhnikov, *The Standard Model Higgs boson as the inflaton*, *Phys. Lett.* B659 (2008), pp. 703–706, arXiv: [0710.3755 \[hep-th\]](#) (p. 115).
- [385] F. Bezrukov and M. Shaposhnikov, *Standard Model Higgs boson mass from inflation: Two loop analysis*, *JHEP* 07 (2009), p. 089, arXiv: [0904.1537 \[hep-ph\]](#) (p. 115).
- [386] J. L. F. Barbon and J. R. Espinosa, *On the Naturalness of Higgs Inflation*, *Phys. Rev. D* 79 (2009), p. 081302, arXiv: [0903.0355 \[hep-ph\]](#) (p. 115).
- [387] G. F. Giudice and H. M. Lee, *Unitarizing Higgs Inflation*, *Phys. Lett.* B694 (2011), pp. 294–300, arXiv: [1010.1417 \[hep-ph\]](#) (p. 115).
- [388] J. L. F. Barbon, J. A. Casas, J. Elias-Miro, and J. R. Espinosa, *Higgs Inflation as a Mirage*, *JHEP* 09 (2015), p. 027, arXiv: [1501.02231 \[hep-ph\]](#) (p. 115).
- [389] J. M. Ezquiaga, J. Garcia-Bellido, and E. Ruiz Morales, *Primordial Black Hole production in Critical Higgs Inflation*, *Phys. Lett.* B776 (2018), pp. 345–349, arXiv: [1705.04861 \[astro-ph.CO\]](#) (p. 115).
- [390] F. Bezrukov and M. Shaposhnikov, *Higgs inflation at the critical point*, *Phys. Lett.* B734 (2014), pp. 249–254, arXiv: [1403.6078 \[hep-ph\]](#) (p. 115).
- [391] Y. Hamada, H. Kawai, K.-y. Oda, and S. C. Park, *Higgs Inflation is Still Alive after the Results from BICEP2*, *Phys. Rev. Lett.* 112.24 (2014), p. 241301, arXiv: [1403.5043 \[hep-ph\]](#) (p. 115).
- [392] Y. Hamada, H. Kawai, K.-y. Oda, and S. C. Park, *Higgs inflation from Standard Model criticality*, *Phys. Rev. D* 91 (2015), p. 053008, arXiv: [1408.4864 \[hep-ph\]](#) (p. 115).
- [393] I. Masina, *Ruling out Critical Higgs Inflation?*, (2018), arXiv: [1805.02160 \[hep-ph\]](#) (p. 115).
- [394] M. Cicoli, V. A. Diaz, and F. G. Pedro, *Primordial Black Holes from String Inflation*, *JCAP* 1806.06 (2018), p. 034, arXiv: [1803.02837 \[hep-th\]](#) (p. 115).
- [395] O. Özsoy, S. Parameswaran, G. Tasinato, and I. Zavala, *Mechanisms for Primordial Black Hole Production in String Theory*, *JCAP* 1807.07 (2018), p. 005, arXiv: [1803.07626 \[hep-th\]](#) (p. 115).
- [396] I. Dalianis, A. Kehagias, and G. Tringas, *Primordial Black Holes from α -attractors*, (2018), arXiv: [1805.09483 \[astro-ph.CO\]](#) (p. 115).
- [397] M. Biagetti, G. Franciolini, A. Kehagias, and A. Riotto, *Primordial Black Holes from Inflation and Quantum Diffusion*, *JCAP* 1807.07 (2018), p. 032, arXiv: [1804.07124 \[astro-ph.CO\]](#) (p. 116).
- [398] V. Desjacques and A. Riotto, *The Spatial Clustering of Primordial Black Holes*, (2018), arXiv: [1806.10414 \[astro-ph.CO\]](#) (p. 116).
- [399] J. Yokoyama, *Chaotic new inflation and formation of primordial black holes*, *Phys. Rev. D* 58 (1998), p. 083510, arXiv: [astro-ph/9802357 \[astro-ph\]](#) (p. 116).
- [400] J. Garcia-Bellido, A. D. Linde, and D. Wands, *Density perturbations and black hole formation in hybrid inflation*, *Phys. Rev. D* 54 (1996), pp. 6040–6058, arXiv: [astro-ph/9605094 \[astro-ph\]](#) (p. 116).

- [401] M. Kawasaki, N. Sugiyama, and T. Yanagida, *Primordial black hole formation in a double inflation model in supergravity*, *Phys. Rev. D* 57 (1998), pp. 6050–6056, arXiv: [hep-ph/9710259](#) [[hep-ph](#)] (p. 116).
- [402] M. Kawasaki, T. Takayama, M. Yamaguchi, and J. Yokoyama, *Power Spectrum of the Density Perturbations From Smooth Hybrid New Inflation Model*, *Phys. Rev. D* 74 (2006), p. 043525, arXiv: [hep-ph/0605271](#) [[hep-ph](#)] (p. 116).
- [403] M. Kawasaki, A. Kusenko, Y. Tada, and T. T. Yanagida, *Primordial black holes as dark matter in supergravity inflation models*, *Phys. Rev. D* 94.8 (2016), p. 083523, arXiv: [1606.07631](#) [[astro-ph.CO](#)] (p. 116).
- [404] J. Yokoyama, *Formation of MACHO primordial black holes in inflationary cosmology*, *Astron. Astrophys.* 318 (1997), p. 673, arXiv: [astro-ph/9509027](#) [[astro-ph](#)] (p. 116).
- [405] K. Ando, K. Inomata, M. Kawasaki, K. Mukaida, and T. T. Yanagida, *Primordial Black Holes for the LIGO Events in the Axion-like Curvaton Model*, (2017), arXiv: [1711.08956](#) [[astro-ph.CO](#)] (pp. 116, 133).
- [406] E. Cotner, A. Kusenko, and V. Takhistov, *Primordial Black Holes from Inflaton Fragmentation into Oscillons*, (2018), arXiv: [1801.03321](#) [[astro-ph.CO](#)] (p. 116).
- [407] E. Cotner and A. Kusenko, *Primordial black holes from supersymmetry in the early universe*, *Phys. Rev. Lett.* 119.3 (2017), p. 031103, arXiv: [1612.02529](#) [[astro-ph.CO](#)] (p. 116).
- [408] F. Ferrer, E. Masso, G. Panico, O. Pujolas, and F. Rompineve, *Primordial Black Holes from the QCD axion*, (2018), arXiv: [1807.01707](#) [[hep-ph](#)] (p. 116).
- [409] L. Amendola, J. Rubio, and C. Wetterich, *Primordial black holes from fifth forces*, *Phys. Rev. D* 97.8 (2018), p. 081302, arXiv: [1711.09915](#) [[astro-ph.CO](#)] (p. 116).
- [410] K. Jedamzik and J. C. Niemeyer, *Primordial black hole formation during first order phase transitions*, *Phys. Rev. D* 59 (1999), p. 124014, arXiv: [astro-ph/9901293](#) [[astro-ph](#)] (p. 118).
- [411] F. Kühnel and M. Sandstad, *Ellipsoidal collapse and primordial black hole formation*, *Phys. Rev. D* 94.6 (2016), p. 063514, arXiv: [1602.04815](#) [[astro-ph.CO](#)] (p. 118).
- [412] M. Shibata and M. Sasaki, *Black hole formation in the Friedmann universe: Formulation and computation in numerical relativity*, *Phys. Rev. D* 60 (1999), p. 084002, arXiv: [gr-qc/9905064](#) [[gr-qc](#)] (p. 118).
- [413] K. A. Malik and D. Wands, *Evolution of second-order cosmological perturbations*, *Class. Quant. Grav.* 21 (2004), pp. L65–L72, arXiv: [astro-ph/0307055](#) [[astro-ph](#)] (pp. 118, 128).
- [414] M. Maggiore and A. Riotto, *The Halo mass function from excursion set theory. III. Non-Gaussian fluctuations*, *Astrophys. J.* 717 (2010), pp. 526–541, arXiv: [0903.1251](#) [[astro-ph.CO](#)] (p. 119).
- [415] J. R. Chisholm, *Clustering of primordial black holes: basic results*, *Phys. Rev. D* 73 (2006), p. 083504, arXiv: [astro-ph/0509141](#) [[astro-ph](#)] (pp. 119, 125).
- [416] **ATLAS, CMS** collaboration, G. Aad et al., *Combined Measurement of the Higgs Boson Mass in pp Collisions at $\sqrt{s} = 7$ and 8 TeV with the ATLAS and CMS Experiments*, *Phys. Rev. Lett.* 114 (2015), p. 191803, arXiv: [1503.07589](#) [[hep-ex](#)] (pp. 119, 142).
- [417] **CMS** collaboration, V. Khachatryan et al., *Measurement of the top quark mass using proton-proton data at $\sqrt{s} = 7$ and 8 TeV*, *Phys. Rev. D* 93.7 (2016), p. 072004, arXiv: [1509.04044](#) [[hep-ex](#)] (pp. 119, 142).
- [418] **ATLAS** collaboration, M. Aaboud et al., *Measurement of the top quark mass in the $t\bar{t} \rightarrow \text{lepton} + \text{jets}$ channel from $\sqrt{s} = 8$ TeV ATLAS data*. ATLAS-CONF-2017-071. 2017, URL: <https://inspirehep.net/record/1630585/files/ATLAS-CONF-2017-071.pdf> (pp. 119, 142).
- [419] A. Vilenkin, *Quantum Fluctuations in the New Inflationary Universe*, *Nucl. Phys. B* 226 (1983), pp. 527–546 (p. 120).
- [420] A. D. Linde, *Particle physics and inflationary cosmology*, *Contemp. Concepts Phys.* 5 (1990), pp. 1–362, arXiv: [hep-th/0503203](#) [[hep-th](#)] (p. 121).
- [421] C. Gross, A. Polosa, A. Strumia, A. Urbano, and W. Xue, *Dark Matter in the Standard Model?*, (2018), arXiv: [1803.10242](#) [[hep-ph](#)] (pp. 121, 122).

- [422] A. D. Linde, D. A. Linde, and A. Mezhlumian, *From the Big Bang theory to the theory of a stationary universe*, *Phys. Rev. D* 49 (1994), pp. 1783–1826, arXiv: [gr-qc/9306035 \[gr-qc\]](#) (p. 121).
- [423] A. Linde and V. Vanchurin, *How many universes are in the multiverse?*, *Phys. Rev. D* 81 (2010), p. 083525, arXiv: [0910.1589 \[hep-th\]](#) (pp. 121, 122).
- [424] J. Elias-Miro, J. R. Espinosa, G. F. Giudice, H. M. Lee, and A. Strumia, *Stabilization of the Electroweak Vacuum by a Scalar Threshold Effect*, *JHEP* 06 (2012), p. 031, arXiv: [1203.0237 \[hep-ph\]](#) (p. 122).
- [425] N. Bartolo, S. Matarrese, and A. Riotto, *On nonGaussianity in the curvaton scenario*, *Phys. Rev. D* 69 (2004), p. 043503, arXiv: [hep-ph/0309033 \[hep-ph\]](#) (p. 128).
- [426] N. Bartolo, E. Komatsu, S. Matarrese, and A. Riotto, *Non-Gaussianity from inflation: Theory and observations*, *Phys. Rept.* 402 (2004), pp. 103–266, arXiv: [astro-ph/0406398 \[astro-ph\]](#) (p. 128).
- [427] D. H. Lyth, K. A. Malik, and M. Sasaki, *A General proof of the conservation of the curvature perturbation*, *JCAP* 0505 (2005), p. 004, arXiv: [astro-ph/0411220 \[astro-ph\]](#) (p. 129).
- [428] S. Young, C. T. Byrnes, and M. Sasaki, *Calculating the mass fraction of primordial black holes*, *JCAP* 1407 (2014), p. 045, arXiv: [1405.7023 \[gr-qc\]](#) (p. 130).
- [429] C. Caprini and D. G. Figueroa, *Cosmological Backgrounds of Gravitational Waves*, (2018), arXiv: [1801.04268 \[astro-ph.CO\]](#) (p. 132).
- [430] N. Bartolo et al., *Science with the space-based interferometer LISA. IV: Probing inflation with gravitational waves*, *JCAP* 1612.12 (2016), p. 026, arXiv: [1610.06481 \[astro-ph.CO\]](#) (pp. 132, 144, 145).
- [431] B. Sathyaprakash et al., *Scientific Objectives of Einstein Telescope*, *Class. Quant. Grav.* 29 (2012). [Erratum: *Class. Quant. Grav.* 30,079501(2013)], p. 124013, arXiv: [1206.0331 \[gr-qc\]](#) (p. 132).
- [432] **Ligo Scientific** collaboration, D. Hoakon, *Advanced LIGO: Status and prospects*, *Nuovo Cim.* C40.3 (2017), p. 119 (p. 132).
- [433] **LIGO Scientific** collaboration, B. P. Abbott et al., *Exploring the Sensitivity of Next Generation Gravitational Wave Detectors*, *Class. Quant. Grav.* 34.4 (2017), p. 044001, arXiv: [1607.08697 \[astro-ph.IM\]](#) (p. 132).
- [434] E. Thrane, *Measuring the non-Gaussian stochastic gravitational-wave background: a method for realistic interferometer data*, *Phys. Rev. D* 87.4 (2013), p. 043009, arXiv: [1301.0263 \[astro-ph.IM\]](#) (pp. 132, 145).
- [435] V. Acquaviva, N. Bartolo, S. Matarrese, and A. Riotto, *Second order cosmological perturbations from inflation*, *Nucl. Phys. B* 667 (2003), pp. 119–148, arXiv: [astro-ph/0209156 \[astro-ph\]](#) (pp. 133, 134, 138).
- [436] S. Mollerach, D. Harari, and S. Matarrese, *CMB polarization from secondary vector and tensor modes*, *Phys. Rev. D* 69 (2004), p. 063002, arXiv: [astro-ph/0310711 \[astro-ph\]](#) (pp. 133, 138).
- [437] K. N. Ananda, C. Clarkson, and D. Wands, *The Cosmological gravitational wave background from primordial density perturbations*, *Phys. Rev. D* 75 (2007), p. 123518, arXiv: [gr-qc/0612013 \[gr-qc\]](#) (pp. 133, 138).
- [438] D. Baumann, P. J. Steinhardt, K. Takahashi, and K. Ichiki, *Gravitational Wave Spectrum Induced by Primordial Scalar Perturbations*, *Phys. Rev. D* 76 (2007), p. 084019, arXiv: [hep-th/0703290 \[hep-th\]](#) (pp. 133, 138).
- [439] M. Maggiore, *Gravitational wave experiments and early universe cosmology*, *Phys. Rept.* 331 (2000), pp. 283–367, arXiv: [gr-qc/9909001 \[gr-qc\]](#) (p. 139).
- [440] H. Audley et al., *Laser Interferometer Space Antenna*, (2017), arXiv: [1702.00786 \[astro-ph.IM\]](#) (p. 143).
- [441] C. Caprini et al., *Science with the space-based interferometer eLISA. II: Gravitational waves from cosmological phase transitions*, *JCAP* 1604.04 (2016), p. 001, arXiv: [1512.06239 \[astro-ph.CO\]](#) (p. 143).
- [442] **Virgo, LIGO Scientific** collaboration, B. P. Abbott et al., *Upper Limits on the Stochastic Gravitational-Wave Background from Advanced LIGO's First Observing Run*, *Phys. Rev. Lett.* 118.12 (2017). [Erratum: *Phys. Rev. Lett.* 119,no.2,029901(2017)], p. 121101, arXiv: [1612.02029 \[gr-qc\]](#) (p. 143).

- [443] C. J. Moore, R. H. Cole, and C. P. L. Berry, *Gravitational-wave sensitivity curves*, *Class. Quant. Grav.* 32.1 (2015), p. 015014, arXiv: [1408.0740 \[gr-qc\]](#) (p. 143).
- [444] B. S. Sathyaprakash and B. F. Schutz, *Physics, Astrophysics and Cosmology with Gravitational Waves*, *Living Rev. Rel.* 12 (2009), p. 2, arXiv: [0903.0338 \[gr-qc\]](#) (p. 143).